TECHNICAL UNIVERSITY OF LIBEREC

FACULTY OF MECHANICAL ENGINEERING

DISSERTATION

Research of actual limit states and tribology of applied materials for more efficient construction and longer service life of combustion chamber components of TEDOM engines

2023 Ing. Jakub Mráz

FAKULTA STROJNÍ TUL

Disertační práce

Výzkum skutečných mezních stavů a tribologie aplikovaných materiálů k efektivnejší konstrukci a vyšší životnosti komponent spalovacího prostoru motoru TEDOM

Studijní program: P2301 Strojní inženýrství
Studijní obor: Materiálové inženýrství

Autor práce: **Ing. Jakub Mráz**
Školitel práce: doc. Ing. Břetislav Skrbek, CSc.
Katedra materiálu

Liberec 2023

Prohlášení

Prohlašuji, že svou disertační práci jsem vypracoval samostatně jako původní dílo s použitím uvedené literatury a na základě konzultací s vedoucím mé disertační práce a konzultantem.

Jsem si vědom toho, že na mou disertační práci se plně vztahuje zákon č. 121/2000 Sb., o právu autorském, zejména § 60 – školní dílo.

Beru na vědomí, že Technická univerzita v Liberci nezasahuje do mých autorských práv užitím mé disertační práce pro vnitřní potřebu Technické univerzity v Liberci.

Užiji-li disertační práci nebo poskytnu-li licenci k jejímu využití, jsem si vědom povinnosti informovat o této skutečnosti Technickou univerzitu v Liberci; v tomto případě má Technická univerzita v Liberci právo ode mne požadovat úhradu nákladů, které vynaložila na vytvoření díla, až do jejich skutečné výše.

Současně čestně prohlašuji, že text elektronické podoby práce vložený do IS/STAG se shoduje s textem tištěné podoby práce.

Beru na vědomí, že má disertační práce bude zveřejněna Technickou univerzitou v Liberci v souladu s § 47b zákona č. 111/1998 Sb., o vysokých školách a o změně a doplnění dalších zákonů (zákon o vysokých školách), ve znění pozdějších předpisů.

Jsem si vědom následků, které podle zákona o vysokých školách mohou vyplývat z porušení tohoto prohlášení.

24. srpna 2023 Ing. Jakub Mráz

ABSTRACT

This study analyzes materials used in valves, valve seats, and valve guides in internal combustion engines. It aims to understand their properties and performance under varied operating conditions. The research also investigates the impact of cylinder head stiffness on valve seat wear, exploring how different seating surface geometries influence valve and seat lifespans. Additionally, a section is dedicated to the manufacturing process of cylinder heads, including the freezing of valve seats before installation, which is a crucial part of the production procedure for cylinder head assemblies. Furthermore, the study examines the influence of cryogenic temperatures on the physical properties of materials utilized for valve seat applications.

Considering the challenges posed by gaseous fuels and their effect on valve seats, the study examines self-lubricating supermaterials used by competitors. It also develops cost-effective cast iron processing technology to enhance its properties, akin to superalloys used by competitors.

Tribological testing compares material properties of the world´s biggest manufacturers, assessing performance and durability under simulated operating conditions. The research contributes to understanding valve and valve seat behavior, providing insights to enhance gas engine performance and longevity in alternative fuel applications.

Key words:

Internal Combustion Engines, Valves, Valve seats, Valve guides, Cobalt materials, Cryogenic treatment, Heat treatment, Cylinder head, Tribological testing, Alternative fuels, Gas engines, Self-lubricating materials, Cast iron, Superalloys, Material properties, Stellite.

ANOTACE

Tato studie analyzuje materiály používané pro výrobu ventilů, sedel ventilů a vodítek ventilů spalovacích motorů. Cílem je porozumět jejich vlastnostem a výkonu za různých provozních podmínek. Výzkum také zkoumá vliv tuhosti dosedací plochy hlavy válců na opotřebení sedel ventilů a zkoumá, jak různé geometrie a materiály dosedacích ploch ovlivňují životnost ventilů a sedel. Kromě toho je věnována sekce výrobnímu procesu hlav válců, včetně mražení sedel ventilů před instalací, což je klíčová část výrobního postupu pro montáž hlav válců.

Dále studie zkoumá vliv kryogenních teplot na fyzikální vlastnosti materiálů používaných pro aplikace sedel ventilů. S ohledem na výzvy spojené s plynnými palivy a jejich vliv na sedla ventilů, studie zkoumá samomazné supermateriály používané konkurenty. Zároveň vyvíjí technologii cenově efektivního zpracování litiny, aby se zlepšily její fyzikální vlastnosti srovnatelné se super-slitinami, které používají konkurenti.

Provádí se tribologické testování k porovnání materiálových vlastností největších výrobců motorů na světě, hodnotí výkon a odolnost za simulovaných provozních podmínek. Výzkum přispívá k porozumění chování ventilů a sedel ventilů, poskytuje náhledy pro zlepšení výkonu a životnosti plynových motorů v aplikacích alternativních paliv.

Klíčová slova:

Spalovací motory, Ventily, Sedla ventilů, Vedení ventilů, Kobaltové materiály, Kryogenní úprava, Tepelné zpracování, Hlava válců, Tribologické testování, Alternativní paliva, Plynové motory, Samomazné materiály, Litina, Superslitiny, Vlastnosti materiálu, Stelit.

PODĚKOVÁNÍ

Chcel by som poďakovať pánovi docentovi Skrbkovi za vynikajúce vedenie mojej práce a cenné rady, ktoré mi poskytol počas celej mojej doktorandskej štúdie.

Rovnako chcem vyjadriť veľkú vďaku pani doktorke Bakalovej za jej trpezlivosť, podporu a cenné rady, ktoré mi poskytla počas tvorby mojej práce.

Taktiež by som sa chcel úprimne poďakovať mojej manželke Tatiane za jej obrovskú trpezlivosť a podporu počas celého štúdia.

CONTENTS

CONTENT OF FIGURES

CONTENT OF TABLES

LIST OF USED ABBREVIATIONS

Unit	Symbol	Meaning
AGI	[-]	Austempered Grey Iron
ADI	[-]	Austempered Ductile Iron
ASTM	[-]	American Society for Testing and Materials
BCC	[-]	Body-Centered Cubic
CGI	[-]	Compacted Graphite Iron
dAF	[-]	Lower ausferite
EDI	[-]	Electrical Discharge Machining
FCC	[-]	Face Centered Cubic
GCI	[-]	Grey Cast Iron
hAF	[-]	Upper ausferite
HB	[-]	Material hardness according to Brinell
HCP	[-]	Hexagonal Close Packed
HB	[-]	Material hardness according to Brinell
HRC	[-]	Material hardness according to Rockwell
h-BN	[-]	Hexagonal Boron Nitride
NCI	[-]	Nodular Cast Iron
NbC	[-]	Niobium Carbide
PM	[-]	Powder metallurgy
WC	[-]	Tungsten carbide
AC	[A]	Alternating Current
Br	[T]	Residual magnetism
Bs	[T]	Saturation induction
C_L	[$m.s^{-1}$]	Speed of propagation of longitudinal wave in cast iron
C_{L0}	[$m.s^{-1}$]	Speed of propagation of longitudinal wave in steel
C_T	[$m.s^{-1}$]	Speed of propagation of transverse wave in cast iron
DC	[A]	Direct Current
E	[MPa, GPa]	Young's modulus
E_{0T}	[MPa, GPa]	Theoretical Young's modulus

Fp	[N]	Loading force
Fn	[N]	Pressure force
Ft	[N]	Friction force
H_0	[$A.m^{-1}$]	Magnetic pulse size
Hc	[Oe]	Coercive force
Hr	[A.m-1]	Magnitude of remanent magnetic field
Ir	[A.m-1]	Remanent polarization
L_R	[m, mm]	Real distance
L_U	[m, mm]	Ultrasonic distance
M	[kg]	Testing bar mass
N	[-]	Demagnetizing agent
$R_{p0,2}$	[MPa]	Yield strength
Rm	[MPa]	Tensile strength
τ	[Pa]	Shear strength of the material
τ	[mm]	Delay of the transformed transverse wave
μ_d	[-]	Dynamic coeficient of friction
μ_s	[-]	Static coeficient of friction
μ	[-]	Coeficient of friction
T	[s]	True delay of the transverse wave
V	[m^3]	Rod volume
V_V	[m^3]	Calculated rod volume
Vp	[m^3]	Rod volume by immersion
Wt	[%]	Weight Percent
Z	[$MPa.s^{-1}$]	Ultrasonic impedance
Zi	[$MPa.s^{-1}$]	Ultrasonic impedance of inclusion
Zm	[$MPa.s^{-1}$]	Ultrasonic impedance of matrix

RESEARCH OBJECTIVES

This study focuses on addressing several issues related to valves and valve seats in internal combustion engines. The study aims to analyze the materials used for valves, valve guides, valve seats, and valve hard-facing, focusing on their properties and performance under different operating conditions.

Another objective is to examine the effect of cylinder head stiffness on potencial valve seat wear. The research explores how variations in the geometry of the gasket plate impact the service life of valves and their valve seats. Additionally, a specific chapter will be dedicated to manufacturing cylinder heads and freezing valve seats before pressing them into the cylinder head.

Considering the adverse properties of gaseous fuels and the resulting drying out of valve seats, the study will address using self-lubricating supermaterials commonly employed by competitors. However, due to the high cost associated with these materials, the work will also focus on developing new technology for processing cost-effective cast iron. The aim is to enhance the properties of this material to achieve similar characteristics to the superalloys used by competitors.

To compare the properties of different materials, tribological testing will be conducted. The study will assess the performance and durability of the tested materials under simulated operating conditions. Through these investigations, the research aims to contribute to understanding valve and valve seat behavior and provide insights into improving the performance and longevity of gas engines in alternative fuel applications.

1 INTRODUCTION

Internal combustion engines generally have a relatively short lifespan compared to other types of engines, such as electric motors. This can have several effects on the costs associated with engine repair. Increasing the frequency of necessary repairs and maintenance can shorten the life of engines. This can significantly increase the overall cost of ownership for a vehicle or machine with an internal combustion engine. In addition, the short lifespan of internal combustion engines can also make it more difficult to find replacement parts. Because these engines wear out quickly, the demand for replacement parts may be higher, which can drive up the cost of these parts. This can make it more expensive to repair an internal combustion engine than it would be to repair other types of engines.

Efforts to make combustion engines more efficient and reduce their negative environmental impact lead to the use of alternative fuels. One of the serious problems of internal combustion engines is the wear of valves and valve seats and their knocking due to insufficient lubrication. In the original gasoline engines with indirect fuel injection, lead added to gasoline was used to lubricate these parts. However, the burning of lead turned out to be non-ecological, and therefore, they began to switch to alternative additives, which accelerated corrosion at high temperatures during operation. The transition from indirect injection gasoline internal combustion engines to direct injection and the use of diesel engines saw the development of materials with self-lubricating properties. Due to the principle of operation of the diesel combustion engine, there is no controlled washing of the intake valve with fuel, which would lubricate the structural pair valve-valve seat. For this reason, the original LIAZ diesel engines had special cast iron valve seats with flake graphite developed by Buzuluk Komárov under the trade name BX and BY.

The carrier of the lubricating properties of this material is graphite. TEDOM's conversion of these engines to gas engines created several problems. The combustion temperature of gas engines is about 200 °C higher than that of diesel engines, which causes an increase in the temperature of valves and valve seats. The valve seats are not able to remove the heat from the valves. The valves overheat and degrade. The original cast-iron seats of diesel engines, when running on alternative fuels, have poor resistance to thermal corrosion and are subject to high wear, which causes a very short service life. Furthermore, gas as a fuel has very poor lubricating properties. It dries out the valve seats and thus promotes valve knocking. For this reason, in the original LIAZ diesel engines converted to alternative fuels by TEDOM, structural modifications

such as the replacement of valves and valve seats and the modification of pistons and cylinder heads had to be made.

The new TEDOM gas engines use bimetallic valves with a cobalt weld on the seating surface. Stellite 6 and Stellite 12 were used for the intake and exhaust seats. However, in operation, it turns out that some engines are subject to knocking off the intake valves. Knocking is random, with no connection to the fuel used (natural gas, biogas) or operating performance. This work is devoted to valves and valve seats. Their materials, the materials used for the valve seats, and the materials of the valve overlays. It investigates the reason for valve knocking and the effect of cylinder head stiffness on valve seat wear. It describes the influence of the geometry of the seating surface on the service life of valves and their seats.

Due to the negative properties of gaseous fuels and thus the drying out of the valve seats, the competition uses self-lubricating super materials, the production of which is financially demanding, and therefore in the final chapters of the work, we pay attention to the development of a new technology for processing cheap cast iron with globular graphite, which acquires the properties of the superalloys used by the competition. We will use tribological testing to compare the properties of these materials.

2 VALVE USED IN COMBUSTION ENGINES

In a combustion engine, valves are used to control the flow of air and fuel into the engine's cylinders, as well as the exhaust gases that are produced during the combustion process. There are typically two types of valves in an internal combustion engine: intake valves and exhaust valves. The intake valves are located in the cylinder head, and they open to allow air and fuel to enter the cylinder. The intake valves are typically controlled by a camshaft, which uses lobes to open and close the valves at the appropriate times. The exhaust valves are also located in the cylinder head, and they open to allow the exhaust gases to escape from the cylinder. Like the intake valves, the exhaust valves are typically controlled by the camshaft.

The opening and closing of the valves is an essential part of the engine's operation, as it allows the air/fuel mixture to be compressed and combusted in the cylinder, and it allows the exhaust gases to be expelled from the engine. This process is known as the "four-stroke cycle," and it occurs in most internal combustion engines. [1 - 3]

The Intake and exhaust valves of the internal combustion engine are precision components for sealing the intake and exhaust channels, which are used to control the gas exchange process. They are designed to seal the working space of the cylinder from the outside. Intake valves, which are less thermally stressed, are cooled by fresh gases that flow around them. In contrast, exhaust valves are exposed to high thermal stress and chemical corrosion during the exhaust cycle. Both types of valves, are therefore manufactured from different materials suitable for their function. The most important parts of the valve are shown in Fig. 1. [1 - 3]

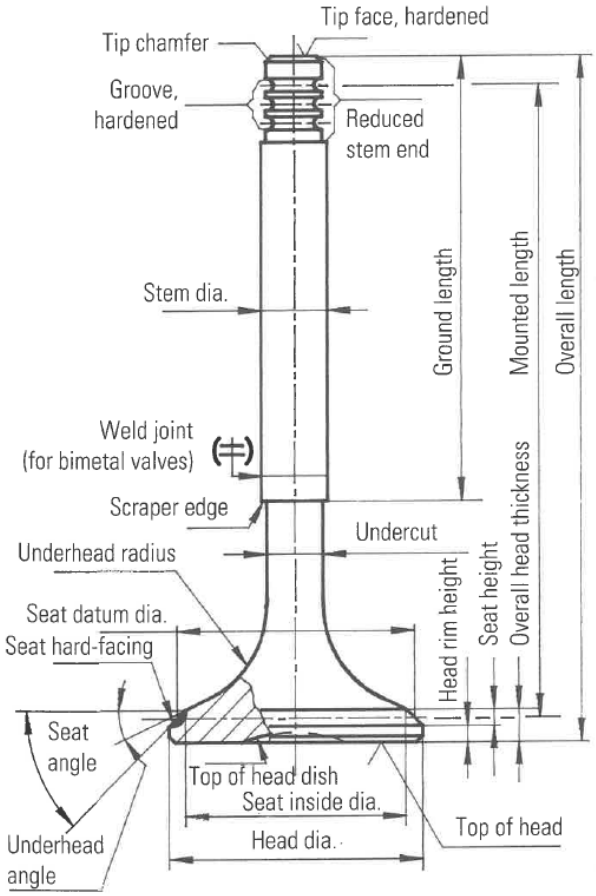

Fig. 1 Main part of valve [1]

Distribution of valves are divided into three main groups: [1 - 3]

1. Mono-metal valves
2. Bimetal valves
3. Hollow valves

2.1 Mono-metal valves

Monometallic valves Mono-metal valves can be produced by both the hot extrusion process and the tamping process. The starting point for hot extrusion is a rod part with a diameter of about 2/3 of the diameter of the finishing head and a length corresponding to the volume of the finished blank. The induction-heated blank is forged on a press. During tamping, a ground rod section, the diameter of which is slightly larger than the diameter of the valve stem, is heated at one end and tamped into a "flask", which is then formed into a valve head in a forging die. [1 - 3]

2.2 Bimetallic valves

Bimetal valves enable an optimal combination of materials for the valve stem and head. Preferred material pairs are listed in Tab. 1

Tab. 1 Example combination of materials for bimetallic valve [1]

Norm	**Valve head**			**Valve stem**
EN 100 90	X53CrMnNiN219	X50CrMnNiNbN219	NiCr20TiAI	X45CrSi93

The materials are welded together using friction welding, which ensures a perfect connection of the materials. The weld to the head is positioned so that when the valve is closed, it is halfway up the valve stroke inside the valve guide. The static tensile strength in the weld is approx. 90% of the weaker material partner. Considering the normal statistical variance, a tensile strength of 700 N/mm^2 can be assumed for the weld. Bimetallic valves can be welded to the seat part with wear-resistant carbide. [1 - 3]

2.3 Hollow valves

Hollow valves represent a special type of construction. They are used for many reasons, both on the intake side and on the exhaust side. The reasons for using hollow valves are: [1 - 3]

- Temperature reduction, especially in the valve head area.
- Weight reduction.

When hollow valves are used, about 60 % of the cavity volume is filled with sodium metal. Sodium melts at 97.5 °C and has a density of 0.97 g/cm^3. The liquid sodium undergoes a "shaker" in the valve cavity depending on the engine speed, thereby transferring heat from the valve head to the stem. Here, the temperature reduction is greater, the better the heat transfer through the valve

guide to the cylinder head. This means that long and well-cooled valve guides with as tight clearances as possible improve the efficiency of hollow valves. Research has shown that a temperature reduction of 80 °C to 150 °C can be achieved in this way. An important quality feature of hollow valves is the cleanliness of the cavity. If moisture, such as water or oil, reaches the sodium in the cavity, a chemical reaction will occur during production. This results in very high gas pressures that can cause dangerous static valve bias and premature failure. Another disadvantage of this chemical reaction is the formation of oxide layers on the wall of the cavity. As is well known, oxide layers are characterized by high resistance to heat conduction and reduce the heat flow from the cavity to the cylinder head with increasing thickness. At the same time, the proportion of nitrogen in the cavity is transformed into a compound with a low dissociation pressure. Thanks to this, the gas pressure is significantly reduced, which allows free movement of sodium and thereby optimizes heat transfer. [1 - 3]

There are a few types of hollow valves: [1 - 3]

- "Single tube" type represents the lowest price option. A solid cap is attached to the shank, which is drilled from the end by friction welding. The end of the shank is hardenable.

- Extruded valve This variant is significantly more expensive to manufacture than the above type. The base shank is also drilled from the end. The bore is closed by induction heating the end of the shaft with a larger diameter and subsequent forging. The stem end is connected by friction welding. The advantages of this type of valve are a larger cavity through a larger bore, greater weight savings, and increased strength during friction welding.

- Hollow head valves are mainly used in high-performance engines and strategic engines.

The hollow head valve represents the optimum for weight reduction and heat dissipation from the center of the valve head. Due to the high production costs, this is an expensive option. Unlike the above types, these valves are drilled and machined from the head side. The opening is closed by inserting a cover through a special process. Valves of this type are mainly used in motorsport. [1 - 3]

2.4 Characteristics of the valve head

The requirements for valve head design are quite conflicting. The valve head must be rigid enough to withstand mechanical stress even at high temperatures and not deform, while it must also be flexible to adapt to even a slightly deformed seat. Fig. 2 shows the requirements for a raw valve head (the normal case for intake valves in gasoline engine vehicles).

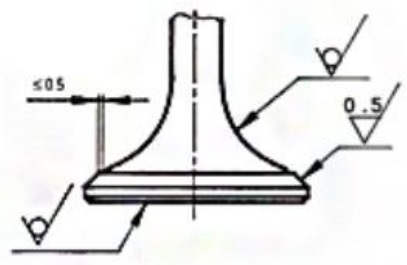

Fig. 2 Roughness prescription on the standard valve head [1]

Fig. 3 shows the requirements for the machined lower part of the valve head. This is a standard type of exhaust valve with a hard surface. It is also used when the distance between the piston and the valve is less than 2 mm.

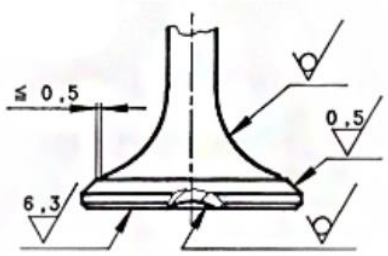

Fig. 3 Roughness prescription on the machined head with hard facing [1]

In order to achieve the maximum possible safety against surface defects in the area of the valve head, the valves of high-performance engines are machined as standard in the area under the head. The goal is to remove possible defects in the forging in the edge layer caused by heat treatment Fig. 4.

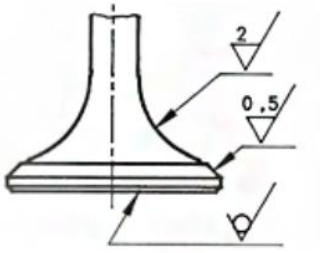

Fig. 4 Roughness prescription on the forged valve head [1]

Where valves have a stem diameter of less than 6 mm, the valve head is generally fully machined for strength reasons. This case is shown in Fig. 5.

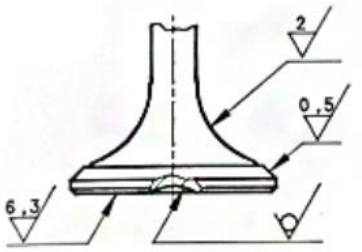

Fig. 5 Roughness prescription on the entire machined valve head [1]

The contact surfaces of the valves are heavily stressed by both thermal and chemical corrosion. As a rule, they are therefore welded with special alloys, wear-resistant and corrosion-resistant materials. Materials are detailed in chapter 2.6.

2.5 Valve head modifications to increase reliability

Hardening of the contact surface of the valve head by induction hardening of the seat, as shown in Fig. 6, can reduce the wear of intake valves made of martensitic materials. In order to keep the hardness reduction of the induction hardened valve seat within acceptable limits, care must be taken not to exceed valve temperature values of 550 to 600°C. An alternative option to increase the service life of the valve is the use of a hard metal weld on the seating part. [1 - 3]

Fig. 6 Hardened valve head on the left side and hard facing on the valve head on the right side [1]

2.6 Valve materials

The material used for valves in internal combustion engines depends on several factors, including the type of engine, the operating conditions, and the desired performance characteristics. In addition to geometry, the choice of suitable material also significantly influences the correct design of the valve. Valves are the most stressed parts of an internal combustion engine, both mechanically and thermally. The valves are exposed approx. Two hundred million load cycles during the life of the engine. Valve material requirements include adequate high-temperature

fatigue strength, wear resistance, high-temperature corrosion, oxidation resistance, and resistance to corrosive elements deposited as combustion residues, primarily on exhaust valves. [1 – 3, 9]

The high thermal stress, especially on the exhaust valves, requires that the valves will be made of special steels that do not lose strength and hardness at high temperatures, have high-notch toughness, and resist the corrosive effect of combustion products, the effect of which increases rapidly with increasing temperature. The steel must also not be self-hardening. Valve steels are also required to have good thermal conductivity and resistance to tanning (formation of scales). Sufficient hot formability and satisfactory machinability must also be required for economical production. In Tab. 2 are summarized the standard materials used for valves, their applications, chemical composition, and selected physical properties. In Tab. 3 are summarized the standard materials used as hard facing for valves. [1 – 3, 9]

Tab. 2 General table of materials used for valves [1]

Materials						
Marking of the material EN 100 90	**1.4718**	**1.4748**	**1.4871**	**1.4882**	**1.4785**	**2.4952**
Marking of the material EN 100 90	X45CrSi93	X85CrMoV182	X53CrMnNi	X50CrMnNiNb	X60CrMnMo	NiCr20TiAl
Business name	Cr Si-Steel	Cromo 193	21-4 N	LV 21-43	ResisTEL	Nimonic 80 A
Aplication						
	Intake valve under normal load, stem for bimetallic valves	Intake valve under increased load, increased resistance to wear	Intake and exhaust valve with increased hot strength corrosion resistance, exhaust valve with stellite weld	Intake and exhaust valve with increased hot strength corrosion resistance, exhaust valve for trucks	Intake and exhaust valve with high hot strength, fatigue resistance and corrosion resistance, truck exhaust valve without welding	Very high load exhaust valve, motorsport valves
Chemical composition wt%						
C	0.4 - 0.5	0.8 - 0.9	0.5 - 0.6	0.5 - 0.6	0.6 - 0.7	≤ 0.1
Si	2.7 - 3.3	≤ 1.0	≤ 0.3	≤ 0.5	≤ 0.3	≤ 1.0
Mn	≤ 0.8	≤ 1.5	8.0 - 10.0	8.0 - 10.0	9.5 - 11.5	≤ 1.0
Cr	8.0 - 10.0	16.5 - 18.5	20.0 - 22.0	20.0 - 22.0	20.0 - 22.0	18.0 - 21.0
Ni	≤ 0.5	-	3.3 - 4.5	3.5 - 5.0	≤ 1.5	Balance
Mo	-	2.0 - 2.5	-	-	0.8 - 1.3	-
W	-	-	-	0.8 - 1.5	-	-
V	-	0.3 - 0.6	-	-	0.8 - 1.0	-
Co	-	-	-	-	-	≤ 2.0
Al	-	-	-	-	-	1.0 - 1.8
Ti	-	-	-	-	-	1.8 - 2.7
Nb/Ta	-	-	-	1.8 - 2.5	1.0 - 1.2	-
N	-	-	0.4 - 0.5	0.4 - 0.6	0.4 - 0.6	-
S	≤ 0.03	≤ 0.03	≤ 0.03	≤ 0.03	≤ 0.03	≤ 0.015
P	≤ 0.04	≤ 0.04	≤ 0.04	≤ 0.04	≤ 0.04	≤ 0.02
Fe	Balance	Balance	Balance	Balance	Balance	≤ 3

Strength and hardness						
Rm [N/mm^2]	1100 -1350	1000-1200	≥ 1000	≥ 950	≥ 1000	≥ 1000
Rp $_{0.2}$ [N/mm^2]	750	800	600	580	800	900
A	12	8	8	12	8	15
$R_{p\ 0.2}$ % [N/mm^2]						
500 °C	400	500	350	340	500	800
600 °C	240	280	300	310	450	780
700 °C	80	120	250	260	400	750
800 °C	-	-	200	220	350	550
900 °C	-	-	-	120	-	360
Hardness						
Valve stem HRC	≥ 56	≥ 50	-	-	-	-
Contact surface valve head HV 30	≥ 500	≥ 480	≥ 30	≥ 30	≥ 32	≥ 38
Tip face HV 30	≥ 550	≥ 490	-	-	-	-
Physical properties						
Density [g/cm^3]	7.6	7.8	7.8	7.9	7.8	8.17
Thermal conductivity [W/cm . K]	0.210	0.210	0.147	0.147	0.147	0.122
Coef. thermal expansion [1/K] at 20 - 800 °C	13×10^{-6}	12×10^{-6}	18.5×10^{-6}	19×10^{-6}	18×10^{-6}	15.1×10^{-6}

Tab. 3 Most common material used for hard facing [1]

Materials of coating	**P 37**	**P 37 S**	**P82**	**P 39 S**	**P 25**
	Stellite F	**Stellite FS**	**X 782**		
Application method	Flame	Plasma arc	Plasma arc	Plasma arc	Plasma arc
Characteristics					
	Maximum heat hardness and wear resistance	Maximum heat hardness and wear resistance	Maximum hardness when hot, increased resistance to oxidation and corrosion at elevated temperatures	For exhaust valves in unleaded operation and for intake valves	For intake and exhaust valves in petrol engines in unleaded operation, for intake and exhaust valves in diesel engines
Composition [%]					
C	1.75	1.75	2	0.9	0.6
Si	1.1	1.1	≤ 0.5	≤ 0.4	≤ 0.4
Mn	-	≤ 0.3	≤ 0.5	10.0	10.0
Cr	25.5	28.0	26.0	27.0	25.0
Ni	22.5	22.5	Balance	12.0	10.0
Co	Balance	Balance	≤ 0.3	-	-
W	12.3	12.3	8.5	-	-
Fe	≤ 1.4	≤ 1.4	≤ 4.0	Balance	Balance
Mo	-	-	-	5.5	3.0
Nb/Ta	-	-	-	2.5	2.0
Material base	Cobalt base	Cobalt base	Nickel base	Iron foundation	Iron foundation
Hardness	≥ 40	≥ 40	≥ 32	≥ 39	≥ 32
Density [g/cm^3]	8.5	8.5	9.1	7.9	7.9
Coef. thermal expansion [1/K] at 20 - 800°C	13.9×10^{-6}	13.9×10^{-6}	14.8×10^{-6}	17.2×10^{-6}	17.3×10^{-6}

2.6.1 Ferritic-martensitic valve steels

In the group of martensitic, i.e., hardenable valve steels, there are materials:

- X 45 Cr Si 9 3 (Cr Si)
- X 85 Cr Mo V 18 2 (ChroMo)

X 45 Cr Si 9 3 is the standard material for monometallic intake valves and is used exclusively as a bimetallic valve stem material. As a standard, it is refined to 1100 N/mm^2 to 1350 N/mm^2. [1]

X 85 Cr Mo V 18 2 is a high alloy steel used to manufacture intake valves where the level of mechanical and thermal stress is too high for the use of Cr-Si material. Better mechanical properties result from many finely dispersed carbides in the matrix. [1]

2.6.2 Austenitic valve steels

Austenitic Cr-Mn steels have proven to be the best economical solution. The material X 53 Cr Mn Ni N 21-9, considered a classic exhaust valve material, is also used for hollow valves. In X 50 Cr Mn Ni Nb 21-9 and X 60 Cr Mn Mo V Nb N 21-10 materials, quantitatively precisely matched elements such as Nb/Ta and W or Mo, V, and Nb/Ta are present in Cr-Mn the matrix. These combinations increase the hot strength without having a negative effect on ductility. The classic heat treatment for these austenitic valve materials consists of solution annealing at high temperatures followed by cooling in water. The subsequent precipitation hardening–aging increases the hot fatigue strength and hardness due to the agglomeration of carbide and carbonitride in the structure. [1 - 3, 9, 31]

2.6.3 Valve steels with a high nickel content

When Cr-Mn steel is insufficient, switching to materials with high nickel content is necessary. They are required where maximum operational reliability is required, i.e., increased service life and resistance to high-temperature corrosion. Typical applications are valves for aircraft engines, motorsport, and highly turbocharged diesel engines running on heavy oil. With the nickel-based alloy Ni Cr 20 Ti Al (Nimonic 80 A), the above requirements are met in an ideal way. However, the price difference from the Cr-Mn group of steels due to the high nickel content and the difficulty of machining should be pointed out. [1 - 3, 9]

2.6.4 Ferritic-pearlitic steels

We can include steels without chromium and nickel, alloyed only with silicon. At higher temperatures, the strength and hardness of these steels decrease compared to other steels used, and the corrosion resistance is also lower. These steels are easily hardenable. Either the end of the stem, which is acted upon by the rocker arm or the tappet, is tarnished. Ferritic-pearlitic steels are good hot formable, and easy to work. They are used for intake and less stressed exhaust valves up to an operating temperature of 700 °C. Typical examples of these steels are ČSN 13 251 and ČSN 17 029. [1 - 3]

2.6.5 Special materials

Demands on valves are constantly increasing. With the introduction of emission limits for exhaust gases, engine manufacturers are forced to allow more aggressive combustion mixtures. This increases the combustion temperature, and the exhaust valves are exposed to an increasingly oxidizing atmosphere.

The ideal technology to meet these requirements is powder metallurgy - PM. For metal powder production, molten steel of a given specification is used and atomized in an inert gas. The powder produced in this way is then cold isostatically pressed into billets, which are then transformed into valve rod material during hot pressing. Another method is the hot isostatic pressing of the powder into ingots, which are then rolled into bars.

From this moment, valve production takes place in the usual way, i.e., pieces of rod material are transformed into valve semi-finished products by the forging process. The advantage of valve materials produced by PM is the quality of the material. It differs from cast ingots by a finer distribution of elements in the matrix. Following the better distribution of elements, there is a more homogeneous structure, which positively affects strength and resistance to high-temperature corrosion. PM can create entirely new alloys that could not be created using conventional methods. Heat treatment provides an excellent means of influencing and shaping the technological properties of valve steels, which in turn have a decisive effect on operational performance. [1 - 3]

2.7 Hard-facing materials for valves

In modern internal combustion engines with high loads, hard facing is already used as standard on the contact surfaces of the valve heads. It is used to reduce wear and tear. An overview

of the materials used for coatings is shown with their characteristics, chemical composition, and selected physical properties. Two hard coating processes are used: [1 - 3]

- A fusion welding process in which the welding rod material is applied using an oxy-acetylene flame [1 - 3]
- Plasma spraying, in which the powder coating material is melted and sprayed onto the workpiece. The advantage of this method is that the alloying elements in the powder can be easily changed, and the process can be fully automated [1 - 3]

2.8 Surface treatment of valves

Ferritic-martensitic steels used for monometallic intake valves (X 45 Cr Si 9 3) have good sliding properties, and it is not necessary to modify their stem, as they do not tend to jam in the guide. For bimetallic valves, austenitic steel X 50 Cr Mn Ni Nb is usually chosen as the stem material, which has worse sliding properties than the valve head material, and the coefficients of thermal expansion for these materials are different. For this reason, the tendency for valve stems to wear or rub against the valve guide is higher. Valve surface treatments are used to compensate for this phenomenon. [1 - 3]

2.8.1 Chrome plating of the valve stem

The chrome coating forms a homogeneous surface of the stem, which is several times harder than the material of the valve. This results in substantially improved wear and corrosion resistance. The surface roughness after chrome plating is a maximum of Ra 0.2 (non-chromed Ra 0.4 max.), which has a very favorable effect on the wear of the valve guide and therefore allows for minimal play in the valve guide. The chrome coating has a finely branched characteristic network of cracks that can be widened by high-temperature corrosion and could penetrate the base material and have a notch effect. Chrome plating should not extend beyond the edge of the valve guide. [1 - 3]

2.8.2 Nitriding of the valve stem

In addition to chrome plating, which is considered a classic surface treatment of the shank, plasma and gas nitriding are used in practice. Common to both nitriding processes is that the valves are exposed to nitrogen emitting media for extended periods of time at temperatures of approx. 500 °C until very hard compounds or diffusion layers form on the surface. Since the diffusion rate

of nitrogen is low, the valves must be treated for a correspondingly long time to obtain the required nitriding hardness. Nitride layers about 10 to 30 microns thick are very hard in the surface layer, about 900 HV 0.025, and thus the layer provides good wear resistance. Nitrided valves are ground, just like chrome-plated valves. [1 - 3, 100 - 111]

2.9 Seating of the valve in the valve seat

The valve seat diameter is the basis of the valve design. As a rule, the maximum diameter of the valve seat is used for this. The total thickness of the head is dependent on the specific combustion pressure and temperature. It is desirable that it be determined by finite element analysis. It is advantageous if the valve remains elastic enough to follow the deformations of the valve seat in the cylinder head, which is deformed to some extent by engine operating conditions.

The contact surface of the valve is ground at an angle 0.5° - 1° smaller than the contact surface of the valve seat. Fig. 7 graphically shows this difference in valve and valve seat sealing angles. These differences are for the following reasons: [1- 3]

Under operating conditions, the hottest part of the valve is the underside of the valve head, and this solution allows the valve head to thermally expand.

When the valve is very hot, the spring load can cause a slight bowing of the head which can lift the inside edge of the valve seat (closest to the combustion chamber) of the valve seat insert if the cold angles are the same.

Reduces the risk of catching combustion particles between two contact surfaces.

The sealing apex angle for spark-ignition and diesel engines is usually 90°. Petrol engines working on alternative fuels (CNG, et al. gas) have a main angle of 120°. This difference is due to the higher combustion temperature and the need to increase the contact surface of the valve and the seat, and therefore to dissipate more heat into the valve seat. [1 -4, 97 -105]

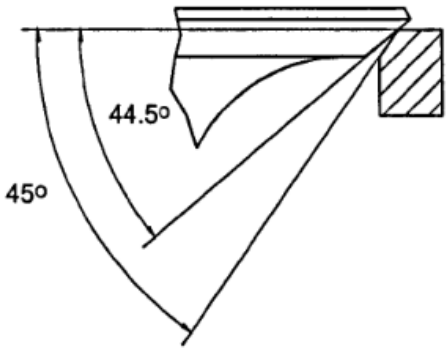

Fig. 7 Differences in valve and valve seat seal angles [3]

2.10 Valve clearance

Individual components of the internal combustion engine expand more or less (depending on the type of material used), and there is a need for a valve clearance in the valve train or a hydraulic limitation of this clearance. The valve clearance of the valve train is defined in such a way that, with a fully warmed-up engine, reliable seating of the valve in the valve seat is ensured. The valve clearance setting is greater for the exhaust valve than for the intake valve, according to the engine manufacturer. With the OHC (Over Head Camshaft) distribution, the valve clearance is set with an adjustment screw on the rocker´s arm, where the appropriate valve clearance setting is checked with a caliper inserted between the valve stem and the rocker´s arm. If it is an OHC distribution, where the cam acts directly on the tappet, the clearance is adjusted by inserting spacers between the tappet and the cam. According to the regulations of the engine manufacturers, the valve clearance is set in the range from 0.1 mm to 0.5 mm, while its observance is important for the flawless operation of the engine. The definition of valve clearance is similar to the OHV (Over Head Valve) distribution, where the clearance is adjusted directly on the rocker´s arm. Another option is self-limiting the valve clearance using hydraulic tappets. [1 - 4, 97 – 111, 116 - 119]

If the valve clearance is small, the valve opens earlier and closes later. This results in insufficient heat transfer from the valve head to the valve seat and can result in insufficient valve closure, reduced power, increased consumption, or even valve burnout in a hot engine. For diesel engines in the winter, starting the engine worsens due to the loss of compression pressure. If the valve clearance is too large, this setting leads to higher engine noise and higher mechanical stress. In addition, the valve opening time is shortened, as the valve opens earlier and closes later, which leads to a reduction in the mass filling of the cylinder and a reduction in engine power. [3, 97 - 105]

2.11 Valve dynamics

The geometry of the cam defines the theoretical movement of the valve. Valve travel is modified due to the finite weight and stiffness of the elements in the valvetrain. Movement can be divided into 5 phases: [3, 97 – 111, 116 - 119]

Stage 1: Before the valve starts to move, the clearance between the rocker arm and the valve stem must be defined. This clearance ensures that the valve can sit in the seat under all operating conditions. The cam is designed to provide an initial constant speed to control the shock stresses as the clearance runs out. The impact speed is usually limited to 500 mm/s at rated engine speed.

Stage 2: During the second phase, the cam accelerates the valve. The cam will give the valve a constant acceleration, sine, polynomial, or spline function that will cause the acceleration to rise from zero to a maximum and then fall back to zero.

Stage 3: Deceleration is controlled by the valve spring.

Stage 4: The final deceleration is controlled by the cam.

Stage 5: The cam is designed to provide a constant closing rate to reduce valve slam into the valve seat. This impact velocity value should not be greater than 2 m/s. The actual movement of the valve is modified by the elasticity of the components in the valve train.

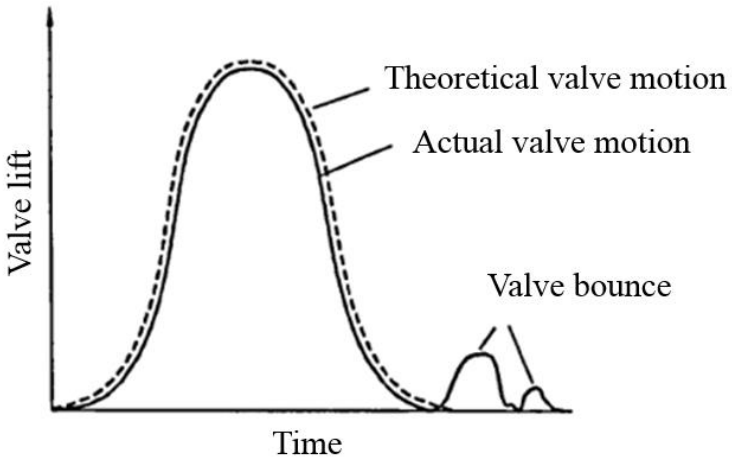

Fig. 8 Comparison of actual and theoretical valve movement [3]

A comparison of actual and theoretical valve movement is shown in Fig. 8. Valve bounce can occur if the stroke speed is too high or if the valve spring preload is too low. Valve seat bounce causes a reduction in engine power rating and, over time, can cause valve burn if this bounce is present on the exhaust valve. [3, 97 – 111, 116 - 119]

Combustion generates cyclic stresses peaking above 200 MPa on the underside of the valve head in Fig. 9. The magnitude of the stress is a function of the combustion pressure. The voltage is higher in diesel engines than in petrol engines due to higher combustion pressures. [3, 97 – 111, 116 - 119]

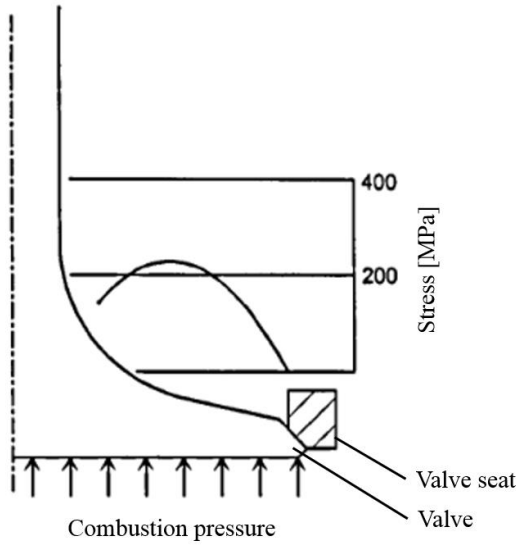

Fig. 9 Magnitude of the stress in valve during combustion cycle [3]

When the valve hits the valve seat, cyclic stresses act on the joint of the valve stem and the valve head. If thermal deformation of the cylinder head has caused misalignment of the valve and valve seat, seating will occur at a single point of contact, as shown in Fig. 10 on the right.

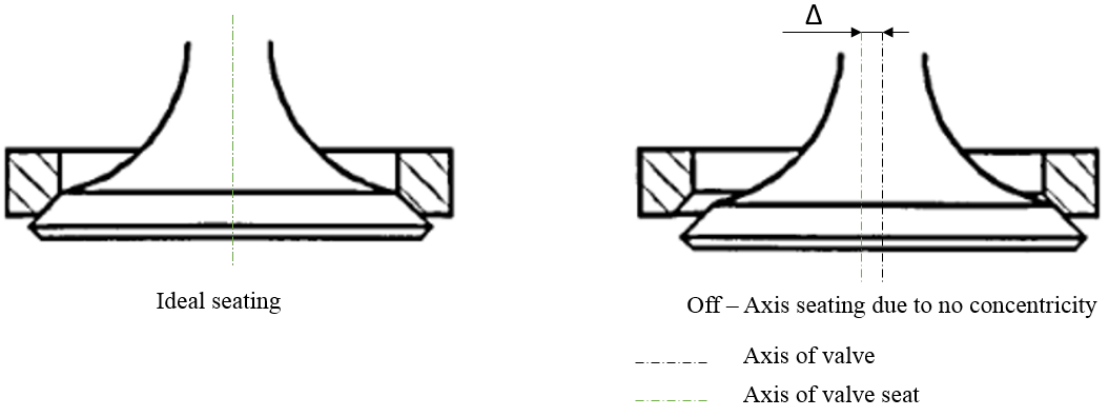

Fig. 10 Graphically shown correct and off-axis valve seating [3]

Bending stresses due to this point contact increases the load on the valve seat and the valve itself. As a result of the point contact, optimal cooling does not occur, local overheating of the valve may occur, and the valve and seat may subsequently catch fire. Fig. 10 on the left is an illustration of the optimal seating of the valve in the seat. In this case, the contact between the valve and the valve seat is circular. [3, 97 – 111, 116 - 119]

2.12 Valve temperatures

75-80 % of the heat flow from the valve is dissipated through contact with the valve seat, while the remaining heat is conducted through the valve stem, into the valve guide, and subsequently transferred to the cylinder head and engine coolant. Efficient heat transfer to the valve seat and cylinder head is crucial. In Fig. 11. the thermal gradient from the center of the valve head to the coolant in the cylinder head is shown. It shows a large temperature difference at the seat interface. Heat transfer can be affected by valve bounce. However, the effect of deposits on the valve seat is much more significant. If deposits build up on the valve seat, this may not only lead to an increase in the temperature of the valve, but it may also break off locally and create an escape path leading to the chute and so-called valve burning. [1 -3, 9]

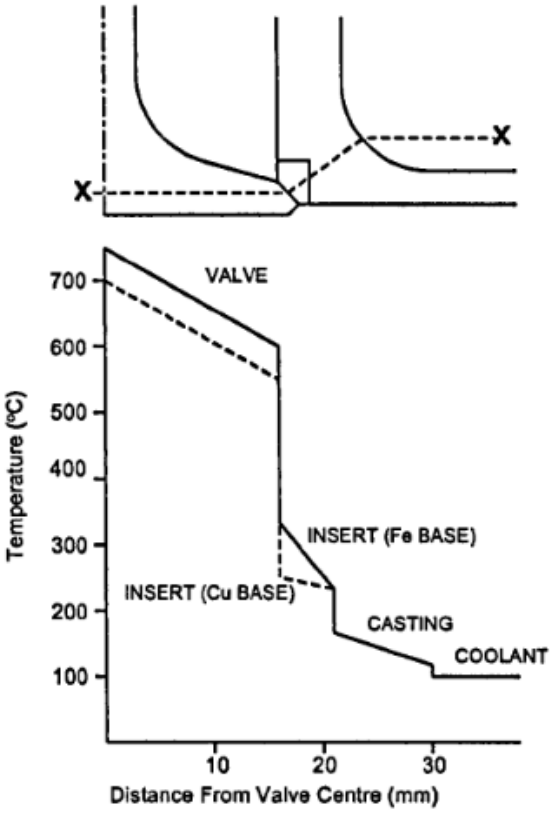

Fig. 11 Diagram of heat distribution from the valve to the cylinder head [3]

2.13 Failure of valves

Valve knocking or recession in Fig. 12 is the most common intake valve wear. High temperatures and a corrosive process usually cause deposits on the sealing surface. Combustion can be initiated by the hot side of the valve head, causing premature ignition or abnormal combustion.

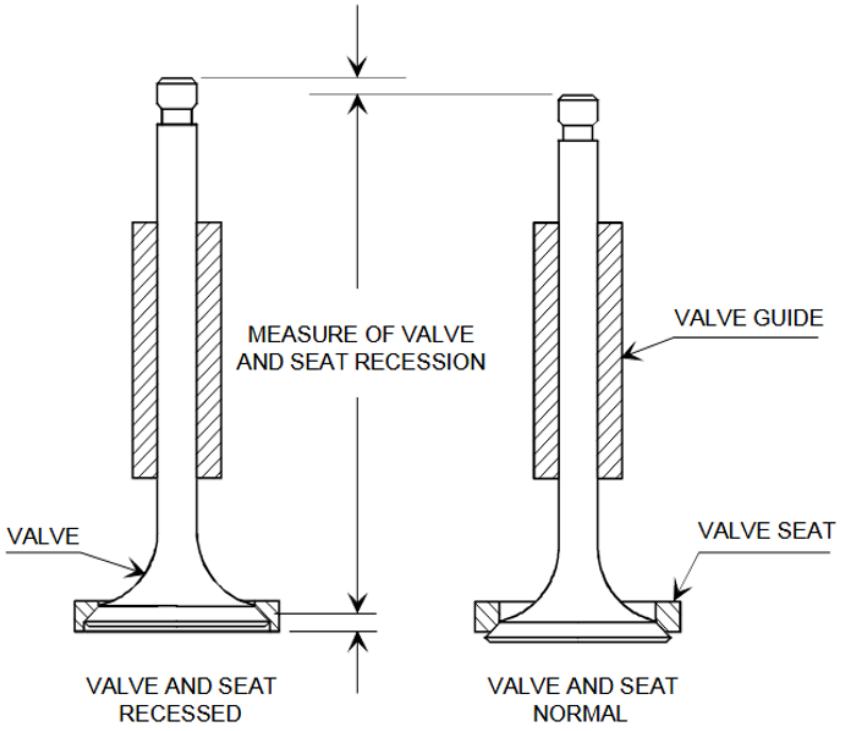

Fig. 12 Schematic illustration of a knocked valve [3]

Intake valve wear is a particular problem in diesel engines because the fuel is fed directly into the cylinder. The intake valve is, therefore, not lubricated with any lubricant, and the valve seats are operated under relatively dry conditions. This problem is also typical for engines working on alternative fuels (most often CNG, LPG, and Biogas), which, in comparison with conventional fuels, have no lubricating properties. Knock wear on exhaust valves is less pronounced than wear on intake valves. Combustion products deposited on the exhaust valve seating surfaces ensure relatively good lubrication (carbon deposits - carbon). Exhaust valves are more likely to fail due to dripping or burning. Such malfunctions are rarely seen with intake valves, also because the intake valve is cooled by flowing fresh air when the working filling is changed. Valve knocking occurs when the valve contact and the valve seat insert are worn. Knocking changes, the relative position of the valve with respect to the cylinder head and timing mechanism. Engines are usually designed to tolerate a certain amount of valve knock - this effect is compensated for by valve clearance. Therefore, it is important to check and adjust this clearance on engines that do not have

automatic valve clearance. If the valve cannot seat properly, combustion pressure will be lost, and the hot exhaust gases that escape will cause the valves to burn or burn out, quickly leading to engine failure. [3, 4, 83, 97 -105, 108]

2.14 Causes of valve knocking

Valve knocking is caused by the loss of material from the valve seat or the valve itself. This occurs gradually over a large number of operating hours. Sometimes there is material loss on the valve seat side, and sometimes the material loss is greater from the valve head. The nature of weight loss is still not clearly understood, although we know that the knockdown can occur through the following mechanisms: [3]

- Metal abrasion
- Adhesion mechanisms
- High temperature corrosion

Knocking problems can be caused by valve grinding due to uneven seating, as contact pressure varies inversely with contact area. Incorrect valve seating can be caused by the cylinder head and its deformation due to thermal effects. Thermal effects are often associated with the construction of cooling channels in the cylinder head near the valve seats. Modern internal combustion engines try to avoid this phenomenon by using natural or artificial rotation of the valves around their axis. This rotation helps to distribute the heat more evenly to the valve seat and thus extends the life of this structural pair. [1 - 4, 83 - 87]

2.15 Analysis of forces on the valve – valve seat interface

The main wear factor is the sliding friction between the valve and the valve seat caused by the "wedging" of the valve into the seat due to gas pressure. The force that wedges the valve into the seat is greater than the sliding force, or rotary, which rotates the valve around its axis. If, due to the deformation of the cylinder head, uneven seating of the valve in the seat occurs, uneven cooling will occur. Frictional movements are the result of the elastic bending of the valve and the working surface of the cylinder head due to combustion pressure. The force acting on the valve seat consists of a component of the inertial force of the valve train - the force due to acceleration when the valve hits the seat and forces acting on the valve, such as spring pressure and gas pressure force when the valve is seated in the seat. This force can be divided into two components:

Fig. 13 Psinθ parallel to the seating surface and Pcosθ perpendicular to the seating surface. If the Psinθ component exceeds the shear stress of the valve seat materials, plastic shear deformation of the surface material may occur. This can lead to the formation of cracks and, eventually, after repeated loading, to the breaking off of particles from the surface. Debris can either be blown away by the gas stream when the valve opens or remain on the landing surface. [2 - 4, 83 -87, 108]

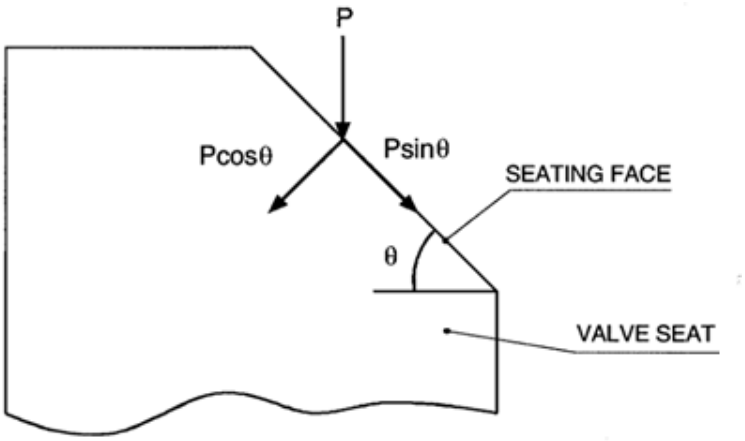

Fig. 13 Force distribution on the valve seat [3]

Micro debris from the landing surface can: [3, 97 -105, 108]

- Prevent complete sealing of combustion gases.
- Lead to increased valve temperature due to reduced seat contact area.
- Lead to abrasive wear of the seating surfaces as the valve slides over the seat insert (if there are microchips of hard material).

The use of a smaller apex angle for the bearing surface is also suggested to reduce surface shear stresses. Reducing the seating angle from 90° to 120° decreases the shear force component (Psinθ) by approx. 29 %, but the normal force component (Pcosθ) increases by approx. 22 %. If the Pcosθ component exceeds the yield strength of the material in compression, it may fail in a manner known as knocking. Therefore, the reduction of the sealing angle, hardness, and toughness of the material is compensated. Valve knocking can occur by systematic "gouging" of a deformed valve seat due to uneven seating. Deformation of the seat can lead to the formation of concentric ridges on the valve seat, which can be "single wave" or "multi-wave". [3, 4, 83 -87]

2.16 Effect of engine operating parameters

The intake valve temperatures are not high enough to cause significant corrosion or thermal fatigue disorders. Such failures are far more likely to occur with exhaust valves. However, studies of intake valve failures lead to the conclusion that deposits on the intake valve seat (formed by engine oil and fuel) reduce heat transfer from the valve head, resulting in loosening and reduced hardness. As a result, some valves have suffered failures due to thermal fatigue-induced radial cracking of the seating surface. The temperatures that occur on exhaust valves and valve seats do not cause any significant reduction in mechanical properties, and therefore temperature does not have a major effect on exhaust valve wear. [1, 3, 116 - 119]

2.17 Valve lubrication on the interface with the valve seat

Engine lubricants reduce valve and valve seat wear. For intake valves, liquid film lubrication is the most dominant because temperatures are usually not high enough to volatilize the lubricating hydrocarbons and additives. However, exhaust valves are largely lubricated by solid films formed at higher operating temperatures, oil additives of ash compounds such as alkaline earth and other metals, oxides, sulfates, and phosphates (e.g., calcium, barium, magnesium, sodium, zinc, and molybdenum). Very thin films of metal oxides are beneficial in reducing valve wear. [1, 3, 4]

2.18 Valves used by TEDOM

The TEDOM company uses in its engines an intake and an exhaust valve of bimetallic construction produced by the company TRW. The valve head is made of material X 53 Cr Mn Ni N 21 9. Both valves have a hard metal weld on the seating surface made of P37S material. The stem of both valves is chrome-plated. [Internal TEDOM documentation, 1]

3 VALVE SEATS USED IN COMBUSTION ENGINES

Valve seats are integral components found within internal combustion engines in cylinder heads, establishing a reliable seal between the valve and the cylinder head, and are typically composed of robust materials. They are designed to withstand the extreme temperatures, pressures, and mechanical strains of engine operation. The role of valve seats is crucial as they contribute to the prevention of leaks and enable the valves to establish an effective seal against the cylinder head. This is essential for optimizing combustion efficiency and ensuring the engine's overall

performance. Valve seats often pose challenges in internal combustion engines and may necessitate replacement or repair in the event of damage or wear.

The valve seat, formed at the begining of the intake or exhaust channel into the cylinder's combustion chamber, must be shaped so that the combustion chamber is perfectly sealed when the valve seats into seat. In addition to sealing, however, the seat has an even more critical task with the exhaust valve - removing the most significant part of the heat from the valve head. Therefore, a good metal contact between the seat and the valve and between the seat and the cylinder head is necessary. However, the wider the seat of the valve in the seat, the more difficult it is to achieve the seating of the valve in the entire surface, and the more difficult it is to adapt the seating surface of the valve to the surface in case of manufacturing inaccuracies or deformations during operation. For good contact and perfect sealing, choosing the valve seat as narrow as possible would be desirable. Between these extremes, a suitable optimum must always be found.

If the cylinder head is made from cast iron, the seat can be made directly in cast iron. It is not possible if the mechanical stress is within the limit where the hardness of the cast iron is no longer sufficient. It is said that unique seat rings, so-called valve seats, should be used for more excellent thermal or mechanical stress. Similarly, valve seats are chosen for cylinder heads made of aluminum alloys. Inserting seats made of a unique material always worsens heat dissipation, which must pass through a greater thickness of the material, and worsens heat transfer between the valve seat and the head itself. However, valve seats reduce the effect of head deformation on valve tightness. The deviation of the alignment of the seat and the valve guide must be in the range of 0.02-0.03 mm. The perpendicularity deviation against the seat's plane should not be more significant than 0.05/100 mm. The most common shape of valve seats is cylindrical with a rectangular cross-section. The valve seat is pressed into the hole in the cylinder head at room temperature or frozen in solid carbon dioxide (dry ice) or liquid nitrogen before being inserted into the head. The overlap of the seats with the head is 0.02 – 0.1 mm. [1 - 4, 86, 97 - 105, 111]

The processing of the outer diameter of the seats must be as smooth as possible and without a wavy surface so that it fits nicely into the hole in the head and that the transfer of heat is as perfect as possible and uniform over the entire circumference. For the valve seat not to be deformed by tension during pressing, which increases even more during operation by expanding the seat, it must have sufficient thickness. Seats inserted into cylinder heads made of light alloys (most often silumin) must have properties adapted to this material, especially expansion. [1 - 4, 97 -105, 111]

Aluminum and beryl bronze have proven to be suitable for medium-duty engines. Cobalt alloys, on the other hand, are used for highly stressed engines. The most modern trend in the production of valve seats is the use of powder metallurgy. According to the number of uses of the material, seats made with the help of PM can be divided into three basic groups: [1 - 4, 97 - 105, 111]

a) Monometallic
b) Bimetallic
c) Trimetallic

a) Monometallic valve seats are made from a single layer of metal, typically steel or stainless steel, chosen for their strength and wear resistance. The monometallic valve seat is typically machined to a precise shape and size, allowing it to form a tight seal against the valve when installed in the engine. The seat is also typically hardened to improve its wear resistance and durability. When the engine operates, the monometallic valve seat expands and contracts with the temperature changes. This allows the valve seat to maintain a tight seal against the valve, even as the temperature and pressure in the engine fluctuate. Overall, monometallic valve seats are a durable and cost-effective solution for sealing valves in internal combustion engines. They are often used in lower-performance engines, where they can provide reliable sealing without the need for more expensive materials or manufacturing processes. [1, 97 - 105, 111]

b) Bimetallic valve seats are made from two layers of different metals that are bonded together, typically with a layer of soft metal, such as lead, copper or tin, between the two layers. The two metal layers in a bimetallic valve seat are chosen for their different characteristics. The outer layer is typically made from rugged and durable metal, such as steel or stainless steel, which provides strength and wear resistance. The inner layer is made from a softer metal, such as lead, tin, or copper, which provides a more conformal and flexible seal against the valve. Bimetallic valve seats are a durable and effective solution for sealing valves in internal combustion engines. They are often used in high-performance engines, where they can withstand the extreme temperatures and pressures found in these applications. [1, 97 -105, 111]

c) Trimetallic valve seats are made from three layers of metal, which are bonded together to form a composite material. The three metal layers in a trimetallic valve seat are chosen for

their different characteristics. The outer layer is typically made from rugged and durable metal, such as steel or stainless steel, which provides strength and wear resistance. The middle layer is made from a softer metal, such as lead or tin, which provides a more conformal and flexible seal against the valve. The inner layer is made from a metal resistant to high temperatures, such as cobalt or chromium, which helps prevent the seat from deforming or melting under extreme operating conditions. [1, 97 -105, 111]

Valve seats made by powder metallurgy can be well-shaped geometrically, and as a rule, a division of the seat material into two is chosen in a horizontal plane, where the part in contact with the valve is made of a complex and wear-resistant material, and the other half of the seat is made of a rigid material with good thermal conductivity. The precisely assembled valve seat is the subject of trademarks and patents of all current engine manufacturers. [1, 97 -105, 111]

3.1 Materials used for valve seats

The most common materials for valve seats are steel, alloys, Ceramics, Powder metallurgy, and Cast iron. Steels, such as martensitic and austenitic steels, are known for their high strength and durability but can be brittle and prone to cracking at high temperatures. Alloys, such as cobalt and nickel-based alloys, e.g., Stellite, have high wear resistance and good thermal stability, making them suitable for high-temperature applications. Ceramics, such as silicon nitride, are known for their excellent wear resistance and high-temperature stability but are brittle and difficult to machine. [1, 97 - 111]

Recently, there has been an increasing interest in using new materials, such as intermetallics and nanocomposites, for valve seats. These materials offer improved wear resistance, thermal stability, and corrosion resistance, making them suitable for high-performance engines.

The most widespread material for the production of valve seats was cast iron. The properties of cast iron are well suited for this application for the following reasons: [1, 60, 97 - 111]

- Good damping properties
- Good lubricating properties
- Low production costs
- Good machinability

- Good thermal conductivity

However, cast iron seats produced by conventional methods had low wear resistance and hardness compared to super cast irons, so they began to be replaced by superalloys or materials produced using PM. Valve seats are currently manufactured from many materials and surface treatments. The use of materials depends on the specific manufacturer and application. [1, 83 - 87, 97 - 111]

3.2 Cobalt alloys used for valve seats

Cobalt-based alloys, specifically Stellites, are categorized as superalloys. These alloys possess exceptional mechanical and tribological properties, including high hardness and strength, excellent resistance to adhesive and abrasive wear, and remarkable resistance to cavitation and erosion. Stellites find extensive application across various industries, particularly in scenarios demanding superior wear resistance in non-lubricated systems operating at elevated temperatures. Stellite alloys encompass a range of cobalt and chromium alloy compositions. They may also contain tungsten or molybdenum and minor (< 3 wt %) but essential amounts of carbon. Therefore, Stellite alloys are generally strengthened by the precipitation of carbides in a cobalt solid solution matrix.

Many of the properties of Stellite alloys result from the crystallographic nature of cobalt, the reinforcing effects of chromium on the solid solution, tungsten, and molybdenum, and the corrosion resistance imparted by chromium. [7, 22, 42]

The main difference between individual wear-resistant stellites is the carbon content and, thus, the volume fraction of carbides in the materials. Stellites are commonly categorized as medium and high-carbon alloys designed for wear resistance. Chromium has a dual function in stellite alloys. It is a central carbide-forming element, meaning that most carbides are rich in chromium, and it is also the most important alloying element in the matrix, where it provides corrosion and oxidation resistance as a solute. Tungsten and molybdenum are used to ensure additional strength of the matrix. This property results from their sizeable atomic size, i.e., when present as solute atoms, they impede the flow of dislocations. They also generally improve the corrosion resistance of alloys. In addition, tungsten carbides can contribute to the formation if they are present in large quantities. Critical properties of stellite alloys include: [7, 22, 42]

- Excellent tribological properties
- Excellent mechanical strength
- Excellent resistance to static loading, fatigue and creep
- Good surface stability
- Excellent resistance to oxidative corrosion
- Good phase stability at high temperatures

Stellite 6 typically adopts a face-centered cubic (FCC) crystal lattice structure. This arrangement consists of cobalt atoms occupying the corners of the unit cell and additional alloying elements, such as chromium, tungsten, and carbon, distributed within the lattice. The FCC crystal structure provides Stellite 6 with good ductility, high melting point, and excellent resistance to wear and corrosion. Microstructure of Stellite 6 is in Fig. 14. [95, 96]

Stellite 12 has a hexagonal close-packed (HCP) crystal lattice structure. Cobalt atoms form closely packed hexagonal layers in this arrangement, with additional alloying elements distributed within the lattice. The HCP crystal structure imparts Stellite 12 with high hardness, excellent thermal stability, and resistance to oxidation and deformation at elevated temperatures. Microstructure of Stellite 12 is in Fig. 15. [95, 96]

Stellite alloys are primarily used in applications with increased wear resistance in corrosive environments and are valued for their ability to operate at elevated temperatures beyond the capabilities of conventional materials such as steel. Elwood Haynes invented it in the early 20th century, later becoming the Deloro Stellite Company trade name. Initially, the high strength of binary cobalt and chromium alloys was discovered. He later introduced the ternary alloys Co-Cr-Mo and Co-Cr-W. They discovered strong strengthening effects of molybdenum and tungsten within the cobalt-chromium system. [7, 22, 42]

3.2.1 Hardness and tribological properties of Stellites

Most cobalt alloys (except low carbon alloys) have a very high hardness - 40 ~ 63 HRC because they contain a high proportion of wear-resistant hard carbides together with a complex solid-solution interface, which makes them very suitable for application in frictional wear conditions. Cobalt alloys retain their hardness at temperatures above 760 °C. Wear can generally be defined as the interaction between surfaces that results in material loss. Wear can act in many modes, but three basic types of wear include: [22, 42, 52, 129]

- Abrasive wear
- Sliding wear
- Erosive wear

Abrasive wear occurs when rigid particles or solid projections with a high hardness on a counterface are compelled to interact with and traverse a surface. The terms "high-stress" and "low-stress" abrasion pertain to the state of the abrasive medium (whether composed of hard particles or projections) after its interaction with the surface. When the abrasive medium undergoes fragmentation, it corresponds to the dominance of the high-stress condition. Conversely, if the abrasive medium retains its integrity, the process is denoted as low-stress abrasion. Typically, high-stress abrasion materializes due to the entrapment of robust particles between metallic surfaces undergoing relative motion. On the other hand, low-stress abrasion manifests when mobile surfaces make contact with compacted abrasives like soil and sand. [22, 42, 52, 129]

In alloys such as cobalt-based wear-resistant alloys, wherein a rigid phase is present, the abrasion resistance generally escalates with the augmentation of the volume fraction of the rigid phase. Nonetheless, the abrasion resistance is profoundly affected by the dimensions and configuration of the precipitates of the rigid phase embedded within the microstructure, as well as the dimensions and configuration of the substances causing abrasion. [129]

The sliding wear mechanism typically arises under elevated contact stresses, leading to the deterioration of oxide films to an extent where direct metal-to-metal contact ensues. This situation introduces the potential for cold welding of surfaces, and subsequent movement can lead to the detachment of small fragments from the initial interface, usually from the weaker two mating materials. This mechanism, known as galling, often involves substantial transfer of metal from one surface to the other, accompanied by significant deformation of surface materials. [129]

Solid-particle erosion results from the collision between small, solid particles and a surface. Generally, these particles are either airborne or transported by other gaseous agents. These particles typically have sizes ranging from 5 to 500 μm. The velocities linked with solid-particle erosion display a broad spectrum, from 2 $m.s^{-1}$ in fluidized bed combustors to 500 $m.s^{-1}$. The erosion rate is influenced by particle velocity, the angle at which they impact (which has distinct implications for ductile versus brittle materials), and the inherent characteristics of the eroding particles (their shape, size, and strength). [129]

Tab. 4 summarizes the chemical composition of various types of cobalt alloys - Stellite.

Tab. 4 Chemical composition of various types of cobalt alloys [22]

Material	**Chemical composition** [%]								**Hardness**
	C	**Mn**	**Si**	**Cr**	**Mo**	**W**	**Ni**	**Co**	**HRC**
Stellite 3	2 - 2.7	1	1	31	-	13	3	Balance	52 - 53
Stellite 6	0.9 - 1.4	1	1.5	29	1.5	4.5	3	Balance	42 - 45
Stellite 12	1.1 - 1.7	1	1	30	-	8	3	Balance	44 - 48
Stellite 19	1.5 - 2.1	1	1	31	-	10.5	3	Balance	47 - 50
Stellite 25	0.1 - 0.2	1.5	1	20	-	15	10	Balance	44 - 46

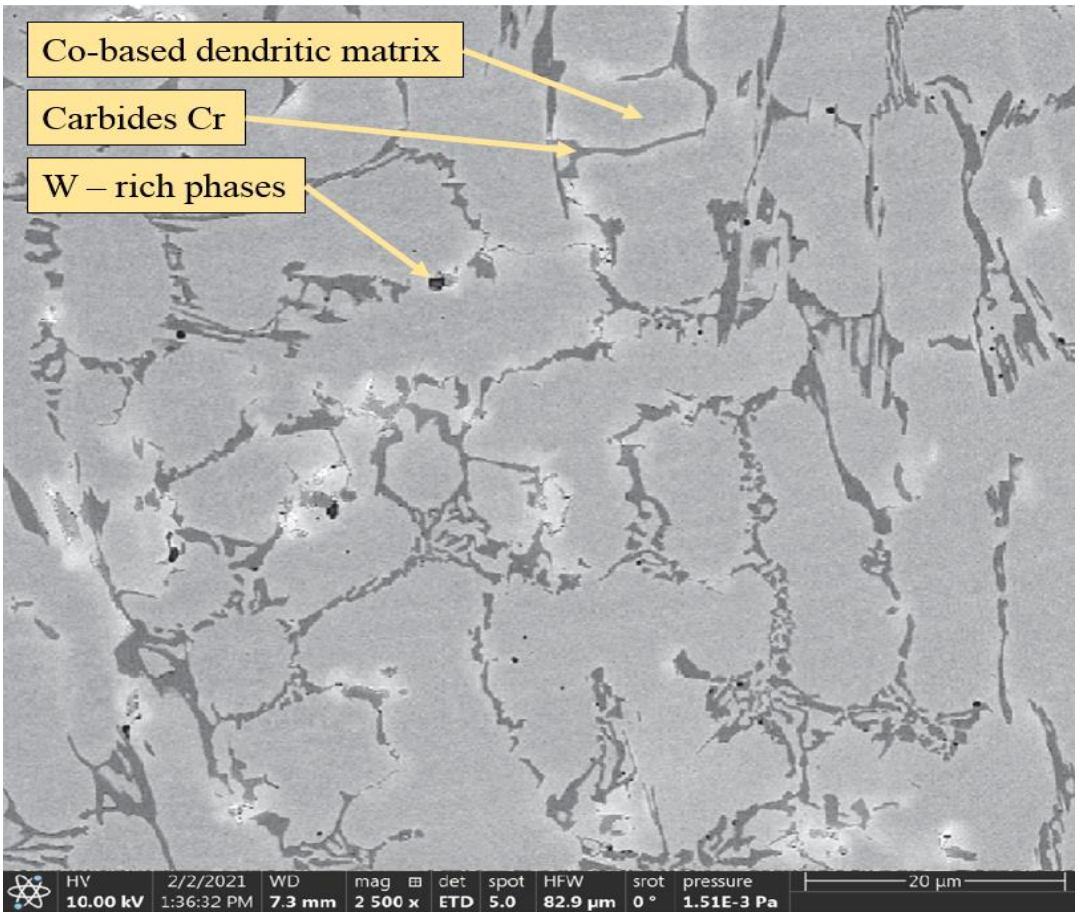

Fig. 14 Microstructure of Stellite 6 [113]

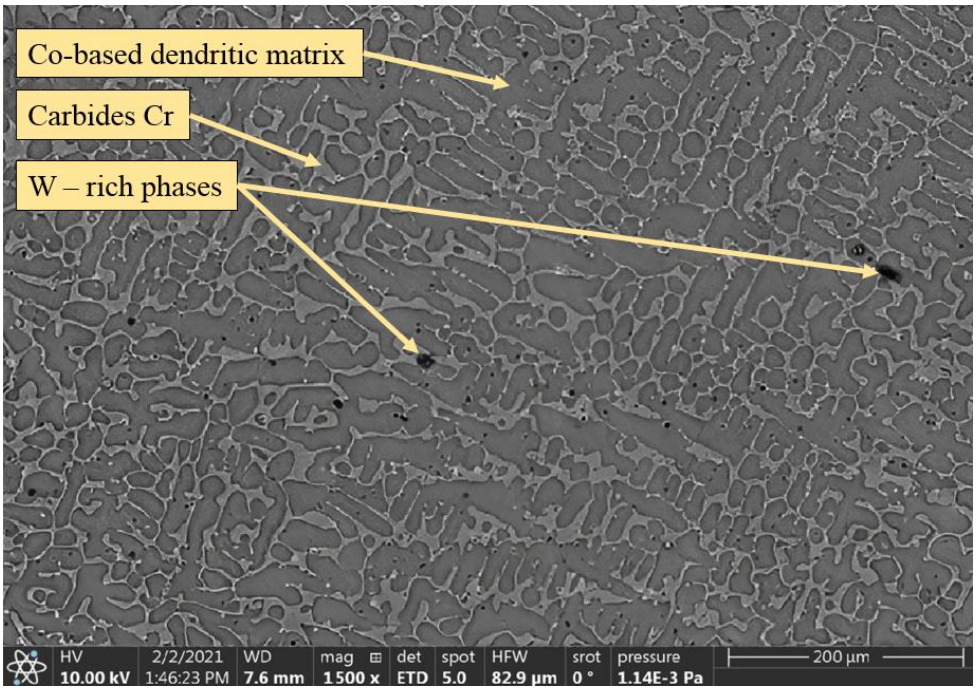

Fig. 15 Microstructure of Stellite 12 [114]

3.3 Mechanical Properties of Stellites

Stellite alloys have high Young's modulus and tensile strength but generally low ductility due to the nature of their microstructures. Large amounts of carbides make these alloys very brittle, but low-carbon stellite alloys, i.e., solution-strengthened stellite alloys, have better ductility. The requirements for the high mechanical strength of stellite alloys are mainly assessed by measuring the short-term tensile strength and deformation during CREEP. Hardening of stellite alloys is partly ensured by solid solution matrix hardening and partly by precipitation of carbides. The morphology and location of carbide precipitates influence the strengthening effect and are required for optimal precipitation enhancement at grain boundaries and within grains. At grain boundaries, precipitates prevent the sliding of crystal planes and [36] boundary migration and, if present in sufficient quantity, can form an underlying network that can support some of the imposed stress to some extent. Intragranular precipitation strengthens the matrix by preventing the movement of dislocations, thereby inhibiting crystallographic slip. In Tab. 5, are shown the mechanical properties of Stellite 6 and Stellite 12. [2, 7, 11, 66, 129]

Tab. 5 Mechanical properties of select cobalt alloys [129]

	Density [g/cm^3]	**Tensile strength Rm [MPa]**	**Yield strength R_{p02} [MPa]**	**Elongation [%]**
Stellite 6	8.3	834	640	1.2
Stellite 12	8.6	827	630	1

The solidification conditions initially determine the distribution of carbides in any alloy - the casting temperature of the melt and the cooling rate both during and after solidification. The short-term tensile properties of Stellite alloys can be relevant to manufacturing operations associated with component fabrication - ductility, in particular, controls the amount of hot or cold working that can be enforced. In the as-cast state, the tensile elongation is about 8% at room temperature and increases relatively smoothly with increasing temperature. After the alloy was aged for 50 hours at 732 °C, however, carbide precipitation hardening reduced the elongation at room temperature to 1~2%, and ductility recovery only occurred at temperatures above the aging temperature. Wrought alloys typically exhibit significantly higher elongation in tension compared to cast alloys. Stellite alloys, in particular, rapidly increase hardness due to cold work when their compositions are not fully stabilized concerning the charge-hep transformation. [7, 11, 22, 42]

The article "Microstructural evolution and wear behaviors of laser-clad Stellite 6/NbC/h-BN self-lubricating coatings"[41] explores the utilization of Stellite 6 as a self-lubricating coating in tribological applications. The coating exhibits a homogeneous microstructure characterized by small, refined grains, enhancing wear resistance, and a reduced friction coefficient. Incorporating NbC and h-BN particles into the coating further improves its tribological properties. These findings suggest that the laser-clad Stellite 6/NbC/h-BN coating holds excellent promise for tribological applications, offering improved wear resistance and self-lubricating characteristics. [2, 39, 43]

The study "Temperature-dependent sliding wear behavior of Stellite 6 alloy" [42] provides an in-depth analysis of the wear behavior of the alloy at various temperatures. The results indicate that the wear rate of Stellite 6 increases as the temperature increases, which is attributed to the thermal softening of the alloy and a decrease in hardness. The study also showed that the wear mechanism changes from abrasive wear at lower temperatures to adhesive wear at higher temperatures. These findings have critical tribological implications for industries that use Stellite 6 alloy in high-temperature applications such as aerospace, power generation, and oil and gas. To improve the performance of the alloy at high temperatures, the study suggests alloying with elements such as chromium and tungsten and using coatings or surface modifications. These results provide valuable information for researchers studying Stellite 6 alloy, highlighting the need for further research to explore the potential of alloying and surface modification techniques to enhance the tribological properties of the alloy at high temperatures. [2, 39, 43]

3.4 Heat treatment of cobalt alloys

Cobalt alloys are alloys from the group of supermaterials for applications requiring high abrasion resistance. Chromium, tungsten, or molybdenum and a small amount of carbon are used as alloying elements. The microstructure of cobalt alloys contains chromium carbides, which have a melting temperature between 1250 – 1895 °C, and tungsten carbides up to around 2870 °C.

The heating temperature of the Stellite solid solution is in the range of 1000 °C to 1200 °C. Due to the high-temperature resistance of these materials, heat treatment is limited to annealing to remove residual stresses in castings, welded parts, and cold-drawn parts. Annealing temperatures range from 250 °C to 650 °C. [2, 39, 41, 43]

Post-casting heat treatment of Stellite materials involves a process called solution annealing. During this treatment, Stellite castings are subjected to specific temperatures, typically ranging from 1050 °C to 1200 °C, and held at those temperatures for a designated period. This allows for the dissolution of carbides and the transformation of the material's microstructure. Consequently, residual stresses are alleviated, and a more uniform and refined grain structure is formed. [2, 39, 41, 43]

Subsequent to the solution annealing, the Stellite castings undergo rapid cooling, which can be achieved through methods like water quenching or air cooling. This controlled cooling process is crucial to prevent the reprecipitation of carbides, as their presence could adversely affect the material's mechanical properties. [2, 39, 41, 43]

The heat-treated Stellite materials exhibit several improvements, including enhanced dimensional stability, reduced internal stresses, and superior mechanical properties such as increased hardness, strength, and wear resistance. These attributes are particularly significant for applications wherein Stellite components are exposed to high temperatures, abrasive environments, or extreme mechanical loads. [2, 39, 41, 43]

3.5 Cryogenic heat treatment of cobalt alloys

Cryogenic heat treatment is still an underexplored area, and research is mainly focused on ferrous metals or cast iron. The field of cryogenic heat treatment of cobalt alloys has not yet been sufficiently, or even at all, explored.

The cryogenic processing of these materials results in WC (Wolfram carbide) refinement and their spheroidization. It also has a significant effect on increasing the service life of these tools. According to this work, cryogenic processing does not have a significant effect on the hardness of tools. The process of cryogenic heat treatment consists of 3 basic steps: [22, 39, 41, 43,129]

1. Cooling to cryogenic temperature
2. Remaining at this temperature for a defined time
3. Heating to room temperature and subsequent annealing to remove residual stresses.

3.6 Process of cooling cobalt to cryogenic temperature

Cryogenic processing is a thermal treatment process that involves cooling the material to temperatures ranging from around -30 °C to -196 °C using liquid nitrogen, which is the most commonly used cryogenic medium. Lower temperatures close to absolute zero can be achieved using liquid helium. The cooling time required to remain at this temperature depends on the temperature of the cryogenic medium, as the speed of movement of atoms and molecules in the material decreases at such low temperatures. Previous research has used cooling times ranging from 2 to 180 hours in liquid nitrogen. The rate of cooling and heating of samples is a critical factor in cryogenic processing, as a cooling rate in the range of 20 °C - 30 °C/h can prevent high internal stresses from occurring in the material and causing damage. [22, 39, 41, 43, 113]

The article "Microstructural evolution and wear behaviors of laser-clad Stellite 6/NbC/h-BN self-lubricating coatings" explores the utilization of Stellite 6 as a self-lubricating coating in tribological applications. The coating exhibits a homogeneous microstructure characterized by small, fine grains, leading to enhanced wear resistance and a reduced friction coefficient. The incorporation of NbC and h-BN particles into the coating further improves its tribological properties. These findings suggest that the laser-clad Stellite 6/NbC/h-BN coating holds great promise for tribological applications, offering improved wear resistance and self-lubricating characteristics. [22, 39, 41, 43]

The article by Skalante, E.M., Makich, H., and Nouari, M. titled "Effect of cryogenic friction conditions on surface quality" [43] delves into an examination of how cryogenic conditions influence the surface quality of materials employed in tribological applications. The study aims to shed light on the changes that occur in surface characteristics, such as roughness, wear, and friction when subjected to cryogenic friction conditions. Through experimental investigations and analysis, the researchers provide valuable insights into the effects of cryogenic treatments on

the performance and durability of materials in tribological systems. The study reveals that cryogenic conditions can significantly enhance the surface quality of materials by reducing the formation of surface defects, such as micro-cracks and surface roughness. The findings of this research have significant implications for industries employing materials in tribological applications, including cutting tools, mining, and drilling equipment, and automotive components. The study recommends the use of cryogenic conditions as an effective method to improve the surface quality of these materials, thus extending their service life. In conclusion, this study highlights the potential of cryogenic conditions as a post-treatment to enhance the surface quality of materials used in tribological applications. Future research is necessary to explore the impacts of different cryogenic conditions and to gain a better understanding of the mechanisms that lead to improved surface quality. [41, 113]

3.7 Magnetism of Cobalt Alloys

Magnetism plays an important role in cobalt alloys due to their inherent magnetic properties. Cobalt alloys are known for their high saturation magnetization and excellent magnetic performance, making them desirable for various applications. The magnetic behavior of cobalt alloys is primarily governed by their crystal structure and composition. The arrangement of atoms and the presence of certain elements can influence the magnetic domains and the overall magnetization of the material. Understanding the magnetic properties of cobalt alloys is essential for optimizing their performance in magnetic devices and applications. [94 – 96, 129]

3.7.1 Magnetism of Stellite 6 and Stellite 12

Stellite 6 and Stellite 12 possess a high saturation magnetization, which refers to the maximum magnetization that can be achieved in the material. This property makes Stellite 6 suitable for applications requiring strong magnetic performance. The alloy also demonstrates magnetic hysteresis, displaying a lag in magnetization response during changes in the applied magnetic field. This hysteresis effect leads to the retention of a residual magnetization even when the external magnetic field is removed. [94 – 96, 129]

In terms of physical parameters, Stellite 6 and Stellite 12 have a crystalline structure that can vary depending on the specific processing and heat treatment. The crystal structure affects the arrangement of atoms within the alloy, which in turn influences its magnetic properties. The composition of Stellite 6 and 12 typically consists of cobalt as the base element, along with varying amounts of chromium, tungsten, and carbon. These alloying elements contribute to

the mechanical strength and corrosion resistance of Stellite 6 and 12 while also influencing its magnetic behavior. [94 – 96, 129]

3.8 Heat treatment of materials for valve seats

Technological procedures of heat treatment of metals used in technological practice can be divided into four basic groups: [1, 12, 25, 84, 85]

1. Procedures in which we obtain a more balanced structure compared to the initial state. They are used with a different specific purpose in all metal materials.

2. Procedures in which we create structures with a certain degree of imbalance. For steels, these procedures remain from hardening and tempering. For non-ferrous metals, a process called hardening is used.

3. Procedures in which, in addition to structural changes, there are also changes in the chemical composition of the surface layers of materials, i.e., chemical-thermal treatment.

4. Procedures in which the desired change in properties is achieved by a combination of intensive forming and heat treatment, i.e., thermomechanical treatment.

3.9 Heat treatment of cast iron

Heat treatment of cast iron can provide several benefits, including increased strength, hardness, and wear resistance. It can also improve the toughness of the material, making it less brittle and less susceptible to cracking. Heat treatment can also be used to refine the microstructure of the cast iron, which can improve its machinability and other mechanical properties. As standard, isothermal finishing is chosen, which gives the material the necessary properties and, at the same time, a low level of internal stress. [5, 30, 33-36, 46]

3.9.1 Isothermal refinement of cast iron

The foundation for ADI/AGI/AVGI consists of cast iron with a ferritic or ferritic-pearlitic matrix and exhibiting flake, vermicular, or nodular graphite. When the matrix is pearlitic, machining the casting becomes more intricate, yet it gains advantages from improved austenitization (resulting from shorter diffusion paths and reduced time at the austenitization temperature). Conversely, in cases of a ferritic matrix, the casting is notably conducive to

machining (far more efficient than steel), but a prolonged austenitization period is necessary. [5, 30, 33-36, 46]

The graphite should exhibit an ideal shape and size in the original cast irons, while graphite particles need to be uniformly dispersed within the structure. Fine dispersion and consistent graphite distribution are the foundational prerequisite for maximizing matrix utilization. In ADI production, deviations from a spherical shape of graphite nodules in initial GJS should not surpass 20%. For all cast irons, it is essential to have graphite particles that are adequately small and present in substantial quantities. For ADI, a minimum of 160 particles/mm² is specified. Although specific parameters (prior lengths and densities of flakes/vermicular structures) have not been explicitly recommended for AGI and AVGI, it is unquestionably essential for graphite to be as finely distributed as possible (e.g., GI - A size 5-6 for AGI) to achieve the intended isothermal transformation effect. [5, 30, 33-36, 46]

These requirements also necessitate adjustments to the chemical composition, primarily concerning the content of fundamental elements C and Si. This needs to be determined considering wall thicknesses so that the eutectic reaction progresses close to the optimum, resulting in the formation of numerous small, regular graphite particles in the case of GJS. [5, 30, 33-36, 46]

Carbide-forming elements, especially Mn but also Mo, segregate along grain boundaries during solidification, reducing ductility and toughness. On the other hand, elements like Cu and Ni have higher concentrations adjacent to graphite particles compared to areas between matrix grains (similarly to Si). Alloys of Mo and Ni or Cu are added to initial cast irons because they shift the onset of isothermal decay to longer times, thereby increasing hardenability. Typically, the maximum bainite hardenability for non-alloyed cast iron is around 13-15 mm wall thickness. In contrast to Mo, Mn has no balancing positive effect, and its content as a carbide-forming element in initial cast irons should not exceed 0.2%. Due to their segregation into intergranular spaces, the carbide-forming elements' content negatively impacts castings' machinability. Maintaining the lowest possible content of elements such as P and S, minimal impurities, and pores, particularly near the surface, is essential. [5, 30, 33-36, 46]

The resultant structure emerges through the isothermal decomposition of austenite within the bainitic region. The schematic representation of isothermal heat treatment for cast irons can be found in Fig. 16 [5, 30, 33-36, 46]

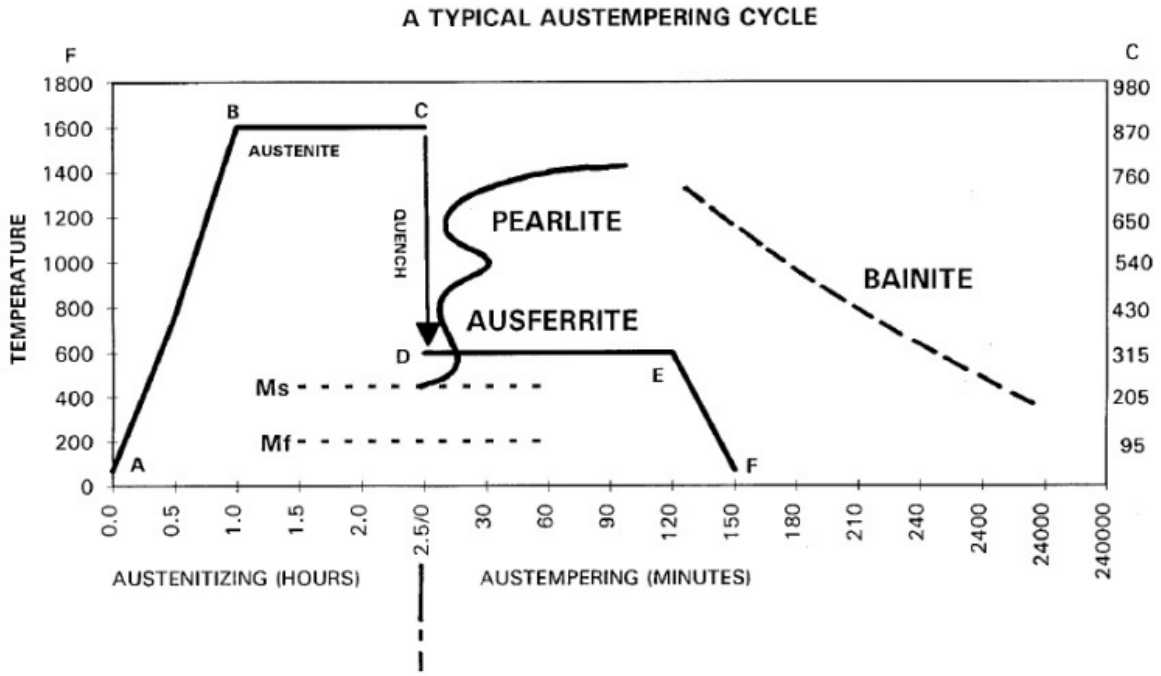

Fig. 16 Scheme of isothermal refining of ADI [5]

Austenitization should take place in an inert atmosphere to prevent undesirable surface decarburization. The austenitization temperature falls within the range of 820-950 °C, depending on the % Si in the iron and the desired level of carbon saturation of austenite from graphite particles. In cases where higher hardness and wear resistance are required at a given strength, a temperature closer to the upper limit is selected. Conversely, greater ductility is achieved with lower carbon content in austenite, which calls for a lower austenitization temperature. The heating to the austenitization temperature (segment A-B) should occur at 100-200 °C/hour. The holding time at the austenitization temperature (segment B-C) ranges from 0.5 to 2 hours, based on the initial Ferrite / Pearlite structure. [5, 30, 33-36, 46]

The length of isothermal holding varies according to the type of cast iron and the chosen isothermal temperature and is determined based on the requirements for mechanical properties. The width of the process window increases as the isothermal holding temperature decreases. The optimal duration of holding for a complete transformation to ausferrite ranges from 30 minutes (upper ausferrite region, as in ADI) to 4 hours (lower ausferrite region, as in AGI and alloyed cast irons). When the holding time is shorter than what is suitable for the specific material and temperature, martensite can form in the structure upon cooling to room temperature. On the other hand, with longer holding times, the proportion of retained austenite (Az) decreases, leading to its decomposition and the potential emergence of carbides. [5, 30, 33-36, 46]

The subsequent step after austenitization involves rapid quenching (segment C-D), usually into a salt bath with temperatures ranging from 240 °C to 400 °C (based on mechanical property requirements), accompanied by optimal holding times of 0.5 to 4 hours (depending on the type of ADI/AGI/AVGI and the height of the isothermal transformation temperature, segment D-E). During this phase, the formation of lower to upper ausferrite (referred to as per ASTM A644-92) takes place. This structure resembles bainite and comprises ferrite needles or plates (60-80%) embedded in carbon-saturated (stabilized) austenite (ideally 20% to 40%). Notably, carbides are absent in this structure. The structure should also avoid the presence of martensite or pearlite. The cooling from the austenitization temperature to the isothermal transformation temperature is conditioned to ensure that the temperature-time curve does not intersect the pearlite formation range in any part of the casting. The duration of isothermal holding primarily limits the martensite content. The cooling to ambient temperature occurs in the open air (segment E-F). [5, 30, 33-36]

In Tab. 6 are shown tabulated values of the mechanical properties of GJS and GJL cast iron.

Tab. 6 Overview of the mechanical properties of selected cast iron EN-GJS and EN-GJL [29, 30]

Material	**Rm [MPa]**	**$R_{p0,2}$ [MPa]**	**A [%]**	**HB**
EN-GJS-400-18	400	250	18	130-175
EN-GJS-450-10	450	310	10	140-200
EN-GJS-800-8	800	500	8	260-320
EN-GJS-1000-5	1000	700	5	300-360
EN-GJS-1200-2	1200	850	2	340-440
EN-GJS-1400-1	1400	1100	1	380-480
EN-GJL-150	150	-	-	150
EN-GJL-200	200	-	-	160
EN-GJL-250	250	-	-	180

3.9.2 Cryogenic heat treatment of ADI cast iron

Cryogenic heat treatment of ADI (Austempered Ductile Iron) cast iron is a process that involves subjecting the material to extremely low temperatures, typically between -80 °C and -196°C, for an extended period of time. This process alters the microstructure of the material, making it more durable and resistant to wear and tear. Cryogenic heat treatment can improve the toughness, fatigue resistance, and dimensional stability of ADI cast iron, making it useful for applications that require high strength and durability. It can also improve the machinability of the material, making it easier to work with. Cryogenic heat treatment is a relatively new technique

in the field of material science, and it is still being studied and developed, but it has been shown to be a promising method for improving the properties of ADI cast iron. [8, 38, 67 - 69, 76]

The cryogenic process can be divided according to the applied temperature into shallow freezing (to a temperature of around - 80 °C) and deep freezing (a temperature of around -190 °C). A typical deep freeze (cryogenic treatment) consists of a slow cooling of approx. 2.5 °C per minute. Cooling takes place from room temperature to the temperature of liquid nitrogen (approx. -195 °C). Once the material reaches approximately -190 °C, the casting is held at this temperature for a period of time approximately 24 hours. At the end of the cycle, the material is removed from the cryogenic chamber and heated to room temperature in air. After cryogenic treatment, it is recommended to further temper the material. From a technical point of view, cryogenic treatment is a technological operation performed immediately after classic clouding (before tempering). However, a distinction must be made between cryogenic processing and conventional low-temperature processing, which has been commonly used in industrial practice for many years. [67- 69, 76]

The primary objective of low-temperature treatment, along with multiple tempering, is the elimination of residual austenite from the microstructure. In traditional quenching methods, clouded cast iron often retains varying amounts of residual austenite, leading to insufficient hardness. Low-temperature processing is an effective approach for achieving complete martensitic transformation. In contrast, the elimination of residual austenite is an incidental outcome of cryogenic processing. This technique transforms the microstructure of cast iron into a structure that exhibits enhanced wear resistance, with the austenitic phase converting to martensite. Austenite, being an unstable and soft phase, is replaced by hard and brittle martensite. Consequently, cast iron undergoes tempering after cryogenic processing, similar to tempering performed after conventional quenching. Tempering yields tempered martensite, which retains relatively high hardness and toughness. Additionally, fine carbides precipitate within the matrix structure during the process. Oppenkowski's [6] research indicates a higher proportion of martensite with reduced tetragonality and finer twin structures. These microstructural modifications likely contribute to the subsequent precipitation of a substantial quantity of very fine carbides during tempering, which is frequently mentioned in the literature as a cause of the improved wear resistance. The research conducted by Liqing Chen on cryogenic processing of austempered bainitic ADI cast iron provides further support for these findings. [65, 67, 69, 76, 115]

3.10 Valve seat materials used in TEDOM engines

Historically, high-alloy cast iron with flake graphite under the trade names BX and BY was used as valve seat material at TEDOM. These seats were developed by BUZULUK Komárov (now Piston Rings a. s.). These were cast irons with high hardness and good abrasion resistance. An overview of the chemical composition is shown in Tab. 7, and hardness is shown in Tab. 8. The use of these materials for valve seats was abandoned after a while because these seats started to become uncomfortable with the increasing performance of engines and the transition to alternative fuels.

That is why the TEDOM company was forced to start using valve seats that would work safely with increased demands on engine life and reliability. Using seats made of cobalt alloys seemed to be the ideal choice. Currently, Stellite 6 material is used for the intake seat, and Stellite 12 for the exhaust seat. [Internal TEDOM documents]

Tab. 7 Chemical composition of material for valve seats of LIAZ engines [64, Internal TEDOM documents]

Chemical composition [%]	BX	BY
C	3.5 - 3.9	3.2 - 3.8
Si	2.2 - 3.5	2.2 - 3.3
Mn	0.5 - 0.8	0.6 - 1
P	0.3 - 0.6	0.3 - 0.6
S	≤ 0.1	≤ 0.1
Cr	1.1 - 1.6	1.1 - 1.6
Ni	≤ 0.5	0.3 - 0.6
Cu	≤ 0.5	0.6 - 1
Mo	1.1 - 1.6	1.1 - 1.6
V	-	0.1 - 0.3

Tab. 8 Hardness of special cast irons for valve seats used in LIAZ engines [Internal TEDOM documents]

Hardness HB	BX	BY
Casting	109 - 119	109 - 119
After heat treatment	108 - 114	108 - 114

3.10.1 Production of valve seats

The valve seats of the intake and exhaust valves for TEDOM Engines are produced using the technology of precision casting in wax molds in the company PBS Velká Bíteš. Tree-like structures are cast. With each batch of seats, experienced samples are cast to calculate the mechanical properties. To remove internal stress and improve hardness values, castings are annealed in an annealing furnace with gradual heating to 900 °C to 950 °C with "hold" at this temperature for 3 to 4 hours. They are then cooled in an oven to 500 °C. In Tab. 9 are requirements

for hardness of stellite using in TEDOM engines. The chemical composition for Stellite 6 and Stellite 12 prescribed by TEDOM for valve seats is shown in Tab. 10. [Internal TEDOM documents]

Tab. 9 Required hardness of castings after heat treatment [Internal TEDOM documents]

Material	HRC
Stellite 6	42 - 48
Stellite 12	48 - 52

Tab. 10 Required chemical composition of valve seats [Internal TEDOM documents]

	C [%]	Cr [%]	W [%]	Fe [%]	Ni [%]	Si [%]	Mn [%]	Mo [%]	B [%]	Co [%]
Stellite 6	1.0 – 1.4	26 – 32	4 – 7	max. 3	max. 3	max. 2	max. 1	max. 1	max. 0.5	Balance
Stellite 12	1.4 – 1.9	28 – 33	7 – 11	max. 3	max. 3	max. 2	max. 1	max. 1	max. 0.5	Balance

3.11 Technology of mounting valve seats into cylinder heads

There are several methods for mounting valve seats into cylinder heads, each with its own advantages and disadvantages. The most common methods include: [25, 116 - 119, Internal TEDOM documents]

1. Press-fitting: This method involves pressing the valve seat into the cylinder head using a press. This is a simple and cost-effective method that is suitable for most materials. However, press-fitting can cause deformation of the valve seat or cylinder head, and the press-fit may not be as secure as other methods.
2. Brazing: This method involves using a braze alloy to join the valve seat and cylinder head. Brazing is a strong and reliable method that is suitable for high-temperature applications. However, brazing requires specialized equipment and is more expensive than press-fitting.
3. Welding: This method involves welding the valve seat to the cylinder head. Welding is a strong and reliable method that is suitable for high-temperature applications. However, welding requires specialized equipment and is more expensive than press-fitting and brazing.
4. Cementing: This method involves using cement to join the valve seat and cylinder head. Cementing is a strong and reliable method that is suitable for high-temperature applications. However, cementing requires specialized equipment and is more expensive than press-fitting and brazing.

5. Interference fit: This method involves using a tight fit between the valve seat and cylinder head to hold the valve seat in place. It is simple, cost-effective, and suitable for most materials, but it can cause deformation of the valve seat or cylinder head. [25, 116 -119]

3.11.1 Press-fitting of valve seats

In order to safely install and position the valve seats in the head, the valve seats are pressed into the cylinder heads. Depending on the performance of the engine, the material of the cylinder head, the material of the valve seat, and the application, the pressing overlap between the seat and the head is selected. In practice, this overlap ranges from 0.03 mm to 0.2 mm. In order to be able to press the seats into the head without damaging the head or the seat, the manufacturers of internal combustion engines choose a technological procedure in order to reduce the pressing overlap to the necessary minimum in a few ways: [25, 116 -119, Internal TEDOM documents]

- Freezing seats
- Cylinder head heating
- Combination of head heating and seat freezing

4 VALVE GUIDES USED IN COMBUSTION ENGINES

Valve guides are components in internal combustion engines, specifically in the cylinder head, that support the valves and help to guide them as they open and close. Their primary function is to keep the valves aligned and centered as they move, which helps to ensure that they seal properly and do not come into contact with the cylinder walls or piston. Valve guides also help to reduce friction and wear on the valves, which can improve the overall performance and efficiency of the engine. [53, 62]

Valve guides in combustion engines are typically made of durable and wear-resistant materials, such as hardened steel, bronze, or cast iron. These materials are chosen for their ability to withstand the high temperatures, pressures, and mechanical stresses that are present in the engine. Hardened steel is a common material for valve guides because it has a high hardness and strength, which makes it resistant to wear and deformation. Bronze is also commonly used because it has good wear resistance and can provide good lubrication properties, which can help to reduce friction and wear on the valves. [53, 64, 116 - 119]

Cast iron is a commonly used material for valve guides because it is strong, durable, and relatively cheaper for production. However, there are some limitations to using cast iron for this application. One of the main drawbacks is that cast iron is not very wear-resistant at high temperature, which means that it may not be able to withstand the high levels of friction and wear that are present in internal combustion engines. Additionally, cast iron is not very good at conducting heat, which means that it may not be able to dissipate heat effectively from the valves. This could lead to overheating and potential failure of the valve guides. [25, 53, 116 -119]

4.1 Load of valve guides

Force analysis of valve guides in internal combustion engines typically involves evaluating the forces that the guides are subjected to during operation. These forces include the radial and axial loads exerted by the valve stem, as well as the thermal loads caused by the high temperatures encountered in the engine.

The radial load is the load that acts perpendicular to the valve stem and is caused by the valve spring force. The axial load is the load that acts parallel to the valve stem and is caused by the combustion pressure.

The thermal load is caused by the high temperatures encountered in the engine and can cause thermal expansion of the valve guide and valve stem. This can cause increased clearance between the valve stem and guide, leading to increased wear and possible seizing. [25, 64, 116 - 119]

5 CONTACT BETWEEN VALVE AND VALVE SEAT

Contact between the valve and valve seat plays a critical role in the performance and durability of internal combustion engines. The valve and valve seat come into contact during the opening and closing of the valve, and the contact area is subject to high temperatures, pressures, and wear. When designing the valve timing, it is also important to consider the correct selection of the impact velocity of the valve into the valve seat. In general, this velocity should not exceed 1 m/s. [Internal TEDOM Documentation]

5.1 Tribological contact

During relative movement between solid bodies, the occurrence of friction and wear processes is inevitable. For most systems, both a low coefficient of friction and minimal wear are desirable. The requirement is connected with ensuring the reliable operation of this system, and lower energy consumption, which leads to an extension of its life. Some systems require a high coefficient of friction (i.e., tires), and some even high wear (i.e., crayons). However, most efforts focus on the development of application systems with a low coefficient of friction and minimal wear and tear. Wear is usually defined as "damage to a solid surface involving progressive loss of material due to relative motion between this surface and the surface of another material or substance." Friction and wear depend on many parameters and conditions, including: [19, 27, 40, 61]

- material of solid friction elements, their composition, physical and chemical properties, their microgeometry and macrogeometry
- loading of the surface by point, edge, surface (possibility of static permanent or dynamic and intermittent loads)
- movement system
- system temperature
- system humidity
- speed of mutual movement (movement of one or both friction surfaces), test duration, distance traveled, area covered. [27]

The tribological properties of the surface are determined using a Tribometer for both dry and liquid surfaces environment. The "Pin-on-Disc" method was used for the experiments (Fig. 17). The principle of the exam is pressing a firmly attached body - Pin with specific radius *R [m]*, with a defined load, into the test sample - Rotating disk with radius r_0 *[m]*. The sample rotates at a predetermined speed and is executed in advance with a set number of rotation cycles or travels a certain length of track. The test device is equipped with a sensitive position sensor to which a holder is attached with an inserted body - pin or ball. The coefficient of friction between the body and the disc is evaluated from the measurement of the applied forces. It is possible to evaluate: [27]

1. The course of the coefficient of friction depending on the number of cycles.
2. Size and character of body wear.

3. Size and character of the tribological trace created on the sample.

Friction is resistance to the mutual movement of two bodies in their area of intercourse. The friction force *Ft [N]* depends on the friction coefficient μ and the load force F_N *[N]*. The fundamental relationship between individual quantities is given by the equation (Equation 1). [27]

$$\mu = \frac{F_t}{F_N} \qquad \textit{Equation 1}$$

where:

Ft [N] - is the frictional force acting against the direction of movement; F_N *[N]* - is a pressure force acting perpendicular to the direction of movement, μ *[–]* - is the coefficient of friction.

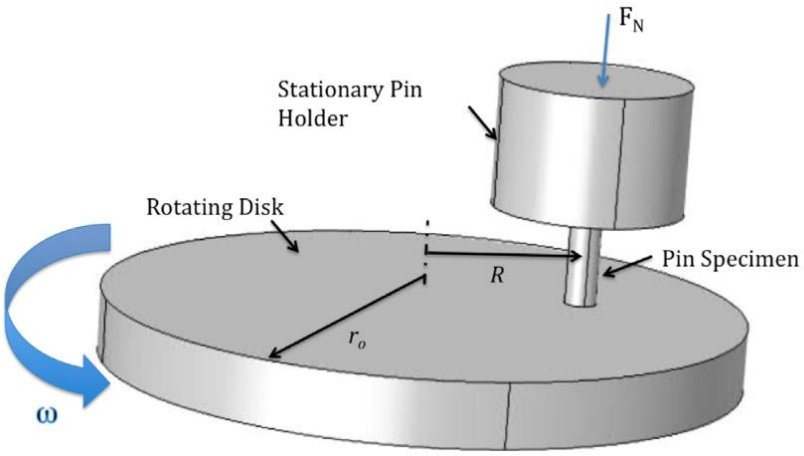

Fig. 17 Schematic representation Pin on Disc method [28]

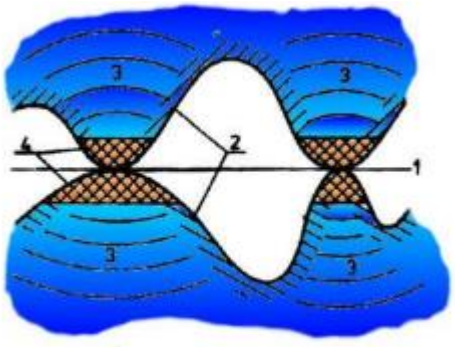

Fig. 18 Real contact between two surfaces [27]

Sliding friction occurs if two bodies come into contact with each other, and their movement occurs relative to each other. Actual contact between them occurs only in a limited number of

small areas Fig. 18. On Fig. 18 Represent numbers: 1 - Ideal surface, 2 - Real surface, 3 - Region of elastic deformation, 4 - Region of plastic deformation.

The size of the contact area increases with increasing load. A connection can occur at the peaks, and resistance to mutual movement is created. In the literature equation for the friction coefficient was derived [27, 90]

$$F_t = A_{mech}.\tau_s = \frac{P}{p}.\tau_s = \frac{\tau_s}{p}.P = \mu.F_p \qquad \textit{Equation 2}$$

where: *Ft [N]* - is the friction force acting against the direction of movement, A_{mech} *[m^2]* - is the actual contact surface of the fixed connection, τ_s *[Pa]* - is the shear strength of the material, *Fp [N]* - is the loading force, *p [Pa]* - is the pressure causing plastic deformation, μ *[–]* - is the coefficient of friction.

In Bakalova's doctoral thesis "Impact of Material and Technological Parameters of Machining on the State of Stress in Surface Layers and Properties of Machine Parts under Dynamic Load" [27] explores the description of the friction coefficient curve. (Fig. 19), the author presents six different stages of friction, differing from each other in the mechanism of friction. [27]

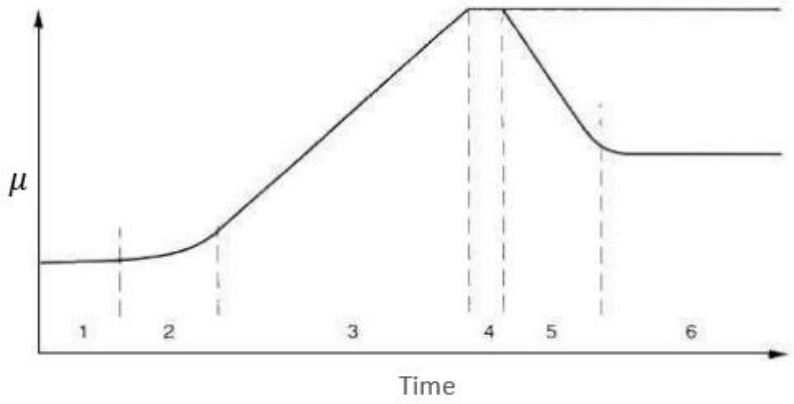

Fig. 19 Course of theoretical friction coefficient [27]

The first stage (1) is characterized by the dominant mechanism of surface furrowing with sharp irregularities. The mechanism of gradual deformation of surface irregularities is also applied. The adhesion mechanism does not significantly affect the coefficient of friction because the surface of the material is usually contaminated with foreign particles, for example, oxides. The coefficient of friction is not dependent on the friction conditions or the material of the sliding pair at this stage. In the second stage (2), due to increasing adhesive forces, there is a slight increase in the coefficient of friction, and adhesive joints may be formed. The third stage (3) is characterized

by an increase in the coefficient of friction due to the increase of particles stuck at the point of contact. There is also an increase in the activated surface area subject to adhesive friction. When the hardness of both materials is comparable, the scoring mechanism reaches its maximum. In the fourth stage (4), the friction coefficient is constant. The amount of particles, the deformation, and the amount of adhesion friction are also constant. The fifth stage (5) appears in the case of a sliding pair with a very soft and tough surface. The unevenness of the softer surface is polished, and the coefficient of friction decreases. During the sixth stage (6), a mirror gloss is achieved, and the coefficient of friction is constant. [27]

5.2 Static friction coefficient

The static coefficient of friction (μs), refers to the force required to overcome static friction and initiate motion between two surfaces. It is denoted by the symbol μs and is typically higher than the coefficient of dynamic friction (μd), which is the force required to maintain motion between two surfaces. The coefficient of static friction depends on various factors, such as the type of materials in contact, the surface roughness, the temperature, the humidity, and the applied pressure. For example, rough surfaces tend to have higher coefficients of static friction than smooth surfaces because the asperities of the surface interlock and create more excellent resistance to motion. The static friction coefficient is an essential parameter in tribological applications, where the goal is often to minimize friction and wear between surfaces. Understanding the factors influencing the static friction coefficient can help design more effective tribological systems. [88 - 91]

6 NON-DESTRUCTIVE MEASUREMENT OF PHYSICAL PROPERTIES

In modern industrial production, Non-Destructive Testing (NDT) is important for ensuring product quality while minimizing production costs. NDT methods, such as those used in the study of isothermally hardened cast irons, allow for directly measuring the product's properties without causing damage. This is particularly important for cast irons such as ADI/AGI, which require adherence to strict material and process tolerances in order to achieve optimal performance. [13, 30, 34, 51]

The use of NDT in this context allows for the examination of properties such as the excluded graphite and homogeneity of the cast iron, which are known to be essential factors in

determining the performance of these castings. However, achieving these properties can be challenging due to the less favorable inputs of raw materials and the increasing diversity of foundries' assortments. By mastering NDT techniques, it is possible to understand the properties of cast iron better and thus improve the reproducibility and efficiency of the production cycle.

Additionally, NDT allows for the examination of the physical and mechanical properties of cast iron castings, such as the properties of the matrix and the morphology and distribution of graphite particles, without causing any damage to the product. This type of analysis helps understand the relationship between the microstructure and the material's properties and can help improve the performance and longevity of cast iron castings. [20, 21, 30]

6.1 Ultrasonic analysis of cast iron

We have focused on the use of ultrasonic structural analysis for the examination of cast iron. Using this technique, it is possible to determine the speed of ultrasound propagation through the material, which can provide important information about the quality and performance of the cast iron. Additionally, this method allows for the examination of the material's microstructure and the properties of the matrix and graphite particles, which can be used to optimize production processes and improve the final product's performance. [13, 30, 34, 51]

Overall, ultrasonic structural analysis is a powerful tool for understanding the properties of cast iron and other materials. By utilizing the principles of wave propagation and non-destructive testing, it is possible to gain valuable insights into the microstructure and properties of the material, which can be used to improve product quality and production efficiency. [14, 26, 30, 34, 37]

The attenuation of a material refers to the loss of acoustic pressure that occurs as sound waves pass through it. This loss can be caused by two main factors: absorption and scattering.

Absorption occurs when sound energy is converted into heat due to internal friction within the material structure. This results in a decrease in the intensity of the sound field without generating any additional noise. Absorption is the dominant factor when testing plastics, as these materials tend to have high internal friction and thus absorb a significant amount of sound energy. [26, 30, 34]

Scattering, on the other hand, occurs when sound waves encounter irregular or inhomogeneous structures within a material, which causes them to deviate from their original

path. This deviation is reflected as structural noise on the testing device and can reduce the intensity of the primary sound field and increase the emergence of disturbing noise. This can make detecting material defects or other vital information more difficult. Scattering is more prevalent when testing metals, as these materials tend to have a more irregular structure and thus scatter more sound energy. [26, 30, 34, 37]

Attenuation losses, which include both absorption and scattering, increase exponentially with the frequency of the probe used. This means that attenuation also increases as the frequency of the sound waves being used for testing increases. This is important to consider when selecting a given material's appropriate testing method and frequency. [30]

Scattering is caused by:

- reflection on small inhomogeneities, such as gas pores and inclusions
- reflection on natural inhomogeneities, such as graphite particles in cast iron, porosity in cast materials or crystals of various compositions
- bending at the grain structure boundaries (especially coarse-grained structure)
- different elastic properties of grains (sound velocities) in different directions (anisotropy).

Generally, as the size of the inhomogeneity or anisotropy of the crystals forming the structure increases, scattering losses increase. An inhomogeneity can be considered an inclusion with an acoustic (wave) impedance *Z [MPa/s]* significantly different from the matrix. The more significant the difference in the acoustic impedance of the matrix *Zm* and the inclusion *Zi* (e.g., graphite), the greater the amount and size of the pressure reflections *R [-]* of the acoustic wave back from the interface. c represents the velocity of ultrasound waves in a given medium, and ρ represents the specific density of that medium. [14, 26, 30, 34, 37]

$$Z = c \cdot \rho \qquad [MPa \cdot s^{-1}] \qquad \textit{Equation 3}$$

$$R = \frac{(Z_i - Z_m)}{(Z_i + Z_m)} \quad [-] \qquad \textit{Equation 4}$$

Measuring the velocity of ultrasonic waves, whether longitudinal or transverse, is a relatively straightforward process. One of the most common methods is the pulse-echo method, which involves sending a pulse into an object and measuring the reflection from the interface between two different media. This can be done using specialized equipment, ultrasonic thickness

gauges, and universal defectoscopes. The principle behind these gauges is based on measuring the time delay, or Δt, between the emission of a short acoustic pulse by the ultrasonic emitter and its absorption by the detector. The emitted signal travels through the medium being measured from the input surface to the second interface, from which it is reflected. [26, 30, 34]

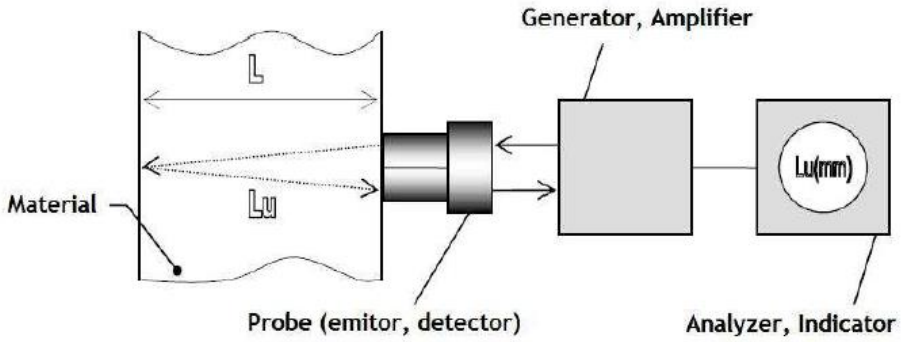

Fig. 20 Ultrasonic measuremet diagram [30]

It is crucial to consider the laws of reflection and refraction for plane waves to determine the difference between measuring longitudinal and transverse waves. A direct probe is sufficient for measuring longitudinal waves, and measurement is performed by perpendicular excitation. In contrast, an angled probe is required to generate and measure transverse waves, and measurement is performed by oblique excitation. The specific method will depend on the application and the available equipment. Overall, measuring the velocity of ultrasonic waves' velocity is essential in many industries, including manufacturing, materials testing, and nondestructive testing. Fig. 20 is shown of ultrasonic measurement diagram. [5, 26, 30, 34, 37]

Calculation of the velocity of propagation of longitudinal ultrasonic waves: [30]

$$2Lu = C_L \,.\Delta t \;\rightarrow Lu = \frac{1}{2}\, C_L.\Delta t \;\; [m] \qquad \textit{Equation 5}$$

$$C_L = \; C_{L_0} \,.\frac{L}{L_u} \;\; [m.s^{-1}] \qquad \textit{Equation 6}$$

The quantity C_L *[m.s^{-1}]* - is the speed of propagation of longitudinal ultrasonic waves in cast iron, C_{Lo} *[m.s^{-1}]* - is the speed of propagation of longitudinal waves of ultrasonic waves in steel (steel matrix of cast iron, calibrated on a standard), *L [m]* - is the actual thickness of the material, *Lu [m]- is* the path of the acoustic wave measured by an ultrasonic thickness gauge. [5, 26, 30, 34]

Determining the morphology, or shape and size, of graphite in cast iron can be achieved by measuring the speed of propagation of ultrasonic waves, also known as the speed of sound. This applies to both longitudinal and transverse waves. While this can be done for both types of waves, most often, the longitudinal ultrasonic wave is used, as its detection is more straightforward and requires only a direct probe. Much research and experimentation has been done using ultrasonic testing of cast iron, and the results have been processed into graphical representations of functional relationships. These relationships are often given in numerical form and show that the speed of the longitudinal ultrasonic wave is lowest (4300 $m \cdot s^{-1}$) in cast iron with rough flake graphite and highest (5600 - 5700 $m \cdot s^{-1}$) in cast iron with globular graphite. By measuring the speed of propagation of ultrasonic waves, it is possible to gain valuable insight into the microstructure of cast iron and identify variations in morphology. [5, 26, 30, 34]

Measuring the speed of ultrasonic waves can provide valuable information about the microstructure of cast iron. It can be used for various purposes, such as checking and sorting castings based on the correct exclusion of graphite or determining the degree of spheroidization of graphite (known as the nodularity test). The relationship between these two values is often linear, and by measuring the speed of ultrasonic waves, it is possible to gain insight into the morphology of the graphite in the cast iron. [5, 26, 30, 34]

The speed of ultrasonic waves is also closely related to the mechanical properties of the material being tested. This is because the speed of ultrasonic wave propagation is a function of Young's modulus*(E)*, specific density *(ρ),* and Poisson's ratio *(μ).* For longitudinal ultrasonic waves, the propagation speed can be calculated using Equation 6. Understanding the speed of ultrasonic waves can provide important information about the material's mechanical properties and can be used in quality control and research applications. [5, 26, 30, 34]

$$C_L = \sqrt{\frac{E}{\rho} . \frac{1-\mu}{(1+\mu).(1-2\mu)}} \; [m.s^{-1}] \qquad \textit{Equation 7}$$

With the known speed of longitudinal and transverse waves, the elastic constants can be determined, such as tensile Young´s modulus *E [MPa]* (Equation 8), shear Young´s modulus *G [MPa]* (Equation 9) or Poisson's constant μ (Equation 10). [26, 30, 34, 37]

$$E = \rho . \frac{3C_L^2 C_T^2 - \frac{4}{3} C_T^2}{C_L^2 - C_T^2} \qquad [MPa] \qquad \textit{Equation 8}$$

$$G = \rho . C_T^2 \qquad [MPa] \qquad \textit{Equation 9}$$

$$\mu = \frac{C_L^2 - 2C_T^2}{2(C_L^2 - C_T^2)} \ [-] \qquad \textit{Equation 10}$$

Determining the elastic constants of a material requires measuring the propagation velocities of ultrasound waves with great precision. Therefore, the shape and preparation of the sample is essential material. It must have a constant thickness, sufficient dimensions in the direction perpendicular to the axis of the ultrasound beam, and a good surface. To optimize the measurement accuracy se, they use high-damping probes. The choice of probe frequency depends on the thickness sample and the acoustic resistance of the material. [26, 30, 34]

The rates C_L $[m{\cdot}s^{-1}]$ and C_T $[m{\cdot}s^{-1}]$ for calculating the elastic constants can also be determined by measurement on semicircular sections (cutouts or castings) - Angular, the probe U placed in the center of the circle, emits transverse waves, while it does not matter the directional angle of radiation: [26, 30, 34]

$$C_L = \frac{L}{L_U} . C_{L_0} \ [m.s^{-1}] \qquad \textit{Equation 11}$$

$$C_T = \frac{R}{r} . C_{T_0} \ [m.s^{-1}] \qquad \textit{Equation 12}$$

L [m] – is the actual slice width, *R [m]* – is the actual radius of the slice, *and Lu [m]* - is the width of the section measured with an angle probe after calibration on a steel standard with longitudinal velocity C_{L0} $[m{\cdot}s^{-1}]$, *r [m]* - is the radius of the section measured with an angle probe after calibration on a steel standard with a transverse velocity C_{T0} $[m{\cdot}s^{-1}]$. [26, 30, 34]

Much more often, the so-called initial modulus is measured directly on the components of elasticity E_0, Young's modulus at the initial stress. It is a physical quantity expressing material stiffness (force-elastic deformation); its measurement is, therefore, instrumental in controlling the mechanical properties of castings. However, there is also a mathematical model for E_0, which numerically characterizes the shape, size, and amount of graphite in the sounding wall casting - concerning calculating E_0 (Equation 13), it is characterized by the term L/Lu. The material the constant *K*, inserted into the relation (Equation 17), is determined experimentally and depends on the specific type of sounding material. It includes data on specific mass and Poisson's constant of the given material. [2, 5, 26, 30, 34, 37]

$$E_0 = \left(K . \frac{L}{L_u}\right)^2 [MPa] \qquad \textit{Equation 13}$$

Determination of the constant K for a specific type of material is carried out by calculation from measurements on slender rods. The rods must meet the condition L/d>7, where *L* is the length of the rod [mm] and *d* is the diameter of the rod [mm]. Next, the data detected on the bars are:

M - bar mass in [kg]; *V* - rod volume [m^3]; *Vv* - rod volume by calculation [m^3]; *Vp* - rod volume by immersion [m^3]; *Lu* - rod length measured by ultrasound [mm]; τ - delay of the transformed transverse wave [mm]

Which is read from the display as the pitch of secondary echoes behind the primary reflection from the bar face. [5, 26, 30, 34]

Calculation procedure:

$$\mu = 0{,}5.\left[1 - \left(\frac{d}{2T}\right)^2\right] \qquad \textit{Equation 14}$$

$$T = \tau.\frac{L}{L_U} \qquad \textit{Equation 15}$$

where *T [s]* - is the true delay of the transverse wave. By comparing the above relations, the resulting relation for the constant *K* was created: [30, 34]

$$K = C_{L_0}\sqrt{2.\frac{M}{V}.\frac{1{,}5-\left(\frac{d^2}{8T^2}\right)}{1+\left(\frac{2T}{d}\right)^2}}\ \left[N^{\frac{1}{2}}.m^{-1}\right] \qquad \textit{Equation 16}$$

Which we can modify:

$$K = C_{L_0}\ .\sqrt{\rho.\frac{(1+\mu).(1-2\mu)}{1-\mu}}\ \left[N^{\frac{1}{2}}.m^{-1}\right] \qquad \textit{Equation 17}$$

6.2 Magnetic structure analysis of cast iron

Magnetic structure-scopic methods are based on the relationship between the magnetic properties and a material's structural, mechanical state. These methods can be used to check various properties such as heat treatment, chemical composition, mechanical stress, and the depth of a surface layer. They are an indirect method of measurement and involve measuring a selected magnetic parameter of the hysteresis loop, corresponding to the property of the inspected component. [5, 30, 47]

It has been experimentally shown that the hysteresis loop and its characteristic parameters, such as Coercive force *Hc [A·m^{-1}]*, Remanent induction *Br [T]*, Saturation induction *Bs [T]*, and specific (hysteresis) power losses, are often very sensitive to mechanical properties and can provide more excellent resolution than traditional mechanical testing methods. The information about the hysteresis loop and its parameters can be obtained either by direct measurement or its indirect effect on the induced voltage in the measuring device coil of the sensing unit. In the first case, a DC or slowly varying excitation magnetic field is used, referred to as the magnetic structuroscopy method. In the second case, an alternating current is used, and the magnetic field is time-varying; these methods are called electromagnetic structuroscopy methods. These methods can be helpful in various industries, such as metallurgy, materials science, and manufacturing, providing important information about the internal structure and properties of the tested materials. [5, 30, 32, 34]

The interaction of a ferromagnetic structure with a magnetic field is a crucial characteristic of materials such as ferromagnetic steels and cast irons. These materials are composed of blocks of atoms with the same orientation, known as domains, which make up the subgrains of the crystalline structure. When exposed to an external magnetic field, these domains will polarize in the same direction and close to each other, leading to growth by displacement of Bloch zones or step changes in polarization through Barkhausen jumps. After the external magnetic field is removed, not all domains will return to their original state, resulting in a remanent polarization. *Ir [A·m^{-1}]*. The magnetized area will also have its magnetic field with an intensity of *Hr [A·m^{-1}]*. These reversible changes are prevented by atoms bound in molecules, atomic stress, and lattice disorder. Therefore, areas that contain carbides, martensite, dislocations, and grain boundaries have a higher value of *Ir*. [30, 34, 47]

$$H_r = H_0 - \frac{N.I_r}{\mu} \; [A \cdot m^{-1}] \qquad \textit{Equation 18}$$

Hr [A·m^{-1}] - is magnitude of the remanent magnetic field, *H_0 [A·m^{-1}]* - is magnetic pulse size; *N [-]* - is demagnetizing agent; *Ir [A·m^{-1}]* - is remanent polarization; *μ [-]* - is permeability.

The so-called demagnetization factor *N* characterizes the geometric ratios of the interface ferromagnetism. The extreme values of *N* (0;1) belong to a thin plate, slender rod, or ferromagnetic half-space. If measured on surfaces, the demagnetization factor is significant. [5, 30, 34]

The hysteresis loop reflects the behavior of the magnetic domains in itself magnetization. As mentioned, with its characteristic parameters, the hysteresis loop reacts sensitively to some mechanical properties, such as hardness or strength. The coercive force and hysteresis loss increase, and permeability decreases with increasing carbon content in steels. These effects are attributed to carbide particles' increased filling of Bloch walls in the domain structure. Samples with lamellar pearlite exhibit higher coercive force than samples with carbides from small particles (as lamellar pearlite plates impede the movement of Bloch walls more effectively compared to small carbide particles). In eutectoid steel, the pearlitic microstructure has the lowest coercive force, hysteresis loss, and initial permeability. Martensite has the highest coercive force, the highest hysteresis loss, and the lowest initial permeability. Bainitic structures exhibit intermediate values for all three parameters. The coercive force increases with the square root of the obstacle density, such as dislocations. However, this relationship has not been universally proven, as its simplicity does not account for the structure and distribution of dislocations. [5, 30, 34]

The principle of the magnetic spot method is based on the relationship between the mechanical properties of ferromagnetic materials, such as hardness, and their coercivity. However, measuring coercivity directly can be difficult and is not typically used in practical applications. Instead, the coercivity $Hc\ [A \cdot m^{-1}]$ of the tested product can be inferred from the remanence $Br\ [T]$ value, which is a more straightforward measurement. This is based on the assumption that the tested subjects usually have a significant demagnetization factor, which causes the steepness of the hysteresis loop to decrease. The loop transitions from its original shape to a new shape, where the relation between the coercivity and linear remanence forms the hypotenuse of a right-angled triangle in the second quadrant of the coordinate system. It is important to note that as the coercivity changes, the remanence value also changes proportionally, allowing for the inference of coercivity from the remanence value. Remanence measurement can be quickly done by measuring the magnetic field in the test object's surroundings that were previously magnetized to saturation. This method can be used in various industries, such as metallurgy, materials science, and manufacturing, to understand the properties of ferromagnetic materials. [5, 30, 34, 37]

The principle of the magnetic spot method is based on the ability of a tested object to create a magnetic spot on its surface with the help of an attached magnetizing coil, also known as a "point pole." After the current pulse in the magnetizing coil is turned off, sensitive sensors measure the remanent magnetic field $Hr\ [A \cdot m^{-1}]$ at the sample's surface. The shape of the pulses sent to the

coil, or their precisely defined sequence, can define the flow of parasitic eddy currents and the structure-selective sensitivity of the method. [30, 34]

The contribution of individual ferromagnetic grains to the resulting Hr value depends on the shading effect and the distance of the domains from the sensor. As the depth of penetration of the magnetization field increases, the influence of individual grains on *Hr* decreases. The sensor used for measuring *Hr* can be a Hall probe or a Förster probe. These probes are typically connected differentially and measure the tangential or normal field components. The normal component of *Hr (Hrn)* is usually used for structural analysis and is measured perpendicular to the surface. A common device used for this method is the DOMENA B3 device, which is set up according to the magnetically hard standard or normal of the field intensity $H\ [A \cdot m^{-1}]$. This method can be used in various industries, such as metallurgy, materials science, and manufacturing, to understand the properties and microstructure of ferromagnetic materials. Quantification of structural components (e.g., pearlite) or *HB* hardness is obtained by linear regression analysis (Equation 18). [5, 30, 34]

As already mentioned, the magnitude of the measured intensity of the remanent of the magnetic field *Hr* is related to the structure matrix of the measured casting. [5, 30, 34]

The relationship between the monitored quantity and the measured intensity of the magnetic field must be experimentally determined and then used to calibrate the instrument. The magnetic spot method can be used to accurately measure the hardness, strength, or depth of hardening of ferromagnetic materials. It was found that repeated magnetization can even identify the structure of the matrix under certain conditions. The method can also be used to measure the depth of decarburization and to roughly determine the type of graphite as the value of *Hr* increases with the slenderness of the l/d graphite formations. This method has been successfully applied to steel and cast-iron products and is commonly used in quality control of castings, primarily through measurement of the *HB* value. [5, 30, 34]

The devices of the DOMENA series are portable battery-powered devices with a measurement cycle of 3-5 seconds. In normal mode, they are capable of one charge and perform at least 600 measurements. Magnetization is done by three discharges of a 20 μF capacitor (charged to a selectable voltage) in opposite polarities. *Hr* is measured by Hall by the sensor after the second and third discharges have faded. The resulting number on the device display shows the sum of the absolute values of both measurements (Equation 18). [5, 30, 34]

6.3 NDT Hardness measurement

Determination of *HB* hardness by the magnetic spot method is governed by the relationship: [5, 30]

$$HB = M.A + B\ [-] \qquad \textit{Equation 19}$$

The Equation 19 applies to measured thicknesses above 15 mm. Conversion relationship between remanence and hardness for measurements on a thin wall is given by: B and L and M.

$$HB = \frac{A.M_L}{a.L^{-b}+1} + B \qquad \textit{Equation 20}$$

HB or magnetic hardness, is a measure of the residual magnetic field retained by a material after it has been magnetized. *A [-],* and *B [-]* - are material constants that are obtained through linear regression from experimental measurements of *M* $[A \cdot m^{-1}]$ (magnetization) and *HB*. M_L $[A \cdot m^{-1}]$ - is the remanence for a given wall thickness and *L [m]* - is the wall thickness. This method can be used to accurately measure the *HB* of thin-walled castings, where a traditional hardness tester cannot be used. However, it is necessary to determine the characteristics of the probe, such as the relationship between M and wall thickness, and establish wall thickness intervals for which certain values of *A [-],* and *B [-]* apply. [5, 30, 34]

This dependence (Equation 19) is used in practice to determine the proportion of pearlite and ferrite in a material's structure. Lamellar pearlite in a metal matrix is magnetically harder than ferrite and retains a stronger residual magnetic field after magnetization, resulting in a higher value of *M* $[A \cdot m^{-1}]$. This method can be useful in industries such as metallurgy, materials science, and manufacturing, providing important information about the internal structure and properties of the materials being tested. [5, 30, 34]

6.4 NDT measurement of Yield strength

The magnetic spot method is a technique that can be used to accurately measure the properties of ferromagnetic materials, such as castings and test Y-blocks. It involves measuring the magnetization *M* $[A \cdot m^{-1}]$ at a suitable location on the set of castings or test Y-blocks. The data collected should also include out-of-tolerance *Rm [MPa]* values. Afterward, test bars are taken from the relevant parts of the castings or *Y*-blocks for tension testing to determine the actual values of the tensile strength *Rm [MPa]* by determining the constants:

A - mathematical constant *[-]*, *B* - Constant accounting for the influence of hardness on strength *[-]*, *C* - Constant considering the influence of graphite *[-]*, through linear regression, it is then possible to use the following relation: [5, 30]

$$Rm = A * M^B * (\frac{L}{Lu})\text{^}C\ [MPa] \qquad \textit{Equation 20}$$

Magnetic measurement of *Rm [MPa]* can only be used if it is warranted constant exclusion of graphite. [5, 30, 34]

6.5 Thermal resistance of cast irons

Mechanical stresses created by non-uniform cooling (or restrained thermal expansion) and heating of different parts of a component can lead to permanent deformations at a given temperature and thermal fatigue. The resistance to this stress is characterized by the Eichelberg factor.

The Eichelberg factor for cast irons depends on various factors, such as the type of iron, the alloying elements, the casting process, and the heat treatment. Cast irons are known for their high thermal conductivity, low thermal expansion, and good mechanical properties at elevated temperatures, which make them suitable for many high-temperature applications. However, their thermal resistance can be affected by non-uniform cooling and heating during operation, which can lead to thermal stresses and permanent deformations.

Studies have shown that the Eichelberg factor for cast irons typically ranges from 10 to 30, depending on the specific type and composition of the iron. For example, gray cast iron has an

EF value of around 10-15, while ductile iron has an *EF [-]* value of around 20-25. The presence of alloying elements, such as silicon, nickel, and molybdenum, can also affect the *EF [-]* value by modifying the microstructure and mechanical properties of the iron. Therefore, optimizing the composition and processing of cast irons is critical for enhancing their thermal resistance and ensuring their performance and reliability in high-temperature applications. Fig. 21 is shown how to see the thermally damaged cylinder head TEDOM after operating. [70 - 78]

$$EF = \left(\frac{Rm\ .\lambda_T}{\alpha\ .E_0}\right).1000 \qquad \textit{Equation 22}$$

where:

Rm [MPa] - is the tensile strength of the material, λ_T *[W/cm·K]* - is the coefficient of thermal conductivity, α *[1/K]* is the coefficient of thermal expansion, and E_0 *[GPa]* - is Young's modulus. The higher the *EF [-]* value, the more resistant the material is to thermal fatigue.

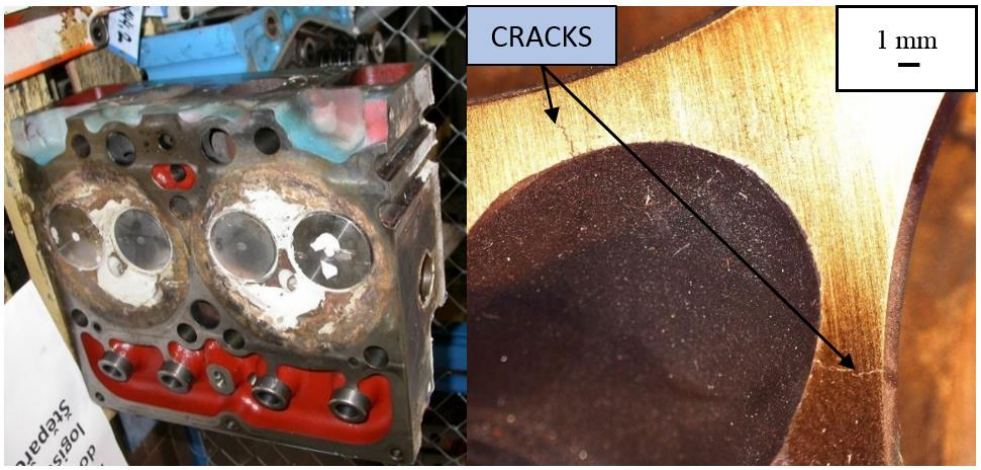

Fig. 21 Thermally damaged cylinder head TEDOM [Internal TEDOM documentation]

Thermal fatigue is a common failure mode in cast irons used for high-temperature applications. In a study by Suárez and González-Doncel (2016) [72], the thermal fatigue resistance of compacted graphite iron (CGI) and grey cast iron (GCI) was investigated. The results showed that the thermal fatigue resistance of CGI was superior to that of GCI due to its higher thermal conductivity and lower coefficient of thermal expansion. Gupta et al. (2019) also investigated the effect of silicon content on the thermal fatigue behavior of ductile iron. They found that increasing the silicon content from 2.5 % to 4.5 % improved the thermal fatigue resistance of the ductile iron. The improved thermal fatigue resistance was attributed to the finer graphite structure and the formation of a protective silicon oxide layer on the graphite surface. [70 - 78]

In addition to thermal fatigue resistance, the thermal conductivity of cast irons is also an important property for high-temperature applications. Roh et al. (2016) [75] investigated the effects of microstructure on the thermal conductivity of cast irons. The results showed that the thermal conductivity of cast irons is strongly influenced by the type and morphology of the graphite phase. Nodular cast iron (NCI) with nodular graphite exhibited higher thermal conductivity than grey cast iron (GCI) with lamellar graphite due to the more continuous and interconnected graphite structure in NCI. Adachi et al. (2019) [76] studied the thermal fatigue properties of cast iron for engine cylinder blocks. They found that the use of high-strength CGI improved the thermal fatigue resistance of the cylinder blocks while maintaining the desired thermal conductivity for efficient heat transfer. This study highlights the importance of balancing

thermal conductivity and thermal fatigue resistance in the design of cast iron components for high-temperature applications. [70 - 78]

6.6 Cast irons used as material for cylinder heads

Cylinder heads are critical components in internal combustion engines, and their material selection is crucial for their performance and durability under high-temperature conditions. Cast iron is a common material used for cylinder heads due to its high thermal conductivity, low cost, and good machinability. However, the thermal resistance of cast iron varies depending on its microstructure and graphite morphology. [25, 116 -119]

A study by Sharifian et al. (2019) [77] investigated the effect of different graphite morphologies on the thermal conductivity and thermal resistance of gray cast iron (GCI) and compacted graphite iron (CGI) cylinder heads. The results showed that the thermal conductivity of the cylinder heads increased with an increase in the amount of lamellar graphite in GCI and the amount of nodular graphite in CGI. Moreover, CGI cylinder heads exhibited higher thermal conductivity and lower thermal resistance than GCI cylinder heads due to their finer and more uniform graphite morphology. [10, 70 -77],

In addition to graphite morphology, alloying elements can also affect the thermal resistance of cast iron cylinder heads. In a study by Wang et al. (2019) [78], the effects of alloying elements, including copper and nickel, on the thermal conductivity and mechanical properties of CGI cylinder heads were investigated. The results showed that the addition of copper and nickel significantly increased the thermal conductivity and strength of the cylinder heads while reducing their thermal expansion coefficient. This suggests that the addition of alloying elements can improve the thermal resistance of cast iron cylinder heads, making them suitable for use in high-temperature applications. [79 - 82]

Cast iron's chemical composition is critical in determining its mechanical and thermal properties. The addition of alloying elements such as silicon, carbon, and manganese can improve the material's strength, wear resistance, and thermal conductivity. Moreover, using inoculants can control the graphite morphology and distribution, which can impact the mechanical and thermal properties of the cylinder head. For instance, magnesium inoculants can improve the mechanical properties of cast iron by refining the graphite morphology and promoting the formation of nodular graphite. [70, 79 - 82]

Heat treatment is another critical factor that can significantly impact the properties of cast iron cylinder heads. Heat treatment processes such as annealing, normalizing, ishothermic processing, and quenching can improve the material's strength, ductility, and thermal stability. For example, quenching and tempering can improve cast iron's wear and thermal shock resistance by forming a martensitic microstructure. [10, 79 - 82]

The design of the cylinder head can also impact its performance and durability. The contact plate between the cylinder head and the valve seat is critical for minimizing valve recession and maintaining valve sealing. Therefore, the rigidity and thermal stability of the contact plate are crucial for ensuring long-term performance. Reinforced materials, such as aluminum-silicon alloys, can improve the stiffness and thermal stability of the contact plate, reducing valve recession and maintaining valve sealing. [51, 79 - 82]

In conclusion, cast iron's chemical composition and heat treatment can be tailored to improve the mechanical and thermal properties of cylinder heads. Moreover, the design of the cylinder head can impact the rigidity and thermal stability of the contact plate, reducing valve recession and maintaining valve sealing. These factors must be considered when selecting and processing cast iron for cylinder heads in high-temperature applications. [51, 70, 79 - 82]

7 EXPERIMENTS

The experimental part of this research can be divided into three sections:

1. The first section focuses on testing TEDOM cylinder heads to gather information about their behavior, directly impacting the component lifespan of cylinder heads.

2. The second section of the experimental part investigates the progressive heat treatment methods applied to materials used for manufacturing cylinder head components.

3. The third section of the research involves evaluating the tribological properties of materials used for valves and valve seats. This part considers both materials with progressive heat treatment and their tribological properties.

The experiments evaluate the alterations in mechanical, magnetic, ultrasonic, and tribological properties. The research outlines the testing procedures employed and presents the findings related to the changes in mechanical properties of the materials for components for cylinder heads.

Utilizing cost-effective materials with progressive heat treatment techniques can offer economic advantages while achieving properties that can compete with modern expensive materials. Additionally, the development of cryogenic techniques can be a tool for repairing non-conforming parts that may fail hardness inspections or possess other deficiencies. Applying cryogenic processing may enhance the material properties and bring them within acceptable specifications, thereby reducing the need for costly material replacements or rejections due to quality control issues.

7.1 Deformation of TEDOM cylinder head gasket plate

This experiment served as a pilot test for a dissertation study in which we investigated the properties of cylinder head materials and examined the operation's impact on their mechanical properties, significantly affecting the cylinder head's lifespan. Deformation of the cylinder head's gasket surface also deforms the valve seats, affecting the engine's performance. (see Fig. 10)

7.1.1 Objectives of the experiment

As part of the experiment, it was planned to research:

1. Using NDT methods, compare the Young´s modulus of the gasket plate of the new cylinder head and the cylinder head plate after an operating time.

2. Identify areas on the gasket plate where thermal fatigue of the material is most likely to occur using calculation of the Eichelberg factor.

7.1.2 Material for testing

The parameters were investigated on a new cylinder head TEDOM that had never been in operation and on a cylinder head that has been in operation since 2014. Both cylinder heads were made from cast iron EN-GJL 250 according to EN ISO 1561 at Heunisch foundry in Brno. The cylinder heads underwent quality control and were free of internal inhomogeneities and defects. Tab. 11 is shown the chemical composition of the cylinder heads used for testing. The chemical composition of the cylinder head was obtained from the material test certificate according EN 10204 / 3.1 [123] sent with each batch of cylinder heads.

Tab. 11 Chemical composition of cylinder head TEDOM from EN-GJL 250

C [%]	3.36
Si [%]	1.96
Mn [%]	0.70
P [%]	0.05
S [%]	0.04
Cr [%]	0.08
Sn [%]	0.08
Cu [%]	0.08
Matrix	Pearlite + Ferrite

7.1.3 Measurement methodology

Young´s modulus was calculated using an ultrasonic method by measuring the ultrasonic and actual thickness of the gasket plane according to Equation 13. Hardness was measured at selected points using the HB5/187.5 method according to EN ISO 6507-1 [44] with a WPM hardness tester. The measured values are statistically processed in Tab. 50 and Tab. 51 in the Appendix 10.5 of the thesis.

Eicheberg factor was calculated to determine the resistance to thermal fatigue according to Equation 22. The ultrasonic thickness measurements were taken at the points indicated in Fig. 22 on the left side - A. The measurement hardness of the cylinder head plate is shown on the right side of Fig. 22 - B.

To determine the relative velocity of ultrasonic propagation was necessary to measure the material thickness *L* at the measurement point using a caliper. Ultrasonic thickness *Lu* measurements were taken using a DiO 562 Starmans instrument with a dual 5 MHz probe after measuring the ultrasonic thickness, where we measure the time for the reflected signal to return.

The cylinder head plate was machined so that the cutting planes were parallel to the seating surface for the head gasket. (The parallelism requirement was 0.05mm.) After being cut on a band saw, the cylinder head plates were milled to achieve parallelism and surface roughness. The surface roughness was specified at Ra 3.2.

We used PTC CREO software for the graphical representation of the results. We use linear interpolation to calculate the values in the remaining portions of the cylinder heads.

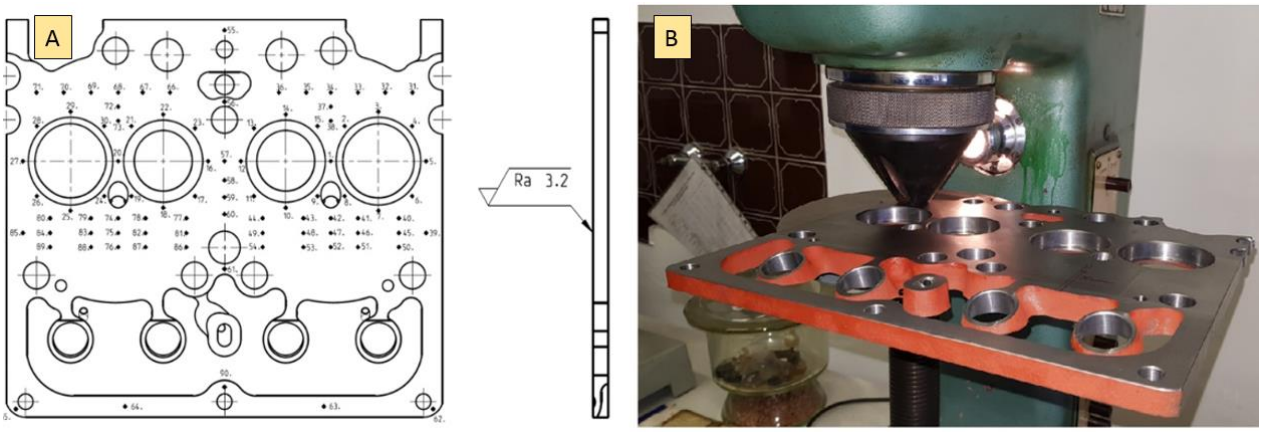

Fig. 22 Cylinder head plate TEDOM

7.1.4 Measured data

Fig. 23 and 24 graphically depict the measured and calculated values of Young´s modulus for the gasket plate of the TEDOM cylinder head. Fig. 25 and 26 show the graphical representation of the Eichelberg factor on the new and used gasket surfaces of the cylinder head.

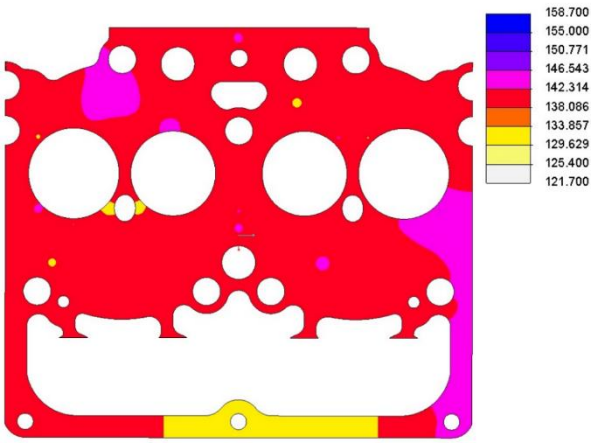

Fig. 23 Graphical representation of the dispersion of Young´s moduluson a new cylinder head

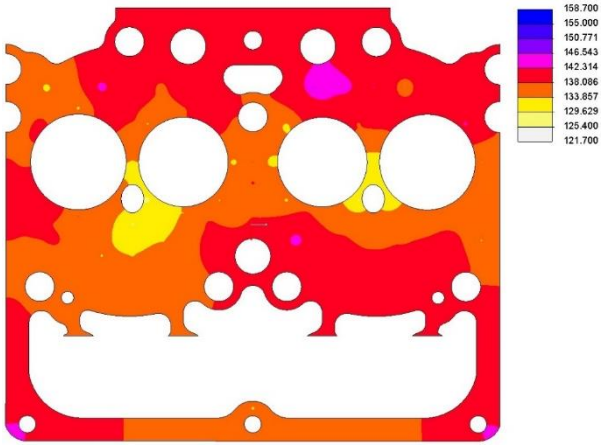

Fig. 24 Graphical representation of the dispersion of the Young´s moduluson the used cylinder head

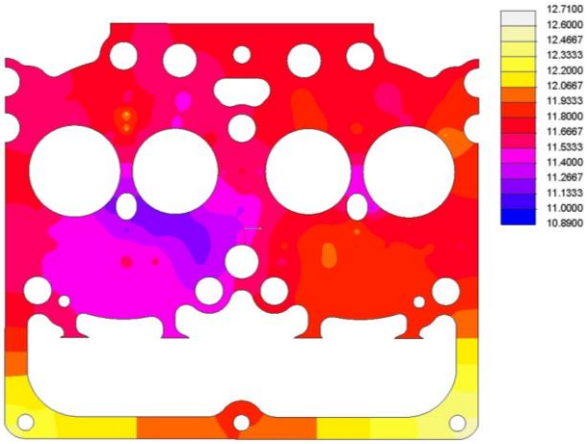

Fig. 25 Graphic representation of the Eichelbeg factor on new cylinder head

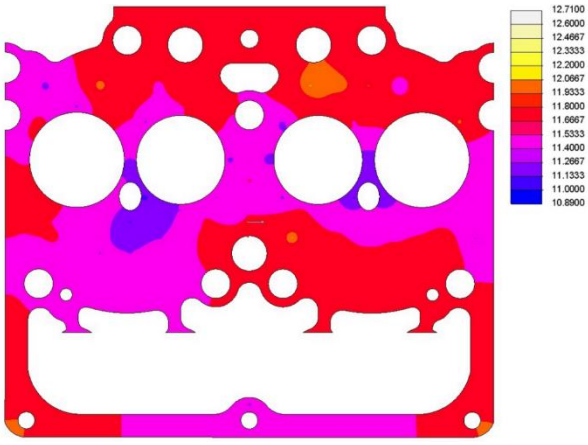

Fig. 26 Graphic representation of the Eichelbeg factor on the used cylinder head

7.1.5 Discussion of measured data

The Eichelberg factor *EF [-]* and Theoretical Young's modulus E_{0T} were measured and calculated on a new cylinder head gasket plane and a used one with 14 000 operating hours.

The measurements of the Eichelberg factor and Young's modulus were performed to evaluate the thermal resistance of the cylinder head gasket. Theoretical Equations 13 and 22 were applied to calculate the Eichelberg factor and Young's modulus based on the physical properties of the cylinder head gasket.

The results showed that the Eichelberg factor and Young´s modulus of the used cylinder head gasket was significantly lower than those of the new one. This indicated that the thermal

resistance of the used cylinder head gasket was compromised due to the accumulation of wear and tear during the 14 000 operating hours.

- The critical point in terms of a lower Young´s modulus is in the bridge area between the intake and exhaust valves closer to the spark plug, where the local minimum of Young´s modulus reaches a value of 121.7 GPa.
- Hardness measurements have shown that there are no changes in material hardness due to operation.
- The Young´s modulus range in the new cylinder head varies from 126.4 to 145.3 GPa.
- The Young´s modulus range in the used cylinder head varies from 121.7 to 158.7 GPa.
- The Eichelberg factor is lowest in the areas exposed to the highest thermal load, namely in the bridge area between the exhaust valves and at the spark plug.

The results of the experiment show that the critical point in terms of a relatively low Young´s modulus is in the bridge area between the valves closer to the spark plug, where the local minimum of Young´s modulus is located. This area is exposed to high thermal loads and is prone to deformations and damage. However, the hardness measurements have shown that the material hardness is not affected by the operation, indicating good quality and durability of the material used in the cylinder head. The range of Young´s modulus in the new cylinder head and the used cylinder head varies, indicating possible differences in the material properties due to wear and tear. The graphical representations of Young´s modulus provide a visual reference for the analysis and evaluation of the material properties in different areas of the cylinder head.

The results of the Eichelberg factor show the areas with the highest thermal load and, therefore, the most prone to damage and failure. The visual representation of the Eichelberg factor provides a clear and concise overview of the areas that require attention and possible improvements. These results are significant in the design and manufacturing of high-performance engines and can contribute to the improvement of their durability and reliability. In the article "Non-destructive testing of cylinder heads valve seat, and valves in manufacturing and servicing" [63], we focus more on the issue of measuring the stiffness of the cylinder head mating surfaces. Skrbek [132] conducted an analysis on gray cast irons used for brake discs in the automotive industry, confirming the suitability of using the Eichelberg factor as a measure indicating

the distinctiveness of a specific material in terms of thermal fatigue. The company TEDOM systematically collects cylinder heads that have been taken out of operation and inspect all the mating surfaces of these cylinder heads for the purpose of collecting statistics on hardness, modulus of elasticity, and the Eichelberg factor.

The main motivation behind this experiment was to determine whether the stiffness of the lower part of the cylinder head so called gasket plate, where valve seats are pressed, changes over time. In the event that the stiffness of the gasket plates was changed, it would imply that as engine mileage increases, there is a gradual misalignment of valves and valve seats. So far, this has not been proven, and a significant number of samples must be statistically analyzed to confirm or refute the impact of seating plate stiffness on the durability of TEDOM cylinder heads.

7.2 Effect of cylinder head material on stiffness

The focus of this experiment was to investigate whether utilizing a higher-quality cast iron EN-GJS 400-15 as the cylinder head material compared to the standard material EN-GJL 250 would positively influence the stiffness of the cylinder head in real engine. This material change would result in reduced deformations of the valve guides axis perpendicularity to the gasket surface of the cylinder head, roundness of the pressed valve seat, and flatness of the contacting sealing surface. All of these parameters are crucial for the proper and long-term functioning of the combustion engine. The tightening sequence was chosen to reflect the actual procedure used during the assembly of cylinder heads in the engine assembly line at TEDOM company.

7.2.1 Objectives of the experiment

As part of the experiment. it was planned to research:

1. Measure the differences in the perpendicularity of the valve guide axis to the cylinder head contact surface when tightening the cylinder head bolts to 0 Nm, 200 Nm, and 370 Nm, and then when loosening them to 0 Nm. These differences should be compared for cylinder heads made of EN-GJL 250 and EN-GJS 400-15 materials.
2. Measure the differences in the flatness around valve seats of the cylinder head contact surface when tightening the cylinder head bolts to 0 Nm, 200 Nm, and 370 Nm, and then when loosening them to 0 Nm. These differences should be compared for cylinder heads made of EN-GJL 250 and EN-GJS 400-15 materials.

3. Measure the differences in the roudness of valve seats when tightening the cylinder head bolts to 0 Nm, 200 Nm, and 370 Nm, and then when loosening them to 0 Nm. These differences should be compared for cylinder heads made of EN-GJL 250 and EN-GJS 400 materials.

7.2.2 Material for testing

For the purpose of testing, we used serial cylinder heads provided by TEDOM. The cylinder heads were cast at Foundry Heunisch Brno. Ltd., where both EN-GJL 250, according to ČSN 42 2425 [133], and EN-GJS 400-15, according to EN 1563 (ČSN 42 0951) [29] cylinder heads were manufactured. The EN-GJS 400-15 cylinder heads were produced at the company's branch located in Germany. The casting molds used for both types of cylinder heads were identical, ensuring consistency in the casting process. Subsequently, the cylinder heads were processed using the standard serial procedures employed by TEDOM. This standardized approach allowed us to compare the performance of the two materials under similar manufacturing conditions, minimizing potential confounding factors. The cylinder heads were equipped with standard valve guides made from AGI 410 and valve seats. Material of intake valve seat was Stellite 6. Material of exhaust valve seat was Stellite 12. The chemical composition of cylinder head EN-GJL 250 is shown in Tab. 11. Chemical composition of cylinder head EN-GJS 400-15 is shown in Tab. 12. The chemical composition of the cylinder head was obtained from the material test certificate according to EN 10204 / 3.1 [123].

Tab. 12 Chemical composition of cylinder head EN-GJS 400-15

C [%]	3.58
Si [%]	2.77
Mn [%]	0.22
P [%]	0.04
S [%]	0.01
Cr [%]	0.03
Mo [%]	0.01
Sn [%]	0.01
Cu [%]	0.06
Mg [%]	0.05
Matrix	Ferrite

7.2.3 Measurement methodology

We conducted testing on three-cylinder heads for each material. These cylinder heads were mounted with head gaskets onto the engine block. The tightening torque for the cylinder head bolts was selected as follows:

1. Initial measurement: The cylinder head was measured without tightened bolts.
2. The bolts were tightened to 200 Nm.
3. The bolts were further tightened to 370 Nm.
4. The bolts were then loosened and the cylinder heads were measured again.

All measurements were performed using the Coordinate Measuring Machine (CMM) Zeis PRISMO Ultra at TEDOM. The engine block and cylinder heads were positioned on the machine to ensure that the valve axis of the engine block was perpendicular to the measuring machine's base. This setup ensured accurate and reliable measurements of the cylinder heads and allowed for the assessment of any dimensional changes or deformations resulting from different torque levels.

The configuration of each cylinder head is as follows: There are intake valve seats and guides on the edges of the heads, while in the center, there are exhaust channels. In Tab. 13 -18 are shown the measured geometrical differencies of cylinder heads. Fig. 27 illustrates a CAD model of the cylinder head TEDOM which provides a visual approximation of configuration where valve seats are labeled as "I" for intake and "E" for exhaust. This labeling system allows for clear identification and differentiation of the components during the analysis and discussion of the experimental results.

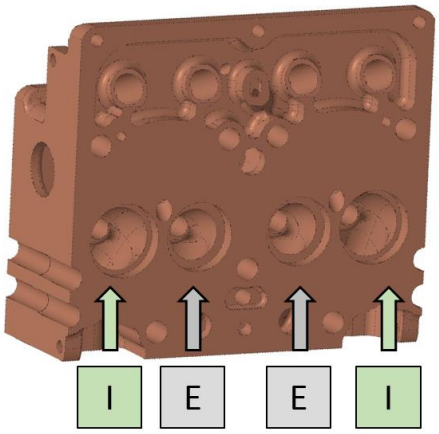

Fig. 27 TEDOM cylinder head configuration

Measuring setting of CMM machine was:

Diameter of measuring ball – 3 mm, Scannig speed – 8 mm/s, Evaluation method: Gauss, Filter Gauss, Low frquency speed / rev:50, Elimination of outliers: Factor 3,00/3,00;

Ic:0,0-1000,0 mm; Iteration -1, Number of measurements: Number of points per cut – 3600; Initial measuring angle – 0°; Angular range – 450°.

7.2.4 Measured data

The measured data of geometrical differences are shown in Tab. 13 to 18.

Tab. 13 Perpendicularity of valve guide axis to contact surface cylinder head made from EN-GJL 250

		Perendicularity of valve guide axis to contact surface cylinder head [mm]											
		Cylinder head 1				**Cylinder head 2**				**Cylinder head 3**			
Material	**Torque**	**I 1**	**E 1**	**E 2**	**I 2**	**I 3**	**E 3**	**E 4**	**I 4**	**I 5**	**E 5**	**E 6**	**I 6**
EN-GJL-250	**0Nm**	0.0381	0.0187	0.0325	0.0236	0.0381	0.0187	0.0325	0.0236	0.0076	0.0055	0.0136	0.0312
EN-GJL-250	**200Nm**	0.0606	0.0133	0.0541	0.0068	0.0363	0.033	0.0371	0.0598	0.0242	0.0141	0.0199	0.0529
EN-GJL-250	**370Nm**	0.0802	0.0117	0.0541	0.0531	0.0535	0.0336	0.0383	0.0719	0.0392	0.0105	0.0232	0.0633
EN-GJL-250	**0Nm**	0.0399	0.0219	0.0335	0.0224	0.0128	0.0265	0.0251	0.0434	0.0065	0.0044	0.0138	0.0319

Tab. 14 Perpendicularity of valve guide axis to contact surface cylinder head made from EN-GJS 400

		Perendicularity of valve guide axis to contact surface cylinder head [mm]											
		Cylinder head 1				**Cylinder head 2**				**Cylinder head 3**			
Material	**Torque**	**I 1**	**E 1**	**E 2**	**I 2**	**I 3**	**E 3**	**E 4**	**I 4**	**I 5**	**E 5**	**E 6**	**I 6**
EN-GJS-400	**0Nm**	0.0257	0.0176	0.0294	0.0224	0.0224	0.0247	0.0169	0.0221	0.0230	0.0049	0.0187	0.0232
EN-GJS-400	**200Nm**	0.0399	0.0163	0.0323	0.0499	0.0408	0.0303	0.0109	0.0369	0.0487	0.0246	0.0370	0.0422
EN-GJS-400	**370Nm**	0.0533	0.0187	0.0342	0.0627	0.0496	0.0340	0.0095	0.0493	0.0561	0.0204	0.0354	0.0533
EN-GJS-400	**0Nm**	0.0242	0.0167	0.0286	0.0228	0.0207	0.0237	0.0163	0.021	0.0226	0.0059	0.0187	0.0244

Tab. 15 Flatness of contact surface cylinder head made from EN-GJL 250

		Flatness of contact surface [mm]											
		Cylinder head 1				**Cylinder head 2**				**Cylinder head 3**			
Material	**Torque**	**I 1**	**E 1**	**E 2**	**I 2**	**I 3**	**E 3**	**E 4**	**I 4**	**I 5**	**E 5**	**E 6**	**I 6**
EN-GJL-250	**0Nm**	0.0205	0.0205	0.0205	0.0205	0.0205	0.0205	0.0205	0.0205	0.0186	0.0186	0.0185	0.0185
EN-GJL-250	**200Nm**	0.0169	0.0169	0.0336	0.0336	0.0160	0.0160	0.0175	0.0175	0.0175	0.0175	0.0167	0.0167
EN-GJL-250	**370Nm**	0.0235	0.0235	0.0266	0.0266	0.0215	0.0215	0.0270	0.0270	0.0258	0.0258	0.0247	0.0247
EN-GJL-250	**0Nm**	0.0199	0.0199	0.0199	0.0199	0.0193	0.0193	0.0193	0.0193	0.0197	0.0197	0.0197	0.0197

Tab. 16 Flatness of contact surface cylinder head made from EN-GJS 400

		Flatness of contact surface [mm]											
		Cylinder head 1				Cylinder head 2				Cylinder head 3			
Material	**Torque**	**I 1**	**E 1**	**E 2**	**I2**	**I 3**	**E 3**	**E 4**	**I 4**	**I 5**	**E 5**	**E 6**	**I 6**
EN-GJS-400	**0Nm**	0.0187	0.0187	0.0187	0.0187	0.0209	0.0209	0.0209	0.0209	0.0194	0.0194	0.0194	0.0194
EN-GJS-400	**200Nm**	0.0097	0.0097	0.0110	0.0110	0.0121	0.0121	0.0128	0.0128	0.0120	0.0120	0.0129	0.0129
EN-GJS-400	**370Nm**	0.0161	0.0161	0.0181	0.0181	0.0153	0.0153	0.0178	0.0178	0.0162	0.0162	0.0166	0.0166
EN-GJS-400	**0Nm**	0.0213	0.0190	0.0190	0.0191	0.0191	0.0213	0.0213	0.0213	0.0199	0.0200	0.0201	0.0202

Tab. 17 Roudness sealing surface of valve seats in cylinder head made from EN-GJL 250

		Roundness of valve seats [mm]											
		Cylinder head 1				Cylinder head 2				Cylinder head 3			
Material	**Torque**	**I 1**	**E 1**	**E 2**	**I2**	**I 3**	**E 3**	**E 4**	**I 4**	**I 5**	**E 5**	**E 6**	**I 6**
EN-GJL-250	**0Nm**	0.0151	0.0173	0.0157	0.0164	0.0151	0.0173	0.0157	0.0149	0.0117	0.0175	0.0150	0.0237
EN-GJL-250	**200Nm**	0.0143	0.0210	0.0165	0.0302	0.0090	0.0111	0.0108	0.0115	0.0202	0.0326	0.0175	0.0175
EN-GJL-250	**370Nm**	0.0099	0.0086	0.0168	0.0130	0.0084	0.0146	0.0101	0.0132	0.008	0.0120	0.0123	0.0111
EN-GJL-250	**0Nm**	0.0103	0.0139	0.0128	0.0093	0.0175	0.0117	0.0152	0.0117	0.0149	0.0170	0.0136	0.0122

Tab. 18 Roudness sealing surface of valve seats in cylinder head made from EN-GJS 400

		Roundness of valve seats [mm]											
		Cylinder head 1				Cylinder head 2				Cylinder head 3			
Material	**Torque**	**I 1**	**E 1**	**E 2**	**I2**	**I 3**	**E 3**	**E 4**	**I 4**	**I 5**	**E 5**	**E 6**	**I 6**
EN-GJS-400	**0Nm**	0.0198	0.0234	0.0210	0.0196	0.0212	0.0165	0.0197	0.0193	0.0176	0.0216	0.0191	0.0174
EN-GJS-400	**200Nm**	0.0169	0.0180	0.0095	0.0109	0.0153	0.0074	0.0082	0.0120	0.0173	0.0112	0.0130	0.0132
EN-GJS-400	**370Nm**	0.0148	0.0211	0.0156	0.0118	0.0280	0.0220	0.0088	0.0150	0.0163	0.0106	0.0106	0.0127
EN-GJS-400	**0Nm**	0.0113	0.0127	0.0103	0.0118	0.0142	0.0100	0.0099	0.0095	0.0098	0.0109	0.0105	0.0095

7.2.5 Discussion of measured data

All measured values of perpendicularity, flatness, and roudness of the cylinder heads from both materials consistently met the specifications outlined in the engineering drawings defined by TEDOM. This indicates that the manufacturing process for both materials was capable of consistently producing cylinder heads that adhered to the required dimensional and geometric tolerances.

Based on this finding, the company TEDOM has made a decision to discontinue the production of cylinder heads made from the EN-GJS 400 material for economic reasons.

The company will continue the production of cylinder heads using the EN-GJL 250 material. By focusing on the production of cylinder heads from the EN-GJL 250 material, the company aims to optimize its manufacturing operations and enhance cost-effectiveness. This decision is supported by the fact that the measured values of the desired parameters were consistently within the specified tolerances for both materials.

The choice to continue manufacturing cylinder heads from the EN-GJL 250 material is based on various factors, including cost-efficiency and material availability, and the ability to meet the required quality standards. The recommendation for future testing is to try isothermal annealing of the cylinder head followed by cryogenic treatment.

7.3 Development of valve guide material

The experiment quantifies the impact of cryogenic treatment on the properties of isothermally quenched material used for valve guides used in engine TEDOM made from cast iron with flake graphite EN-GJL 200 and isothermally processed for AGI 410. Cryogenic freezing in liquid nitrogen is often a part of the pre-assembly process for parts (such as valve seats) with overlap into TEDOM engines and similar applications.

7.3.1 Objectives of the experiment

As part of the experiment, it was planned to research:

1. Measure the effect of cryogenic processing on the mechanical properties of isothermic quenched EN-GJL 200 to AGI 410.

2. Measure the impact of the time interval between hardening and freezing on the mechanical properties of the material.

7.3.2 Material for testing

We used raw-parts products as the testing material, which are used for the production of intake and exhaust valve guides for TEDOM engines, made from EN-GJL 200 material according to ČSN 42 2420 [48]. Chemical composition is shown in Tab. 19. The chemical composition was taken from the material certificate according to EN 10204 / 3.1 [123], provided by the supplier of

the valve guide semi-finished products - TSS Třebechovice. In Fig. 28. on the left side is the casting of the semi-finished valve guide, and on the right side, there is a drawing for the machining of the valve guide.

Tab. 19 Chemical compound of valve guides used in testing

C [%]	3.35
Si [%]	1.85
Mn [%]	0.85
Cr [%]	0.03
P [%]	0.06
S [%]	0.07
Matrix	Pearlite

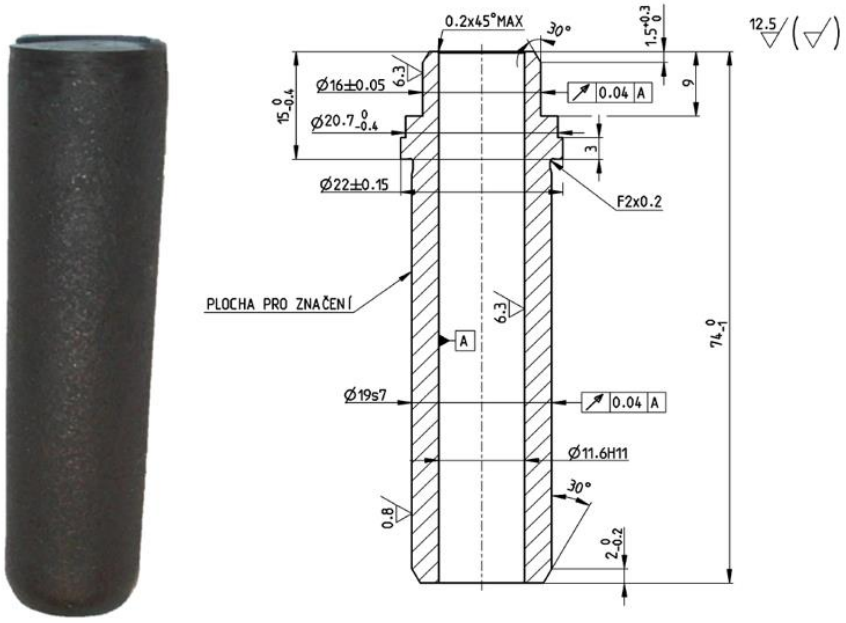

Fig. 28 TEDOM valve guide raw part and drawing for valve guide

7.3.3 Heat treatment of valve guides

The valve guides raw parts were isothermally quenched to AGI 410 from 860 °C to 890 °C for 30 minutes and then tempered in a salt bath at 400 °C to 410 °C for 30 minutes to achieve a hardness of 250-275 HB according to serial production drawing. For the freezing of the samples were used liquid nitrogen with gradual cooling. The valve guides were subjected to cryogenic treatment at specific intervals after hardening to investigate the influence of time intervals between hardening and freezing on the mechanical properties of the material.

For sample was chosen cryogenic treatment in liquid nitrogen with gradual cooling and holding for 30 minutes - N_{30}

7.3.4 Measurement methodology

Hardness was measured using the HB2.5/187.5 method according to EN ISO 6507-1 with a WPM hardness tester. Changes in the structure were specified using magnetic and ultrasonic measurements. The Tensile strenght tests where performed on threaded rods with a diameter of d12 mm according to ČSN 42 0316 [121]. The microstructure was observed using a NEOPHOT 2 microscope.

The speed of sound V_L and ultrasonic thickness *Lu* was determined using an ultrasonic flaw detector DIO 562 (Starmans s.r.o. Prague) with a dual probe of 10 mm diameter and 5 MHz frequency for *L* up to 100 mm. For measuring the real thickness of sample *L*, a micrometer was used. The intensity of residual magnetic field *M* was measured using the magnetic spot method with DOMENA B3 ELKOSO s.r.o. Brno instruments (set at 3rd level of magnetization). Values of speed of sound was used for calculation theoretical Young´s modulus. Theoretical Young´s modulus E_{0T} was calculated according to Equation 13.

For measuring the tensile strength of the materials was used the Universal Testing Tensile Machine TiraTest2300 with the extensometer MFX500-B. Test rods were prepared from raw-parts products for valve guides using mechanical machining with a diameter of d_0 12mm. The test rods complied with the ČSN 42 0316 [121].

7.3.5 Measured data

Fig. 29 – 31 illustrate the progression of tensile tests, highlighting the impact of cryogenic processing and the relationship between the time interval between hardening and cryogenic treatment. In Tab. 20 are shown the measured results of experiments obtained by non-destructive testing methods. In Tab. 21 are shown the results of destructive mechanical tests.

Tab. 20 Influence of time delay between quenching and cryogenic treatment to AGI cast iron to magnetic properties and elastic modulus

	Hardness HB	**E_{0T} [GPa]**	**M [A/m]**
EN-GJL 200	219 ± 1	132.1	357.7 ± 3
AGI 410	268 ± 2	124.6	683.7 ± 2
AGI 410 + N_{30} after 1h	295 ± 2	125.8	539.0 ± 3
AGI 410 + N_{30} after 2h	307 ± 3	124.9	468.0 ± 3
AGI 410 + N_{30} after 16h	306± 2	125.2	519.5 ± 4

Tab. 21 Influence of heat treatment on mechanical properties of EN-GJL 200

	d_0 [mm]	**$R_{p0.2}$ [MPa]**	**Rm [MPa]**	**A3 [%]**
EN-GJL 200	12	223.2	245.3	0.35
AGI 410	12	284.5	328.7	0.52
AGI 410 + N_{30} after 1h	12	317.5	398.7	0.50

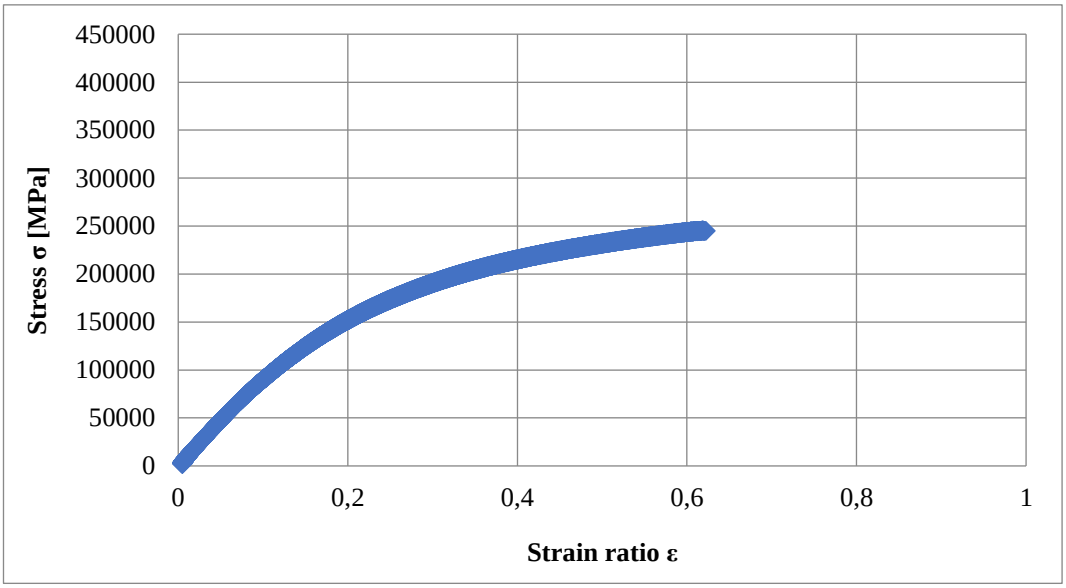

Fig. 29 Reference sample EN-GJL 200

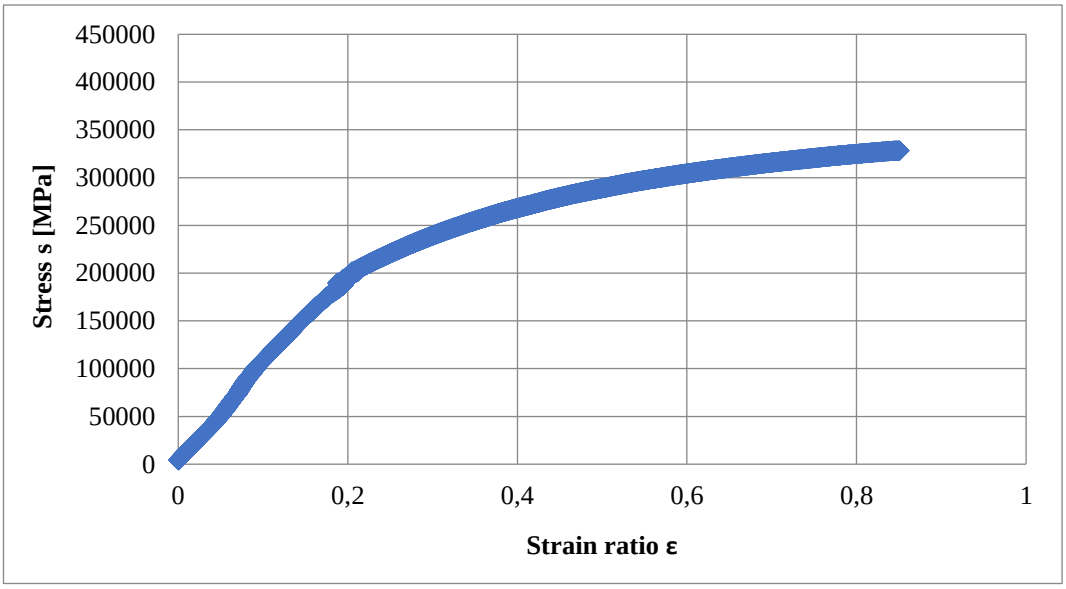

Fig. 30 AGI 410 sample

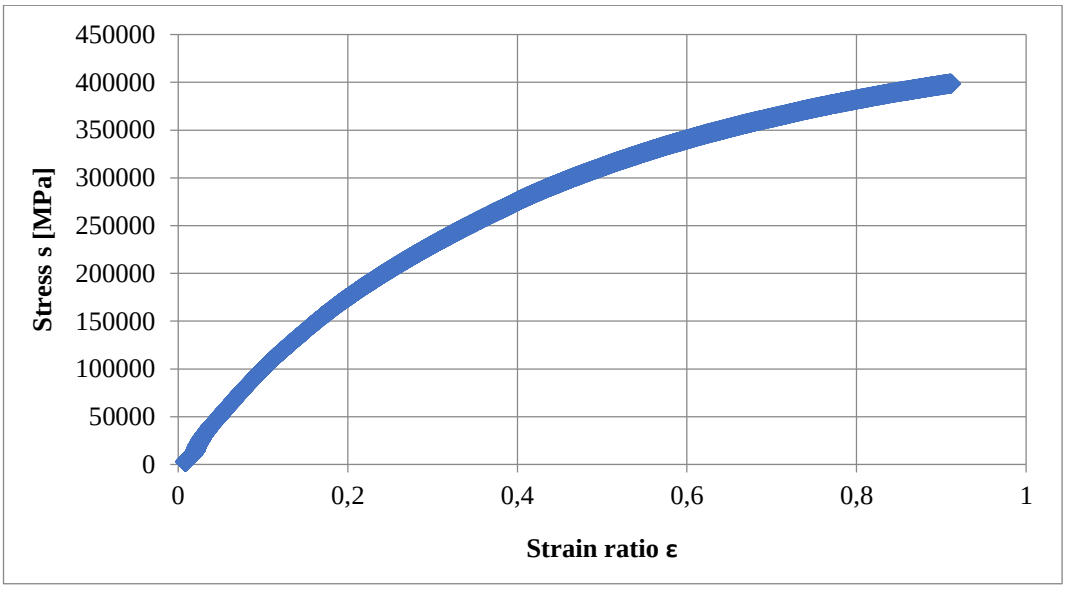

Fig. 31 AGI 410 N_{30} after 1h sample

7.3.6 Phase analysis

Samples for metallographic observation were sectioned from the bulk material using a precision saw, the Struers Secotom-50, equipped with a SiC cutting disc. The sections were then securely affixed using the Struers Citopress-10 hot-mounting press, embedding them in conductive resin known as Struers Polyfast. Subsequent grinding was performed using Struers Tegramin-25, progressing through sandpapers with grit sizes of #220, 500, 1200, and 2000.

For the polishing phase, polycrystalline diamond suspension with particle sizes of 3 µm and 1 µm was applied onto textile cloth disks. This polishing process refined the samples.

The resulting sample structures were characterized using light optical microscopy, specifically the Zeiss Axio Imager M2m model with a 100x magnification, utilizing reflected bright-field illumination. Analysis of graphite shapes and sizes was conducted through image processing, following the DIN EN ISO 945 – 2019 standard, utilizing ZEISS ZEN Core software.

To achieve a highly polished surface devoid of deformities and contaminants, a final mechanical-chemical polishing step was executed using colloidal silica OP-S, a product from Struers. Furthermore, Ar-Ion Milling, performed using the Fischione SEM Mill 1060, was employed to attain a perfectly smooth surface. This process ensured the elimination of deformations and any residual contamination. The mitigation of carbon contamination was achieved through plasma cleaning using the Evatron system integrated within the SEM chamber.

The meticulously prepared samples were then subjected to scanning electron microscopy (SEM) and electron backscatter diffraction (EBSD) analyses. In the context of optical microscopy, the sample's structure was revealed by etching with Nital, a solution comprising 3% nitric acid in ethanol.

Tab. 22 shows the results of the phase analysis of the examined materials. The table evaluates the percentage distribution of the BCC phase, FCC phase, Graphite, and Martensite.

Tab. 22 Phase analysis of various heat treatments of EN-GJL 200

Material	**Crystal Structures**	**Phase Fraction [%]**	**Standart deviation σ**
EN-GJL 200	Iron BCC	91.4	1.1
	Graphite	8.6	1.1
AGI 410	Iron BCC (old)	57.2	2.4
	Iron FCC	32.6	3.3
	Graphite	10.2	1.2
AGI 410 N $_{30}$*	Iron BCC (old)	57.9	1.8
	Iron FCC	17.0	1.1
	Graphite	10.1	1.2
	Martensite	15.1	1.5

* Freezing in liquid nitrogen, 1 hour after isothermal quenching

Fig. 32 shows the microstructure of the initial structure of EN - GJL 200 - LOM image, Bright Field, MAG = 100×, polished.

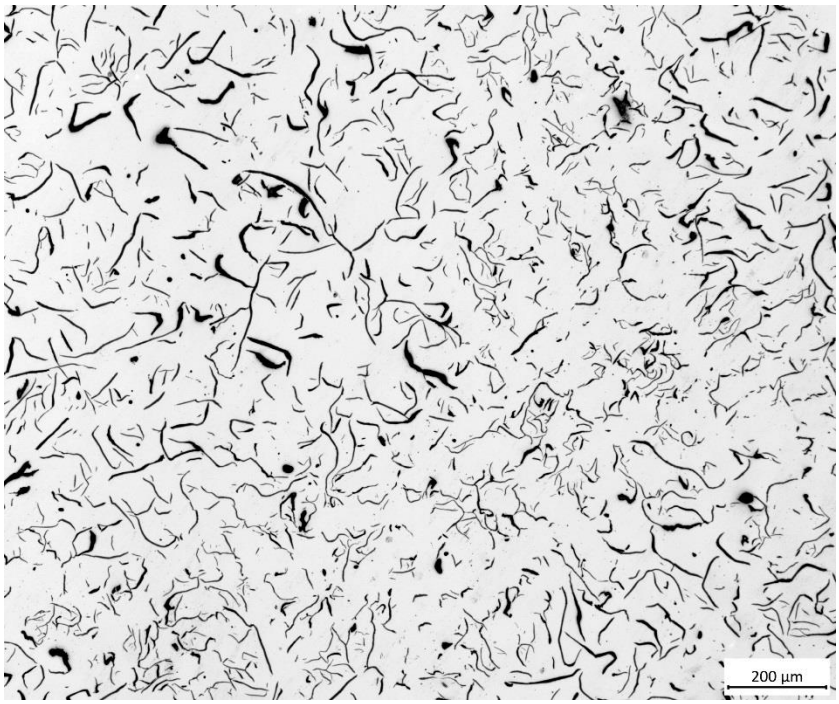

Fig. 32 The Initial structure of graphite EN-GJL 200

Fig. 33 shows the Structure of AGI 410 °C - LOM image, Bright Field, MAG = 100×, polished. Fig. 34 shows the structure after cryogenic treatment N_{30} after 1 hour of isothermall hardening - LOM image, Bright Field, MAG = 100×, polished. In the Appendix of this work (section 10.6), are Fig. 105 – Fig. 110, which show microstructure and EBDS maps of the materials EN-GJL 200, AGI 410, and AGI 410 N_{30}.

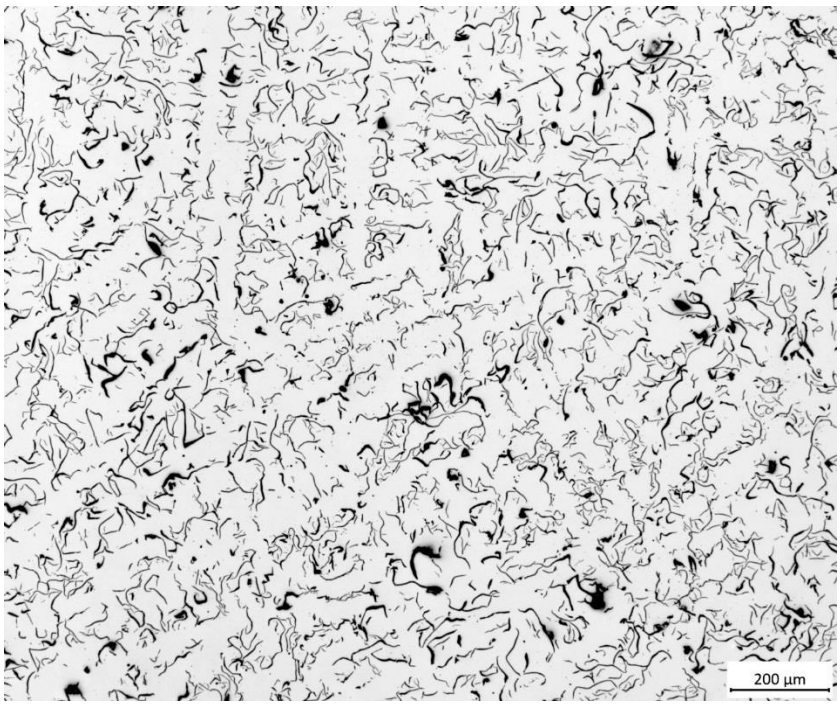

Fig. 33 Structure of graphite AGI 410

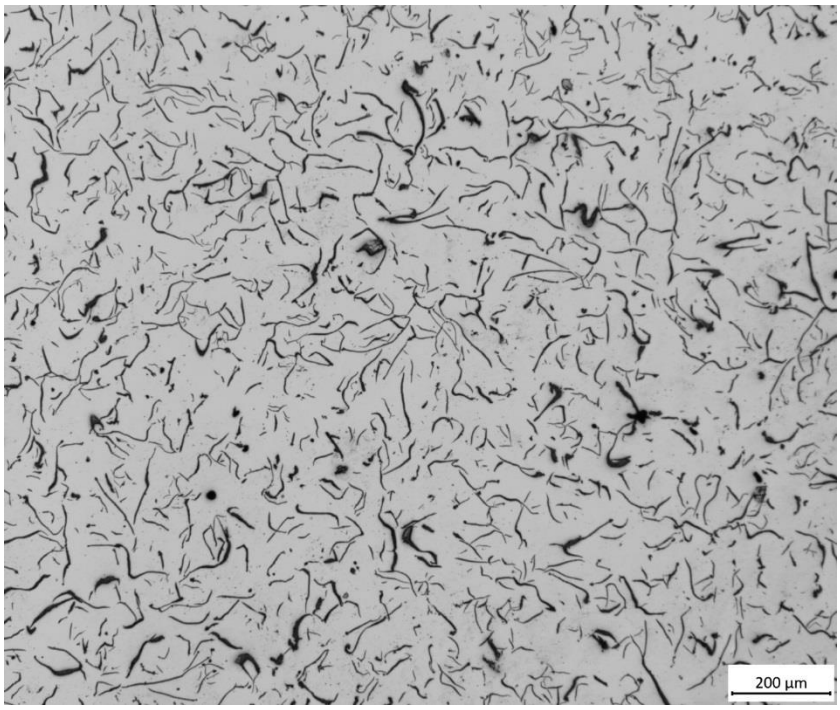

Fig. 34 Structure of graphite AGI 410 N_{30}

7.3.7 Discussion of measured data

The following discussion is divided into the individual materials chapters according to heat treatment.

7.3.7.1 AGI 410

- The AGI 410 processing increases the Tensile strength *Rm* of the initial material EN-GJL 200 by 34 %. (From 245.3 MPa to 328.7 MPa).
- The AGI 410 processing increases the Yield strength R_{p02} of the initial material EN-GJL 200 by 27.5 %. (From 223.2 MPa to 284.5 MPa).
- The AGI 410 processing increases the hardness of the initial material EN-GJL 200 by 22.3 %. (From 219 HB to 268 HB).
- AGI 410 heat treatment process shows a decrease in the calculated theoretical Young´s modulus by 5.7 %. (From 132.1 GPa to 124.6 GPa).
- The ductility of the AGI 410 material has increased to a level of 0.52 %, which is 48.6% less than the original EN-GJL 200 material.

7.3.7.2 AGI 410 N_{30} after 1 h

- The AGI 410 N_{30} processing increases the Tensile strength Rm of the initial material EN – GJL 200 by 62.5 %. (From 245.3 MPa to 398.7 MPa).
- The AGI 410 N_{30} processing increases the Yield strength R_{p02} of the initial material EN – GJL 200 by 42.2 %. (From 223.2 MPa to 317.5 MPa).
- The AGI 410 N_{30} processing increases the hardness of the initial material EN-GJL 200 by 34.7 %. (From 219 HB to 295 HB).
- Cryogenic procesing show potencial to increase the hardness of AGI 410 from original value of 268 HB to 295 HB. The increase in hardness was by 10.1%.
- The ductility of the material has decreased to a level of 0.5 %, which is 42.9 % less than the original EN-GJL 200 material.
- Cryogenic processing show potencial to increase the tensile strength of AGI 410 from the original value of 328.7 MPa to 398.7 MPa while maintaining practically the same ductility. The increase in strength was by 21.3%.

From the measured results of phase analysis, it is evident that in the case of cryogenic treatment, the residual austenite after isothermal quenching transforms into martensite. In our case, out of the 32.6% residual austenite, approximately 15 %, transformed into martensite.

In the article of Wang [130], it is described that cryogenic treatment has the capability to significantly reduce the retained austenite content following the destabilization heat treatment. However, it's important to note that cryogenic treatment alone does not achieve a complete transformation of retained austenite into martensite. Despite this, cryogenic treatment demonstrates the ability to substantially enhance the hardness and abrasion resistance of high-cast irons. The notable enhancement in hardness and wear resistance is primarily attributed to the additional formation of fine secondary carbides during cryogenic treatment after destabilization, as compared to air cooling. Our measured results confirm Wang's findings, particularly the observed increase in martensitic structure within the cryogenically processed samples.

Our measurements have revealed that the delay between quenching and cryogenic treatment has an impact on the material's hardness. In our case, the hardness increased by 3.7 % from the original 295 HB when frozen 1 hour after quenching to 307 HB when frozen 2 hours after quenching. Notably, the sample subjected to cryogenic treatment after a delay of 16 hours

following quenching exhibited a hardness value approximately similar to the sample frozen 2 hours after quenching.

Additionally, the experiment has demonstrated the importance of immediately proceeding with cryogenic processing after quenching, as any delay in this process reduces the effectiveness of the thermal treatment. It is worth noting that this method holds great economic significance, as it enables the correction of non-conforming products through the application of this technique. In the appendix of this study, Fig. 106, 108, and 110 depict the microstructures of the EN-GJL 200, AGI 410, and AGI 410 N_{30} materials.

Cryogenic treatment of gray cast iron or AGI seems to be promising way of thermal treatment which is in accordance with the Thornton [131] observation of gray cast iron parts subjected to deep cryogenic treatment exhibited a 9.14 – 81.39 % enhancement in wear rate when compared to those parts with no additional treatment, particularly in cases where significant wear rates ($> 0.01 \times 10^{-3}$ mm^3/m) were observed.

Based on the tensile test diagram obtained from the testing machine in graphical or numerical form, it is only possible to determine the ultimate tensile strength *Rm* for cast iron. From the perspective of the theory of limit states for cast iron under tensile stress, *Rm* is not sufficient to determine permissible stress levels. To achieve this, it is necessary to establish the elastic deformation limit R_e and microplastic deformation limit *I*. Currently, there is no methodology available for determining these limits. One of the possible approaches to determine these limits, suggested by Exner [124], involves using the derivative of the measured curve. We recommend further research in the field of evaluating tensile tests using derivatives to address this issue. Furthermore, we recommend investigating the effect of liquid nitrogen exposure time on the change in material hardness and mechanical properties.

Since 2004, TEDOM engines have been using isothermally quenched gray iron for intake and exhaust valve guides. As part of the measurement results, sets of AGI 410 N_{30} valve guides will be prepared for engine testing, where the practical positive influence of cryogenic treatment on material wear resistance will be measured.

7.4 Development of valve seat material

The experiment was focused on finding a suitable alternative material for the intake valve seat in the TEDOM gas combustion engines instead of the currently used material – Stellite 6. The

initial material EN-GJS 450-8 cast iron was chosen for testing, which is material commonly used in TEDOM company for producing the housing of the injection pump. This component was chosen due to its geometric compatibility for subsequent valve seat production as well as its material composition. Using Non-Destructive Testing methods, we measured the influence of cryogenic temperature on mechanical properties of the raw-parts used for testing. Destructive testing defines the physical properties of samples with various heat treatments. Subsequently, the most suitable material was selected to manufacture intake valve seats, which will then be tested in real operating conditions on an engine dynamometer, often referred to as an "engine dyno".

7.4.1 Objectives of the experiment

As part of the experiment, it was planned to research:

1. Measure the Magnetism, Theoretical Young´s modulus, Hardness on following materials with variuos cryogenic treatment: ADI 280, ADI 350, ADI 410
2. Measure the Magnetism, Theoretical Young´s modulus, Hardness on EN-GJS 450-8 and Q-Nitro material.
3. Prepare testing rods for testing Tensile strength, Yeld strenght, Ductility and of the materials, Q-Nitro, ADI 280, ADI 280 N_5, ADI 280 NT_5, ADI 350, ADI 350 N_5, ADI 350 NT_5 ADI 410, ADI 410 N_5, ADI 410 NT_5 in order to investigate their mechanical properties.
4. Performing a phase analysis on the folowing materials: Q-Nitro, ADI 280, ADI 280 N_5, ADI 280 NT_5, ADI 350, ADI 350 N_5, ADI 350 NT_5 ADI 410, ADI 410 N_5, ADI 410 NT_5
5. Prepare real intake valve seats for the TEDOM engine and install them into the durability test on the engine dyno.

7.4.2 Material for testing

Two sets of samples were prepared for testing. The first set was for Non-Destructive Testing, and the second was for Destructive Testing. For Non-Destructive testing were used four raw - part products M4546 made from EN-GJS 450-8 according to EN 1563 (ČSN 42 0951) [29] and for destructive testing was used one raw part M4546. The chemical composition of these raw parts products is shown in Tab. 23. In Fig. 35 is shown a raw part used for testing. These raw parts were utilized to produce the following material variants:

1. Q – Nitro
2. ADI 280
3. ADI 280 N
4. ADI 350
5. ADI 350 N
6. ADI 410
7. ADI 410 N

Fig. 35 Raw part - M4546

Samples for Non-Destructive testing were tested for hardness *HB*, Theoretical Young´s modulus E_{0T}, and magnetism *M*, measured prior to heat treatment. Tab. 24 shows measured initial values of raw parts used for testing. Subsequently, the semi-finished products underwent heat treatment for ADI 250, 350, and 410. After the heat treatment process, were again measured on the samples hardness, magnetism, and the theoretical modulus of elasticity. Following these measurements, the semi-finished products were divided using a band saw whit cooling. From the original cylindrical semi-finished products, cross-sectional slices with a square profile were cut. Subsequently, individual samples underwent various cryogenic treatments.

A total of 26 pcs. of test samples were prepared for Non-Destructive testing. There were eight samples for the Q-Nitro version, six samples for the ADI 280 version, six samples for the ADI 350 version, and six samples for ADI 410. The measurement of physical properties was conducted on a statistically significant number of measurements.

For the Q - Nitro variant was used raw part A. For the ADI 280 / ADI 280 Nitro material variants was used raw part B, for ADI 350 / ADI 350 Nitro material variants was used raw part C and raw part D was utilized for the ADI 410 / ADI 410 Nitro variant.

Tab. 23 Chemical composition of castings used for testing

C [%]	Si [%]	Mn [%]	P [%]	S [%]	Cr [%]	Mg [%]	Graphite			Pearlite	
3.83	2.72	0.16	0.04	0.03	0.03	0.06	VI	11.6 %*	5.60	20	P2

*volume fraction of graphite in the structure [92].

Tab. 24 Measured data on raw parts used for testing

	HB 2,5	E_{0T} [MPa]	M [A/m]
Raw part A	220 ± 2.4	166.4	119.0 ± 2.7
Raw part B	230 ± 2.0	172.8	98.0 ± 1.8
Raw part C	215 ± 1.7	169.2	84.5 ± 1.4
Raw part D	238 ± 1.6	177.8	72.0 ± 1.5

*The HV30 values were calculated using a conversion table ASTM E 140 - 97.

For the destructive testing were prepared testing rods made from the raw part M4546. Test rods were prepared by mechanical machining, and they were subsequently heat-treated into the following variants: EN-GJS-450-8, EN-GJS-450-8 Quenched, Q-Nitro, ADI 280, ADI 280 N_5, ADI 280 NT_5, ADI 350, ADI 350 N_5, ADI 350 NT_5 ADI 410, and ADI 410 N_5, ADI 410 NT_5. The lower index behind the sample designation, in our case 5, represents the time in minutes of exposure to liquid nitrogen on the sample. In our case, we chose a freezing time of 5 min. because this time corresponds to the practical freezing time during the production of cylinder heads. In Fig. 36 is shown an example of one testing rod after measuring.

Fig. 36 Example of testing rod from material EN -GJS 450-8

The test specimen diameter *Do* was 8 mm and length *Lo* was 40 mm, according to ČSN 42 0316 [121]. The chemical composition of the test rods corresponds to the chemical composition provided in Table 23. In Fig. 36 is shown an example of one testing rod after measuring.

7.4.3 Heat treatment of material variants

The following subsections are described the heat treatment of samples for NDT testing: EN-GJS 450 - 8 Qunched, Q-Nitro, ADI 280, ADI 280 Nitro, ADI 350, ADI 350 Nitro, ADI 410 and ADI 410 Nitro.

7.4.3.1 EN-GJS 450 - 8 Q

The samples were heated up to the austenitization temperature of 870 °C for a duration of 45 minutes, followed by quenching in oil at 20 °C for 30 minutes.

7.4.3.2 Q - Nitro

The samples were heated up to the austenitization temperature of 870 °C for a duration of 45 minutes, followed by quenching in oil at 20 °C for 30 minutes. Following that, rapid freezing was performed in liquid nitrogen, and the samples were kept immersed in liquid nitrogen for a duration of 16 hours to ensure uniform and homogeneous conditions throughout the entire volume of the material. After 16 hours, the samples were removed from the liquid nitrogen and allowed to warm up to room temperature to approximately 22 °C. The next step was to temper samples at a temperature of 180 °C for a duration of 30 minutes.

7.4.3.3 ADI 280

The process of heat treatment of raw parts included austenitization at a temperature of 870 °C for a duration of 45 minutes, followed by hardening in a salt bath type AS140 at 280 °C for 30 minutes. The process is completed with air washing at a temperature of 20 °C.

7.4.3.4 ADI 280 N

The process of heat treatment of raw parts included austenitization at a temperature of 870 °C for a duration of 45 minutes, followed by hardening in a salt bath type AS140 at 280 °C for 30 minutes. The samples were allowed to cool down to room temperature at approximately 22 °C. Immediately after reaching room temperature, the samples were gradually cooled in liquid nitrogen. Six samples were prepared, with one sample being left in its initial state for comparison with the changes caused by freezing. The remaining five samples were sequentially exposed to liquid nitrogen for durations of 5, 10, 20, 60, and 960 minutes.

7.4.3.5 ADI 350

The process of heat treatment of raw parts included austenitization at a temperature of 870 °C for a duration of 45 minutes. followed by hardening in a salt bath type AS140 at 350 °C for 30 minutes. The process is completed with air washing at a temperature of 20 °C.

7.4.3.6 ADI 350 N

The process of heat treatment of raw parts included austenitization at a temperature of 870 °C for a duration of 45 minutes, followed by hardening in a salt bath type AS140 at 350 °C for 30 minutes. The samples were allowed to cool down to room temperature at approximately 22°C. Immediately after reaching room temperature, the samples were gradually cooled in liquid nitrogen. Six samples were prepared, with one sample being left in its initial state for comparison with the changes caused by freezing. The remaining five samples were sequentially exposed to liquid nitrogen for durations of 5, 10, 20, 60, and 960 minutes.

7.4.3.7 ADI 410

The process of heat treatment of raw parts included austenitization at a temperature of 870 °C for a duration of 45 minutes, followed by hardening in a salt bath type AS140 at 410 °C for 30 minutes. The process is completed with air washing at a temperature of 20 °C.

7.4.3.8 ADI 410 N

The process of heat treatment of raw parts included austenitization at a temperature of 870 °C for a duration of 45 minutes, followed by hardening in a salt bath type AS140 at 410 °C for 30 minutes. The samples were allowed to cool down to room temperature at approximately 22°C. Immediately after reaching room temperature, the samples were gradually cooled in liquid nitrogen. Six samples were prepared, with one sample being left in its initial state for comparison with the changes caused by freezing. The remaining five samples were sequentially exposed to liquid nitrogen for durations of 5, 10, 20, 60, and 960 minutes.

7.4.4 Measurement methodology

The properties of the testing samples were evaluated using several measurement methods. Hardness was measured in accordance with EN ISO 6507-1 [120], using the HV method with a Dia Testor 2Rc hardness tester. Hardness HB 2,5 was measured using method according to EN ISO 6507-1 [44] with a WPM hardness tester.

The samples for microstructure analysis were prepared following standard procedures, which involved hot-mounting them in conductive resin (Struers Polyfast), followed by sandpaper grinding (#240, 500, 1200, 2000) and subsequent polishing using a textile cloth with diamond suspension (3 μm and 1 μm). The final step consisted of mechanical-chemical polishing with silica (Struers OP-S).

Microstructural analysis was perfomed by conventional metallographic techniques. A Thermofisher Scientific scanning electron microscope (SEM) and attached backscattered electron detector (BSE) was used. Data acquisition was conducted at an accelerating voltage of 10.0 kV, and the employed evaluation software was from manufacturer.

Optical microstructural analysis was conducted using a NEOPHOT 2 microscope colloidal, with documentation done through Digifoto COOLPIX 4500 Nikon and a USB microscope DTX90 Levenhuk.

The speed of sound V_L was determined using an ultrasonic flaw detector DIO 562 (Starmans s.r.o. Prague) with a dual probe of 20 mm diameter and a 2 MHz frequency probe for larger paths. The intensity of residual magnetic field *M* was measured using the magnetic spot method with B3 (TU Liberec) ELKOSO s.r.o. Brno instruments (set at 3rd level of magnetization). Values of speed of sound was used for calculation of theoretical Young´s modulus. Theoretical Young´s modulus E_{0T} was calculated according to Equation 13.

7.4.5 Measured data

Tab. 25 shows the measured values of hardness HV30 and HRC, Magnetism – *M*, along with the calculated values of Young´s modulus – E_{0T} for material Q-Nitro.

Tab. 25 Measured and calculated data of material Q - Nitro

Sample No.	Q-Nitro			
	HV30	**HRC***	**M [A/m]**	**E_{0T} [GPa]**
1	580	54	148	154.4
2	621	56	115	155.8
3	601	55	157	155.2
4	584	54	144	155.3
5	603	55	174	155.0
6	644	58	166	155.7
7	620	56	164	154.2
8	614	56	159	154.8
Average	**608 ± 20.9**	**56**	**142 ± 18.1**	**155.1 ± 0.6**

* The HRC values were calculated using a conversion table according to ASTM E 140 - 97.

I In Tab. 26 to 28, values of hardness HV30 and HRC, magnetism (M), and calculated values of Young's modulus (E_{0T}) are depicted for material ADI 280, 350, and 410 with various cryogenic treatments compared to original EN-GJS 450-8 material.

Tab. 26 Influence of cryogenic treatment on physical properties of material ADI 280

Sample	Material	HV30	HRC*	M [A/m]	E_{0T} [GPa]	ΔHV30	ΔHRC*	ΔM [A/m]	ΔE_{0T} [GPa]
1	EN-GJS 450 - 8	242 ± 2	21	98 ± 1.8	172.8	-	-	-	-
2	ADI 280	463 ± 4	46	459 ± 2.3	160.8	+221	+25	+361	-12.0
3	ADI 280 N_5	571 ± 5	54	446 ±2.5	161.2	+329	+33	+348	-11.6
4	ADI 280 N_{10}	502 ± 7	49	438 ± 2.1	159.8	+260	+28	+340	-13.0
5	ADI 280 N_{20}	508 ± 6	50	464 ± 2.8	162.8	+266	+29	+366	-10.0
6	ADI 280 N_{60}	535 ± 5	51	426 ± 2.5	163.1	+293	+30	+328	-9.7
7	ADI 280 N_{960}	473 ± 6	47	412 ± 1.9	165.1	+231	+26	+314	-7.7

* The HRC values were calculated using a conversion table according to ASTM E 140 - 97.

Tab. 27 Influence of cryogenic treatment on physical properties of material ADI 350

Sample	Material	HV30	HRC*	M [A/m]	E_{0T} [GPa]	ΔHV30	ΔHRC*	ΔM [A/m]	ΔE_{0T} [GPa]
1	EN-GJS 450 - 8	226 ± 2	18	85 ± 1.4	169.2	-	-	-	-
2	ADI 350	351 ± 4	36	885 ± 2.9	155.5	+125	+18	+800	-13,7
3	ADI 350 N_5	387 ± 2	40	690 ± 2.9	159.6	+161	+22	+605	-9.6
4	ADI 350 N_{10}	381 ± 4	39	662 ± 1.5	158.1	+155	+21	+577	-11.1
5	ADI 350 N_{20}	343 ± 5	35	714 ± 1.4	159.4	+117	+17	+629	-9.8
6	ADI 350 N_{60}	361 ± 1	37	755 ± 1.9	161.1	+135	+19	+670	-8.1
7	ADI 350 N_{960}	384 ± 6	39	720 ± 3.1	161.3	+158	+21	+635	-7.9

* The HRC values were calculated using a conversion table according to ASTM E 140 – 97.

Tab. 28 Influence of cryogenic treatment on physical properties of material ADI 410

Sample	Material	HV30	HRC*	M [A/m]	E_{0T} [GPa]	ΔHV30	ΔHRC*	ΔM [A/m]	ΔE_{0T} [GPa]
1	EN-GJS 450 - 8	250 ± 2	22	72 ± 1.5	177.8	-	-	-	-
2	ADI 410	278 ± 3	27	714 ± 9.7	173.1	+28	+5	+642	-4.7
3	ADI 410 N_5	281 ± 4	27	622 ± 1.7	172.0	+31	+5	+550	-5.8
4	ADI 410 N_{10}	293 ± 6	29	550 ± 2.9	172.8	+43	+7	+478	-5.0
5	ADI 410 N_{20}	281 ± 3	27	544 ± 2.4	172.2	+31	+5	+472	-5.6
6	ADI 410 N_{60}	287 ± 2	28	461 ± 5.5	173.7	+37	+6	+389	-4.1
7	ADI 410 N_{960}	288 ± 6	28	491 ± 3.1	172.6	+38	+6	+419	-5.2

* The HRC values were calculated using a conversion table according to ASTM E 140 - 97.

Tab. 29 presents the results of the destructive tests. Samples were divided into four groups based on the heat treatment:

O – Original state (without freezing or quenching/tempering)

Q – Heated up to the austenitization temperature of 870 °C for a duration of 45 minutes, followed by quenching in oil at 20 °C for 30 minutes.

N 5 – Cryogenic treatment in liquid nitrogen with gradual cooling and holding for 5 min., followed by a 1 - 4 hour interval after austempering.

NT 5 – Cryogenic treatment in liquid nitrogen with gradual cooling and holding for 5 min, followed by a 1 - 4 hour interval after austempering, and subsequently tempering at 180 °C for 1 hour.

Tab. 29 Table of measured values of mechanical properties of the investigated materials

Sample	Heat treatment	$R_{p0.2}$ [MPa]	Rm [MPa]	A5	HV30
EN-GJS 450-8	O	338.1	505.7	9.75	170
EN-GJS 450-8 *	Q	0	590.3	0	627
Q-Nitro **	O	0	721.8	0	600
ADI 280	O	851.0	925.1	1.71	457
	N_5	903.6	1420.2	1.40	462
	NT_5	1153.3	1522.1	1.56	468
ADI 350	O	794.1	880.9	5.14	351
	N_5	965.8	1083.5	4.21	372
	NT_5	959.8	1198.6	4.68	360
ADI 410	O	720.3	812.6	9.53	270
	N_5	742.2	765.4	8.37	266
	NT_5	766.3	884.0	9.21	311

* The quenched material EN - GJS 450-8 exhibited extreme notch sensitivity. As a result, the tensile strength and elongation values were both zero. Three test specimens were prepared from this material, and all of them fractured in the transitional region at the radius.

** Q-Nitro material exhibited extreme notch sensitivity. As a result, the tensile strength and elongation values were both zero. Three test specimens were prepared from this material, and all of them fractured in the transitional region at the radius.

7.4.6 Phase analysis

The samples for phase analysis were prepared following standard procedures, which involved hot-mounting them in conductive resin (Struers Polyfast), followed by sandpaper grinding (#240, 500, 1200, 2000) and subsequent polishing using a textile cloth with diamond suspension (3 μm and 1 μm). The final step consisted of mechanical-chemical polishing with colloidal silica (Struers OP-S).

The sample´s microstructure was examined using a Zeiss Ultra Plus scanning electron microscope equipped with an EBSD detector Oxford Nordlys Nano. Data acquisition was performed at an accelerating voltage of 20 kV, and the SW Oxford AZtec 3.3 software was utilized for both data acquisition and processing.

The graphite area fraction was determined through image analysis of five SEM BSE images, each with an area of 400×300 μm.

The same samples used for testing the physical properties were also utilized for the phase analysis. For the Q-Nitro variant was selected sample No. 6 (Tab. 25) as it exhibited the highest hardness among all eight samples.

For the phase analysis of the ADI 280, ADI 350, and ADI 410 samples was prepared a special batch of samples from the same initial material used for the samples used in the measurement of mechanical properties. The samples were divided into three groups based on their heat treatment:

O – Original state (without freezing or tempering)

N $_5$ – Cryogenic treatment in liquid nitrogen with gradual cooling and holding for 5 min. followed by a 1 – 4 hour interval after ADI.

NT $_5$ – Cryogenic treatment in liquid nitrogen with gradual cooling and holding for 5 min., followed by a 1– 4 hour interval after ADI and subsequently tempering at 180 °C for 1 hour.

Zero Solutions = residual (amorphous) fraction.

The results of phase analysis are presented in Tab. 30 to 34.

Tab. 30 The phase composition of the material initial EN - GJS 450-8

Material	Thermal treatment	Crystal Structures	Phase Fraction [%]	Standard deviation σ
EN-GJS 450-8	O	Iron BCC (old)	94,32	1,88
		Iron FCC	2,11	1,90
		Zero Solutions	3,57	-

Tab. 31 The phase composition of the material Q - Nitro

Material	Thermal treatment	Crystal Structures	Phase Fraction [%]	Standard deviation σ
Q - Nitro	O	Iron BCC (old)	64.71	1.97
		Iron FCC	0.74	1.65
		Zero Solutions	34.55	-

Tab. 32 The phase composition of the material ADI 280 with various thermal treatments

Material		Thermal treatment	Crystal Structures	Phase Fraction [%]	Standard deviation σ
ADI	280	O	Iron BCC (old)	84.19	1.85
			Iron FCC	5.96	1.80
			Zero Solutions	8.75	-
	280	N_5	Iron BCC (old)	66.02	2.00
			Iron FCC	2.928	1.95
			Zero Solutions	30.99	-
	280	NT_5	Iron BCC (old)	60.92	1.99
			Iron FCC	2.23	2.00
			Zero Solutions	41.86	-

Tab. 33 The phase composition of the material ADI 350 with various thermal treatments

Material		Thermal treatment	Crystal Structures	Phase Fraction [%]	Standard deviation σ
ADI	350	O	Iron BCC (old)	71.76	1.99
			Iron FCC	19.71	1.99
			Zero Solutions	8.52	-
	350	N_5	Iron BCC (old)	75.90	1.98
			Iron FCC	17.19	1.99
			Zero Solutions	6.91	-
	350	NT_5	Iron BCC (old)	77.44	1.95
			Iron FCC	19.53	1.98
			Zero Solutions	3.08	-

Tab. 34 The phase composition of the material ADI 410 with various thermal treatments

Material		Thermal treatment	Crystal Structures	Phase Fraction [%]	Standard deviation σ
ADI	410	O	Iron BCC (old)	62.94	2.01
			Iron FCC	33.41	1.99
			Zero Solutions	3.65	-
	410	N_5	Iron BCC (old)	67.12	1.99
			Iron FCC	19.06	1.98
			Zero Solutions	13.82	-
	410	NT_5	Iron BCC (old)	68.53	1.78
			Iron FCC	21.55	1.81
			Zero Solutions	9.92	-

Fig. 37 shows the microstructure of the raw part used for testing before heat treatment. The producer of these semi-finished parts is UXA a.s. Foundry Brno.

Fig. 38 illustrates the microstructure of the Q-Nitro. Fig. 39 illustrates the microstructure of ADI 280 N_5 variant, Fig. 40 illustrates the microstructure of variant ADI 350 N_5, and Fig. 41 illustrates the microstructure of variant ADI 410 N_5.

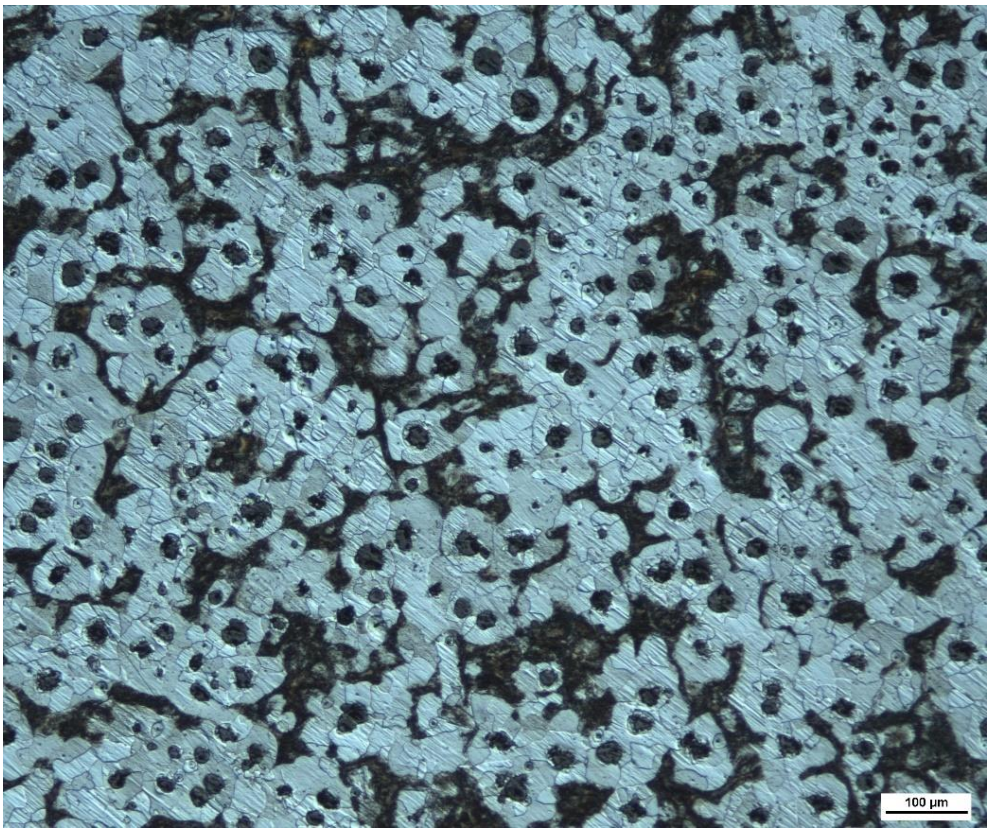

Fig. 37 Microtructure of EN-GJS 450-8 before heat treatment

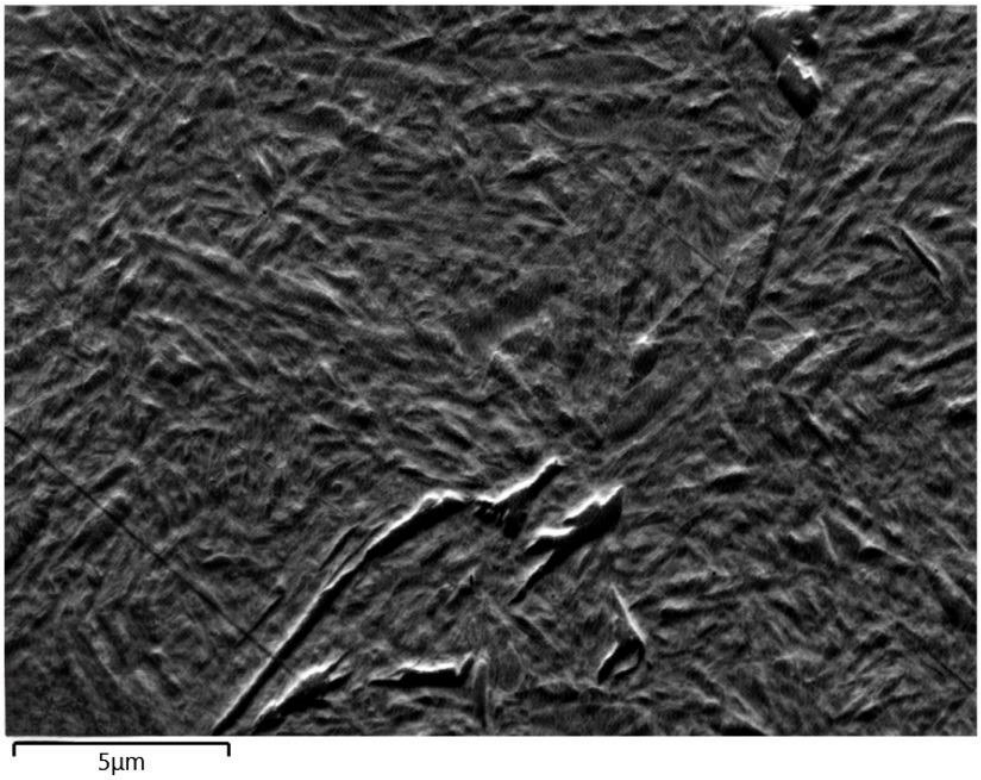

Fig. 38 Microstructure of Q – Nitro from SEM

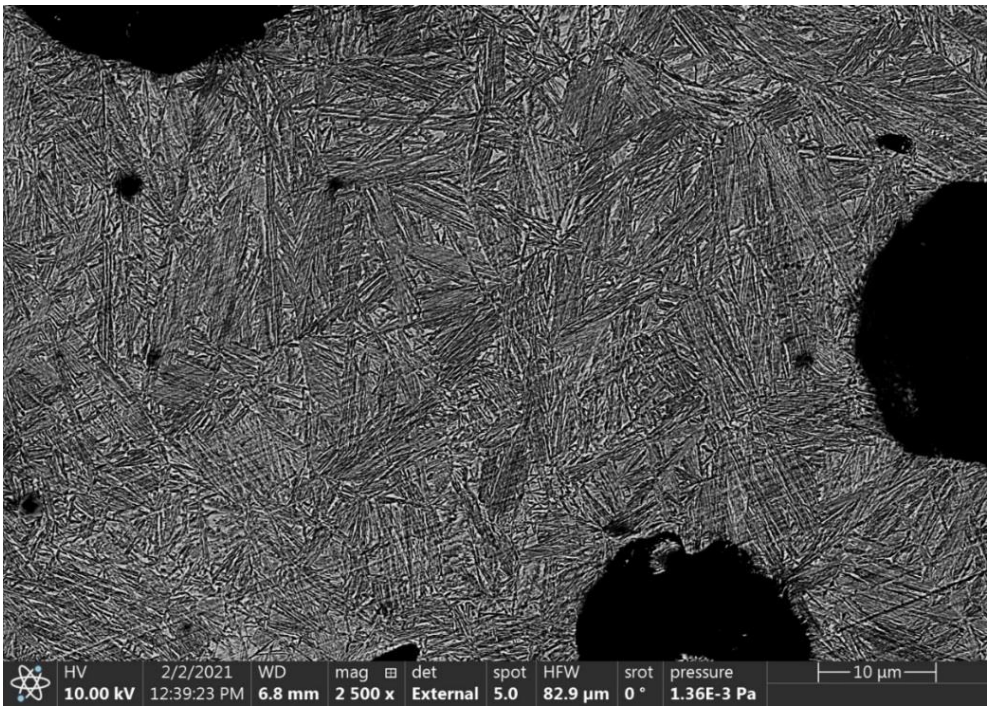

Fig. 39 Microstructure of ADI 280 N_5 from SEM

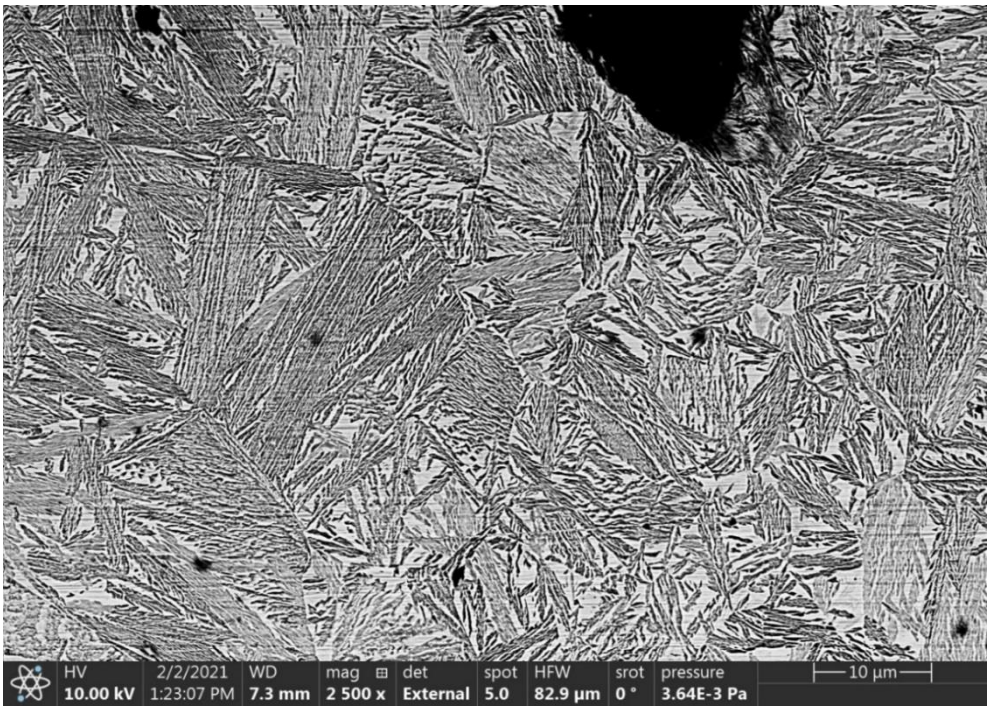

Fig. 40 Microtructure of ADI 350 N_5 from SEM

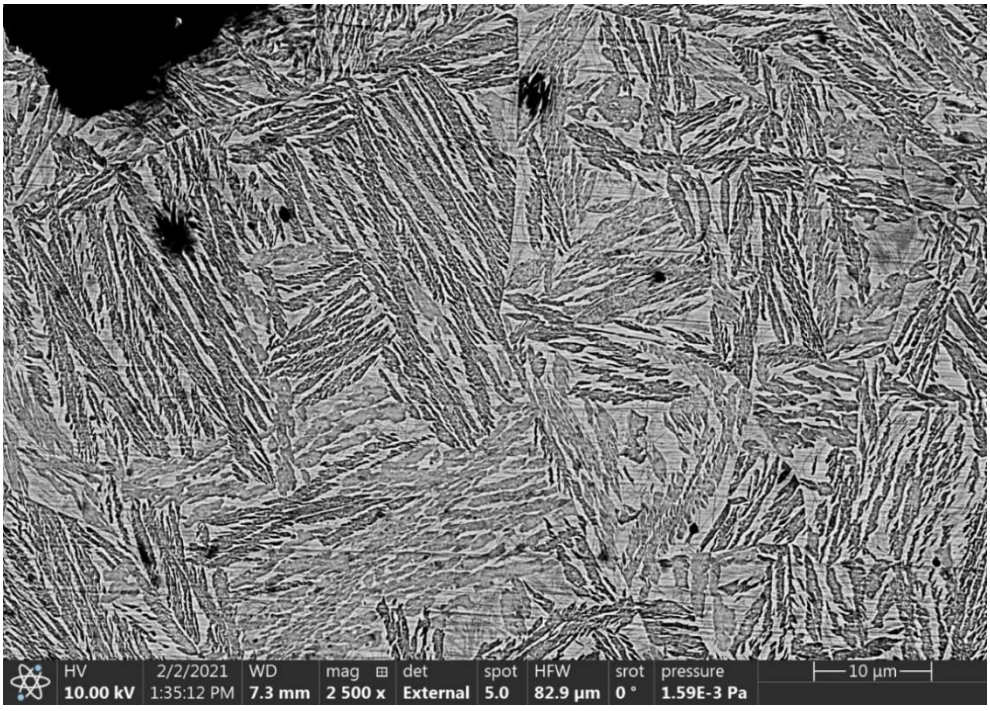

Fig. 41 Microtructure of ADI 410 N_5 from SEM

7.4.7 Valve seat for engine test

For testing in the engine, we decided to use two materials - ADI 280 and Q-Nitro. For these material variants we prepared detailed technical drawings documentation. From each batch, we manufactured six intake valve seats for one engine. The drawings for the valve seat production are

attached as appendices to this work. The motivation for choosing ADI 280 and Q-Nitro materials for testing in the engine was due to their high hardness among the prepared samples. The average hardness of the ADI 280 material variant is approx. 450 HV30 and Q-Nitro is approx. 600 HV30 and this hardness has been deemed suitable for the material pairing with the P37S welding on the intake valve.

The valve seats made from the Q-Nitro variant exhibited significant difficulties in terms of machinability due to its high hardness. The samples cracked and experienced material tear-out during machining. As a result, it was not possible to manufacture valve seats of satisfactory quality, leading us to leave the testing in the engine.

The valve seats made from ADI 280 material were much easier to machine compared to the Q-Nitro material, and there were no issues with material tear-out or other defects during the machining process. As a result, we were able to proceed with testing the valve seats on the engine dyno. However, after approximately 200 engine hours, we were compelled to stop the engine test due to increased valve recession. Upon closer examination, we noticed that some valve seats had structural defects in the form of voids, which resulted in rapid wear. Fig. 38 shows the voids in the seating surface of the intake valve seat, which resulted in the premature termination of the test. The test was not repeated due to limited economy sources.

Another test set of intake valve seats used ADI 280 NT_5 material. The machining characteristics of the valve seats made from ADI 280 NT_5 material are practically identical to those made from ADI 280. These valve seats were installed in a test engine with a nominal mechanical output power of 210 kW, as the fuel for the engine is using natural gas. As of today (08/2023), the cylinder heads with these valve seats are in operation and show no signs of wear. The engine has accumulated 10.000 engine hours to date (as of 08/2023), for the testing where used standard TEDOM intake valves with P37S hardfacing. The engine undergoes valve recession checks every 2.500 hours to monitor the condition of the valve seats.

In Fig. 42, sections A and B depict the non-coaxial seating of the valve in the valve seat ADI 280. The silver part represents the trace left by the valve. This misalignment of the valve seating caused the premature termination of the test. The non-coaxial seating was induced by inhomogeneity in the valve seats, resulting in geometric deformation due to the mating of the cylinder head. Sections C and D show internal inhomogeneities (defects) within the seat.

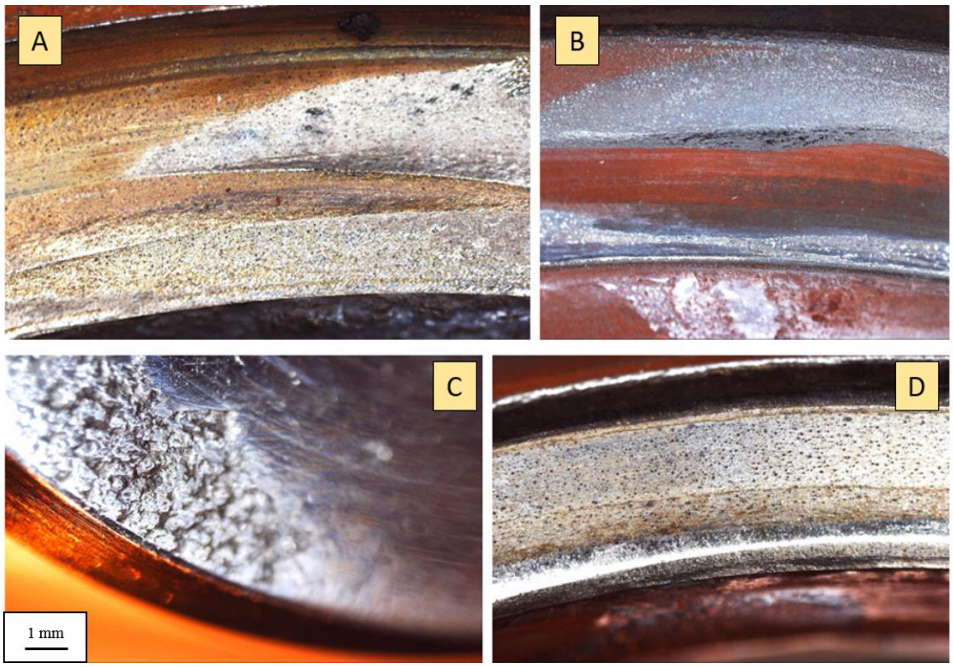

Fig. 42 Detail of ADI 280 intake valve seat after engine dyno test

7.4.8 Discussion of measured data

From measured values, the following can be concluded for individual materials:

GJS 450-8 Q

- The quenching processing increases the tensile strength *Rm* of the initial material EN – GJS 450-8 by 16.7 %. (From 505.7 MPa to 590.3 MPa).
- The quenching processing increases the hardness of the initial material EN – GJS 450-8 by 268.8 %. (From 170 HV30 to 627 HV30).
- The quenched material EN – GJS 450-8 exhibits extreme notch sensitivity, which resulted in zero ductility of the quenched material.

Q-Nitro

- The Q-Nitro processing increases the tensile strength *Rm* of the initial material EN-GJS 450-8 by 42.7 %. (From 505.7 MPa to 721.8 MPa).
- The Q-Nitro processing increases the hardness of the initial material EN – GJS 450-8 by 252.9 %. (From 170 HV30 to 600 HV30).
- When comparing material GJS 450-8 with Q-Nitro to determine the potential impact of freezing in liquid nitrogen and subsequent tempering on hardened cast iron GJS 450-8, we would conclude the following. We measured increase in the tensile strength *Rm* by 22.29% (From 590.3 MPa to 721.8 MPa) and a decrease in hardness by 4.31 %. (From 627 HV30

to 600 HV30). Our samples with cryogenic treatment did not show any improvement in the material's ductility.

ADI 280

- The ADI 280 processing increases the Tensile strength *Rm* of the initial material EN-GJS 450-8 by 82.9 %. (From 505.7 MPa to 925.1 MPa).
- The ADI 280 processing increases the Yield strength R_{p02} of the initial material EN-GJS 450-8 by 151.7%. (From 338.1 MPa to 851.0 MPa).
- The ADI 280 processing increases the hardness of the initial material EN – GJS 450-8 by 168.8 %. (From 170 HV30 to 457 HV30).
- The ductility of the material has decreased to a level of 1.7 %, which is 82.5 % less than the original EN – GJS 450-8 material.

ADI 280 N_5

- The ADI 280 N_5 processing increases the Tensile strength *Rm* of the initial material EN-GJS 450-8 by 180.8 %. (From 505.7 MPa to 1420.2 MPa).
- The ADI 280 N_5 processing increases the Yield strength R_{p02} of the initial material EN-GJS 450-8 by 167.3 %. (From 338.1 MPa to 903.6 MPa).
- The ADI 280 N_5 processing increases the hardness of the initial material EN-GJS 450-8 by 171.8 %. (From 170 HV30 to 462 HV30).
- The ductility of the material has decreased to a level of 1.4 %, which is 85.6 % less than the original EN – GJS 450-8 material.

ADI 280 NT_5

- The ADI 280 NT_5 processing increases the Tensile strength *Rm* of the initial material EN-GJS 450-8 by 201 %. (From 505.7 MPa to 1522.1 MPa).
- The ADI 280 NT_5 processing increases the Yield strength R_{p02} of the initial material EN-GJS 450-8 by 241.1 %. (From 338.1 MPa to 1153.3 MPa).
- The ADI 280 NT_5 processing increases the hardness of the initial material EN-GJS 450-8 by 175.3 %. (From 170 HV30 to 468 HV30).
- The ductility of the material has decreased to a level of 1.6 %, which is 84 % less than the original EN-GJS 450-8 material.

ADI 350

- The ADI 350 processing increases the Tensile strength *Rm* of the initial material EN-GJS 450-8 by 74.2 %. (From 505.7 MPa to 880.9 MPa).
- The ADI 350 processing increases the Yield strength R_{p02} of the initial material EN-GJS 450-8 by 134.9 %. (From 338.1 MPa to 794.1 MPa).
- The ADI 350 processing increases the hardness of the initial material EN – GJS 450-8 by 106.5 %. (From 170 HV30 to 351 HV30).
- The ductility of the material has decreased to a level of 5.1 %, which is 47.3 % less than the original EN – GJS 450-8 material.

ADI 350 N_5

- The ADI 350 N_5 processing increases the Tensile strength *Rm* of the initial material EN-GJS 450-8 by 114.3 %. (From 505.7 MPa to 1083.5 MPa).
- The ADI 350 N_5 processing increases the Yield strength R_{p02} of the initial material EN-GJS 450-8 by 185.7 %. (From 338.1 MPa to 965.8 MPa).
- The ADI 350 N_5 processing increases the hardness of the initial material EN-GJS 450-8 by 118.8 %. (From 170 HV30 to 372 HV30).
- The ductility of the material has decreased to a level of 4.2 %, which is 56.8 % less than the original EN - GJS 450-8 material.

ADI 350 NT_5

- The ADI 350 NT_5 processing increases the Tensile strength *Rm* of the initial materiál EN-GJS 450-8 by 137%. (From 505.7 MPa to 1198.6 MPa).
- The ADI 350 NT_5 processing increases the Yield strength R_{p02} of the initial material EN-GJS 450-8 by 183.9 %. (From 338.1 MPa to 959.8 MPa).
- The ADI 350 NT_5 processing increases the hardness of the initial material EN-GJS 450-8 by 111.8 %. (From 170 HV30 to 360 HV30).
- The ductility of the material has decreased to a level of 4.68 %, which is 52 % less than the original EN-GJS 450-8 material.

ADI 410

- The ADI 410 processing increases the Tensile strength *Rm* of the initial material EN-GJS 450-8 by 60.7 %. (From 505.7 MPa to 812.6 MPa).
- The ADI 410 processing increases the Yield strength R_{p02} of the initial material EN-GJS 450-8 by 113,0%. (From 338.1 MPa to 720.3 MPa).
- The ADI 410 processing increases the hardness of the initial material EN-GJS 450-8 by 58.8 %. (From 170 HV30 to 270 HV30).
- The ductility of the material has decreased to a level of 9.5 %, which is 2.3% less than the original EN-GJS 450-8 material.

ADI 410 N_5

- The ADI 410 N_5 processing increases the Tensile strength *Rm* of the initial material EN-GJS 450-8 by 51.4%. (From 505.7 MPa to 765.4MPa).
- The ADI 410 N_5 processing increases the Yield strength R_{p02} of the initial material EN-GJS 450-8 by 119.5 %. (From 338.1 MPa to 742.2 MPa).
- The ADI 410 N_5 processing increases the hardness of the initial material EN-GJS 450-8 by 56.5 %. (From 170 HV30 to 266 HV30).
- The ductility of the material has decreased to a level of 8.37 %, which is 14.2 % less than the original EN-GJS 450-8 material.

ADI 410 NT_5

- The ADI 410 NT_5 processing increases the Tensile strength *Rm* of the initial material EN-GJS 450-8 by 74.8 %. (From 505.7 MPa to 884 MPa).
- The ADI 410 NT_5 processing increases the Yield strength R_{p02} of the initial material EN-GJS 450-8 by 126.6 %. (From 338.1 MPa to 766.3 MPa).
- The ADI 410 NT_5 processing increases the hardness of the initial material EN-GJS 450-8 by 82.9 %. (From 170 HV30 to 311 HV30).
- The ductility of the material has decreased to a level of 9.2 %, which is 5.5 % less than the original EN-GJS 450-8 material.

In the article "Influence of cryogenic treatment on microstructure and hardness of austempered ductile iron" [125], Myszka states that higher tempering temperatures generally lead

to increased formation of austenite and a higher number of martensitic plates in the austenitic matrix. This results in higher hardness and strength of the material. However, higher tempering temperatures may have a negative impact on the ductility and resilience of the material. Our measurements contradict this claim as the strength values we obtained indicate that higher tempering temperatures result in lower strength but higher ductility of the material. Similarly, we observed that with increasing temperature during isothermal quenching, the hardness of the sample decreases.

Furthermore, Myszka states that cryogenic treatment of ADI leads to an increase in strength and hardness. Our measurements confirm this claim for ADI materials with grades 280 and 350, where the strength of the material was enhanced due to the influence of cryogenic temperatures. However, for ADI grade 410, we observed a decrease in strength after cryogenic treatment. Myszka explains that the principle behind this change is the transformation of austenite into martensite in specific microregions of the material, which results in improved strength and hardness.

Theil states in his article "Effects of refrigeration and cryogenic treatments on austempered ductile iron" [126] that alloys with retained austenite in their structure can have their physical properties altered by treatment at sub-zero temperatures. This treatment involves lowering the material's temperature below the *Ms* temperature, leading to the transformation of retained austenite into martensite. As a result of this transformation, the alloy's tensile strength, Yield strength, and hardness. In our measurements, we observed that cryogenic treatment of ADI 280 material leads to a slight decrease in strength and a slight increase in hardness. For ADI 350 material, the effect of cryogenic temperatures resulted in a significant increase in strength by 23 % and an increase in hardness by 21 HV. However, for ADI 410 material, we observed a decrease in strength of approximately 6 % and a decrease in hardness by 4 HV.

According to Panneerselvam [128], ADI austempering in the temperature range of 288 °C – 399 °C is resulting the elongation of the material decreased, but the fracture toughness remained unaffected. At lower austempering temperatures (260 °C to 288 °C), the formed austenite displayed thermal instability and transformed into martensite after cryogenic treatment. At higher austempering temperatures (371 to 399 °C), the austenite exhibited greater thermal stability and only partially transformed into martensite during cryogenic treatment.

Our measurements in samples subjected to isothermal quenching at lower temperatures also showed that a higher amount of residual austenite remained, which transformed into martensite in a cryogenic environment. Similar to Panneerselvam's findings, we also observed the most significant increase in hardness in samples subjected to isothermal quenching at 350 °C.

Tempering of all the investigated materials resulted in a slight increase in strength, especially in the case of ADI 280. Moreover, tempering after cryogenic treatment also increased the hardness of all examined materials, with the most significant effect observed in ADI 410. Based on the measured values, it appears that tempering after cryogenic treatment will have a positive impact on wear resistance. These findings were reported also by Šolič and colleagues [127], who investigated the effects of deep cryogenic treatment in combination with tempering on the microstructure and abrasion wear resistance of the materials. The result showed that austenite formed during austempering at 673 K (400 °C) is less thermally stable when subjected to 24 hours of exposure to liquid nitrogen temperature at 77 K (196 °C) compared to a previous study where the samples were cryogenically treated at 123 K (150 °C) for 4 hours. As a result of the deep cryogenic treatment, the amount of austenite decreased significantly, from 35 % to 11 %. This transformation led to increased hardness and abrasion wear resistance due to the formation of martensite. Additionally, tempering at both temperatures further improved hardness and abrasion wear resistance by potentially precipitating ultrafine carbides in the martensite during the tempering process. The analysis of the abrasion wear tracks revealed the presence of combined mechanisms of mild and severe abrasion, particularly noticeable in the deep cryogenic-treated samples. Their samples exhibited approximately 10 % to 18 % percent better abrasion wear resistance compared to the other groups. However, both cryogenic-treated and tempered samples showed a similar mass loss, specimens tempered at the higher temperature displayed 20 % higher hardness.

The ADI 280 freezing process has proven to be a tool capable of further exploiting the material's potential. All freezing times resulted in a increasing in hardness From the measured values, it is evident that a freezing time of 5 minutes exhibited the most significant changes compared to the initial ADI 280 material, where we observed an increase in hardness of 108HV (8HRC). All freezing times, except for 20 minutes, showed a decrease in magnetism. During the 20-minute freezing process, we measured a value 5 A/m higher than the initial ADI 280. For the theoretical Young's modulus, we found that the only freezing time 10min exhibited lower magnetism by 1 GPa. However, the measurement uncertainty is greater than the measured difference.

In the case of ADI 350 samples all freezing times resulted in a increasing in hardness. We observed the most significant deviation from the initial state of ADI 350 at a freezing time of 5 minutes, with an increase of 36HV (4HRC) in hardness. We also measured a slight decrease in hardness at a freezing time of 20 minutes, by 8HV (1HRC). All freezing times resulted in a decrease in magnetism. The largest decrease was recorded at a freezing time of 10 minutes, with a decrease of 223A/m. Additionally, all freezing times increased the theoretical modulus of elasticity. The most significant increase was measured at a freezing time of 960 minutes, with an increase of 5.8GPa.

The material ADI 410 responded to cryogenic treatment with the least impact on hardness among the trio of ADI 280, 350, and 410. All freezing times resulted in a increasing in hardness. The most significant change was observed at a freezing time of 10 minutes, where hardness increased by 15HRC (2HRC). All freezing times resulted in a decrease in magnetism compared to the initial ADI 410. The largest decrease was measured at a freezing time of 60 minutes, with a decrease of 253A/m. All freezing times reduced the theoretical modulus of elasticity except for the 60-minute freezing time, where we measured an increase of 0.6GPa. However, the measurement uncertainty is greater than the measured difference. The most significant decrease was observed at a freezing time of 95 minutes, with a decrease of 1.1GPa, where again the measurement uncertainty is greater than the measured difference.

The lowest values of M are exhibited by initial states with a ferritic matrix. Lamellar pearlite cementite increases the M values of initial states (Fe_3C has a higher remanence than Fe). The highest values of M are influenced significantly by the internal demagnetization factor of Ni on M, with an increasing proportion of residual austenite in isothermally quenched laths of carbon-saturated ferrite in the field of paramagnetic A – phase upper bainite. Lower bainite, therefore, shows lower M values. Cryoannealing leads to the precipitation of ferromagnetic micro-martensite within the A – phase. However, further growth in M does not occur, as the Ni value decreases significantly (the ferrite laths no longer behave as individual polarized micromagnets). Cryoprocessing reduces M. Tempering at 180 °C reduces internal stress and thereby further reduces M.

The aim of the experiment was to demonstrate the trend in the alteration of physical properties. Our measurements were not conducted on a statistically significant sample. Therefore, we recommend further research in this area and conducting repeated measurements on a larger number of samples.

The set of measured data was so extensive that within the scope of the dissertation, it was not possible to comment on the influence of proper freezing for isothermal quenching of ductile iron with nodular graphite on each individual measured sample. Therefore, the discussion focuses on the section where the mechanical properties were evaluated in strength tests.

7.5 Influence of Cryogenic Temperature on the Hardness of Stellite 6 and Stellite 12

The investigation of the effects of cryogenic temperatures on the physical properties of cobalt alloys is motivated by the clear evidence from previous experiments that cryogenic temperatures have an impact on the behavior of cast irons. Additionally, in the practical operations of the TEDOM company, there have been unexplained differences in the lifespan of cylinder heads operating under the same conditions. The only discernible difference identified during the research was the freezing time of the valve seats before their installation into the cylinder heads. Due to the absence of explicit guidelines defining the conditions for valve seat freezing, it was not uncommon for the difference in freezing time between the two operators to exceed one hour.

7.5.1 Objectives of the experiment

As part of the experiment, it was planned to research:

1. Determine the effect of cryogenic temperatures on the hardness of valve seats in order to find out if their different hardness after technological freezing during the production of cylinder heads can cause accidentally increased wear of valve seats.
2. Confirm or deny the need to freeze valve seats in a controlled manner due to the fact that in the technological process of manufacturing cylinder heads, there is currently no regulation that would explicitly define the time after which the valve seats should be immersed in liquid nitrogen.
3. In the event that the negative effect of liquid nitrogen on the hardness of the valve seats is confirmed, find the optimal freezing time so that decreased hardness does not affect the life of the cylinder head.

7.5.2 Material for testing

The intake valve seats are cast from Stellite 6 material and the exhaust valve seats are cast from Stellite 12 material. The valve seats are cast by the company PBS Velká Bíteš a.s., using the technology of precision casting into a disposable mold. To eliminate internal stress and improve

hardness values, the castings were annealed in a gradual heating annealing furnace at temperatures ranging from 900 °C to 950 °C with a "soaking" period at this temperature lasting for 3 to 4 hours. Subsequently, they are cooled in the furnace down to 500 °C. Tab. 35 shows the chemical composition of the tested materials, which is in compliance with the specified material composition requirements.

Tab. 35 The chemical composition of Stellite 6 and Stellite 12 used for testing

	C [%]	Cr [%]	W [%]	Fe [%]	Ni [%]	Si [%]	Mn [%]	Mo [%]	B [%]	Co [%]
Stellite 6	1.2	27.3	6.1	1.8	0.29	1.4	0.4	0.2	0.02	Balance
Stellite 12	1.6	32.5	10.2	1.7	0.36	1.1	0.29	0.35	0.01	Balance

7.5.3 Measurement methodology

The measurement was carried out on seven samples of each material, where hardness was first measured before exposure to liquid nitrogen. Then the valve seats were immersed for 5, 10, 15, 30, 60, and 960 min in liquid nitrogen so that the liquid level was always above the examined samples. The test samples used in this test were the same as in the previous test. The use of the same material samples in the testing was done to eliminate any potential changes in structure and properties that could arise from different materials.

After freezing in liquid nitrogen, hardness was measured again on all samples. The freezing process was conducted in a manner that prevented thermal shock to the material. The valve seats were gradually immersed in liquid nitrogen for short periods of time, and the duration of exposure gradually increased.

The hardness was measured around the circumference of the semi-finished product every 45°. Hardness was measured in accordance with EN ISO 6508-1 [45], using the HRC method with a BRIRO VA hardness tester.

7.5.4 Measured data

Tab. 36 and Tab. 37 show the measured data of hardness value for Stellite 6 and Stellite 12 before and after freezing in liquid nitrogen. Fig. 44 and 45 graphically present changes of hardness depending on the length of exposure to liquid nitrogen. Fig. 43 shows the raw part of the valve seats after freezing in liquid nitrogen.

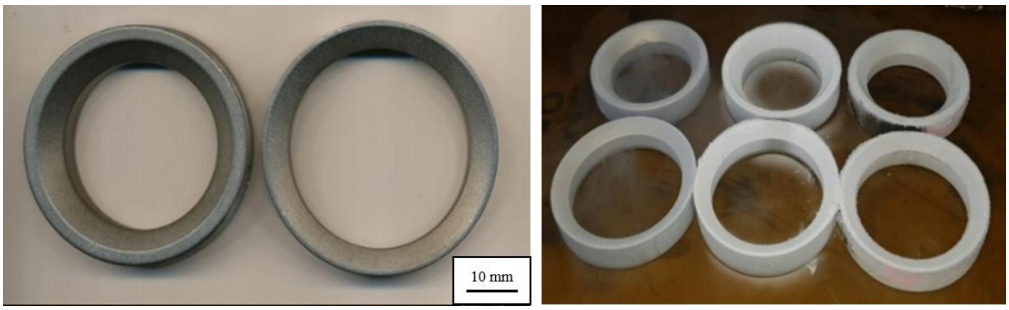

Fig. 43 Cast valve seats – left, semi-finished valve seats after freezing – right

Tab. 36 Measurements of Stellite 6 hardness under the exposure to liquid nitrogen

		Hardness	HRC								Average hardness	Average diference hardness
			Position on seat									
Material	**Sample**	**Time in cryo [min]**	**0°**	**45°**	**90°**	**135°**	**180°**	**225°**	**270°**	**315°**		
Stellite 6	**1**	0	42.1	43.7	43.9	43.6	42.3	43.8	44.2	43.0	43.4 ± 0.8	0.0
Stellite 6	**2**	0	41.3	43.5	43.5	43.4	46.5	46.4	44.2	44.0	44.1 ± 1.7	-0.8 ± 1.6
		5	41.2	42.3	43.1	42.4	44.5	46.4	43.1	43.5	43.3 ± 1.6	
Stellite 6	**3**	0	44.3	45.1	44.7	44.2	44.1	46.3	44.3	42.7	44.7 ± 1.0	-2.1 ± 0.9
		10	41.9	42.2	43.2	44.0	42.6	42.2	42.5	43.0	42.7 ± 0.7	
Stellite 6	**4**	0	41.1	44.7	44.2	43.3	44.2	46.2	45.6	43.5	44.2 ± 1.6	-1.6 ± 1.6
		15	40.2	41.3	42.3	43.0	42.4	45.2	44.0	43.6	42.6 ± 1.6	
Stellite 6	**5**	0	43.3	41.9	45.2	44.0	44.0	45.6	43.2	43.4	43.9 ± 1.2	-1.2 ± 1.2
		30	40.2	41.8	43.5	43.8	43.1	43.2	43.1	42.5	42.7 ± 1.2	
Stellite 6	**6**	0	43.5	42.8	44.3	47.0	45.2	47.0	46.0	44.5	45.1 ± 1.6	1.0 ± 1.7
		60	43.0	41.1	42.3	46.0	45.3	46.1	45.3	44.0	44.2 ± 1.8	
Stellite 6	**7**	0	44.0	44.2	43.2	41.3	44.0	46.5	44.6	46.2	44.0 ± 1.6	-0.2 ± 1.4
		960	41.8	42.4	44.0	44.3	45.0	44.5	44.3	42.6	43.8 ± 1.2	

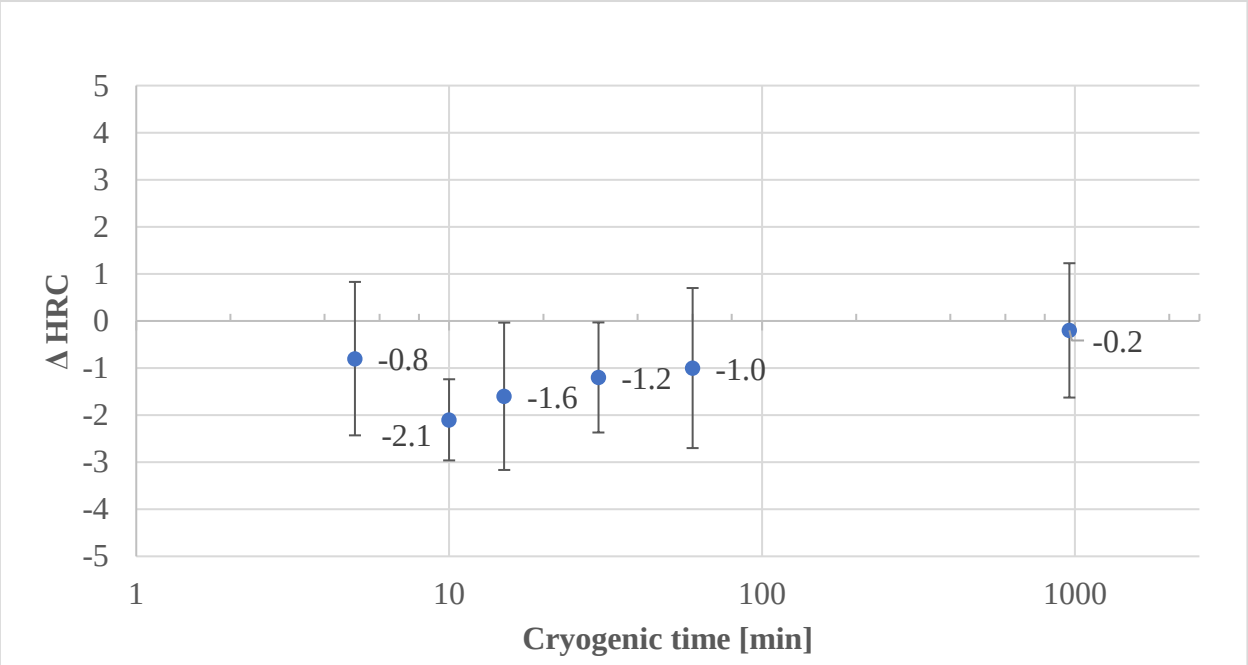

Fig. 44 Graph of the change in the hardness of Stellite 6 depending on the length of exposure to liquid nitrogen

Tab. 37 Measurements of Stellite 12 hardness under the exposure to liquid nitrogen

		Hardness	HRC								Average hardness	Average diference hardness
			Position on seat									
Material	**Sample**	**Time in cyro [min]**	**0°**	**45°**	**90°**	**135°**	**180°**	**225°**	**270°**	**315°**		
Stellite 12	**1**	0	50.2	51.0	50.3	51.1	51.3	50.0	50.9	51.0	50.7 ± 0.5	0.0
Stellite 12	**2**	0	49.5	49.6	50.0	50.5	50.9	50.8	50.3	49.0	50.0 ± 0.7	-1.1 ± 1.2
		5	47.0	46.2	49.2	49.0	50.0	50.5	50.2	48.9	48.9 ± 1.5	
Stellite 12	**3**	0	51.0	50.2	50.8	51.2	50.0	50.3	51.0	51.2	50.7 ± 0.5	-2.7 ± 0.6
		10	49.2	48.0	49.9	47.5	49.0	49.5	49.0	49.0	48.0 ± 0.8	
Stellite 12	**4**	0	48.2	51.3	50.0	50.2	50.5	49.9	50.4	51.0	50.2 ± 0.9	-2.8 ± 1.1
		15	46.2	46.4	46.5	49.7	47.5	48.5	46.2	48.5	47.4 ± 1.3	
Stellite 12	**5**	0	50.0	50.2	50.0	51.2	51.8	51.0	51.0	48.0	50.4 ± 1.2	-1.3 ± 0.9
		30	48.4	49.0	49.9	49.2	49.6	49.0	49.0	48.4	49.1 ± 0.5	
Stellite 12	**6**	0	50.0	50.1	51.2	51.0	51.5	52.0	51.5	51.2	51.1 ± 0.7	-0.4 ± 0.9
		60	49.1	50	50.5	51.2	52.3	51.3	51.2	50.1	50.7 ± 1.0	
Stellite 12	**7**	0	48.0	50.6	50.2	51.0	50.5	50.5	49.5	50.0	50.0 ± 0.9	-0.9 ± 0.8
		960	47.9	49.5	49.3	50.0	49.0	49.8	49.0	48.1	49.1 ± 0.8	

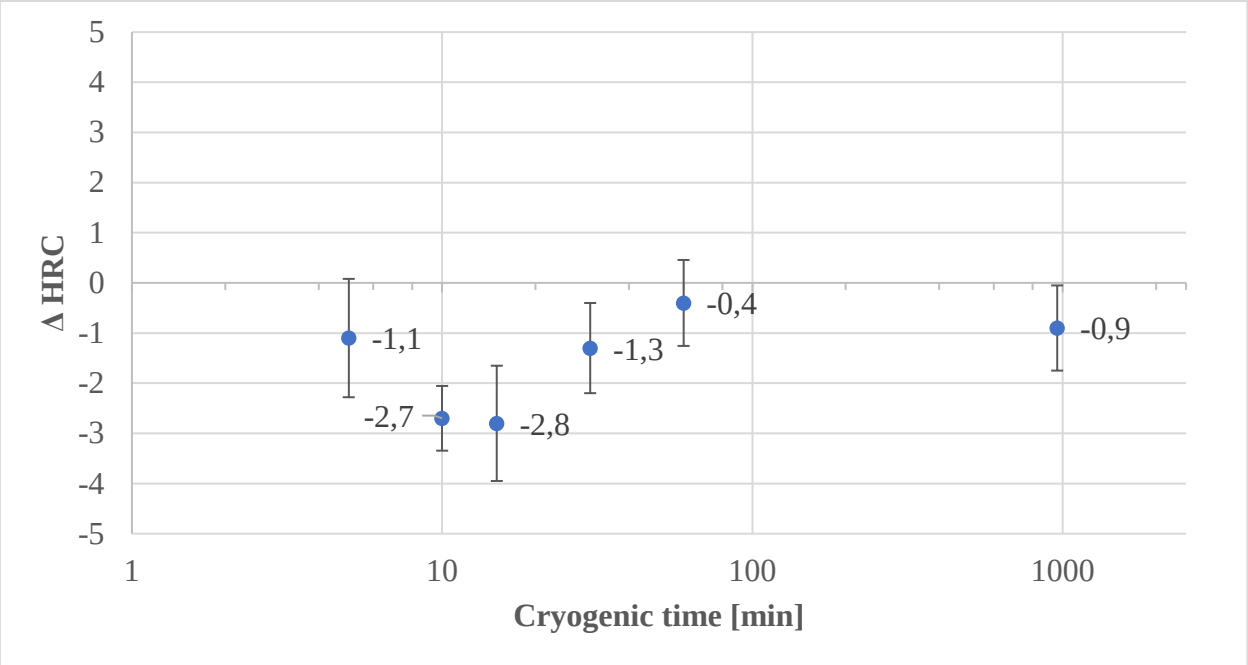

Fig. 45 Graph of the change in the hardness of Stellite 12 depending on the length of exposure to liquid nitrogen

7.5.5 Discussion of measured data

From the measured values for Stellite 6, it can be concluded:

- All exposure times to cryogenic temperatures resulted in a decrease in hardness.
- The smallest impact on hardness was exhibited by the sample with a freezing time of 960 minutes.
- The highest impact on hardness was exhibited by the sample with a freezing time of 10 minutes.

From the measured values for Stellite 12, it can be concluded:

- All exposure times to cryogenic temperatures resulted in a decrease in hardness.
- The smallest impact on hardness was exhibited by the sample with a freezing time of 60 minutes.
- The highest impact on hardness was exhibited by the sample with a freezing time of 15 minutes.

Yang [135] observes that cryogenic processing leads to microstructure refinement in the surface layer and a decrease in residual stress. Furthermore, the results pertaining to

microstructural changes suggested that optical microscopy might not be sufficient for accurately characterizing microstructures resulting from different freezing conditions.

From the measured values, it is evident that it is necessary to regulate the technological freezing time of the valve seat, as there is a possibility that the freezing time could correspond to the greatest decrease in the hardness of the valve seat material. Due to this fact, TEDOM Company has implemented a technological guideline for pressing valve seats into the cylinder head, which defines an optimal freezing time for the intake and exhaust valve seats of 5 min ± 1 min. This procedure can help increase the lifespan of cylinder heads and assist in examining the influence of valve seat freezing, allowing the elimination of the variable effect of different freezing durations.

Differences in Hardness are, in some cases, smaller than the measurement error. The experiment demonstrated trends in the material's hardness changes. As part of further research, we recommend focusing on a statistically significant sample.

7.6 Influence of cryogenic temperature on the Young´s modulus of Stellite 6 and Stellite 12

In the previous experiment, we focused on studying the hardness changes of Stellite 6 and Stellite 12 materials in relation to the duration of exposure to liquid nitrogen. This experiment objective was to investigate the influence of the exposure time to liquid nitrogen on the theoretical Young´s modulus of Stellite 6 and Stellite 12 materials.

For testing mechanical properties, we employed NDT methods, as it was not feasible from a financial standpoint to prepare a sufficient number of samples to test multiple variations of cryogenic exposure times on mechanical characteristics.

7.6.1 Objectives of the experiment

As part of the experiment, it was planned to research:

1. Non-destructively calculate the theoretical Young´s modulus E_{0T} for the material Stellite 6 and Stellite 12, before and after exposure to liquid nitrogen.

7.6.2 Measurement methodology

The measurements were carried out on the same samples as the hardness measurements in the previous experiment. The speed of sound V_L was determined using an ultrasonic flaw detector DIO 562 (Starmans s.r.o., Prague) with a dual probe of 10 mm diameter and 5 MHz frequency for L up to 100 mm.

To measure the theoretical Young´s modulus, it was necessary to calculate the constant K (Equation 17). Test samples, shown in Fig. 46, were used to measure the required physical quantities for the calculation of the constant. Theoretical Young´s modulus E_{0T} was calculated using (Equation 13). Hardness was measured in accordance with EN ISO 6508-1 [45], using the HRC method with a BRIRO VA hardness tester.

7.6.3 Material for testing

The measurements were conducted on the same samples that were used to assess the influence of cryogenic temperatures on hardness. This means that the samples were exposed to cryogenic temperatures for 5, 10, 15, 30, 60, and 960 minutes. The freezing process was conducted in a manner that prevented thermal shock to the material. The valve seats were gradually immersed in liquid nitrogen for short periods of time, and the duration of exposure was gradually increased.

Fig. 46 Testing cones made from Stellite 6 and 12

7.6.4 Measured data

Tab. 38 and 39 shows the calculated values of Young´s modulus. Further, the tables show changes in mechanical and acoustic properties due to the initial state without the action of liquid nitrogen. Fig. 47 and 48 show graphical representation of change in Young´s modulus and speed of sound depending on cryo time.

Tab. 38 Table of calculated changes in the mechanical and acoustic properties of Stellite 6

Material	Sample	Time in cryo [min]	The average speed of sound V_L in the sample [$m.s^{-1}$]	Changing the average speed of sound [$m.s^{-1}$]	Change Young´s modulus E_{0T} [GPa]
Stellite 6	**1**	0	6014.5 ± 32.8	-	206.1
Stellite 6	**2**	0	6043.9 ± 34.5	+ 28.6 ± 45.8	+ 1.9
		5	6072.4 ± 57.1		
Stellite 6	**3**	0	6054.9 ± 17.9	+ 221.2 ± 18.3	+ 15.2
		10	6276.1 ± 18.6		
Stellite 6	**4**	0	6057.6 ± 13.8	+ 241.3 ± 14.1	+ 25.3
		15	6298.9 ± 14.3		
Stellite 6	**5**	0	6021.9 ± 46.6	+ 220.0 ± 47.5	+ 15.1
		30	6241.9 ± 48.3		
Stellite 6	**6**	0	6057.6 ± 5.5	+ 218.3 ±7.6	+ 15.0
		60	6275.9 ± 9.6		
Stellite 6	**7**	0	6019.2 ± 66.8	+ 187.0 ± 72.7	+ 12.8
		960	6206.2 ± 78.5		

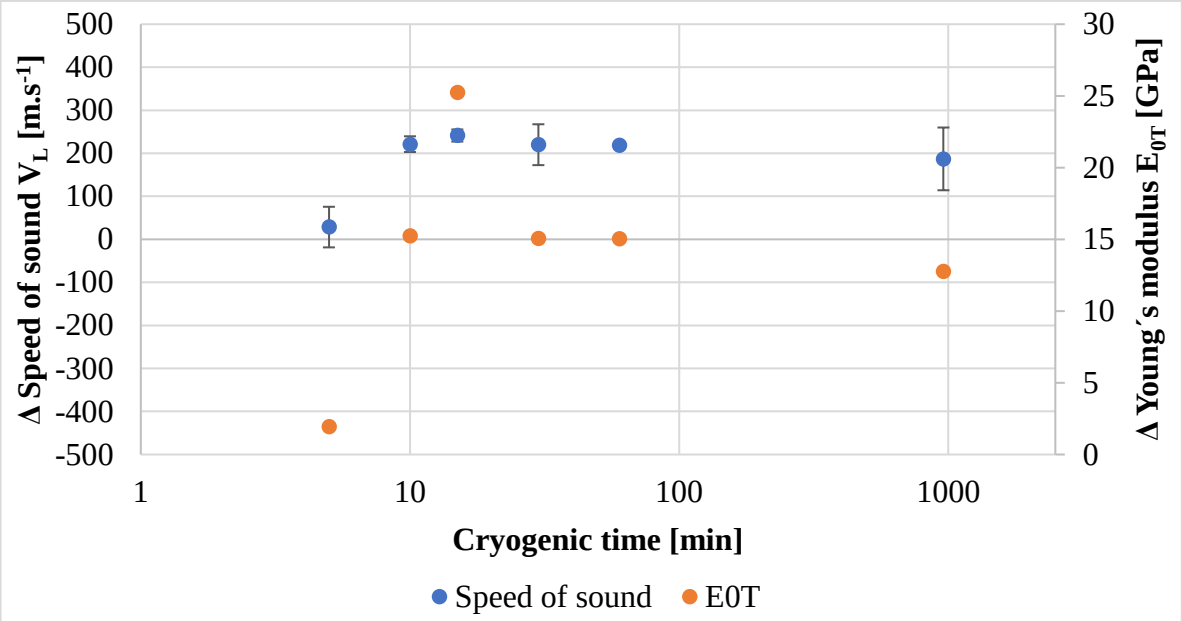

Fig. 47 Graph of the change in speed of sound and Young´s modulus for Stellite 6 depending on the length of exposure in liquid nitrogen

Tab. 39 Table of calculated changes in the mechanical and acoustic properties of Stellite 12

Material	Sample	Time in cryo [min]	The average speed of sound in the sample [m.s^{-1}]	Changing the average speed of sound [m.s^{-1}]	Change Young´s modulus E_{0T} [GPa]
Stellite 12	**1**	0	6349.8 ± 9.6	-	208.2
Stellite 12	**2**	0	6366.1 ± 14.8	-104.0 ± 17.2	-7.3
		5	6262.1 ± 19.5		
Stellite 12	**3**	0	6321.3 ± 4.6	-78.3 ± 16.5	-5.5
		10	6243.1 ± 28.3		
Stellite 12	**4**	0	6368.0 ± 9.3	-56.7 ± 16.5	-4.0
		15	6311.3 ± 23.6		
Stellite 12	**5**	0	6381.3 ± 7.1	-104.2 ± 19.2	-7.4
		30	6277.1 ± 31.2		
Stellite 12	**6**	0	6362.7 ± 8.4	-133.0 ± 10.4	-9.4
		60	6229.7 ± 12.3		
Stellite 12	**7**	0	6375.6 ± 11.4	-85.9 ± 17.6	-6.1
		960	6289.8 ± 23.8		

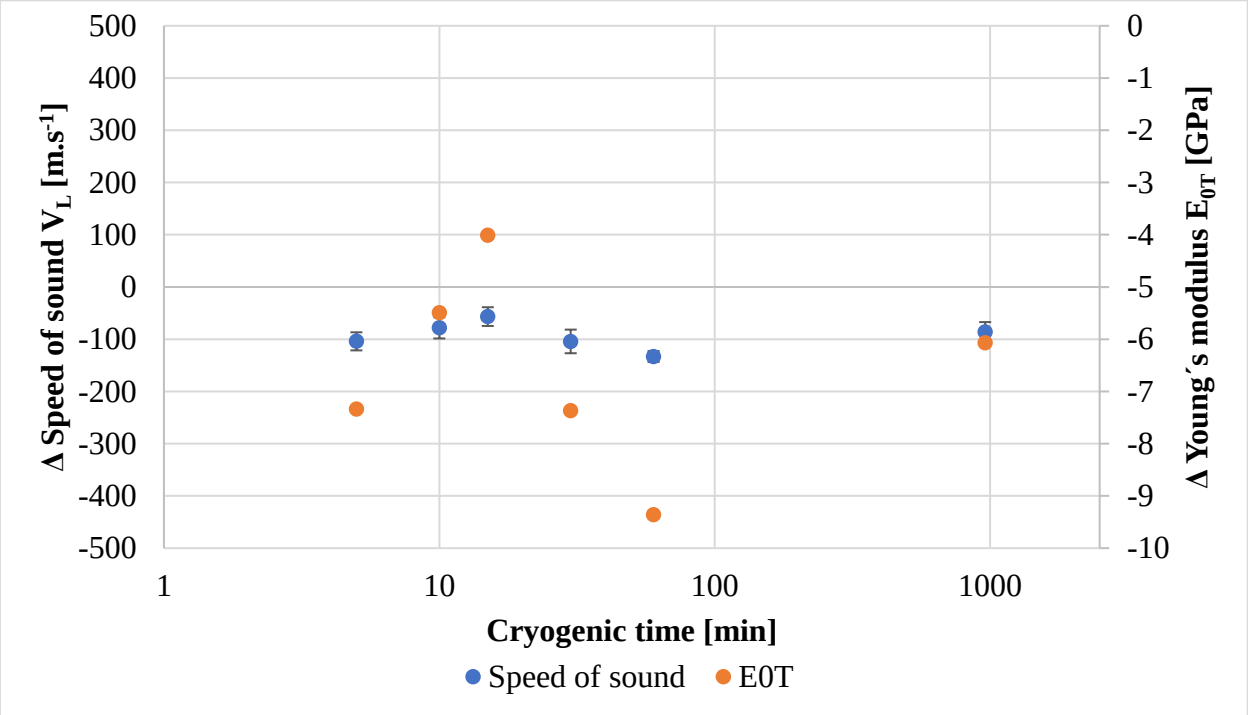

Fig. 48 Graph of the change in speed of sound and Young´s modulusfor Stellite 12 depending on the length of exposure in liquid nitrogen

7.6.5 Discussion of measured data

From measured values, it was possible to state regarding Stellite 6:

- All freezing times exhibited a positive impact on the Young's modulus. The lowest increase was observed in samples frozen for 5 minutes, while the highest increase was recorded in samples frozen for 15 minutes.

- During the 15-minute freezing process, the speed of sound increased by 4%, and the calculated theoretical elastic modulus increased by 12.3%. (From 206.1 GPa to 231.4 GPa)

From measured values it was possible to state regarding Stellite 12:

- All freezing durations exhibited a negative impact on the theoretical elastic modulus. The most significant decrease was observed in the sample subjected to 60 minutes of freezing, while the smallest decrease occurred in the sample frozen for 15 minutes.

- During the 60-minute freezing process, the speed of sound decreased by 2.1%, and the theoretical elastic modulus decreased by 4.5%. (From 208.2 GPa to 198.8 GPa)

Theoretical values of the Young´s modulus need to be verified within the scope of further research on the influence of cryogenic temperatures on the mechanical properties of cobalt alloys. The conducted analysis was not supported by a project that would provide the resources for us to examine in more detail, and on a statistically significant sample, the impact of cryogenic temperatures on the elasticity modulus of the material.

7.7 Influence of cryogenic temperature on the Magnetism of Stellite 6 and Stellite 12

This experiment focuses on studying the changes in magnetism of Stellite 6 and Stellite 12 materials in cryogenic environments. Magnetization measurements allow us to quantify the response of materials to an applied magnetic field, by subjecting Stellite 6 and Stellite 12 samples to varying magnetic fields and measuring their resulting magnetization.

The findings from these magnetization measurements will contribute to a deeper understanding of the magnetic properties and behavior of Stellite 6 and Stellite 12 alloys. This knowledge enhances our ability to optimize their magnetic performance for specific applications, such as in magnetic sensors, motors, or other magnetically sensitive systems. Additionally, it lays

the foundation for further investigations into the underlying mechanisms governing the magnetic response of these alloys, supporting the development of advanced cobalt-based materials with tailored magnetic properties.

7.7.1 Objectives of the experiment

As part of the experiment, it was planned to research:

1. Measure the impact of cryogenic processing on the magnetic properties of Stellite 6 and Stellite 12 materials using the magnetic spot method.

7.7.2 Measurement methodology

The intensity of residual magnetic field M was measured using the magnetic spot method with DOMENA B3 (TU Liberec) ELKOSO s.r.o., Brno instruments (set at 3rd level of magnetization). Fig. 49 is shown the DOMENA B3 measurement device used for samples testing.

Fig. 49 Domena B3

7.7.3 Material for testing

The measurements were conducted on the same castings that were used to assess the influence of cryogenic temperatures on hardness. This means that the castings were exposed to cryogenic temperatures for 5, 10, 15, 30, 60, and 960 minutes. The freezing process was conducted in a manner that prevented thermal shock to the material. The valve seats were gradually immersed in liquid nitrogen for short periods of time, and the duration of exposure gradually increased.

7.7.4 Measured data

In Tab. 40 and 41 is shown the intensity of the residual magnetic field in Stellite 6 and Stellite 12 materials before and after cryogenic processing. These tables provide a visual representation of the changes in the magnetic properties of the alloys resulting from the cryogenic treatment. Fig. 50 and Fig. 51 demonstrate the graphical representation of the changes in magnetism based on the duration of exposure to liquid nitrogen, without any time delay during the natural warming process. These figures provide important insights into the thermal effects on the magnetic properties of the materials and serve as a foundation for further research in the field of magnetism and cryogenic materials.

Tab. 40 The influence of cryogenic treatment on the magnetism values of Stellite 6 material.

Material	**Sample**	**Time in cryo [min]**	**Average magnetism [A/min]**	**The average change in magnetism [A/min]**
Stellite 6	**1**	0	22.8 ± 6.0	0
Stellite 6	**2**	0	22.0 ± 3.6	-8.3 ±3.7
		5	13.7 ± 3.7	
Stellite 6	**3**	0	20.4 ± 1.2	-2.5 ± 4.3
		10	17.9 ± 7.3	
Stellite 6	**4**	0	20.1 ± 0.9	+14.5 ± 2.3
		15	34.6 ± 3.6	
Stellite 6	**5**	0	21.6 ± 2.2	+10.1 ± 2.9
		30	31.5 ± 3.5	
Stellite 6	**6**	0	21.4 ± 2.8	+12.8 ± 4.4
		60	34.2 ± 5.9	
Stellite 6	**7**	0	21.5 ± 1.7	-13.8 ± 2.5
		960	7.6 ± 3.2	

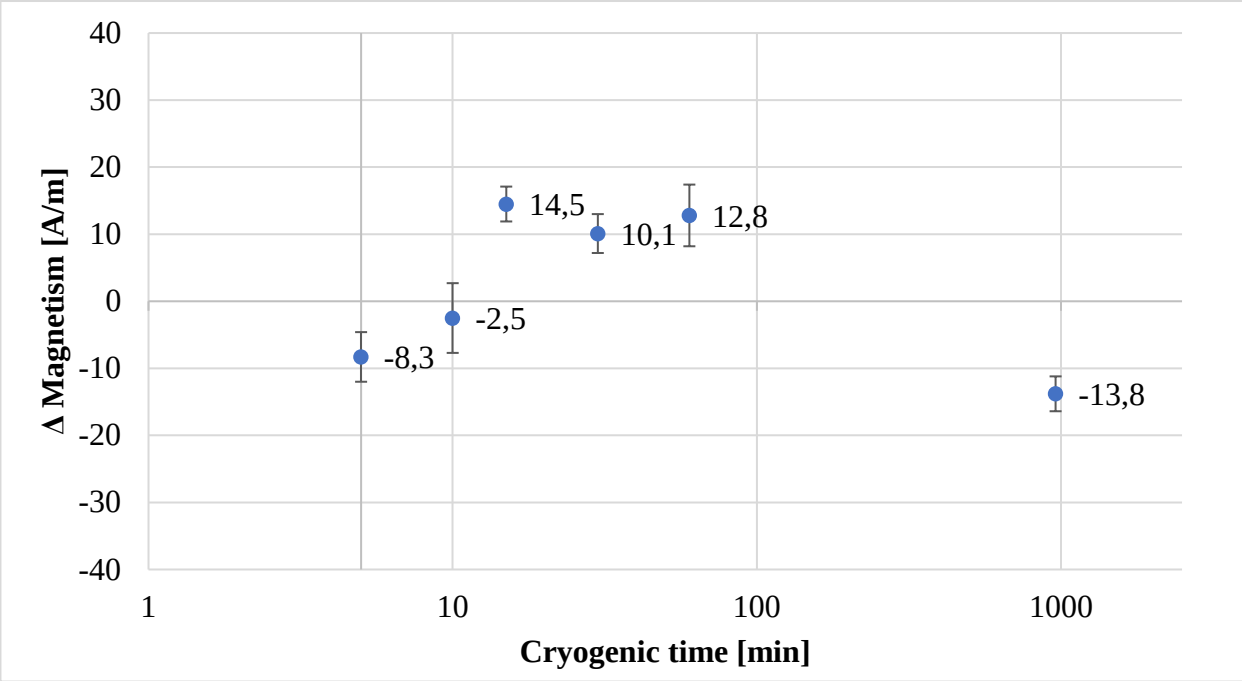

Fig. 50 Change in the magnetism of Stellite 6 depending on the time of exposure in liquid nitrogen

Tab. 41 The influence of cryogenic treatment on the magnetism values of Stellite 12 material.

Material	Sample	Time in cryo [min]	Average magnetism [A/min]	Average change in magnetism [A/min]
Stellite 12	**1**	0	29.7 ± 3.4	0
Stellite 12	**2**	0	28.2 ± 1.8	-7.5 ± 2.9
		5	20.7 ± 3.6	
Stellite 12	**3**	0	29.2 ± 2.5	-3.6 ± 5.0
		10	25.8 ± 6.6	
Stellite 12	**4**	0	29.0 ± 2.3	-13.0 ± 2.4
		15	16.0 ± 2.4	
Stellite 12	**5**	0	30.9 ± 1.8	-13.8 ± 1.9
		30	17.1 ± 1.9	
Stellite 12	**6**	0	30.4 ± 1.7	-18.4 ± 1.7
		60	12.0 ± 1.7	
Stellite 12	**7**	0	30.5 ± 4.2	-26.0 ± 3.3
		960	4.5 ± 2.1	

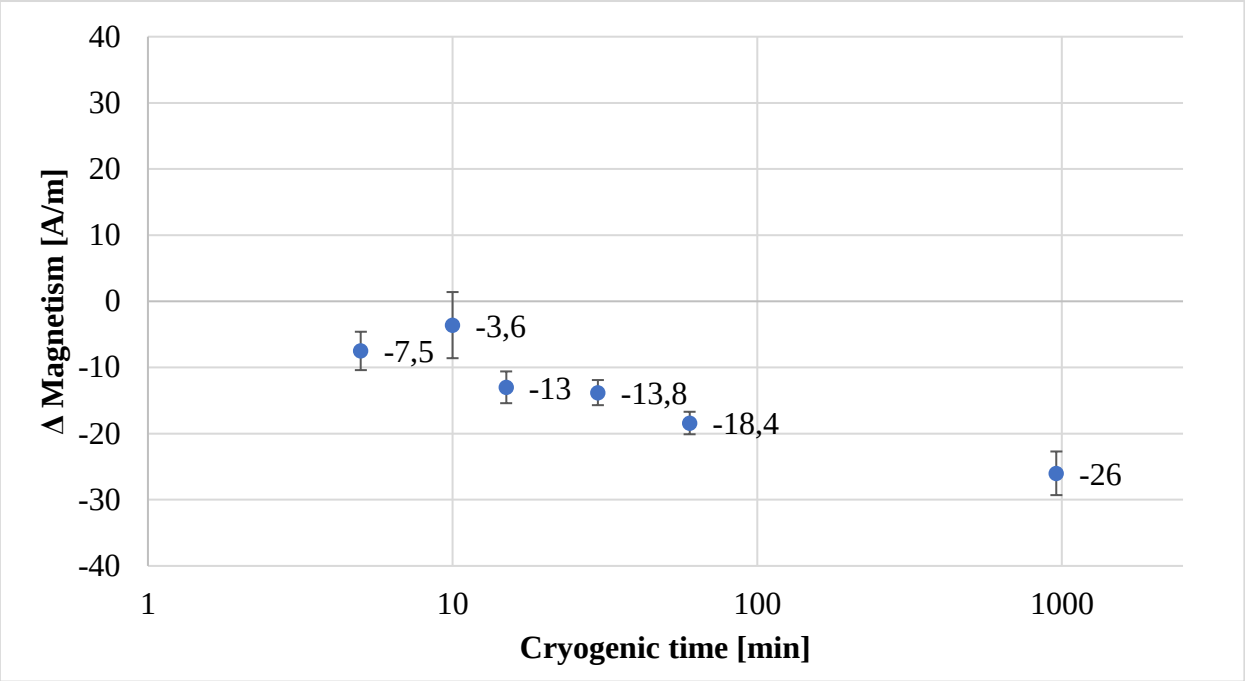

Fig. 51 Change in the magnetism of Stellite 12 depending on the time of exposure in liquid nitrogen

7.7.5 Discussion of measured data

From measured values, it was possible to state regarding Stellite 6:

- The freezing times of 5, 10, and 960 minutes showed a reduction in magnetism. The largest decrease in magnetism was observed during the 960-minute freezing time, where we measured a decrease of 13.8 A/m compared to the original value, which is a decrease of about 64.2%.

- Freezing times of 10, 15, 30, and 60 minutes exhibited an increase in magnetism. The highest value was recorded for the 15-minute freezing time, where we measured increased magnetism about 72.1%.

From measured values, it was possible to state regarding Stellite 12:

- Across all freezing times, we observed a decrease in magnetism. The largest decrease was recorded for the freezing time of 960 minutes, where we measured a reduction of 26 A/m, corresponding to a decrease of 85.3 % in magnetism value. The lowest decrease in magnetism was observed during the freezing time of 10 minutes, where we measured a reduction of 3.6 A/m, which is about 11.6% less than the original value.

One possible reason for the fluctuation in magnetism is the change in the material's structure. Cryogenic temperatures can lead to a modification in the crystal structure of cobalt alloy, thereby affecting the arrangement of magnetic domains. These changes can result in a reduction of the magnetic moment in the material and consequently lower the overall magnetization.

Another factor is the so-called spin-flip scattering phenomenon. The research conducted by Kudrnovský, Drchal, and Turek (2017) [94], in the article titled "Spin-Flip Scattering in Magnetic Materials." shed light on the phenomenon of spin-flip scattering in magnetic materials. At low temperatures, collisions can occur between the magnetic moments of electrons and the crystal lattice. These collisions can transfer the moment from the magnetic moments to the crystal lattice, thus reducing the overall magnetic moment of the material.

To thoroughly investigate changes influenced by cryogenic temperatures, we recommend conducting further research using advanced methods of diagnosing phase transitions in materials. This will enable us to gain a deeper understanding of the alterations and enhancements resulting from these temperature variations.

7.8 Tribological experiment

This experiment was focused on the research conducted on overlay materials used on the valves of internal gas combustion engines, existing friction pairs valve - valve seat from the world´s biggest producer of gas combustion engines and potential valve seat materials made from ADI 280, ADI 280 N_5 and Q - Nitro materials. The experiment evaluates the coefficient of friction as one of the parameters for assessing the performance and durability of these pairs. As an additional parameter, experiment evaluates the width, depth, and material loss of the test specimen. By analyzing the friction behavior, we can identify potential areas for improvement and optimize the material selection, surface treatment. and lubrication techniques.

The tribological experiment was divided into three phases:

Phase 1 was focused on investigating the tribological properties of valve overlay materials. In this phase, valves from global manufacturers of gas combustion engines were examined. The selected valves for these tests were those commonly used in combustion engines for alternative fuels. We included an intake valve from TEDOM TRW in the tests. This valve has been historically used by the LIAZ company. The valve is made of a nickel superalloy called Nimonic 80A, which is commonly used in small automotive engines due to its

excellent mechanical and corrosion properties. We also included an exhaust valve from TEDOM after the operation (8000 engine hours) to investigate the influence of thermal loading and operation on the tribological properties. In this phase, we used standardized tribological pins as test counterparts.

Phase 2 was focused on evaluating the tribological properties of cast irons ADI 280, ADI 280 Nitro, and Q - Nitro. Additionally, in the second phase, we measured the tribological properties of Stellite 6 and Stellite 12, which underwent cryogenic processing. As the friction pair of materials, we used an intake valve from TEDOM with overlay material P37S for ADI 280, ADI 280 Nitro, and Q-Nitro. We chose this friction pair because the investigated cast iron materials were intended for use in valve seat applications. For the Stellite 6 material, we used an intake valve from TEDOM. The choice of these friction pairs was made in order to examine realistic material combinations. For the Stellite 12 material, we used an exhaust valve from TEDOM with overlay material P37S. The choice of these three pairs was made to examine realistic material combinations.

In **Phase 3**, we examined real-life tribological friction pairs of valve and valve seats from global manufacturers of combustion engines. We also included an exhaust valve from TEDOM after the operation (8000 engine hours) to investigate the influence of thermal loading and operation on the tribological properties. Additionally, we included an intake valve from TEDOM TRW in the tests. This valve was historically used in LIAZ engines and featured a valve head made of Nimonic 80A material. The valve does not have hard-facing. Therefore, we wanted to measure the tribological behavior of the Nimonic 80A and Stellite 6 pair, simulating the scenario if this valve were used in today's TEDOM engine.

7.8.1 Objectives of the experiment

As part of the experiment, it was planned to research:

1. Measure and evaluate the coefficient of friction of valve overlay materials and select the overlay material that exhibits the lowest coefficient of friction.
2. Measure and evaluate the coefficients of friction of the ADI 280, ADI 280 N_5 and Q - Nitro materials, and determine the material with the lowest coefficient of friction.
3. Compare the materials ADI 280, ADI 280 N_5, and Q - Nitro with real tribological friction pairs and assess their potential for use as intake valve seats in combustion engines from a tribological perspective.

4. Measure and evaluate the influence of cryogenic temperatures on the coefficient of friction for Stellite 6 and Stellite 12 materials.

The findings from this tribological experiment section will contribute to the understanding of friction and wear characteristics in valve - valve seat systems. Moreover, they will provide insights into the potential of alternative materials and surface treatments for improving the performance and cost-effectiveness of friction pairs.

7.8.2 Measurement methodology

For the tribological experiment was used method “Pin-on-Disc” described in more detail in Chapter 5 of this thesis. The tribological properties of the surface are evaluated using a Tribometer for both dry and liquid environments from Anton Paar company.

The chosen friction pair consists of the examined valve head and the corresponding counterpart. Both parts are in contact during the tribological experiment. The experiment was carried out at room temperature (22 °C – 24 °C with 30 – 60 % relative humidity) without any lubricant. The examined valve head is clamped in the holder Fig. 52 where on the left side is shown a standard TEDOM intake valve, in the middle is a standard TEDOM exhaust valve, and on the right side is an EM-KU manufacturer exhaust valve. The roller is fixed in a holder above the table, without the possibility of rotation and performs sliding friction on the examined surface of the valve. The chair rotates at a speed of 60 rpm, the applied load during the experiment is 10 N, and the length of the experiment was 3000 cycles for phase 1 and 1500 cycles for phase 2 and phase 3. This difference was chosen because for phases 2 and 3, the tested samples were glued to the standardized testing cylinders using Loctite EA 3421 epoxy adhesive. We aimed to eliminate the influence of gradual joint loosening, which could lead to inaccuracies in the measurements.

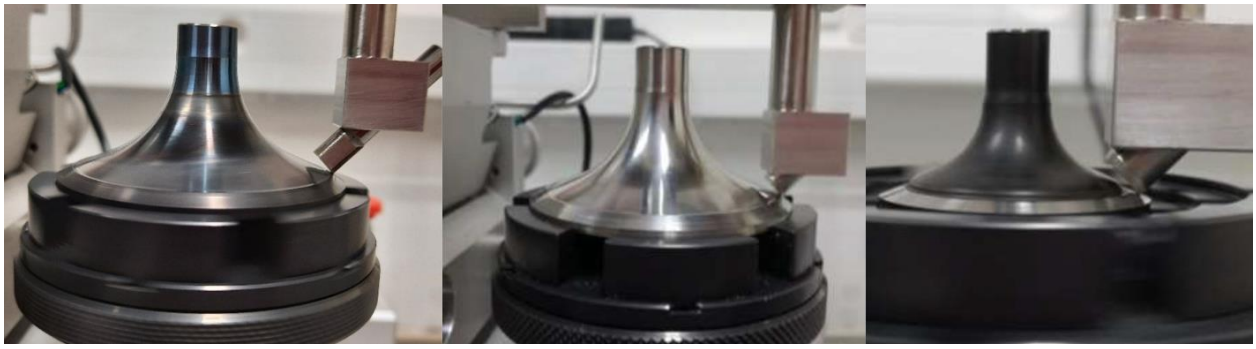

Fig. 52 Examples of a tribological experiment

During the measurement, the working surfaces were in constant contact and under constant load with the counterpart. Contact between the valve head and the counterpart was always on the sealing cone on the valve head, so that the contact corresponded as maximum as possible to real operation.

Evaluation of the amount of wear on the examined surfaces (valve surfaces) was performed on a SENSOFAR S Neox confocal microscope. It is a microscope that enables non-contact scanning of surfaces using confocal and interferometric methods. A Leica DVM6 digital microscope was used to assess pin wear.

In order to analyze the chemical composition of the valve seats used as counterparts, we used the spectrometer BAS DELTA PROFESSIONAL.

7.8.3 Material for testing

Due to copyright law, we will not mention the names of the engine manufacturers in this work. Instead, we will use code designations to maintain anonymity. We will use the abbreviation Engine Manufacturer - EM and alphanumeric code designations.

In the first phase of the testing, we tested the valve heads of various engine producers with a standardized counterpart. As a counterpart material was used a standardized roller from REDHILL company. These rollers were made from ČSN 14 109 steel with a hardness of 60-62 HRC. They were in the shape of cylindrical rollers with dimensions of 6 × 24 mm according to ISO 3290. The design of the counterpart is illustrated in Fig. 53. The specific friction pairs used in the first phase are shown in Tab. 42. Before the experiment were modified the valves by removing the valve stems using an EDM machine. This modification was necessary to fit the valves into the tribometer. The wire cutter was chosen to avoid any thermal influence on the samples.

Fig. 53 Normalized counterpart used as a "PIN"

Tab. 42 Friction couples tested in the First loop of tribological testing

Disc	Pin	Test No.
TEDOM – Exhaust valve *	ČSN 14109	1.
TEDOM – Exhaust valve **	ČSN 14109	2.
TEDOM – Exhaust valve – After operation*	ČSN 14109	3.
TEDOM – Intake valve *	ČSN 14109	4.
TEDOM – Intake valve**	ČSN 14109	5.
EM - SC – Intake valve	ČSN 14109	6.
EM - SC – Exhaust valve	ČSN 14109	7.
EM - LI – Intake valve	ČSN 14109	8.
EM - LI – Exhaust valve	ČSN 14109	9.
EM - SCH – Intake valve	ČSN 14109	10.
EM SCH – Exhaust valve	ČSN 14109	11.
EM KU – Intake valve	ČSN 14109	12.
EM MA – Intake valve	ČSN 14109	13.
EM MA – Exhaust valve	ČSN 14109	14.

* Manufacturer Mahle; **Manufacturer TRW

In the second phase of testing was used as "Disc" intake and exhaust valve TEDOM. Both valves are equipped with a P37S hard facing weld. The chemical composition of this hardfacing is shown in Tab. 3. Before the experiment were modified the valves by removing the valve stems using an EDM machine. This modification was necessary to fit the valves into the tribometer. The wire cutter was chosen to avoid any thermal influence on the samples. As a "PIN" were used cylinders prepared from real valve seats. In Tab. 39 are shown the material variants and their heat treatments. On Fig. 54 on the left side, there is depicted a CAD model of the valve seat with

extracted cylinders. This model was used for EDM machine to extract rollers. On the right side of the image, there is a real valve seat with extracted rollers.

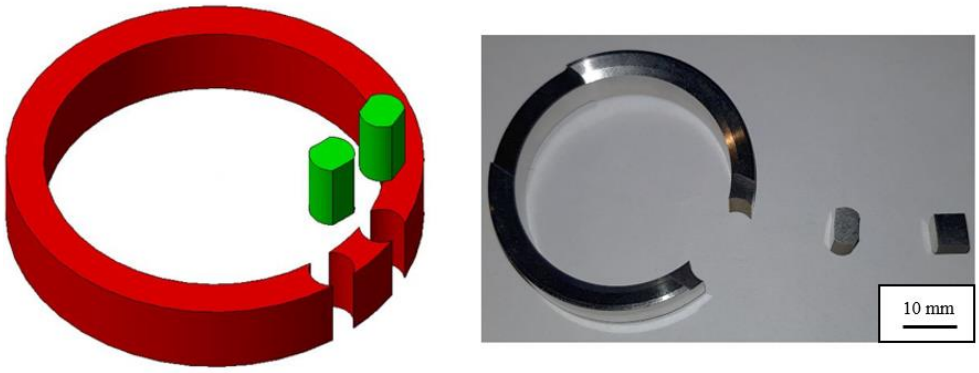

Fig. 54 Prepared cylinders from real valve seat used as a "PIN"

The samples of ADI 280, ADI 280 N_5, and Q-Nitro cast irons, used for tribological tests, were extracted from the specimens that were previously examined for their physical properties. We used ADI 280 N_5 for tribological measurements due to its highest hardness among the frozen samples ADI 280. Similarly, samples of Stellite 6 and Stellite 12 with varying freezing times were obtained from the test material used in the previous tests.

Tab. 43 Friction couples tested in the Second loop of tribological testing

Disc	**Pin**	**Test No.**
TEDOM – Intake valve	ADI 280	15.
TEDOM – Intake valve	ADI 280 N_5	16.
TEDOM – Intake valve	Q-Nitro	17.
TEDOM – Intake valve	Stellite 6 -Without freezing	18.
TEDOM – Intake valve	Stellite 6 – frozen 5 min	19.
TEDOM – Intake valve	Stellite 6 – frozen 10 min	20.
TEDOM – Intake valve	Stellite 6 – frozen 15 min	21.
TEDOM – Intake valve	Stellite 6 – frozen 30 min	22.
TEDOM – Intake valve	Stellite 6 – frozen 60 min	23.
TEDOM – Exhaust valve	Stellite 12 – Without freezing	24.
TEDOM – Exhaust valve	Stellite 12 – frozen 5 min	25.
TEDOM – Exhaust valve	Stellite 12 – frozen 10 min	26.
TEDOM – Exhaust valve	Stellite 12 – frozen 15 min	27.
TEDOM – Exhaust valve	Stellite 12 – frozen 30 min	28.
TEDOM – Exhaust valve	Stellite 12 – frozen 60 min	29.

As part of the first phase, we tested intake valves and exhaust valve TEDOM from different manufacturers to identify potential differences between suppliers. Both TRW valves have the

valve head made of the Nimonic 80A superalloy. In the test, we also included an exhaust valve TEDOM after 8000 engine hours to observe if the coefficient of friction changes over time. These valves and their valve seats are marked in Tab. 44.

The third phase of the testing was used as “Disc“ intake and exhaust valve heads from world manufacturers of gas combustion engines. Each valve in this test is intended for the gas version of the combustion engine. The chemical composition of the valves is depicted in Tab. 45. Before the experiment, the valves were modified by removing the valve stems using an EDM machine. This modification was necessary to fit the valves into the tribometer. The wire cutter was chosen to avoid any thermal influence on the samples. As a “PIN“ cylinders were used prepared from real valve seats. These prepared rollers were glued to standard test cylinders from company REDHILL using Loctite EA 3421 epoxy adhesive. The chemical composition of the valve seats used in testing is depicted in Tab. 46.

Tab. 44 Friction couples tested in the Third loop of tribological testing

Disc	**Pin**	**Test No.**
TEDOM – Exhaust valve – After operation	Exhaust valve seat TEDOM	30.
TEDOM – Intake valve TRW	Intake valve seat TEDOM	31.
EM - SC – Intake valve	Intake valve seat EM - SC	32.
EM - SC – Exhaust valve	Exhaust valve seat EM - SC	33.
EM - LI – Intake valve	Intake valve seat EM - LI	34.
EM - LI – Exhaust valve	Exhaust valve seat EM - LI	35.
EM - SCH – Intake valve	Intake valve seat EM - SCH	36.
EM - SCH – Exhaust valve	Exhaust valve seat EM - SCH	37.
EM - KU – Exhaust valve	Exhaust valve seat EM - KU	38.
EM - MA – Intake valve	Intake valve seat EM - MA	39.
EM - MA – Exhaust valve	Exhaust valve seat EM - MA	40.

Tab. 45 Chemical composition of valve head used in testing as “Disc“

Engine manufacturer	Valve	Part of valve	Chemical composition [%]												
			Cr	Ni	Mo	Cu	Fe	Mn	Co	Nb	Ti	V	W	Al	Si
MA	Exhaust	Hard facing	30.2	21.4	0.1	-	1.0	-	40.7	-	0.7	-	5.9	-	-
		Valve head	19.0	76.1	0.1	-	0.7	-	-	0.1	2.5	-	-	1.5	-
	Intake	Hard facing	27.1	9.6	3.8	-	55.1	3.7	-	0.7	-	-	-	-	-
		Valve head	20.9	3.7	0.2	0.1	62.8	9.1	-	2.0	-	0.1	0.7	-	-
LI	Exhaust	Hard facing	25.9	20.8	0.2	-	18.1	3.2	22.1	0.6	-	-	9.1	-	-
		Valve head	20.9	3.7	0.2	0.1	62.8	9.1	-	2.0	-	0.1	0.7	-	-
	Intake	Hard facing	24.8	20.4	0.1	-	21.4	-	23.5	-	-	-	9.9	-	-
		Valve head	8.7	0.2	0.1	0.0	87.0	0.5	-	-	-	0.1	-	-	3.1
SC	Exhaust	Hard facing	27.4	14.4	3.6	-	51.2	2.9	-	0.5	-	-	-	-	-
		Valve head	21.9	3.7	0.2	0.1	62.1	9.2	1.9	-	-	0.1	0.9	-	-
	Intake	Hard facing	24.8	44.6	0.1	-	1.8	-	19.9	-	1.2	7.6	-	-	-
		Valve head	19.9	74.0	-	-	3.4	-	-	-	2.7	-	-	-	-
SCH	Exhaust	Hard facing	22.0	3.6	0.1	-	61.9	8.8	-	2.1	-	-	0.9	-	-
		Valve head	21.7	3.8	0.1	0.2	62.2	9.0	-	2.1	-	0.1	0.9	-	-
	Intake	Hard facing	21.7	3.6	0.2	-	62.8	8.3	-	2.2	-	-	0.8	-	-
		Valve head	21.5	3.7	0.2	0.2	62.4	8.8	-	2.2	-	0.1	0.9	-	-
KU	Exhaust	Hard facing	9.2	0.2	0.8	0.2	87.6	0.6	-	0.05	-	0.1	-	-	1.2
		Valve head	9.7	0.2	0.8	0.2	88.0	0.6	-	0.05	-	0.1	-	-	0.3

Tab. 46 Chemical composition of valve seats used in testing as “Pin“

Engine manufacturer	Valve seat	Chemical composition [%]												
		Cr	Ni	Mo	Cu	Fe	Mn	Co	Nb	V	W	Al	Si	S
MA	Exhaust	6.1	-	8.7	-	78.8	-	2.5	0.8	3.1	-	-	-	-
	Intake	6.0	11.2	12.9	-	63.8	0.9	-	1.6	2.2	1.4	-	-	-
LI	Exhaust	30.4	0.4	2.2	0.1	64.0	0.7	-	0.05	0.1	-	0.4	1.5	-
	Intake	10.9	0.3	2.0	0.1	84.0	0.6	-	0.05	0.2	-	0.8	1.0	0.2
SC	Exhaust	7.7	5.2	28.0	-	52.6	-	4.7	-	-	-	-	1.6	-
	Intake	7.6	5.2	26.5	-	54.6	-	4.7	-	-	-	-	1.4	-
SCH	Exhaust	16.2	-	22.1	-	4.8	-	55.7	-	-	-	-	1.2	-
	Intake	4.6	-	10.3	15.1	47.4	1.0	15.7	-	2.2	3.3	-	-	0.5
KU	Exhaust	23.8	3.6	0.9	-	10.4	0.4	56.4	0.1	-	4.5	0.05	-	-

7.8.4 Measured data

The measured results from testing are shown in Tab. 47 – 49. The width of the wear is measured on a confocal microscope after the end of the tribological experiment. The depth of the

disc – valve wear is measured on a confocal microscope after the end of the tribological experiment. The volume wear of the pin was calculated from the wear measurements according to ČSN EN 1071-13 [122].

Tab. 47 Results of the First loop of tribological testing

Test No.	Valve (DISC) wear width [µm]	Depth of DISC wear [µm]	PIN wear [mm^3]	Static Friction coeficient [-]	Dynamic Friction coeficient [-]
1.	377.11	10.33	0.0008	**0.211**	**0.359 ± 0.070**
2.	317.03	4.33	0.0008	**0.133**	**0.209 ± 0.061**
3.	497.91	29.37	0.0069	**0.163**	**0.654 ± 0.097**
4.	484.57	6.58	0.0008	**0.238**	**0.378 ± 0.049**
5.	455.63	16.31	0.0007	**0.178**	**0.404 ± 0.140**
6.	773.82	50.27	0.0141	**0.181**	**0.625 ± 0.200**
7.	607.22	46.32	0.0357	**0.480**	**1.030 ± 0.059**
8.	476.42	32.18	0.0028	**0.192**	**0.626 ± 0.089**
9.	693.52	38.82	0.0211	**0.216**	**0.619 ± 0.130**
10.	586.78	32.92	0.0032	**0.168**	**0.667 ± 0.063**
11.	470.24	34.65	0.0033	**0.185**	**0.725 ± 0.052**
12.	495.97	13.82	0.0058	**0.273**	**0.772 ± 0.168**
13.	332.29	11.93	0.0013	**0.221**	**0.580 ± 0.033**
14.	667.01	21.71	0.0096	**0.202**	**0.672 ± 0.078**

Results of second loop of tribological testing:

Tab. 48 Results of the Second loop of tribological testing

Test No.	Valve (DISC) wear width [µm]	Depth of DISC wear [µm]	PIN wear [mm^3]	Static Friction coeficient [-]	Dynamic Friction coeficient [-]
15.	574.96	45.37	0.0042	**0.229**	**0.801 ± 0.086**
16.	475.54	30.32	0.0023	**0.251**	**0.349 ± 0.157**
17.	355.70	29.94	0.0007	**0.257**	**0.376 ± 0.154**
18.	519.27	32.91	0.0033	**0.431**	**0.596 ± 0.074**
19.	721.09	2.31	0.0162	**0.193**	**0.752 ± 0.186**
20.	710.74	4.42	0.0158	**0.221**	**0.846 ± 0.203**
21.	719.15	3.35	0.0163	**0.212**	**0.805 ± 0.195**
22.	840.30	5.20	0.0180	**0.202**	**0.797 ± 0.150**
23.	566.63	3.82	0.0051	**0.208**	**0.872 ± 0.192**
24.	583.13	12.36	0.0295	**0.259**	**0.709 ± 0.073**
25.	527.20	3.94	0.0079	**0.271**	**0.737 ± 0.086**
26.	595.65	7.38	0.0088	**0.321**	**0.683 ± 0.062**
27.	558.75	3.84	0.0054	**0.229**	**0.784 ± 0.108**
28.	534.13	4.72	0.0077	**0.259**	**0.718 ± 0.083**
29.	523.81	5.56	0.0065	**0.221**	**0.757 ± 0.096**

Results of third loop of tribological testing:

Tab. 49 Results of the Third loop of tribological testing

Test No.	Valve (DISC) wear width [µm]	Depth of DISC wear [µm]	PIN wear [mm^3]	Static Friction coeficient [-]	Dynamic Friction coeficient [-]
30.	579.85	22.95	0.0481	**0.431**	**0.715 ± 0.088**
31.	340.22	8.77	0.0008	**0.253**	**0.467 ± 0.055**
32.	317.09	22.13	0.0582	**0.223**	**0.330 ± 0.118**
33.	402.83	4.22	0.0087	**0.448**	**0.676 ± 0.094**
34.	506.47	18.97	0.0065	**0.283**	**0.734 ± 0.060**
35.	572.18	40.29	0.0874	**0.296**	**0.681 ± 0.055**
36.	324.29	29.15	0.1091	**0.205**	**0.659 ± 0.045**
37.	519.27	34.91	0.0005	**0.368**	**0.780 ± 0.044**
38.	237.72	15.83	0.0417	**0.233**	**0.504 ± 0.053**
39.	510.27	23.39	0.0091	**0.265**	**0.663 ± 0.045**
40.	581.36	0.46	0.0211	**0.205**	**0.719 ± 0.282**

7.8.5 Discussion of measured data

The measured values from the first phase of the tribological experiment showed that the lowest dynamic coefficient of friction was observed on sample No. 2 (0.209 ± 0.061). This sample was an exhaust valve TEDOM made of the nickel superalloy Nimonic 80A. For the serially used intake valve, TEDOM with P37S overlay was measured dynamic friction coefficient of 0.378 ± 0.049. For the serially used exhaust valve TEDOM with P37S overlay was measured value of a friction coefficient of 0.359 ± 0.070. These values are practically very close to each other. There is a significant change in the friction coefficient between the new and used exhaust valves TEDOM. The new exhaust valve shows a friction coefficient of 0.359 ± 0.070, while the valve after 8000 engine hours of use shows a friction coefficient of 0.654 ± 0.097. In this case, it could be due to increased abrasive wear due to greater particle release from the exhaust valve. The P37S overlay material exhibits the lowest friction coefficient among the materials tested in the first phase of the test.

Fig. 55 shows a graphical comparison of the coefficient of friction behavior for the materials ADI 280. ADI 280 N_5 and Q-Nitro from the second phase. Materials can be sorted on the basis of their static friction coefficients as follows:

- ADI 280 - static friction coefficient: 0.229
- ADI 280 N_5 - static friction coefficient: 0.251
- Q-Nitro - static friction coefficient: 0.257

Materials can be sorted based on their dynamic coefficient of friction as follows:

- ADI 280 N_5 - average Dynamic friction coefficient: 0.349 ± 0.157
- Q-Nitro - average Dynamic friction coefficient: 0.376 ± 0.154
- ADI 280 - average Dynamic friction coefficient: 0.801 ± 0.086

At the beginning of the friction coefficient behavior, the mechanism of groove formation and gradual deformation of the surface roughness can be observed, which lasts approximately for the first 60 seconds. This is followed by a phase of increasing coefficient of friction due to increasing adhesion forces and accumulation of particles at the contact surface. which lasts from 60s to 100s. This is followed by a period of constant coefficient of friction up to about 200 seconds. The coefficient of friction for ADI 280 N_5 and Q-Nitro then decreases to a level of approximately 0.3. The coefficient of friction for ADI 280 material stabilizes at a value of approximately 0.8. A steady state, in which the value of the coefficient of friction does not change significantly, occurs when sufficient smoothing of the contact surfaces is achieved. It is characterized by the fact that the wear during the tribological process is minimal.

In the course of his tribological investigation of ADI, Hu [134] found that, in comparison to the initial cast iron state of the casting, ADI exhibited significantly enhanced strength, characterized by an ultimate tensile strength reaching approximately 1220 MPa. The friction coefficient of ADI was markedly influenced by operational conditions, with an observed decrease in the friction coefficient corresponding to escalated normal loads and sliding speeds. This phenomenon was primarily linked to the quantity of graphite transferred from the matrix onto the tribosurface, as well as the formation of a graphite-based lubricant layer. Our measured values align with Hu's findings. Different values were obtained in the case of the ADI280 material.

The measured values indicate that cryogenic treatment has a positive effect on the tribological properties of isothermally hardened and oil-hardened cast iron. Further recommended testing includes performing this experiment on a statistically significant sample size and testing the EN- GJS 450-8 cast iron reference material.

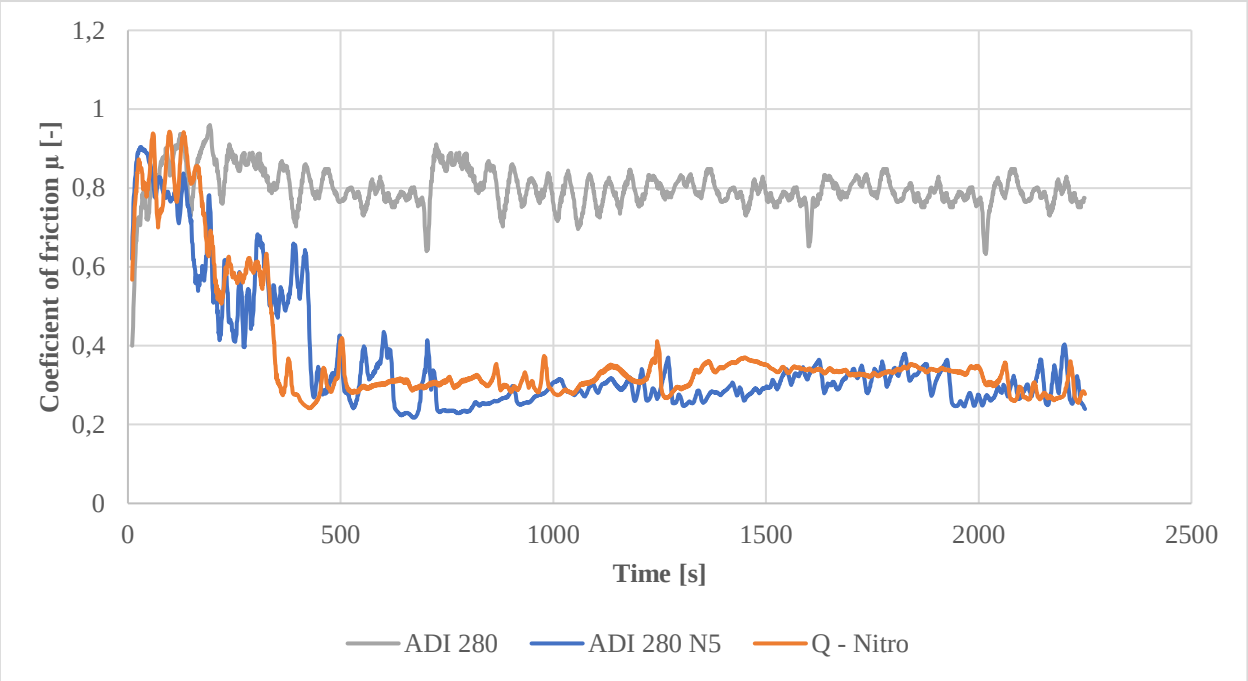

Fig. 55 Comparison of friction coefficient cast irons

The influence of cryogenic temperatures on the coefficient of friction behavior of Stellite 6 is shown in Fig. 55. It is clear from the measured data that the value of the static coefficient of friction decreases due to the influence of cryogenic temperatures. The static friction coefficient of Stellite 6 without cryogenic treatment was measured to be 0.431, which is the highest value of the Stellite 6 samples. Surface strengthening after cryogenic processing can be attributed to the formation of new structural phases or changes in dislocations within the material's crystal lattice. These alterations enhance the surface's resistance to wear, thus reducing resistance during motion or friction. However, the sample without the freezing treatment shows stable behavior over time with no gradual increase in the dynamic coefficient of friction. The static friction coefficients can be ordered as follows:

- Stellite 6 - freezing 5 minutes - Static friction coefficient: 0.193
- Stellite 6 - freezing 30 minutes - Static friction coefficient: 0.202
- Stellite 6 - freezing 60 minutes - Static friction coefficient: 0.208
- Stellite 6 - freezing 15 minutes - Static friction coefficient: 0.210
- Stellite 6 - freezing 10 minutes - Static friction coefficient: 0.221
- Stellite 6 – without freezing - Static friction coefficient: 0.431

Each of the frozen samples exhibits a gradual increase in the friction coefficient. If we organize the samples based on the average dynamic friction coefficient. the order would be as follows:

- Stellite 6 – without freezing - average Dynamic friction coefficient: 0.600 ± 0.074
- Stellite 6 - freezing 5 minutes - average Dynamic friction coefficient: 0.752 ± 0.178
- Stellite 6 - freezing 30 minutes - average Dynamic friction coefficient: 0.797 ± 0.145
- Stellite 6 - freezing 15 minutes - average Dynamic friction coefficient: 0.805 ± 0.187
- Stellite 6 - freezing 10 minutes - average Dynamic friction coefficient: 0.846 ± 0.199
- Stellite 6 - freezing 60 minutes - average Dynamic friction coefficient: 0.872 ± 0.188

The measurements show a significant impact of cryogenic temperatures on the tribological properties of Stellite 6. Consequently, the study suggests further continuing the measurements and directing the focus toward investigating the structural changes responsible for the alteration of the friction coefficient.

The influence of cryogenic temperatures on the change of the coefficient of friction of Stellite 6 is shown in Fig. 56. From the measured data on the influence of cryogenic temperatures on the tribological properties of Stellite 12, it can be concluded that this material is less susceptible to the effects of cryogenic temperatures on the coefficient of friction than Stellite 6. The value of the static coefficient of friction for the material Stellite 12 is affected by the length of freezing.

The material composition of Stellite 6 and Stellite 12 consists of cobalt-based alloys with varying additives and carbon content. These differences in chemical composition can result in distinct structural changes during cryogenic processing, ultimately impacting their tribological properties. The microstructure of a material, including the arrangement and formation of crystals, plays a crucial role in determining its mechanical and tribological characteristics. Cryogenic temperatures can induce phase transformations within the material, potentially leading to alterations in its tribological properties. Depending on the phases that Stellite 6 and Stellite 12 assume at specific temperatures, they may exhibit varying reactions. Various wear mechanisms can influence the tribological behavior of materials. Cryogenic temperatures have the capacity to modify these wear mechanisms. Consequently, affecting the performance of both Stellite 6 and Stellite 12 materials in tribological applications.

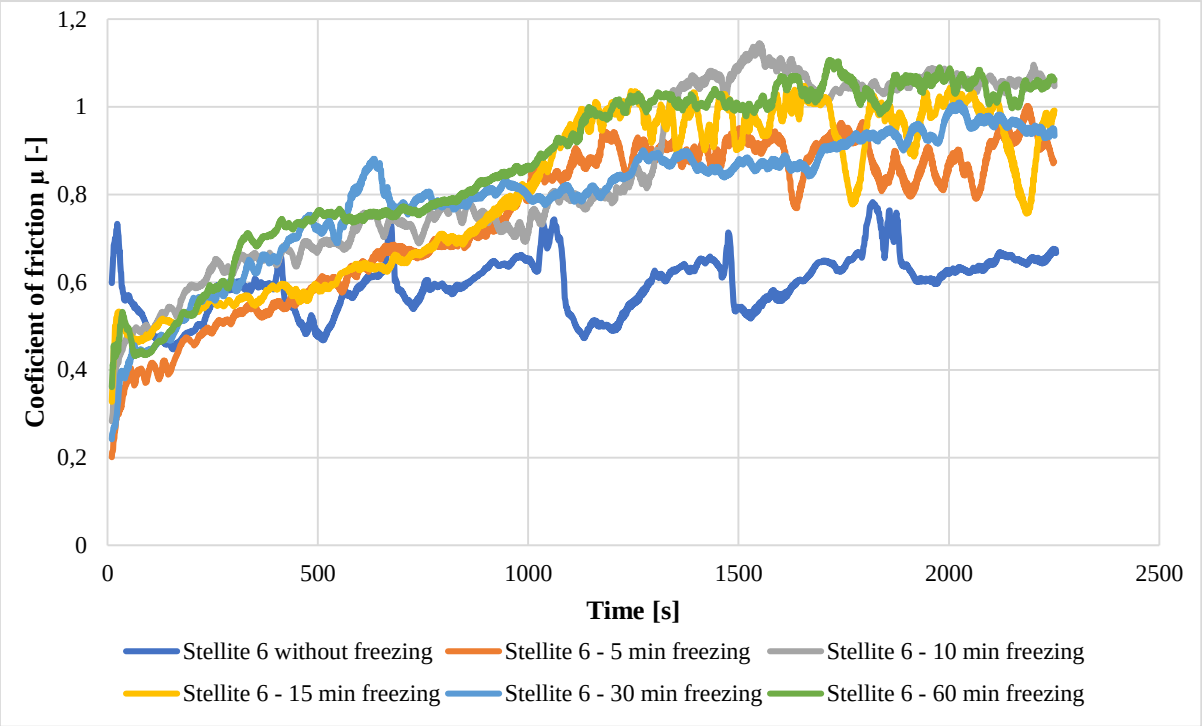

Fig. 56 Influencing of cryogenic treatment to friction coefficient of Stellite 6

The influence of cryogenic temperatures on the change of the coefficient of friction of Stellite 12 is shown in Fig. 57.

Freezing times of 15 min and 60 min show a decrease in the coefficient of static friction. while freezing times of 5 min. 10 min and 30 min show a slight increase in the coefficient of static friction.

The materials. according to the static friction coefficient. can be ordered as follows:

- Stellite 12 - freezing 60 minutes - Static friction coefficient: 0.221
- Stellite 12 - freezing 15 minutes - Static friction coefficient: 0.229
- Stellite 12 - without freezing - Static friction coefficient: 0.259
- Stellite 12 - freezing 30 minutes - Static friction coefficient: 0.259
- Stellite 12 - freezing 5 minutes - Static friction coefficient: 0.271
- Stellite 12 - freezing 10 minutes - Static friction coefficient: 0.320

Each of the frozen samples. except for the one exposed 10 min. exhibits a gradual increase in the friction coefficient. If we arrange the samples according to the average friction coefficient. the order would be as follows:

- Stellite 12 - freezing 10 minutes - average Dynamic friction coefficient: 0.683 ± 0.046
- Stellite 12 - without freezing - average Dynamic friction coefficient: 0.709 ± 0.053
- Stellite 12 - freezing 30 minutes - average Dynamic friction coefficient: 0.718 ± 0.056
- Stellite 12 - freezing 5 minutes – average Dynamic friction coefficient: 0.737 ± 0.073
- Stellite 12 - freezing 60 minutes - average Dynamic friction coefficient: 0.757 ± 0.077
- Stellite 12 - freezing 15 minutes - average Dynamic friction coefficient: 0.784 ± 0.084

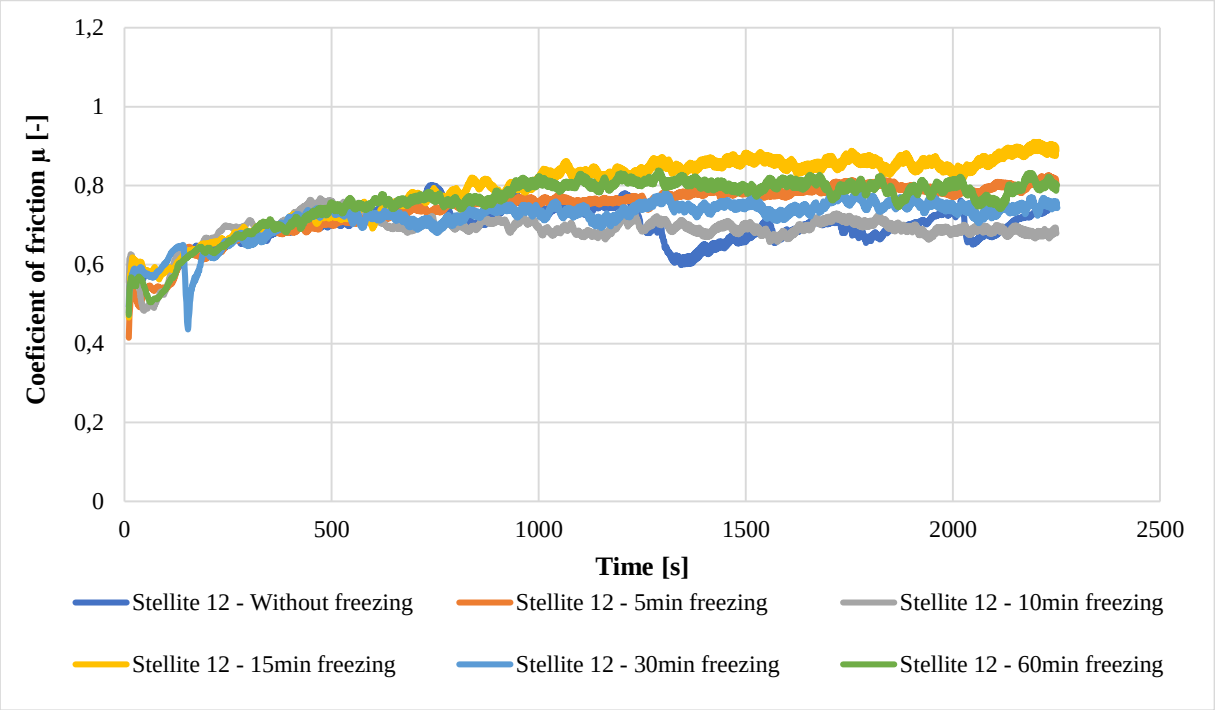

Fig. 57 Influence of cryogenic treatment to friction coefficient of Stellite 12

Based on the measured values, from a tribological perspective, it is recommended to use the shortest possible cryogenic treatment time. i.e., up to 5 min, for cooling the intake valve seat (Stellite 6). Beyond this time, the coefficient of friction begins to increase, and from the experimental measurements of hardness changes. It is evident that the most significant decrease in hardness occurs at 10 minutes. This can lead to increased wear of the intake valves.

Based on the measured values, it is recommended to use a cryogenic freezing time of 10 min, for the exhaust valve seats (Stellite 12). At this duration, the measured friction coefficient values are the lowest, and the decrease in material hardness does not reach its maximum. Both of these recommendations were incorporated into the internal guidelines of TEDOM, and the company began implementing the cryogenic freezing process during the production of cylinder heads. TEDOM started to systematically monitor whether this measure contributed to increasing

the lifespan of cylinder heads. By statistically tracking the results, the company aims to assess the effectiveness of the implemented changes and evaluate any potential improvements in the durability and performance of the cylinder heads.

The ADI 280 material exhibits a relatively stable friction coefficient behavior with an average dynamic coefficient friction of 0.801 ± 0.086. Compared to Stellite 6 without freezing 0.596 ± 0.074, its friction coefficient is higher. However, it is lower compared to the frozen variants. Compared to Stellite 12, ADI 280 shows comparable behavior.

Materials ADI 280 N_5 and Q-Nitro have significantly lower friction coefficients than Stellite 6 without freezing and Stellite 12 without freezing. From a tribological standpointl, these two materials appear to be excellent alternatives for intake valve seat inserts in gas combustion engines or in engines with direct injection. This is due to their good friction properties, even under challenging conditions. The harsh conditions in engines running on alternative fuels are caused by the fact that gaseous fuels are dry and do not provide lubrication to the valve seats, resulting in dry contact between the valve and the seat. Similarly, direct injection engines do not lubricate the valve seats.

In the third phase of testing, where was compared real friction pairs from engines currently used for gas applications, the results indicate that the exhaust valve TEDOM after 8000 operation hours, exhibited a dynamic friction coefficient of 0.715 ± 0.0881. Remarkably, this value is only slightly higher than that of the new valve 0.709 ± 0.0725. These findings suggest that the selected overlay material P37S, remains stable in terms of tribological properties and wear resistance over time. The minimal difference between the dynamic friction coefficients of the new and used exhaust valves implies that the P37S overlay material exhibits excellent long-term stability and durability, making it a suitable choice for gas engine applications.

The measurement of the intake valve from TEDOM with a valve head made of Nimonic 80A material shows that in terms of friction, it is advantageous as a friction material when combined with Stellite 6. Stellite 6 with Nimonic 80A material, exhibits a dynamic friction coefficient of 0.467 ± 0.055. whereas with P37S overlay material, it exhibits a dynamic friction coefficient of 0.596 ± 0.074.

In the last part of the tribological experiment were compared friction pairs of intake valves and valve seats from global manufacturers of gas combustion engines, Fig. 58.

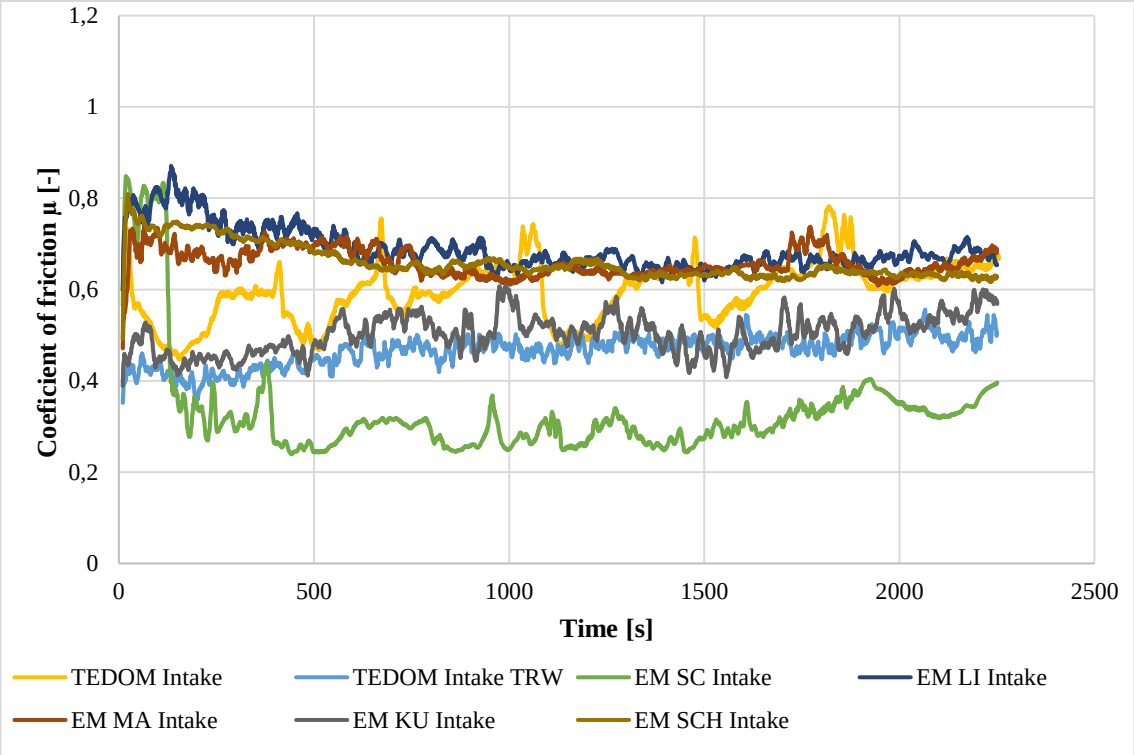

Fig. 58 Comparison coefficient of friction intake valves and valve seat materials

From the measured data, it can be observed that the dynamic friction behavior of the EM – SC friction pair (0.330 ± 0.118) is very similar to that of ADI 280 N_5 (0.349 ± 0.157) or Q - Nitro (0.376 ± 0.154). Fig. 59, is show the behavior of the dynamic coefficient of friction in these materials. From this perspective, the materials ADI 280 N_5 and Q-Nitro appear to be suitable friction pairs with the P37S overlay material as a replacement for modern materials. The similarity in their dynamic friction behavior to that of the EM - SC friction pair suggests their potential as viable alternatives for intake valve seat inserts in gas combustion engines.

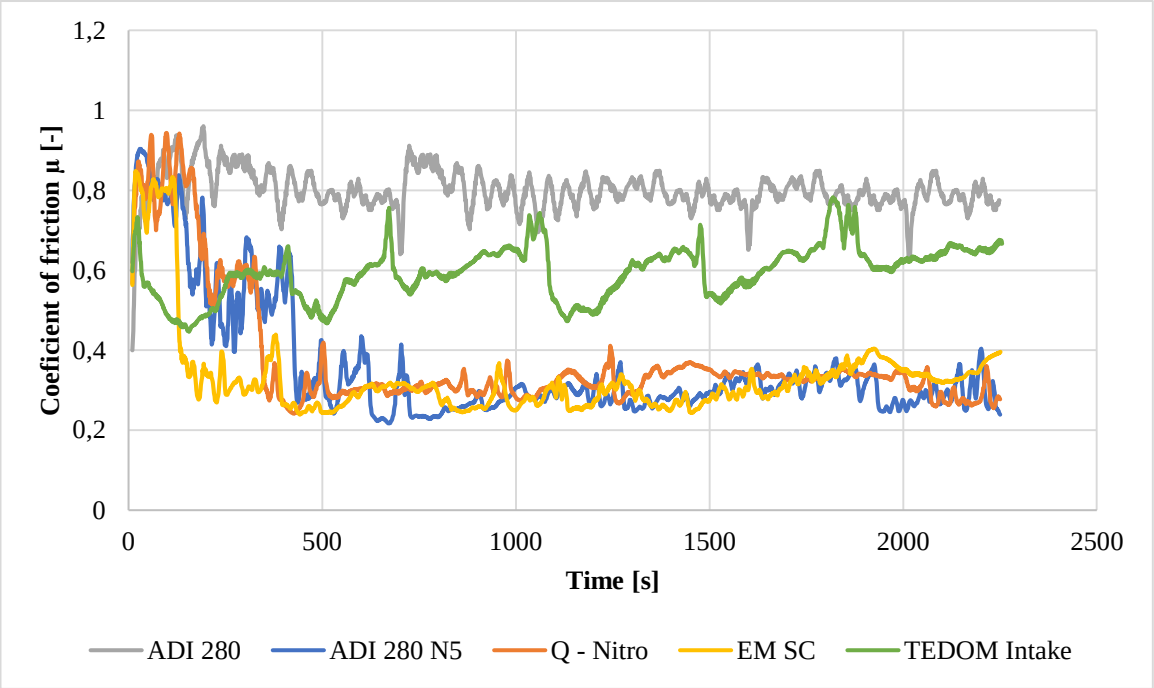

Fig. 59 Comparison cast irons with TEDOM and EM - SC materials

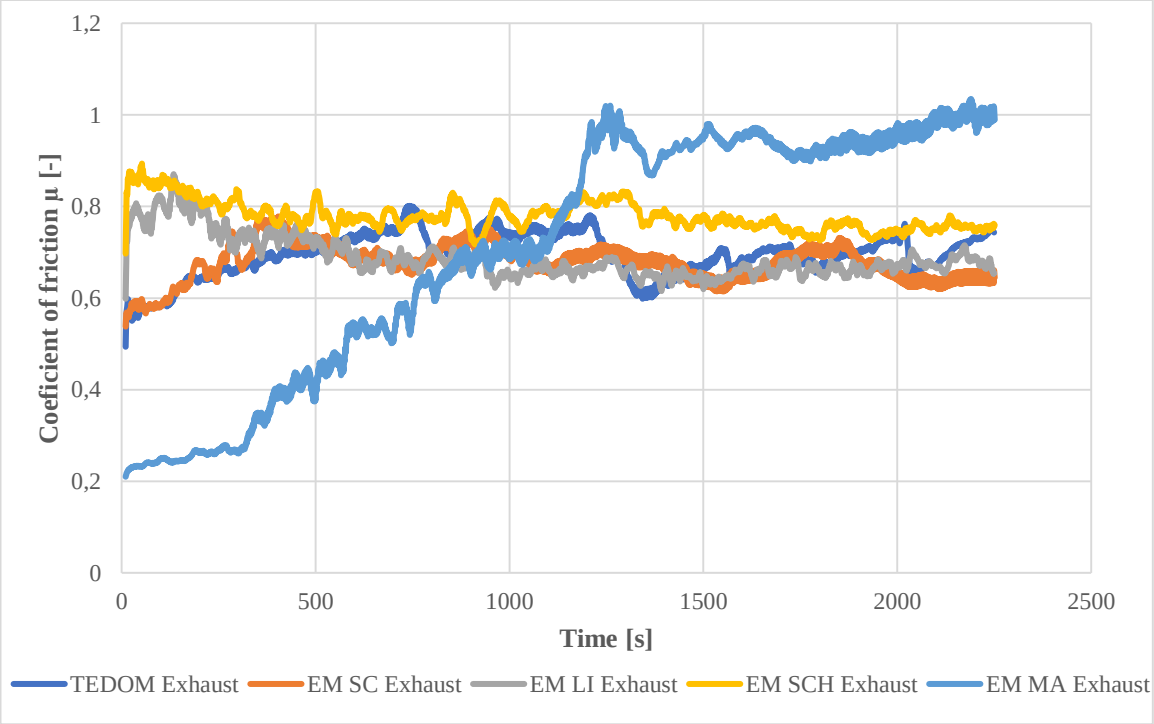

Fig. 60 Comparison coefficient of friction exhaust valves and valve seat materials

Fig. 60 are compared the dynamic friction coefficient behaviors of materials used for exhaust valves and exhaust valve seats. From the measured results, it is evident that, with the exception of the EM - MA material, the materials exhibit similar tribological behavior. The

EM - MA material initially showed the lowest static friction coefficient of 0.205, but over time, abrasive wear increased the friction coefficient up to a value of 1., leading to micro-welding and significant vibrations. All measured graphs depicting the friction coefficient profiles are presented in the appendix of this study. First phase is in Appendix 10.1, second phase is in Appendix 10.2 a third phase is in Appendix 10.3.

Aditional part of material testing, we included the progressive intermetallic material Fe_3Al, developed at the Technical University in Liberec, Department of Materials, in the tribological tests. The results are shown in Appendix 10.4.

The set of measured data was so extensive that within the scope of the dissertation, it was not possible to comment each tribological behavior individual measured samples. Therefore, the discussion focuses on the coeficient of friction as a one of the measured parameters.

8 CONCLUSION

The thesis presented deals with the physical properties of the materials that surround the combustion chamber of the TEDOM internal combustion engine. The influence of cryogenic heat treatment on the physical and tribological properties of these materials is also studied.

The following conclusions are drawn from the measured values:

The experimental results highlight important aspects of the mechanical behavior of the cylinder head material. The bridge area between the valves near the spark plug emerges as a critical point, exhibiting a lower theoretical Young's modulus with a local minimum value of 121.7 GPa. This area is susceptible to high thermal and mechanical stresses. The hardness tests show no significant variation with engine use, confirming the stability and longevity of the material. The observed variations in Young's modulus between different areas of the new cylinder head (ranging from 126.4 to 145.3 GPa) and the wider range in the used cylinder head (121.7 to 158.7 GPa) indicate possible changes in the material during operation. In addition, The Eichelberg factor highlights the areas that are subjected to the highest thermal stress, providing valuable information for addressing potential thermal fatigue issues.

TEDOM has decided to discontinue the production of EN-GJS 400 cylinder heads for economic reasons, based on a comprehensive evaluation of cylinder head measurements in both EN-GJS 400 and EN-GJL 250 materials. The consistently acceptable measurements in both

materials ensure that the manufacturing processes are in line with the design drawing specifications and within the desired tolerances, with the prioritization of EN-GJL 250 material for cylinder head production. TEDOM aim is to optimize manufacturing processes, maintain quality standards and achieve cost-effectiveness.

Research into advanced heat treatment of EN-GJL 200 material has shown that applying specific heat treatment techniques improves the mechanical properties of grey cast iron components. Significant improvements in hardness and Tensile strength have been observed through the use of isothermal quenching and freezing. Mechanical performance was improved by the modified microstructure resulting from these treatments. In addition, a significant increase in Tensile strength and ductility was observed following the cryogenic treatment of AGI cast iron. The results highlight the importance of applying cryogenic treatment promptly after quenching to achieve optimum results. Overall, these heat treatments offer new opportunities to improve the overall performance and reliability of engineering materials. and have great potential to improve the mechanical properties of grey cast iron components.

The thermal processing of EN-GJS 450-8 ductile cast iron with nodular graphite using a variety of heat treatment techniques has been shown to have a significant effect on the mechanical properties of the material. The Q-Nitro treatment resulted in a significant increase in tensile strength but high fragility. The ADI 280 N_5 treatment showed significant strength improvements with reduced ductility. The ADI 280 NT_5 variant showed the most effective combination of high strength and ductility of the materials tested. This makes it a promising choice for practical applications in engine components.

Analysis of Stellite 6 and Stellite 12 valve seats revealed specific freezing times at which local minimum hardness values were observed: 10 minutes for Stellite 6 and 15 minutes for Stellite 12. These findings led to the development of a technological regulation for the freezing of valve seats during the production of cylinder heads at TEDOM. The regulation stipulates that the minimum freezing time for valve seats must be 5 minutes with a tolerance of ± 1 min. The aim of this standardized procedure is to increase the service life of cylinder heads and eliminate the variable effects of different freezing times, thus providing more consistent and reliable results. Cryogenic treatment did not significantly change valve seat hardness.

These variations indicate that specific freezing times can have a subtle effect on hardness levels, highlighting the importance of maintaining a consistent freezing duration to achieve

consistent and reproducible results in the manufacturing process. Overall, the study provides valuable insight into optimizing the valve seat freezing process in cylinder head manufacturing, which can help improve overall cylinder head performance and durability.

The effects of liquid nitrogen exposure on Stellite 6 and Stellite 12 are evident from the measured values of theoretical Young´s modulus. In the case of Stellite 6, both Young's modulus and the speed of sound increased from their initial states with the action of liquid nitrogen, reaching local maximum after 15 minutes of exposure. In contrast, Stellite12 showed a decrease in both Young's modulus and speed of sound with exposure to liquid nitrogen, with the most significant decreases occurring after 60 minutes of exposure.

Changes in the magnetic properties of the cobalt alloys, particularly Stellite 6 and Stellite 12, were observed during cryogenic processing. The decrease in magnetism can be attributed to changes in the crystal structure of the material at low temperatures and the phenomenon of spin-flip scattering. Spin-flip scattering is a collision between magnetic moments and the crystal lattice. which reduces the overall magnetization.

Tribological results show that the influence of cryogenic temperatures on the friction coefficient of Stellite 6 is significant. Short-term exposure to cryogenic temperatures resulted in the decrease of the static friction coefficient for Stellite 6. Stellite 6 shows a variable effect on the dynamic friction coefficient depending on the freezing duration. Stellite 12, on the other hand, showed a lower sensitivity to cryogenic temperatures compared to Stellite 6, with a variable effect on the coefficient of static and dynamic friction depending on the duration of freezing.

The ADI 280 material showed a stable coefficient of friction behavior. Its friction properties were comparable to those of Stellite 6 without freezing, but lower than the frozen grades. The materials ADI 280 Nitro and Q-Nitro showed significantly lower coefficients of friction than Stellite 6 and Stellite 12. making them potential candidates for intake valve seat inserts in gas combustion engines or engines with direct injection.

The last phase was the study of real friction pairs from engines currently in use for gas applications. After 8000 hours of operation, the TEDOM exhaust valve showed a slightly higher coefficient of friction in comparison with the new valve. Of the real-life friction pairs, the EM – SC valve-seat pair had the lowest coefficient of friction, indicating that it has the potential to be the most efficient friction pair.

8.1 This thesis contributes to both theory and practice

At a theoretical level, the thesis enhances our understanding of the mechanical and thermal properties of various materials used in the construction of critical engine components. Valuable insight into the behavior and performance of materials under different conditions is provided by the comprehensive investigation of Young's modulus, hardness, and other mechanical parameters. Studying cryogenic processing and its effect on material properties highlights the potential benefits and limitations of such treatments, enabling researchers and engineers to make informed decisions regarding material selection and processing techniques. Furthermore, studying the tribological properties and coefficient of friction of different materials further contributes to the knowledge in this field, helps to develop advanced materials, and improves our understanding of material interactions in engine systems.

In terms of practical implications, the findings of this thesis have direct relevance and application in the automotive industry, particularly in the design and manufacture of high-performance engines. Detailed analysis of material behavior under operating conditions, including thermal and wear effects, provides critical information for engineers to optimize engine component performance and reliability. Identifying suitable materials for specific engine parts, such as valve seat inserts, enables manufacturers to improve engine efficiency and durability. In addition, valuable guidance for improving the overall performance and efficiency of engine systems in the field is provided by the knowledge gained from real-world friction pairs in gas applications.

Overall, this dissertation is a significant contribution to the advancement of materials science and its practical applications in engine technology. The results of the research will enable informed decisions to be made on the selection of materials and processing methods for engine components, paving the way for the development of more robust and efficient engine components. The findings of the research have the capability to drive innovation in engine design, resulting in more sustainable and higher-performing engines to meet the changing demands of the modern transport and energy industry. This thesis initiated a collaborative research project on the effects of cryogenic temperatures on the mechanical properties of materials used in space applications between the Technical University of Liberec, Warsaw University of Technology and the Politecnico di Milano. The research conducted in this study has provided valuable insights into the behavior of various materials under extreme temperature conditions, which is crucial for space exploration and aerospace engineering.

8.2 Suggestions for further research

There are several promising research directions to explore the microstructural changes induced by cryogenic processing in terms of material characterization. Advanced microscopy techniques, such as electron microscopy and atomic force microscopy, could be used to study the changes in the crystal lattice and the behavior of the dislocations at different cryogenic temperatures. Furthermore, performing in-situ measurements during cryogenic processing could reveal real-time changes in the material's structure and help to understand the dynamics of phase transformations.

In the area of tribology, further research could focus on the study of the long-term wear behavior of materials under real engine conditions. More comprehensive data on the performance and wear resistance of engine components such as valves and valve seats could be obtained through extended durability tests with different material combinations and cryogenic treatments. Investigating the effects of different operating conditions such as temperature, pressure and lubrication on these materials' friction and wear characteristics would help tailor their properties to specific engine applications.

There could be more opportunities to optimize engine components by extending the research to a wider range of materials, such as different alloys and composites. Investigating the effects of cryogenic processing on a wider range of materials could lead to the discovery of new combinations of materials with improved properties, which could lead to further improvements in engine performance and efficiency.

It is of paramount importance to consider the impact of these materials and processes on the environment. A life cycle assessment of the environmental footprint of cryogenic processing and the use of different materials in engine components would be valuable. More sustainable and environmentally friendly options for the automotive industry could be identified by assessing energy consumption, greenhouse gas emissions, and other environmental impacts associated with production use and disposal of these materials.

9 BIBLIOGRAPHY

[1] TRW Inc. Handbook. Barsubhousen. 1998

[2] FORSBERG P. (no date) Combustion Valve Wear. Uppsala University. Department of Engineering Sciences. Applied Materials Sciences. Uppsala. Sweden: Publisher. 58 p. ISBN 1651-6214.

[3] LEWIS R. DWYER-JOYCE R.S. (2002) Automotive Engine Valve Recession. London and Bury St Edmunds. UK: Publisher. 156 p. ISBN 1 86058 358 X.

[4] PYLE. W.R. SMRCKA. N.R. (no date) The Effect of Lubricating Oil Additives on Valve Recession in Stationary Gaseous-Fueled Four-Cycle Engines. SAE Technical Paper Series

[5] SKRBEK B. (no date) Dspace Home [Online]. DSpace Home. Available at: https://dspace.tul.cz/ (Accessed: December 11. 2022). [Online] Available at: https://dspace.tul.cz/bitstream/handle/15240/39334/%2809_Neestruktivni_strukturoskopie_izotermicky_kalenych_litin_teorie_material%29.pdf?sequence=9&isAllowed=y.

[6] OPPENKOWSKI A. Cryobehandlung von Werkzeugstahl [Cryogenic treatment of tool steel]. Doctoral Thesis. Ruhr-Universität Bochum. Universitätsbibliothek. Germany. 2011; 259 p.

[7] PADMAKUMAR M. & DINAKARAN D. (2020) "Investigation on the effect of cryogenic treatment on tungsten carbide milling insert with 11% cobalt (WC–11%CO)." SN Applied Sciences. 2(6). Available at: https://doi.org/10.1007/s42452-020-2872-3.

[8] CHEN L. CUI J. and TONG W. (2015) "Effect of deep cryogenic treatment and tempering on microstructure and mechanical behaviors of a wear-resistant austempered alloyed bainitic ductile iron." MATEC Web of Conferences. 21. p. 08008. Available at: https://doi.org/10.1051/matecconf/20152108008.

[9] COLLECTIVE AUTHORS (2006) Operational Degradation of Austenitic Valve Steels: Proceedings of a Seminar with International Participation: October 9, 2006, Liberec. 1st ed. Liberec: Technical University of Liberec. ISBN 80-7372-113-9

[10] MAKOTO K. (1991) Highly Wear-Resistant Cast Iron for Rocker Arms - New High-Cr Cast Iron Material. JSAE Review. 1/1991.

[11] BLOMBERG R. PERROTT C. (1994) Adhesive wear processes occurring during abrasion of Stellite type alloys. Journal of the Australian Institute of Metals. No. 4. p. 19.

[12] SKRBEK B. NOSEK V. (2005) Material of valve seat. In: METAL 2005: Proceedings of the Conference. pp. 22-26. ISBN 80-85988-38-0.

[13] SKRBEK B. Nosek V. (2014) Combined nondestructive structuroscopy of dispersion metallic materials. In: Proceedings of the 11th European Conference on Non-Destructive Testing. Prague. Poster P 7.16. CD. ISBN 978-80-214-5019-6.

[14] YAMAMOTO E. MOTEGI R. (1979) Direct stress measurement by ultrasound. In: Proceedings of the 9th World Conference on Non-Destructive Testing. Part 4E-9. Melbourne

[15] ŠIMÁČEK M. (2004) Physical and tensile properties of cast iron from different iron foundries. Bachelor's thesis. KMT-B-093. Technical University of Liberec.

[16] SKRBEK B. (2009) Materiály pro konstrukční aplikace [Materials for construction applications]. 2nd edition. Liberec: Technická univerzita v Liberci.

[17] BARTL D. O. & MUDROCH O. (1957) Technologie chemických a elektrochemických povrchových úprav [Technology of chemical and electrochemical surface treatments]. Praha: SNTL.

[18] SLÁMA P., PODANÝ P. MACHÁČKOVÁ K. SVĚTLÁ M. & MACHÁČEK J. (2010) Structure and properties of pressed rods from CuAl10Ni5Fe4 alloy. In: Proceedings of the METAL2010 Conference. Rožnov pod Radhoštěm.

[19] BENEŠ L., KALOČ R. (2006) Tribological aspects of the railway wheel-rail contact. In: Scientific Papers of the University of Pardubice. Series B. The Jan Perner Transport Faculty.

[20] SKRBEK B. (2014) Advances in non-destructive testing [Pokroky v oblasti nedestruktivního zkoušení]. Publikace TU v Liberci.

[21] SKRBEK B., NOSEK V. (2011) Comparative nondestructive testing of automotive parts materials [Srovnávací nedestruktivní testy materiálů autodílů]. In: Defektoskopie 2011: Proceedings of the Conference. Ostrava: VSB - Technical University of Ostrava. pp. 163-168. ISBN 978-80-214-4358-7.

[22] SUCHÁNEK J., et al. (2007) "Abrazivní opotřebení materiálú" [Abrasive Wear of Materials]. Praha: 162 pages. ISBN 970-80-01-03659-4.

[23] SKRBEK B. NOSEK V. (2014) "Combined nondestructive structuroscopy of dispersion metallic materials." Poster P 7.16. CD. 11th European Conference on Non-Destructive Testing. CNDT. Prague. ISBN 978-80-214-5019-6.

[24] ČSN 42 2425. Cast iron with flake graphite. Prague: Czechoslovak State Standard. 1999.

[25] Kolektiv VÚNM a ČKD Praha. (1964). Naftové motory čtyřdobé II. Díl [Four-stroke diesel engines II. Part 2]. (2nd ed.). Prague: SNTL - State Technical Publishing House. (L13-B3-IV-41/2491-VI).

[26] SKRBEK B. (2014). Metoda magnetické skvrny [Magnetic Spot Method]. Publikace TU v Liberci [Publication of the Technical University in Liberec]. ISBN 978-80-7372-428-3.

[27] BAKALOVA T. (2010). Impact of Material and Technological Parameters of Machining on the State of Stress in Surface Layers and Properties of Machine Parts under Dynamic Load [Vliv materiálových a technologických parametrů obrábění na napěťový stav v povrchových vrstvách a vlastnosti strojních dílů při dynamickém zatížení]. Doctoral Thesis. Technical University in Liberec. 120 p.

[28] KENNEDY F.E., LU Y., and BAKER I. (2015) “Contact temperatures and their influence on wear during pin-on-disk tribotesting.” Tribology International. 82. pp. 534–542. Available at: https://doi.org/10.1016/j.triboint.2013.10.022.

[29] ČSN EN 1563 (420951) 2019 Slévárenství - Litina s kuličkovým grafitem [Foundry - Spheroidal Graphite Cast Iron]. Prague: Czech Standards Institute. (ISBN 978-80-02-02755-3)

[30] ANDRŠOVÁ Z. (2014). Non-destructive Structuroscopy of Austempered Iron [Non-destructive strukturoskopie austemitického železa]. Doctoral Thesis. Technical University in Liberec. 223 p.

[31] SKRBEK B. (2011). NDT Diagnostics of Structural Changes in Austenitic Valve Steels [NDT diagnostika strukturních změn austenitických ventilových ocelí]. Časopis Jemná mechanika a optika [Journal of Fine Mechanics and Optics]. vol. 56. 2011. no. 1. ISSN 0447-6441.

[32] SKRBEK B. (2011). Rozlišení struktur slitin železa metodou magnetické skvrny [Differentiation of Iron Alloy Structures by Magnetic Particle Method]. Jemná mechanika a optika [Fine Mechanics and Optics]. vol. 56. no. 1. p. 18-19. ISSN 0447-6441.

[33] SENBERGER J. (2003). Austempered Ductile Iron (ADI) - a Perspective Material for Czech Foundries. Foundry Engineering - Journal for the Foundry Industry. vol. XLIX. no. 11-12. ISSN 0037-6825.

[34] SKRBEK B. (1988). Non-destructive Material Diagnostics of Cast Iron Castings [Nedestruktivní materiálová diagnostika litinových odlitků]. PhD Thesis. Technical University of Liberec.

[35] PLUHAŘ J. MACEK K. (1984). Metody studia struktury kovů [Methods of Studying the Structure of Metals]. Nakladatelství ČVUT. Prague.

[36] ČSN EN 1564 (42 0960): Foundry Engineering - Austempered ductile iron with nodular graphite. Prague: Czech Standards Institute. October 2012.

[37] ČSN EN 14127 (42 0556): Non-destructive testing - Ultrasonic thickness measurement. Prague: Czech Standards Institute. June 2011.

[38] DORAZIL E. VĚCHET S. and KOHOUT J. (1998) "Litina s kuličkovým grafitem a její vysokopevná varianta – ADI." Slévárenství – Journal of Foundry Engineering. vol. XLVI. no. 11-12. ISSN 0037-6825.

[39] SONAR T. LOMTE S. and GOGTE. C. (2018) "Cryogenic treatment of Metal – A Review." Materials Today: Proceedings. 5(11). pp. 25219-25228. Available at: https://doi.org/10.1016/j.matpr.2018.10.324.

[40] KENNEDY F.E. LU Y. and BAKER I. (2015) "Contact temperatures and their influence on wear during pin-on-disk tribotesting." Tribology International. 82. pp. 534-542. Available at: https://doi.org/10.1016/j.triboint.2013.10.022.

[41] CHEN Z. et al. (2019) "Microstructural evolution and wear behaviors of laser-clad stellite 6/NBC/h-BN self-lubricating coatings." Surface and Coatings Technology. 372. pp. 218-228. Available at: https://doi.org/10.1016/j.surfcoat.2019.04.083.

[42] GURRAM A. et al. (2022) "Temperature dependent sliding wear behaviour of stellite 6 alloy." Materials Today: Proceedings [Preprint]. Available at: https://doi.org/10.1016/j.matpr.2022.11.211.

[43] SKALANTE E.M. MAKICH H. and NOUARI M. (2022) "Effect of cryogenic friction conditions on Surface Quality." Procedia CIRP. 108. pp. 675-680. Available at: https://doi.org/10.1016/j.procir.2022.03.105.

[44] ČSN EN ISO 6506-1 (420359) Kovové materiály - Zkouška tvrdosti podle Brinella - Část 1: Zkušební metoda. Praha: Úřad pro technickou normalizaci. metrologii a státní zkušebnictví. 2015.

[45] ČSN EN ISO 6508-1 (420360). Kovové materiály - Zkouška tvrdosti podle Rockwella - Část 1: Zkušební metoda [Metallic materials - Rockwell hardness test - Part 1: Test method]. Praha: Úřad pro technickou normalizaci. metrologii a státní zkušebnictví. 2017.

[46] ROUČKA. J. (1998). Metalurgie litin [Cast iron metallurgy]. Skriptum FSI VUT. 166 s. Brno. ISBN 978-802-141-2637.

[47] SKRBEK B. (2011). Rozlišení struktur slitin železa metodou magnetické skvrny [Resolution of iron alloy structures using the magnetic spot method]. Jemná mechanika a optika. vol. 56. no. 1. p. 18-19. ISSN 0447-6441.

[48] Český normalizační institut. (1990). ČSN 42 2420 - Litina 42 2420 s lupínkovým grafitem. Praha: Český normalizační institut.

[49] ČSN EN 1564 (42 0960): Slévárenství - Izotermicky kalené litiny s kuličkovým grafitem [Foundry engineering - Austempered ductile iron]. Český normalizační institut. Praha. October 2012.

[50] DORAZIL E. VĚCHET S. & KOHOUT J. (1998). Litina s kuličkovým grafitem a její vysokopevná varianta – ADI [Ductile iron and its high-strength variant - ADI]. Slévárenství - časopis pro slévárenský průmysl. XLVI (11-12). ISSN 0037-6825.

[51] SKRBEK B. (1988). Nedestruktivní materiálová diagnostika litinových odlitků [Non-destructive material diagnostics of cast iron castings]. Disertační práce [Doctoral dissertation]. VŠST Liberec.

[52] MRAZ J. SKRBEK B. (2019). Influence of cryogenic temperatures on mechanical properties of valve seats of internal combustion engines. Acta Mechanica Slovaca. 23(4). 52-57. ISSN 1335-2393.

[53] MRAZ J. SKRBEK B. (2020). Sliding couples for valve guides and valves of piston combustion engines. Sborník konference METAL2020; ISSN: 2694-9296; ISBN: 978-80-87294-97-0.

[54] MRAZ J. SKRBEK B. (2019). Rozšířené využití zkušebních tyčí atestů odlitků [Expanded utilization of test bars for casting certifications]. Sborník přednášek z 56. slévárenských dnů–Blok A –Blok F; ISBN 978-80-02-02882-6.

[55] MRAZ J. SKRBEK B. (2019). Technická přejímka důležitých odlitků produktu [Technical acceptance of crucial castings of the product]. Sborník přednášek z 56. slévárenských dnů–Blok A –Blok F; ISBN 978-80-02-02882-6.

[56] MRAZ J. SKRBEK B. (2019). Nedestruktivní magnetické a vířivoproudé testování ve studentských pracích TU v Liberci [Non-destructive magnetic and eddy current testing in student projects at the Technical University of Liberec]. Sborník přednášek z konference DEFEKTOSKOPIE 2019. České Budějovice. 7-9 November 2019. ISBN 978-80-214-5799-7.

[57] MRAZ J. SKRBEK B. (2019). Normy nedestruktivního zkoušení v Slovenské a České republice [Standards of non-destructive testing in Slovakia and the Czech Republic]. Sborník přednášek z konference DEFEKTOSKOPIE 2019. České Budějovice. 7-9 November 2019. ISBN 978-80-214-5799-7.

[58] MRAZ J. SKRBEK B. (2019). Tepelné zpracování jako součást procesu montáže motoru [Heat treatment as a part of the engine assembly process]. Asociace pro tepelné zpracování kovů. Conference Proceedings. Jihlava. 26-28 November 2019.

[59] MRAZ J. SKRBEK B. (2020). Příklady optimálního uplatnění litinových odlitků pro izotermicky kalené součásti [Examples of optimal application of cast iron castings for isothermally hardened components]. Časopis Slévárenství. 3-4/2020. ISSN 0037-6825.

[60] MRAZ J. SKRBEK B. (2020). Vlastnosti materiálů litinových sedel. vedení ventilů a pístních kroužků plynových motorů [Properties of materials for cast iron seats. valve guides. and piston rings in gas engines]. Časopis Slévárenství. 10-11/2020. ISSN 0037-6825.

[61] MRAZ J. SKRBEK B. (2021). Tribotests of valve seats made of ADI and Q-cryo cast iron with spheroidal graphite. Contribution of Metallography to Production Problem Solutions. J. Kasl. VZU Plzeň. 2021. Trans Tech Publications.

[62] MRAZ J. SKRBEK B. (2021). Austempering cast-iron valve guide and circulating wheels in modern gas engines. (Izotermické kalení litinových vedení ventilů a oběžných kol moderních plynových motorů). Conference on heat treatment of metal materials in modern industry 2021. ATZK z. s. Defect and Diffusion Forum.

[63] MRAZ J. SKRBEK B. (2021). Nedestruktivní testování hlav válců. sedel a ventilů ve výrobě a servisu [Non-destructive testing of cylinder heads. seats. and valves in production and service]. Defektoskopie 2021. ČNDT Prague. 2021. Proceedings. pp. 77-84. ISBN 978-80-214-5988-5.

[64] MRAZ J. SKRBEK B. (2021). Vlastnosti materiálů litinových sedel. vedení ventilů a pístních kroužků plynových motorů [Properties of Materials for Cast Iron Seats. Valve Guides. and Piston Rings in Gasoline Engines]. Conference 57th Foundry Days 2021. Foundry Society. Brno.[65] MRAZ J. SKRBEK B. (2021). Vliv výskytu vnitřních vad na funkčnost konkrétních součástí motorů z ADI. [The influence of the occurrence of internal

defects on the functionality of specific components of ADI engines]. 80th meeting of the Professional Commission for Ductile Iron and 54th meeting of Foundrymen's Discount. Czech Technical University in Prague.

[66] LI X. ZHANG Y. GAO Y. & LI G. (2018). Journal of Alloys and Compounds. 766. 243-249.

[67] COSTAGLIOLA F. MARINIELLO L. & PAPPALETTERE G. (2017). Thermal fatigue of cast irons: experiments and numerical simulations. Fatigue & Fracture of Engineering Materials & Structures. 40(7). 1117-1130.

[68] GURUMURTHY S. KRISHNARAJ V. & NARAYANASAMY R. (2013). Microstructural and mechanical characteristics of high silicon ductile cast iron for elevated temperature applications. Materials Science and Engineering A. 577. 167-175.

[69] PALANIKUMAR S. GNANAMOORTHY R. & KUMAR S. (2012). Effect of heat treatment on thermal fatigue properties of austempered ductile iron. International Journal of Cast Metals Research. 25(4). 228-235.

[70] MARINIELLO L. BOCCARUSSO M. & DE MARCO A. (2011). Thermal fatigue of gray cast iron: part II – modelling and simulation. International Journal of Fatigue. 33(1). 62-73.

[71] MRAZ J. SKRBEK B. The rigidity spreading of contact plate of TEDOM cylinder head of cylinders made of cast -iron with lamella's graphite before and after running.

[72] SUÁREZ A. & GONZÁLEZ-DONCEL G. (2016). Thermal fatigue in CGI and grey cast iron. International Journal of Fatigue. 84. 135-144.

[73] GUPTA S. VERMA D. & DWIVEDI D. K. (2019). Effect of silicon on thermal fatigue behaviour of ductile iron. International Journal of Cast Metals Research. 32(4-5). 186-195.

[74] JASKULSKI R. & STROJNY-NĘDZA A. (2018). Thermal fatigue resistance of nodular cast iron for exhaust manifold applications. Archives of Foundry Engineering. 18(2). 73-80.

[75] ROH J. KIM K. M. KWON J. & LEE K. R. (2016). Effects of microstructure on thermal conductivity of cast irons. Materials Science and Engineering A. 675. 436-441.

[76] ADACHI Y. OSHITA S. & AOKI K. (2019). Study on thermal fatigue properties of cast iron and its application to engine cylinder block. SAE International Journal of Engines. 12(2). 348-353.

[77] SHARIFIAN S. A. SOLTANIEH M. & TAHERZADEH MOUSAVIAN. R. (2019). Effects of graphite morphology on the thermal conductivity and thermal resistance of gray and compacted graphite iron cylinder heads. Journal of Thermal Analysis and Calorimetry. 137(2). 661-670.

[78] WANG Y. YU W. GUO H. LI H. & XU J. (2019). Effects of alloying elements on thermal conductivity and mechanical properties of compacted graphite iron cylinder head. Journal of Materials Engineering and Performance. 28(7). 3876-3884.

[79] ROY. G. G. (1984). Cast Irons for Automotive Cylinder Heads – Recent Developments. SAE Technical Paper 840132.

[80] ZHANG H. ZHANG J. & SHEN Y. (2011). Effect of alloying elements on the microstructure and properties of cast iron for cylinder heads. Journal of Materials Processing Technology. 211(5). 936-941.

[81] NELSON L. E. & KRAUSS. G. (2018). Heat Treatment: Principles and Techniques. ASM International.

[82] STRCH M. (1986). Reinforced Aluminum-Silicon Alloys for Automotive Cylinder Head Applications. SAE Technical Paper 860376.

[83] XU B. L. LI T. P. LI J. LIU X. H. BAI J. P. LI Z. H. & QIN. X. H. (2019). Experimental study of valve train noise and wear in an internal combustion engine.

[84] GOUWS B. D. MEYER H. & VAN VUUREN P. M. (2016). Wear of valve seats and inserts in gas engines using biogas.

[85] ZHANG J. LEE R. L. & PRUCKA R. (2015). Experimental study of the factors affecting valve train wear and valve recession in heavy-duty diesel engines.

[86] YANG J. LIU R. & LI Q. (2014). A review of the development of materials and surface treatments for valve seat inserts.

[87] LIU S. YANG R. & LIN W. (2012). Effects of valve bounce and valve seat wear on the performance of internal combustion engines.

[88] BHUSHAN B. (2013). Springer Handbook of Nanotechnology. Springer Science & Business Media.

[89] HOLMBERG K. & MATTHEWS A. (2001). Coefficients of friction. In Tribology of Natural and Artificial Joints (pp. 211-234). Springer.

[90] KOGUT L. & KOMVOPOULOS K. (2004). Coefficient of friction and contact pressure in elastic-plastic sliding contact. Journal of the Mechanics and Physics of Solids. 52(11). 2547-2572.

[91] SAYLES R. S. & THOMAS T. R. (1998). Frictional behaviour of road-surfacing aggregates. Journal of Physics D: Applied Physics. 31(24). 3333-3343.

[92] KEJZLAR P. MYSZKA D. a K. Highly accurate structural analysis of austempered ductile iron using EBSD technique. Metallography & Fractography 2022. poster. konf. April 2022.

[93] ČSN EN 1563:2018 (42 0474). Kovové materiály - Litina s kuličkovým grafitem [Metallic materials - Spheroidal graphite cast iron]. Praha: Úřad pro technickou normalizaci. metrologii a státní zkušebnictví. 2018.

[94] KUDRNOVSKÝ J. Drchal V. & Turek I. (2017). Spin-Flip Scattering in Magnetic Materials. Journal of Magnetism and Magnetic Materials. 432. 135-148. DOI: 10.1016/j.jmmm.2016.11.095.

[95] GALE W. F. Totemeier T. C. & Small C. (Eds.). (2011). Smithells Metals Reference Book. Butterworth-Heinemann.

[96] PORTER D. A. Easterling K. E. & Sherif. M. (2009). Phase Transformations in Metals and Alloys. CRC Press.

[97] FUERST M. et al. (2010). "Development and manufacturing of automotive engine valves." SAE International Journal of Materials and Manufacturing. 3(1). 44-51.

[98] MYSZKA D. et al. (2015). "Effect of manufacturing technology on the microstructure and properties of engine valves." Archives of Metallurgy and Materials. 60(2). 1213-1218.

[99] ŠLAPÁKOVÁ M. et al. (2015). "New trends in the production of engine valves." Procedia Engineering. 100. 1180-1186.

[100] NAIR M. (2011). "Valve manufacturing: challenges and trends." International Journal of Engineering Science and Technology. 3(6). 4812-4819.

[101] KASUYA T. et al. (2016). "Development of a hot isostatic pressed (HIP) sintered valve seat insert with enhanced machinability for automobile engines." Powder Metallurgy. 59(1). 50-56.

[102] HEYWOOD John B. (1988). Internal Combustion Engine Fundamentals. McGraw-Hill Education.

[102] PULKRABEK Willard W. (2004). Engineering Fundamentals of the Internal Combustion Engine. Prentice Hall.

[103] STONE R. (1999). Introduction to Internal Combustion Engines. Macmillan International Higher Education.

[104] TAYLOR Charles F. (1985). The Internal-Combustion Engine in Theory and Practice: Vol. 1 - Thermodynamics. Fluid Flow. Performance. MIT Press.

[105] LEWIS R. (2000). Wear of Diesel Engine Inlet Valves and Seats. Thesis Submitted for the Degree of Doctor of Philosophy. Department of Mechanical Engineering. University of Sheffield.

[106] MILLER J. C. (2012). Valve Mechanisms for High-Speed Engines. Cambridge University Press.

[107] GANESAN V. (2019). Internal Combustion Engines: Performance. Fuel Economy and Emissions. McGraw-Hill Education.

[108] ROTHBART H. A. (Editor). (2004). CAM Design Handbook. College of Science and Engineering. Fairleigh Dickinson University. Retrieved from Online: https://besthope.files.wordpress.com/2010/05/cam-design-handbook_2004.pdf

[109] DAWSON M. (2011). VALVE TRAIN ANALYSIS AND MODIFICATION: The Professional's Handbook. CarTech Inc.

[110] CROZET M. BERTHIER Y. SAULOT A. JONES D. & BOU-SAÏD B. (2021). Valve-seat components in a diesel engine: a tribological approach to limit wear. Mechanics & Industry. 22. 44. doi: 10.1051/meca/2021043. hal-03409761.

[111] KRÜGER G. (2002). Valve Seat Inserts: State of the Art End of 2001. Manager Research & Development. Bleistahl Prod. GmbH & Co. KG. Online: https://www.google.com/url?sa=t&rct=j&q=&esrc=s&source=web&cd=&ved=2ahUKEwih2JKa77v_AhX1SfEDHV9kBZgQFnoECDYQAQ&url=https%3A%2F%2Fdspace.tul.cz%2Fbitstream%2Fhandle%2F15240%2F149326%2FsedlaBleistahl.pdf%3Fsequence%3D18&usg=AOvVaw3eJkac-1otORlvfuo19j1y

[112] Deloro Stellite. (n.d.). Stellite™ Alloys. Retrieved June 19. 2023. from https://www.deloro.com/solutions/metallurgical-expertise/stellitetm-alloys/

[113] SZALA M. & Chocyk D. & Skic A. & Kamiński M. & Macek W. & Turek M. (2021). Effect of Nitrogen Ion Implantation on the Cavitation Erosion Resistance and Cobalt-Based Solid Solution Phase Transformations of HIPed Stellite 6. Materials. 14. 2324. 10.3390/ma14092324.

[114] MOTALLEBZADEH A. & Atar E. & Cimenoglu H. (2015). Microstructure and Tribological Properties of PTA Deposited Stellite 12 Coating on Steel Substrate. 3. 224-228. 10.13189/mst.2015.030505.

[115] CHEN L. Cui J. & Tong W. (Year of publication). "Effect of deep cryogenic treatment and tempering on microstructure and mechanical behaviors of a wear-resistant austempered alloyed bainitic ductile iron." State Key Laboratory of Rolling and Automation. Northeastern University.

[116] VLK F. Vozidlové spalovací motory. Brno: František Vlk. 2003. ISBN 80-238-8756-4.

[117] KOŽOUŠEK J. Spalovací motory. Praha: Státní nakladatelství technické literatury.1956.

[118] ŠTOSS M. Spalovací motory I. Brno: Rektorát Vysokého učení technického v Brně.1987.

[119] MACEK J. a B. SUK. Spalovací motory I. Praha: Vydavatelství ČVUT. 1996. ISBN 80-01-00919-X.

[120] ČSN EN ISO 6507-1 (420359) Kovové materiály - Zkouška tvrdosti podle Vickerse - Část 1: Zkušební metoda. Praha: Úřad pro technickou normalizaci. metrologii a státní zkušebnictví. 2015

[121] ČSN 42 0316 (420316) Zkoušení kovů. Zkušební tyče válcové se závitovými hlavami pro zkoušku tahem. Praha: Úřad pro technickou normalizaci. metrologii a státní zkušebnictví. 1981

[122] ČSN EN 1071-13: Special technical ceramics - Test methods for ceramic coatings - Part 13: Determination of wear rate by the disk method. Praha. Úřad pro technickou normalizaci. metrologii a státní zkušebnictví. 2010

[123] ISO 10204:2017 - Metal products - Types of material control documents. Praha. Úřad pro technickou normalizaci. metrologii a státní zkušebnictví. 1991

[124] EXNER J., Čech J., Rusin K. (1982). On some physical properties on dynamically stressed automobile gray iron castings. In: 49th International Foundry Congress, Chicago, April 14-17, 1982.

[125] MYSZKA D., BOROWSKI T., BABUL T. Influence of cryogenic treatment on microstructure and hardness of austempered ductile iron. Institute of Precision Mechanics, ul. Duchnicka 3, 01-796 Warsaw, Poland.

[126] THIEL G. R. (1996). Effects of refrigeration and cryogenic treatments on austempered ductile iron. University of Northern Iowa.

[127] SOLIĆ S., Godec, M., Schauperl, Z., & Donik, Č. (2016). Improvement in Abrasion Wear Resistance and Microstructural Changes with Deep Cryogenic Treatment of Austempered Ductile Cast Iron (ADI). Metallurgical and Materials Transactions A, 47(11), 5578-5586. DOI: 10.1007/s11661-016-3659-4. The Minerals, Metals & Materials Society and ASM International.

[128] PANNEERSELVAM S., Martis C. J., Putatunda S. K., & Boileau J. M. (Year not provided). An investigation on the stability of austenite in Austempered Ductile Cast Iron (ADI). Department of Chemical Engineering and Materials Science, Wayne State University, Detroit, MI 48202, USA. Research and Innovation Center, Ford Motor Company, Dearborn, MI, USA.

[129] DAVIS J. R. (Ed.). (2000). ASM Specialty Handbook: Nickel, Cobalt, and Their Alloys. Davis & Associates. ISBN: 0-87170-685-7. Printed in the United States of America.

[130] WANG J., Xiong J., Fan H., Yang H.-S., Liu H.-H., & Shen B.-L. (2008). Effects of hig temperature and cryogenic treatment on the microstructure and abrasion resistance of a high chromium cast iron. School of Manufacturing Science and Engineering, Sichuan University.

[131] THORNTON R., Slatter T., Jones A. H., & Lewis R. (2010). The effects of cryogenic processing on the wear resistance of grey cast iron brake discs. Department of Mechanical Engineering, The University of Sheffield, United Kingdom.

[132] SKRBEK B., Hampl J. (bez data). Ausferrite Flake Graphite Cast Iron at Thermal Fatigue. KMT SF TU Liberec, Studentská 2, 461 17, Liberec. 2015

[133] Český normalizační institut. (1990). ČSN 42 2425 - Litina 42 2425 s lupínkovým grafitem. Praha: Český normalizační institut.

[134] Hu Z., & Du Y. (2023). Mechanical and Tribological Behavior of Austempered Ductile Iron (ADI) under Dry Sliding Conditions. School of Materials Science and Engineering, Xi'an University of Technology, Xi'an 710048, China. Published: 18 April 2023.

[135] Yang, Shu, "Cryogenic burnishing of Co-Cr-Mo biomedical alloy for enhanced surface integrity and improved wear performance" (2012). Theses and Dissertations -Mechanical Engineering. 10.

LIST OF AUTHOR PUBLICATIONS

1. **MRÁZ, Jakub** and Břetislav SKRBEK. Technical Parameters of Castings for Valve Seats Made of Cast Iron and Stellite-Type Carbide Structure Alloys. *Proceedings of Lectures from the 55th Foundry Days*, Block F – Iron Metallurgy Section. 1st ed. Brno: Czech Foundry Society, 2018. pp. 41 – 48.

2. **MRÁZ, Jakub** and Břetislav SKRBEK. Ultrasonic Diagnostics of Stiffness of the Cylinder Head Gasket of Tedom Engines Made of Flake Graphite Cast Iron Before and After Operation. *NDT for Safety / Defektoskopie 2018*. 1st ed. Prague: Czech Society for Nondestructive Testing, 2018. pp. 229 – 241. ISBN 978-80-214-5684-6.

3. **MRÁZ, Jakub** and Břetislav SKRBEK. Influence of internal defects on the functionality of specific components in adi engines. *80th Meeting of the Expert Committee for Spheroidal Graphite Iron and 54th Meeting of Foundrymen of the Czech Society of Foundrymen*, 2018 Central Bohemia, Czech Technical University in Prague.

4. **MRÁZ, Jakub** and Břetislav SKRBEK. Technical Acceptance of Critical Castings of the Product. *Proceedings of Lectures from the 56th Foundry Days.* 1st ed. Brno: Czech Foundry Society, z.s., 2019. pp. 179 – 191. ISBN 978-80-02-02882-6.

5. **MRÁZ, Jakub** and Břetislav SKRBEK. Expanded Utilization of Test Bars for Castings Certification. *Proceedings of Lectures from the 56th Foundry Days*. 1st ed. Brno: Czech Foundry Society, z.s., 2019. pp. 192 – 194. ISBN 978-80-02-02882-6.

6. **MRÁZ, Jakub** and Břetislav SKRBEK. Heat Treatment as a Part of the Engine Assembly Process. *27th Days of Heat Treatment with International Participation*. 1st ed. Čerčany: Association for Heat Treatment of Metals - ECOSOND Ltd., 2019. Page numbers not specified (7 pages). ISBN 978-80-907043-2-9.

7. **MRÁZ, Jakub** a Břetislav SKRBEK. Measurement of the Young´s modulus of selected materials for valve seats in internal combustion engines. *Collaboration 2019*, Tatranská Lomnica, Žilinská Univerzita Žilina, ISBN 978-80-554-16548-2.

8. **MRÁZ, Jakub** and Břetislav SKRBEK. Influence of measurement position on the hardness values of precisely cast stellite valve seats. *Collaboration 2019*, Tatranská Lomnica, ŽU Žilina, ISBN 978-80-554-16548-2.

9. **MRÁZ, Jakub** a Břetislav SKRBEK. Components made of agi in Liaz/Tedom engines. *78th meeting of the Expert Commission for Spheroidal Graphite Iron at the Czech Foundry Society*. Prague 2019.

10. SKRBEK, Břetislav, **Jakub MRÁZ**, and Michal BOHÁČIK. Non-Destructive Magnetic and Eddy Current Testing in Student Projects at the Technical University of Liberec. *Defektoskopie 2019 NDT for Safety*. 1st ed. Prague: Brno University of Technology and Czech Society for Nondestructive Testing, 2019. pp. 1 – 5. ISBN 978-80-214-5799-7.

11. SKRBEK, Břetislav, Vladimír NOSEK, Michal BOHÁČIK, and **Jakub MRÁZ**. Standards of Non-Destructive Testing in Slovakia and the Czech Republic. *NDT Welding Bulletin*. 1st ed. 2019, vol. 29, no. 2-3. pp. 45 – 64. ISSN 1213-3825.

12. SKRBEK, Břetislav, Vladimír NOSEK, Michal BOHÁČIK, and **Jakub MRÁZ**. Standards of Non-Destructive Testing in Slovakia and the Czech Republic. *Proceedings of the lectures from the Defectoscopy Conference 2019*, České Budějovice. ISBN: 978-80-214-5799-7.

13. **MRÁZ, Jakub**. Measuring the physical properties of valve seats in combustion engines. LMP (Local Mechanical Properties) Conference, Prague 2019. Poster

14. **MRÁZ, Jakub** and Břetislav SKRBEK. Influence of Cryogenic Temperatures on Mechanical Properties of Valve Seats of Internal Combustion Engines. *Acta Mechanica Slovaca. 1st ed*. Košice: Faculty of Mechanical Engineering – Technical University of Košice, 2020, vol. 23, no. 4, pp. 52 – 57. ISSN 1335-2393.

15. SKRBEK, Břetislav and **Jakub MRÁZ**. Examples of optimal utilization of cast iron castings for isothermally quenched components. *Foundry Engineering*. Brno: Czech Republic Foundry Association, 2020, vol. 68, no. 3-4. pp. 85 – 88. ISSN 0037-6825.

16. **MRÁZ, Jakub** and Břetislav SKRBEK. Material characteristics of cast iron seats, valve guides and piston rings of gas engines. *Proceedings of Lectures from the 57th Foundry Days*. 1st ed. Czech Foundry Society, z.s., member of ČSVTS Prague, 2021. pp. 186 – 192. ISSN 0037-6825.

17. **MRÁZ, Jakub** and Břetislav SKRBEK. Austempering of cast-iron valve guides and circulating wheels in modern gas engines. *Days of Heat Treatment Conference*, ATZK, 2021, Jihlava, published in Materials Special Issue "Heat Treatment of Metallic Materials in Modern Industry." ISSN 1996-1944

18. **MRÁZ, Jakub** and Břetislav SKRBEK. Isothermal Hardening of Cast Iron Valve Seats and Impeller Blades in Contemporary Gas Engines. *Days of Heat Treatment Conference*, ATZK, 2021, Jihlava, published in Materials Special Issue "Heat Treatment of Metallic Materials in Modern Industry." ISSN 1996-1944

19. SKRBEK, Břetislav and **Jakub MRÁZ**. Sliding Couples for Valve Guides and Valves of Piston Combustion Engines. *Conference Proceedings – METAL 2020 – 29th International Conference on Metallurgy and Materials*. Brno: TANGER Ltd., 2021. pp. 696 – 701. ISBN 978-80-87294-97-0, ISSN 2694-9296.

20. SKRBEK, Břetislav and **Jakub MRÁZ**. Non-destructive testing of cylinder heads, seats and valves in production and service. *Defektoskopie 2021*, City conference center, pp 77-81. Prague, ISBN 978-80-214-5988-5

21. **MRÁZ, Jakub** and Břetislav SKRBEK. Cast iron cylinder head seat plates in internal combustion engines. *Collaboration 2019*, Žilinská Univerzita Žilina, Rajecké Teplice, 4/2022, printed in Archives of Metallurgy and Materials, ISSN 1733-3490, IF 0.676.

22. SKRBEK, Břetislav and **Jakub MRÁZ**. Tribotests of valve seats made of ADI and Q - Cryo cast iron with spheroidal graphite. *Solid State Phenomena*. Vol 334. 2022. pp 82-86. 10.4028/p-43z866. ISSN 1662-9779

23. SKRBEK, Břetislav and **Jakub MRÁZ**. Contributions of ultrasound to more reliable engines. *Foundry Engineering*, 2023, pp. 74 – 77, ISSN 0037-6825.

LIST OF APPENDICES

10 APPENDIX

10.1 Friction Coefficient Profiles in the First loop of the Tribological testing

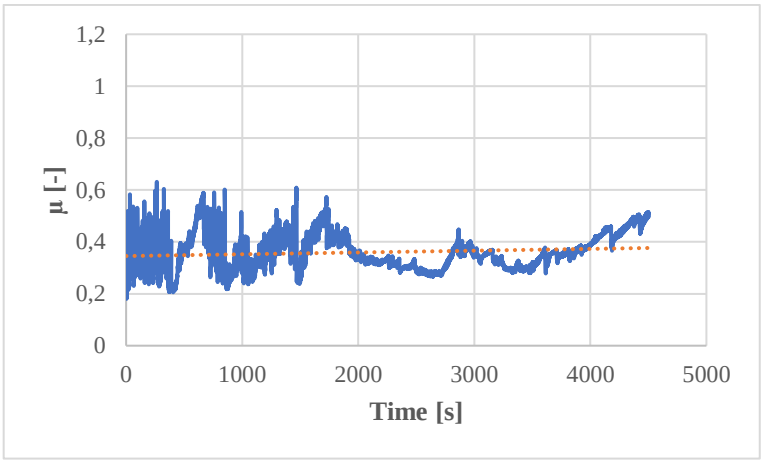

Fig. 61 Test No. 1 Disc - TEDOM Exhaust valve / Pin – ČSN 14 109

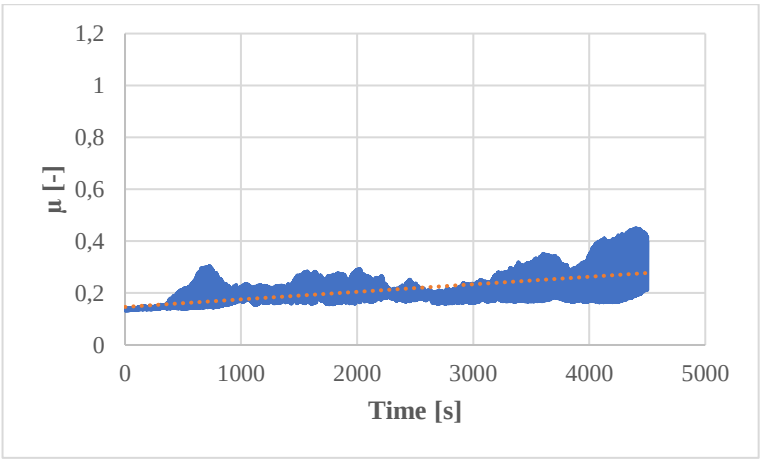

Fig. 62 Test No. 2 Disc - TEDOM Exhaust valve TRW / Pin – ČSN 14 109

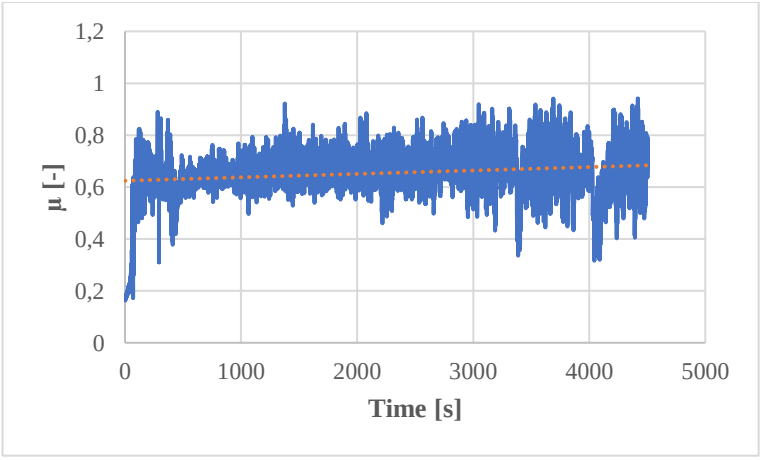

Fig. 63 Test No. 3 Disc - TEDOM Exhaust valve after operation / Pin – ČSN 14 109

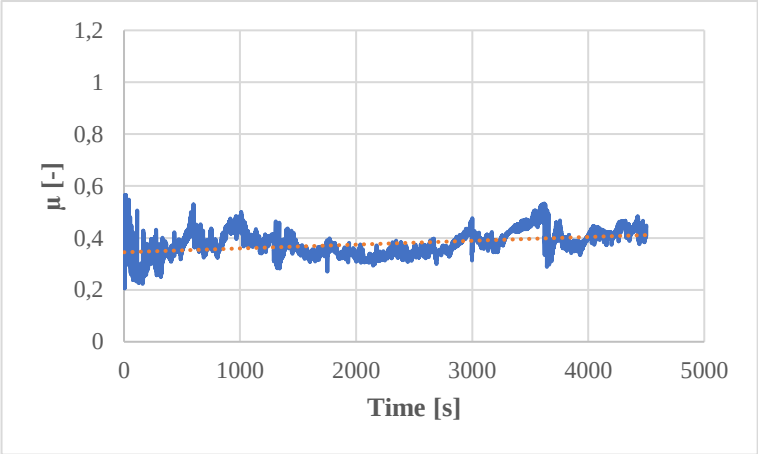

Fig. 64 Test No. 4 Disc - TEDOM Intake valve / Pin – ČSN 14 109

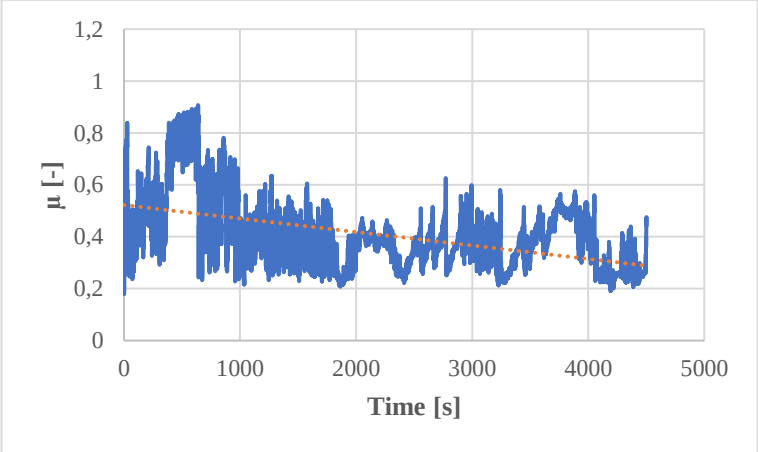

Fig. 65 Test No. 5 Disc - TEDOM Intake valve TRW / Pin – ČSN 14 109

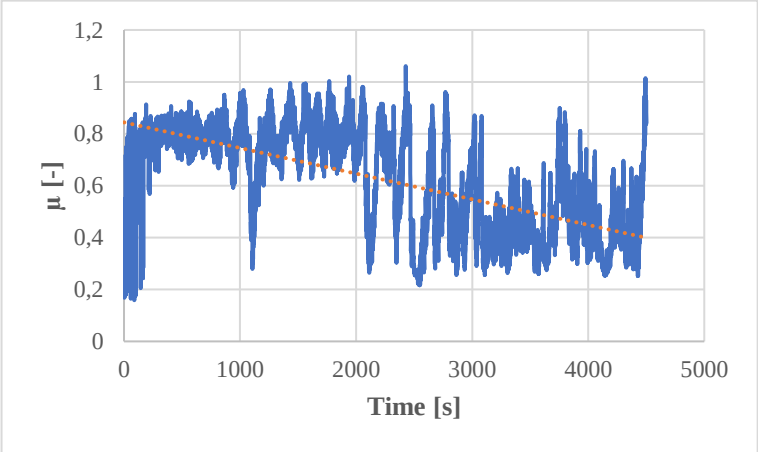

Fig. 66 Test No. 6 Disc - EM - SC Intake valve / Pin – ČSN 14 109

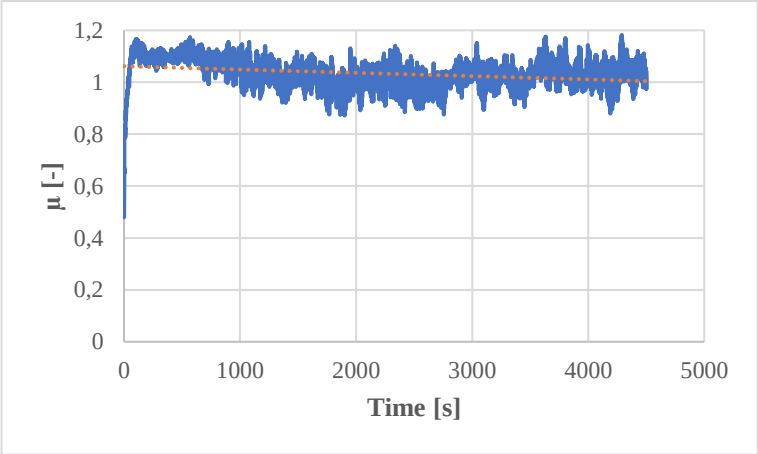

Fig. 67 Test No. 7 Disc - EM - SC Exhaust valve / Pin – ČSN 14 109

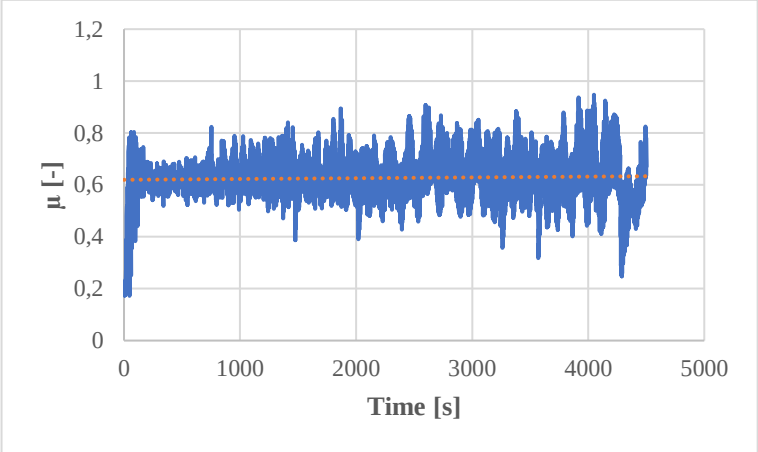

Fig. 68 Test No. 8 Disc - EM - LI Intake valve / Pin – ČSN 14 109

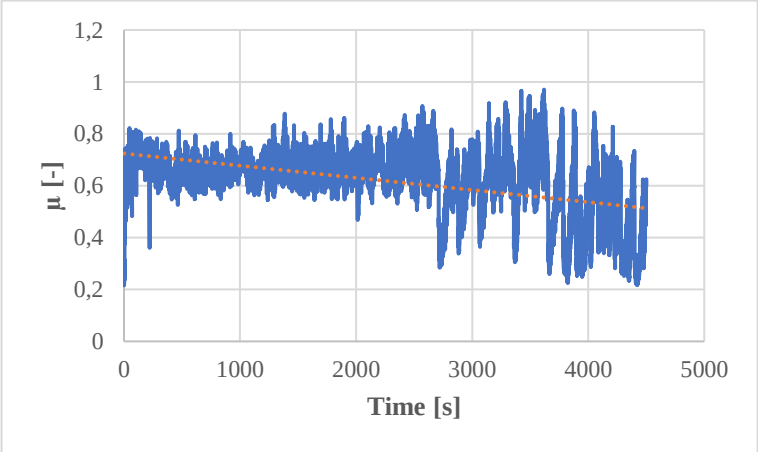

Fig. 69 Test No. 9 Disc - EM - LI Exhaust valve / Pin – ČSN 14 109

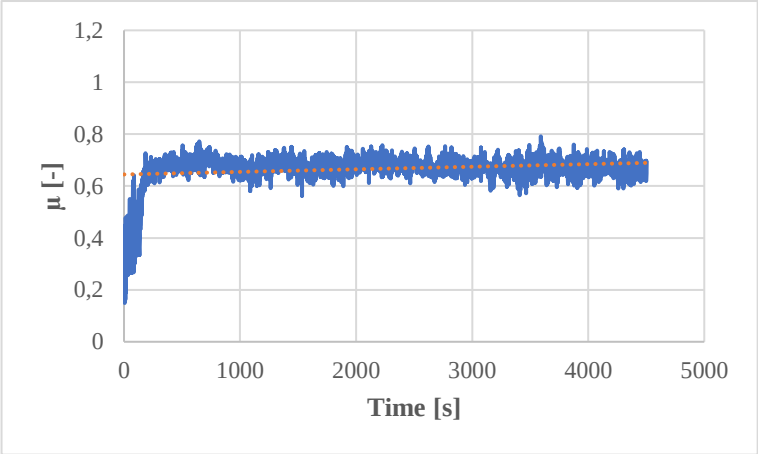

Fig. 70 Test No. 10 Disc - EM - SCH Intake valve / Pin – ČSN 14 109

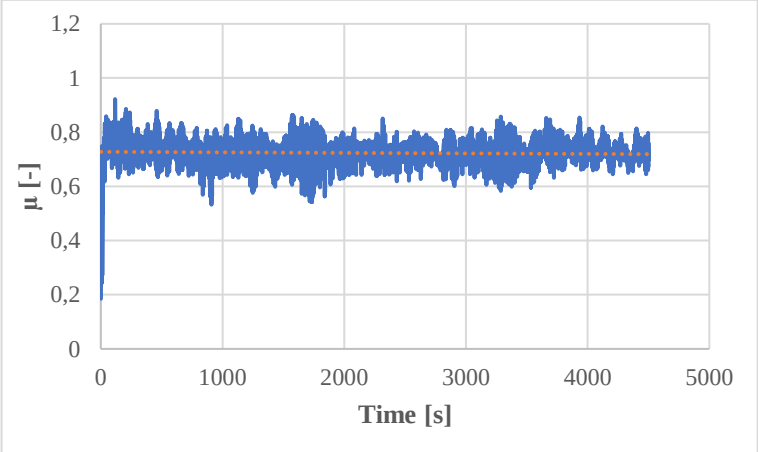

Fig. 71 Test No. 11 Disc - EM - SCH Exhaust valve / Pin – ČSN 14 109

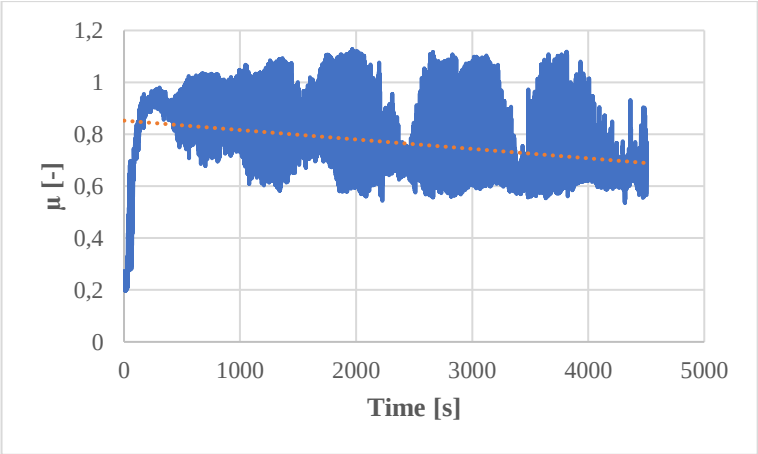

Fig. 72 Test No. 12 Disc - EM - KU Intake valve / Pin – ČSN 14 109

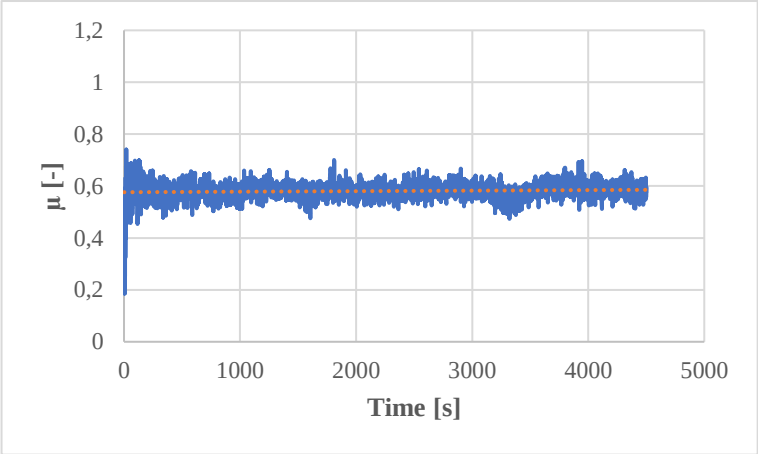

Fig. 73 Test No. 13 Disc - MAN Intake valve / Pin – ČSN 14 109

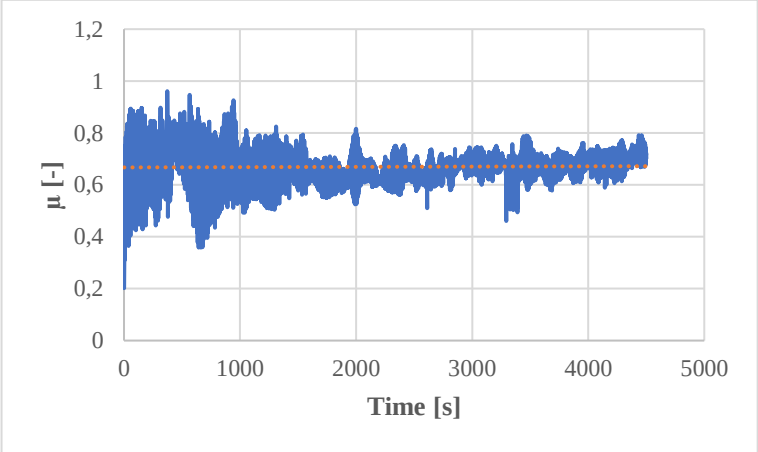

Fig. 74 Test No. 14 Disc - MAN Intake valve / Pin – ČSN 14 109

10.2 Friction Coefficient Profiles in the Second loop of the Tribological testing

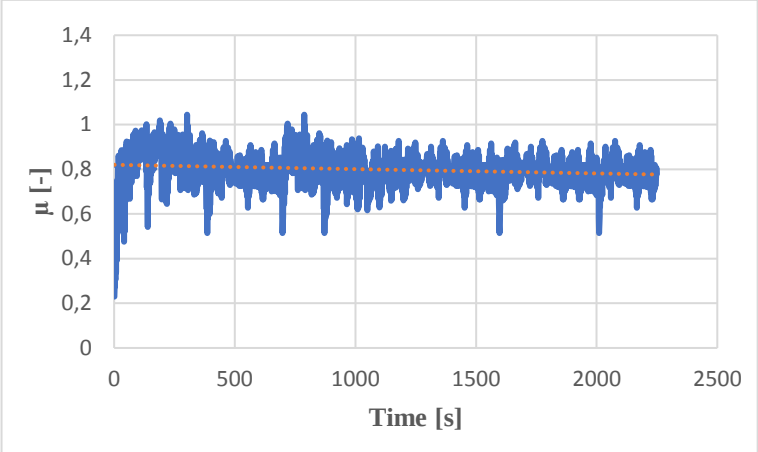

Fig. 75 Test No. 15 Disc – TEDOM Intake valve / Pin – ADI 280

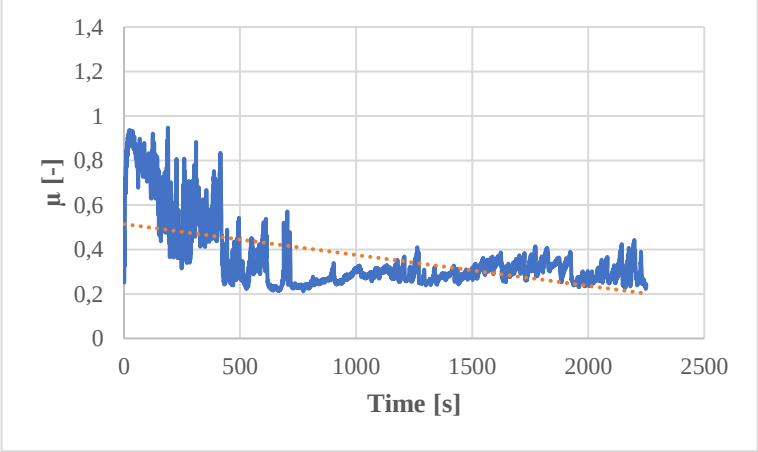

Fig. 76 Test No. 16 Disc – TEDOM Intake valve / Pin – ADI 280 Nitro

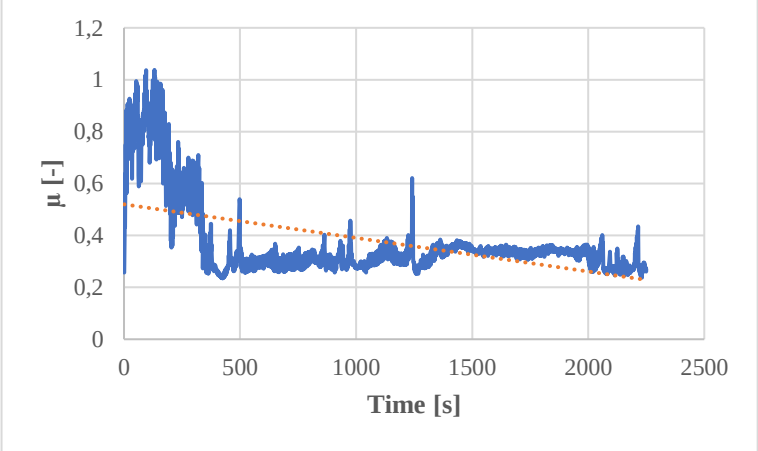

Fig. 77 Test No. 17 Disc – TEDOM Intake valve / Pin Q-Nitro

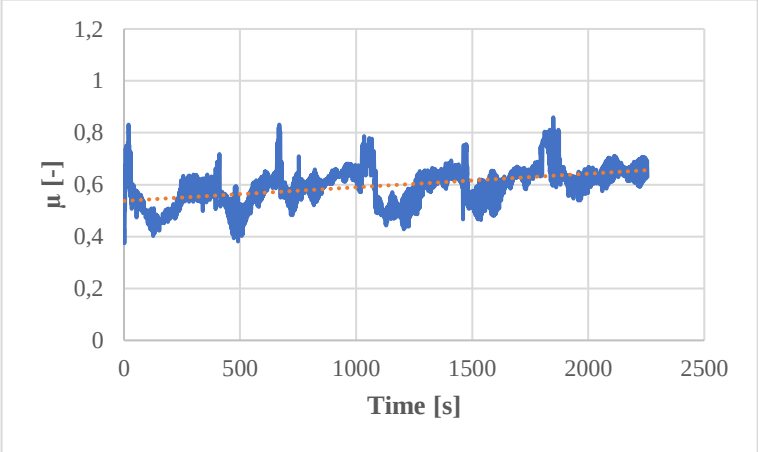

Fig. 78 Test No. 18 Disc – TEDOM Intake valve / Stellite 6 - Without freezing

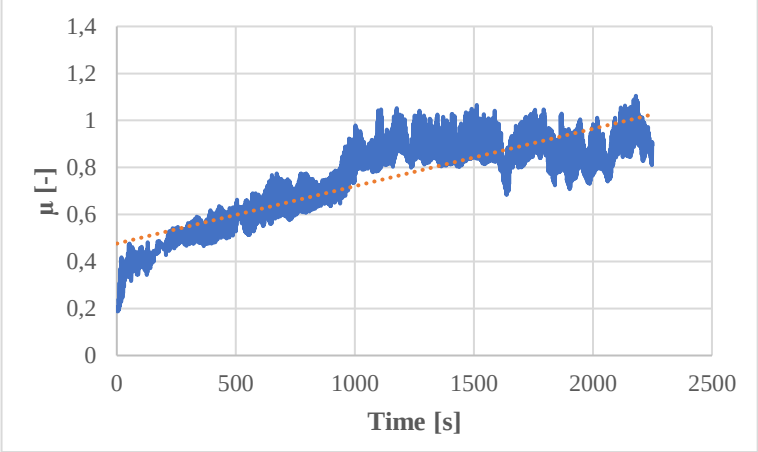

Fig. 79 Test No. 19 Disc – TEDOM Intake valve / Stellite 6 – Frozen 5 min.

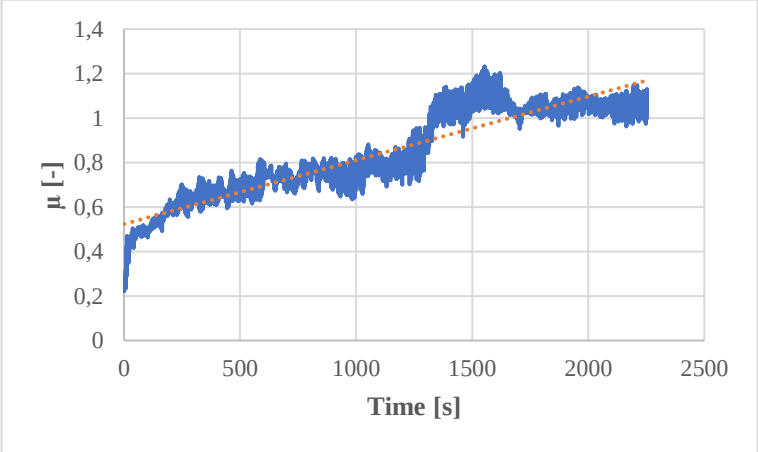

Fig. 80 Test No. 20 Disc – TEDOM Intake valve / Stellite 6 – Frozen 10 min.

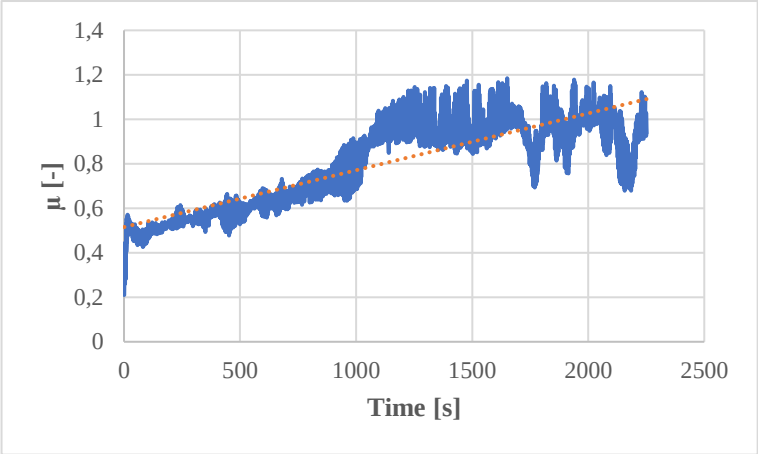

Fig. 81 Test No. 21 Disc – TEDOM Intake valve / Stellite 6 – Frozen 15 min.

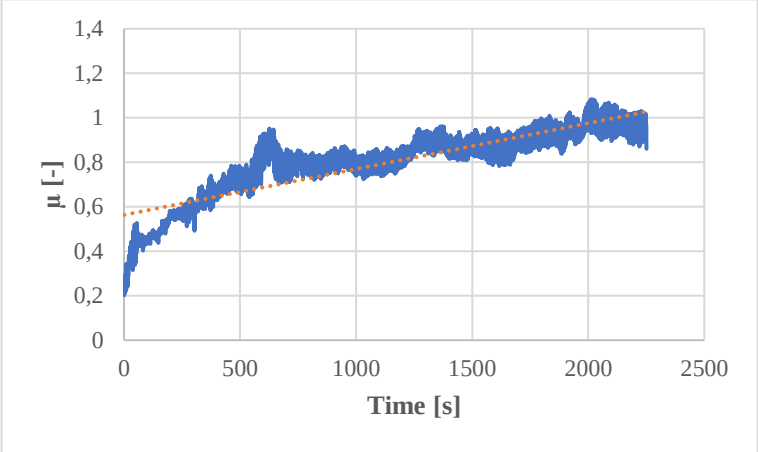

Fig. 82 Test No. 22 Disc – TEDOM Intake valve / Stellite 6 – Frozen 30 min.

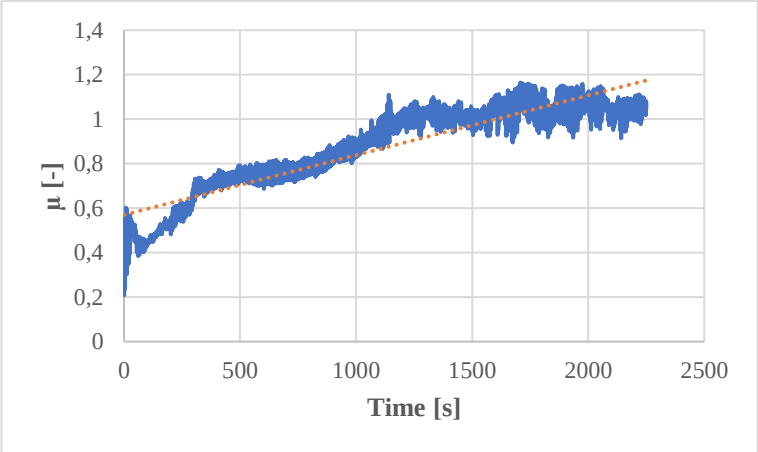

Fig. 83 Test No. 23 Disc – TEDOM Intake valve / Stellite 6 – Frozen 60 min.

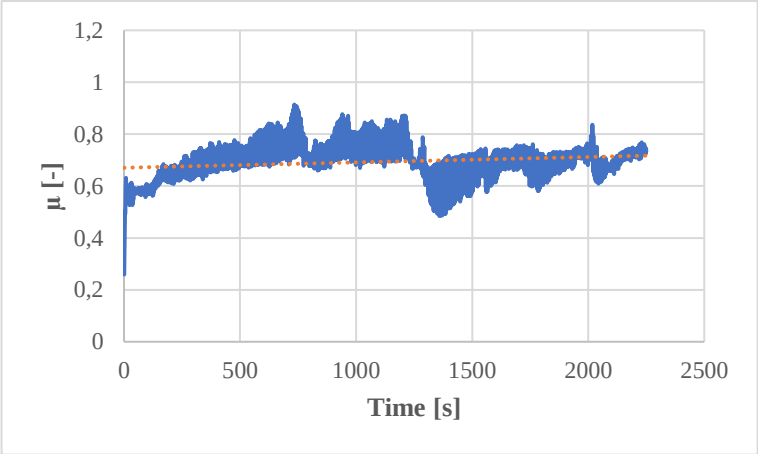

Fig. 84 Test No. 24 Disc – TEDOM Exhaust valve / Stellite 12 - Without freezing

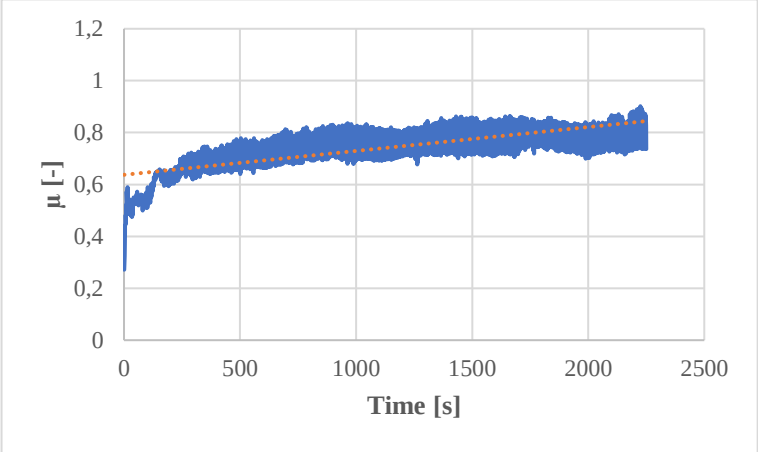

Fig. 85 Test No. 25 Disc – TEDOM Exhaust valve / Stellite 12 – Frozen 5 min.

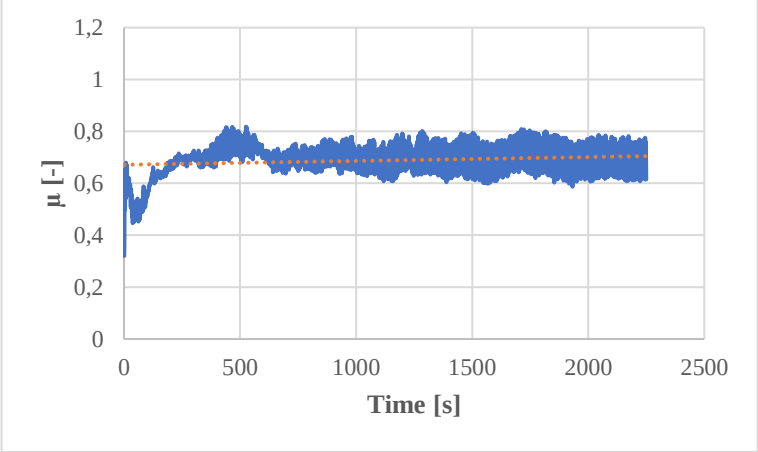

Fig. 86 Test No. 26 Disc – TEDOM Exhaust valve / Stellite 12 – Frozen 10 min.

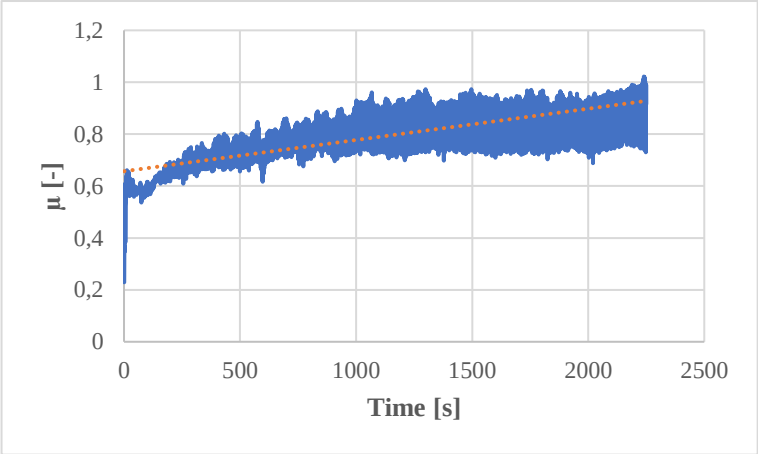

Fig. 87 Test No. 27 Disc – TEDOM Exhaust valve / Stellite 12 – Frozen 15 min.

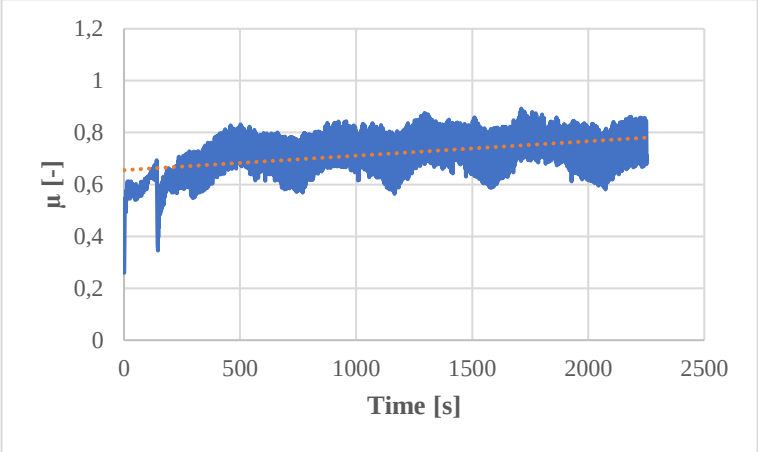

Fig. 88 Test No. 28 Disc – TEDOM Exhaust valve / Stellite 12 – Frozen 30 min.

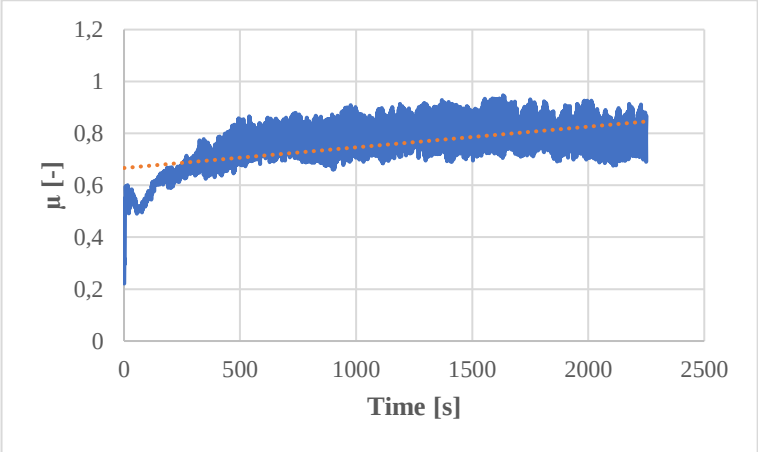

Fig. 89 Test No. 29 Disc – TEDOM Exhaust valve / Stellite 12 – Frozen 60 min.

10.3 Friction Coefficient Profiles in the Third loop of the Tribological testing

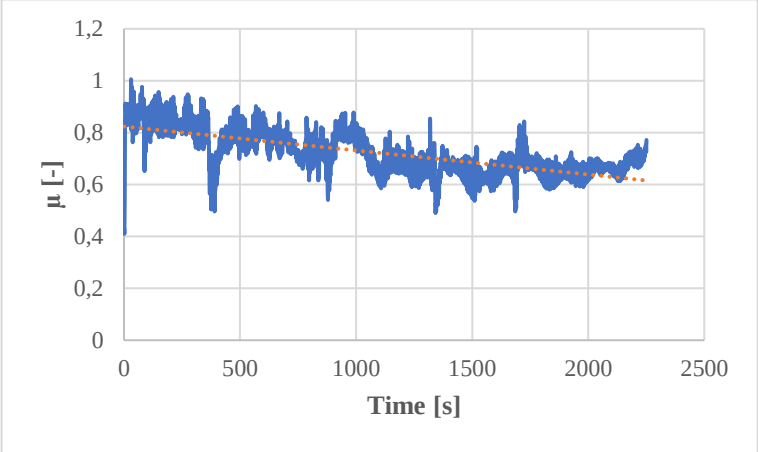

Fig. 90 Test No. 30 Disc – TEDOM Exhaust valve – After operation / Stellite 12

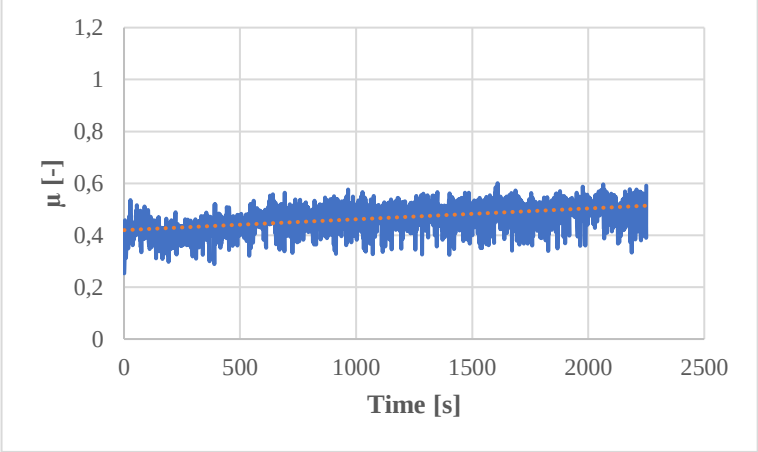

Fig. 91 Test No. 31 Disc – TEDOM Intake valve TRW / Stellite 6

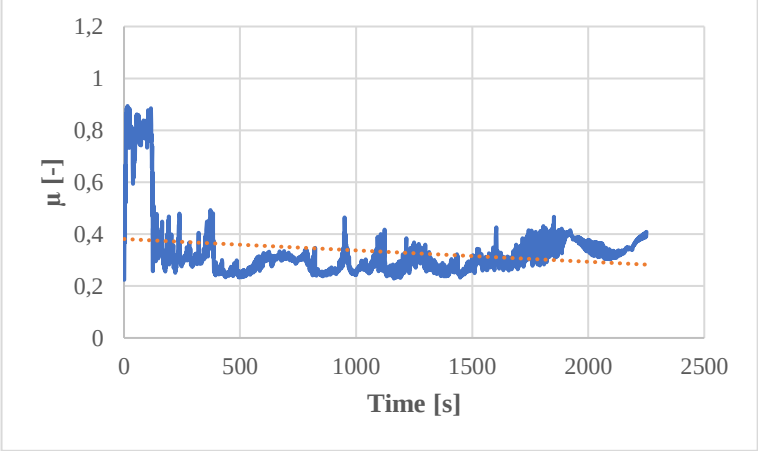

Fig. 92 Test No. 32 Disc – EM - SC Intake valve / EM - SC Intake seat

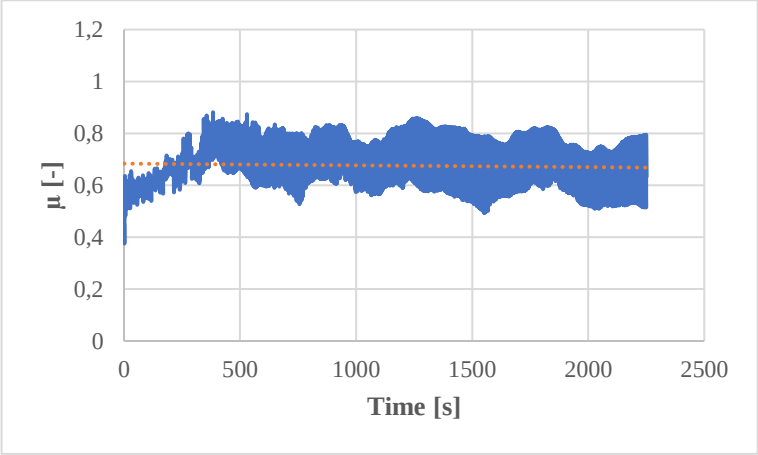

Fig. 93 Test No. 33 Disc – EM - SC Exhaust valve / EM - SC Exhaust seat

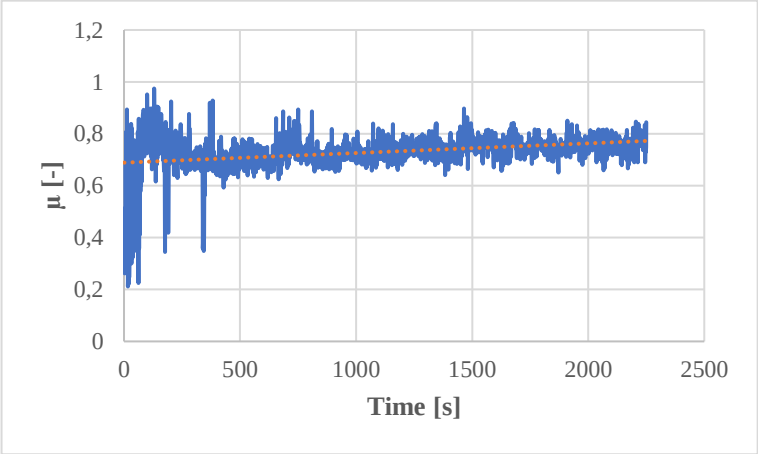

Fig. 94 Test No. 34 Disc – EM - LI Intake valve / EM - LI Intake seat

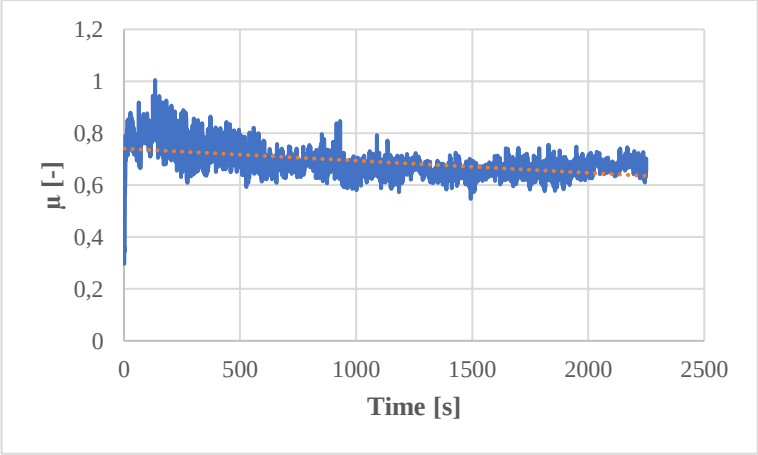

Fig. 95 Test No. 35 Disc – EM - LI Exhaust valve / EM - LI Exhaust seat

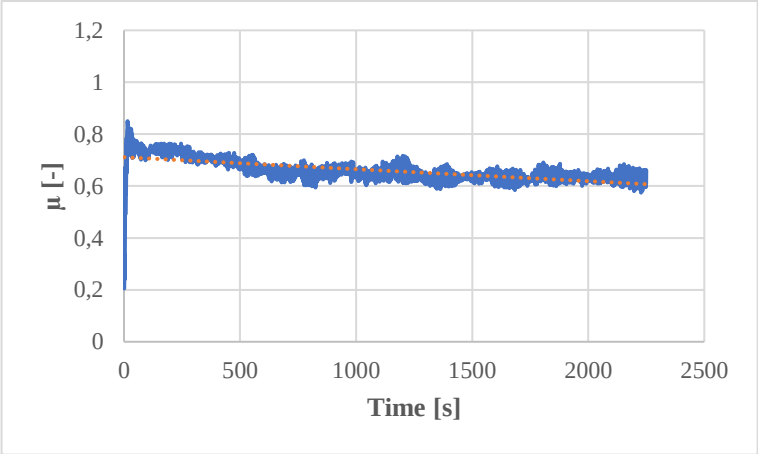

Fig. 96 Test No. 36 Disc – EM - SCH Intake valve / EM - SCH Intake seat

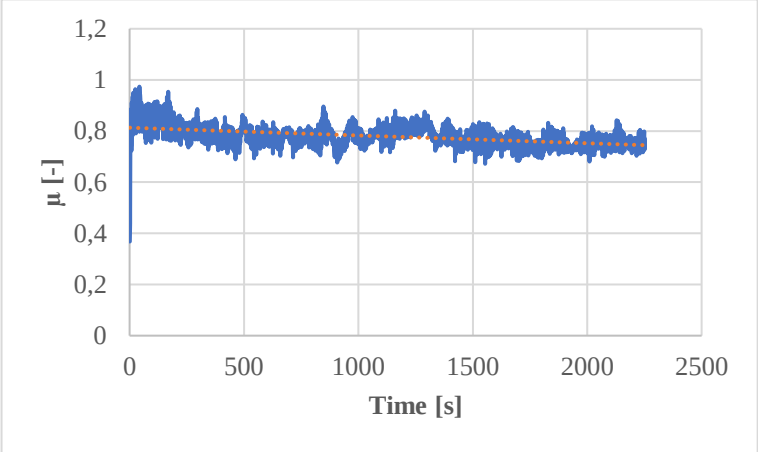

Fig. 97 Test No. 37 Disc – EM - SCH Exhaust valve / EM - SCH Exhaust seat

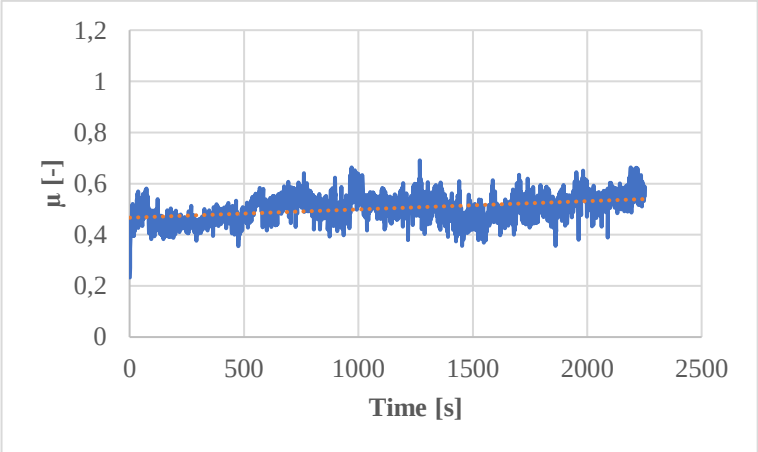

Fig. 98 Test No. 38 Disc – EM - KU Intake valve / EM - KU Intake seat

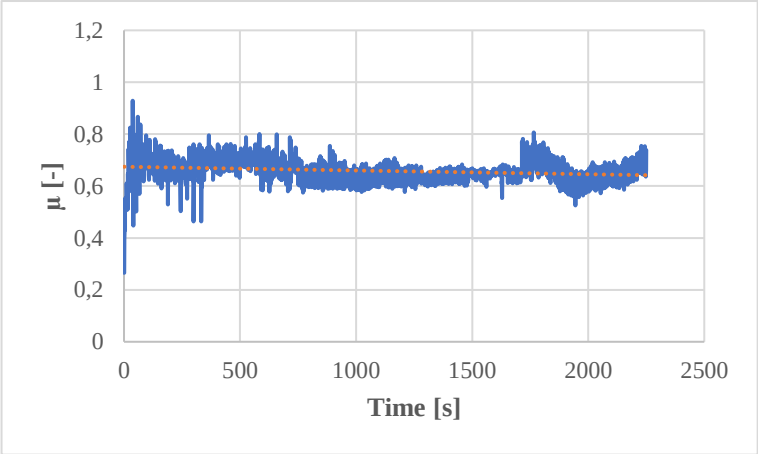

Fig. 99 Test No. 39 Disc – EM - MA Intake valve / EM - MA Intake seat

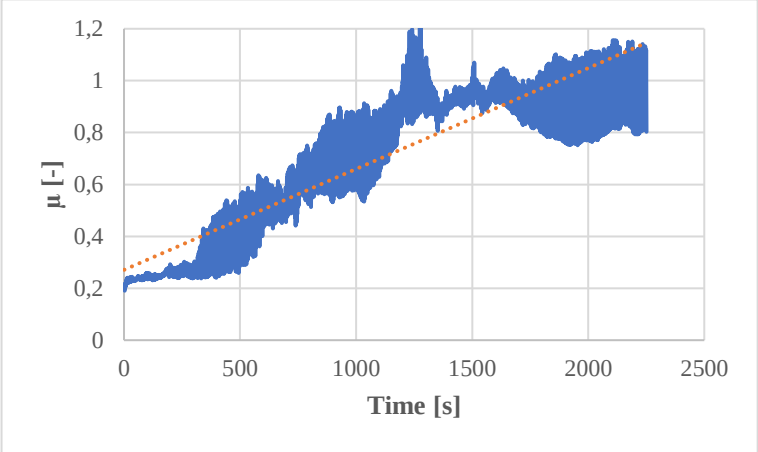

Fig. 100 Test No. 40 Disc – EM - MA Exhaust valve / EM - MA Exhaust seat

10.4 Friction Coefficient Profiles of Intermetallic Fe3Al in Tribological Testing

Aluminide Fe3Al, an intermetallic compound of iron and aluminum, exhibits unique physical properties due to its specific crystal structure. This compound combines high-temperature resistance with relatively low density (around 6.0 to 6.5 g/cm³), good mechanical strength (typically ranging from 100 MPa to 300 MPa), moderate hardness (approximately 150 to 250 HV), and a significant melting point of about 1500 to 1550 °C. It is characterized by this remarkable melting point, rendering it suitable for applications in extremely high-temperature environments, such as exhaust pipes of small combustion engines. With its resistance to oxidation and corrosion, it can serve as a protective coating or material for valve seats in these engines, where it's exposed to high temperatures and aggressive chemical surroundings. The thermal conductivity of Fe3Al ranges between approximately 20 to 40 W/(m·K).

Within the framework of tribological testing, we have decided to test the samples of aluminide on valves produced by EM-KU. We tested the samples on both the intake and exhaust valves.

The obtained results are depicted in Fig. 101 and 102. Test pins are illustrated in Fig. 103. In combination with the intake valve EM - KU, we measured a static friction coefficient of 0.2; on the exhaust valve EM KU, it was 0.26. We measured dynamic friction coefficient 0.550 ± 0.120 on the intake valve and 0.773 ± 0.064 on the exhaust valve.

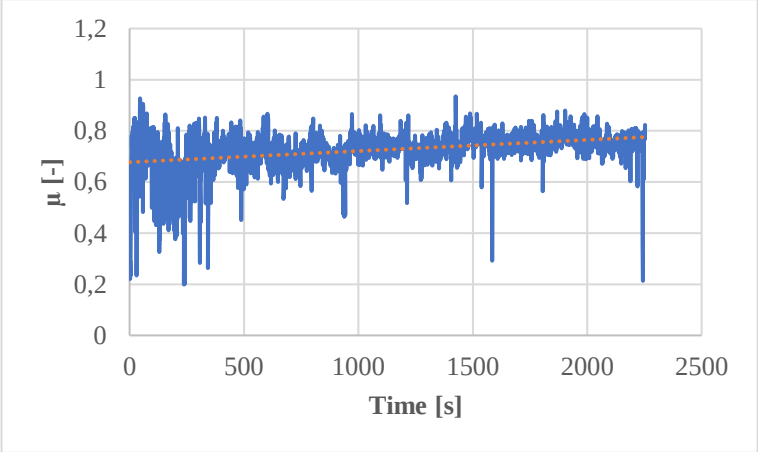

Fig. 101 Test No. 41 Disc – EM - KU Exhaust valve / Fe3Al

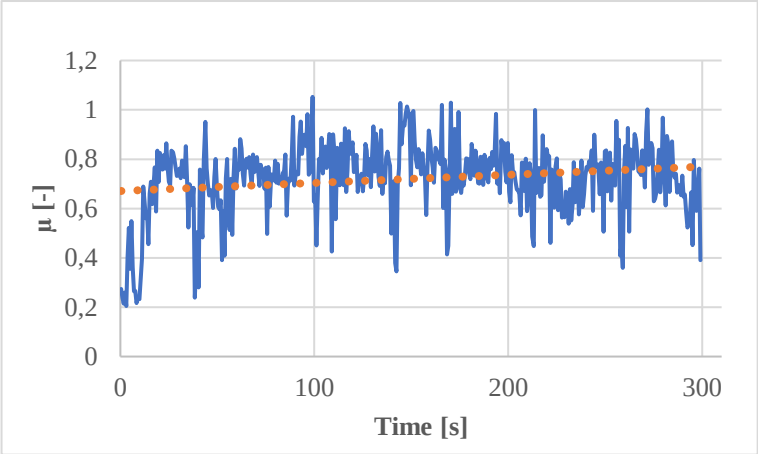

Fig. 102 Test No. 42 Disc – EM - KU Intake valve / Fe3Al

Fig. 103 Testing pins made from Fe3Al

10.5 Measured values of the contact plate of cylinder heads

Tab. 50 Measured values of the contact plate of the new cylinder head

Point	L_u [mm]	L_s [mm]	E_{oT} [GPa]	HB	EF [W/m]
1	20.54	16.54	133,2	205	11.088
2	20.36	16.38	132,9	208	11.23
3	19.24	15.76	137,8	204	11.194
4	17.76	14.94	145,3	199	11.176
5	17.39	13.94	132,0	201	10.843
6	17.76	14.44	135,8	207	11.278
7	18.69	15.02	132,6	209	11.271
8	19.99	15.92	130,3	204	10.934
9	20.73	17.12	140,1	206	11.37
10	21.56	17.46	134,7	207	11.241
11	22.21	17.8	131,9	210	11.295
12	22.58	18.2	133,4	208	11.248
13	22.39	17.96	132,2	208	11.203
14	21.84	17.58	133,1	203	10.983
15	21.47	17.14	130,9	205	11.007
16	15.73	12.34	126,4	202	10.692
17	14.99	12.14	134,7	201	10.938
18	14.8	11.96	134,1	203	11.019
19	15	12.28	137,7	207	11.341
20	17.95	14.42	132,6	207	11.167
21	15.17	12.26	134,2	209	11.323
22	15.73	12.62	132,2	205	11.054
23	20.54	16.5	132,5	195	10.558
24	15.73	13.08	142,0	198	11.022
25	16.28	13.22	135,4	198	10.809
26	22.76	18.36	133,7	200	10.851
27	15.07	12.44	140,0	226	12.369
28	20.36	16.7	138,2	209	11.459
29	22.66	18.36	134,8	207	11.246
30	22.58	18.28	134,6	208	11.289
31	22.21	17.92	133,7	206	11.157
32	22.21	17.68	130,2	207	11.081
33	21.55	17.38	133,6	204	11.05
34	21.84	17.72	135,2	206	11.21
35	21.65	17.88	140,1	206	11.37
36	20.2	18.16	166,0	206	12.11
37	21.28	16.98	130,8	208	11.15
38	20.36	16.28	131,3	205	11.02

39	18.87	15.6	140,4	204	11.28
40	18.69	14.96	131,6	207	11.13
41	18.97	15.04	129,1	208	11.09
42	19.8	16.14	136,5	206	11.25
43	20.91	16.9	134,2	202	10.97
44	18.87	15.26	134,3	202	10.98
45	14.62	12.02	138,8	200	11.02
46	14.25	11.66	137,5	199	10.93
47	14.25	11.58	135,6	198	10.82
48	14.9	12	133,2	202	10.94
49	16.1	13.06	135,1	203	11.05
50	15.91	12.88	134,6	202	10.99
51	20.91	16.82	132,9	202	10.93
52	15.36	12.34	132,6	204	11.02
53	14.99	11.88	129,0	205	10.94
54	14.06	11.3	132,7	219	11.77
55	15.36	12.35	132,8	211	11.38
56	16.19	12.77	127,8	205	10.89
57	22.39	18.04	133,3	207	11.19
58	21.65	17.50	134,2	208	11.03
59	22.58	18.34	135,5	201	11.02
60	22.58	18.15	132,7	202	11.01
61	18.17	14.70	134,3	204	11.01
62	18.15	14.68	134,3	205	11.00
63	18.13	14.66	134,3	205	10.99
64	18.10	14.64	134,2	205	10.98
65	18.08	14.62	134,2	205	10.97
66	18.06	14.60	134,2	205	10.96
67	18.03	14.58	134,2	205	10.96
68	18.01	14.56	134,2	205	10.95
69	17.99	14.54	134,2	205	10.94
70	17.96	14.52	134,2	205	10.93
71	17.94	14.50	134,1	205	10.92
72	17.92	14.48	134,1	205	10.94
73	17.89	14.46	134,1	205	11.02
74	17.87	14.44	134,1	205	11.34
75	17.85	14.42	134,1	205	11.17
76	17.82	14.40	134,1	205	11.32
77	17.80	14.39	134,0	205	11.05
78	17.78	14.37	134,0	205	10.56
79	17.75	14.35	134,0	205	11.02
80	17.73	14.33	134,0	205	10.81

81	17.70	14.31	134,0	205	10.85
82	17.68	14.29	134,0	205	12.37
83	17.66	14.27	134,0	205	10.99
84	17.63	14.25	133,9	205	11.17
85	17.61	14.23	133,9	205	11.32
86	17.59	14.21	133,9	205	11.05
87	17.56	14.19	133,9	205	10.56
88	17.54	14.17	133,9	205	11.02
89	17.52	14.15	133,9	205	10.81
90	17.49	14.13	133,9	205	11.09

Tab. 51 Measured values of the cylinder head contact plate after operation lifetime

Point	**L_u [mm]**	**L_s [mm]**	**E_o [MPa]**	**HB**	**EF [W/m]**
1	17.49	13.84	128,6	213	11.324
2	18.88	15.50	138,4	217	11.870
3	18.40	15.18	139,8	209	11.512
4	16.56	13.95	145,8	221	12.306
5	15.36	12.28	131,3	224	11.968
6	14.15	11.46	134,7	216	11.694
7	13.69	11.06	134,1	220	11.869
8	14.90	11.68	126,2	210	11.085
9	15.25	11.84	123,8	218	11.388
10	14.25	11.58	135,6	217	11.775
11	15.36	12.10	127,5	218	11.529
12	17.58	13.92	128,8	215	11.430
13	15.58	16.76	237,7	210	13.711
14	19.99	16.64	142,3	217	11.997
15	19.06	15.48	135,5	217	11.770
16	17.76	13.98	127,3	216	11.423
17	14.99	12.00	131,6	215	11.534
18	14.25	11.48	133,3	204	11.041
19	15.27	11.98	126,4	210	11.093
20	17.39	13.96	132,4	212	11.411
21	19.99	15.80	128,3	211	11.214
22	20.91	17.10	137,4	207	11.331
23	19.06	15.82	141,5	215	11.870
24	14.99	11.78	126,8	206	10.909
25	13.61	11.20	139,1	210	11.540
26	14.15	11.78	142,4	213	11.797
27	15.56	12.72	137,3	217	11.830

28	17.39	14.52	143,2	207	11.519
29	19.24	15.94	141,0	205	11.347
30	19.43	15.58	132,1	211	11.350
31	17.58	14.64	142,4	213	11.799
32	11.66	9.65	140,7	213	11.743
33	12.58	9.90	127,2	212	11.222
34	11.84	9.92	144,2	209	11.652
35	12.21	10.28	145,6	209	11.695
36	12.21	10.56	153,6	210	11.982
37	11.84	9.90	143,6	214	11.887
38	12.03	9.98	141,4	219	12.066
39	12.95	10.26	128,9	215	11.436
40	12.30	10.04	136,8	211	11.516
41	13.32	10.98	139,6	216	11.857
42	13.02	11.02	147,1	221	12.349
43	13.69	10.98	132,1	220	11.801
44	12.77	10.72	144,7	215	11.973
45	12.12	10.18	144,9	215	11.978
46	13.14	10.68	135,7	216	11.727
47	13.32	10.68	132,0	218	11.698
48	12.77	10.60	141,5	222	12.222
49	12.40	10.90	158,7	211	12.174
50	12.40	10.38	143,9	211	11.745
51	12.21	10.30	146,2	216	12.067
52	12.77	10.64	142,6	216	11.955
53	12.40	10.36	143,4	222	12.281
54	12.77	10.40	136,2	207	11.293
55	24.80	20.42	139,2	215	11.797
56	22.21	18.15	137,2	211	11.526
57	17.39	14.45	141,8	217	11.981
58	15.91	13.18	141,0	211	11.651
59	14.62	11.98	137,9	202	11.095
60	13.60	11.18	138,8	205	11.277
61	12.21	10.16	142,2	211	11.691
62	12.58	10.55	144,5	230	12.714
63	12.75	10.27	133,3	226	12.138
64	12.58	10.28	137,2	222	12.076
65	12.40	10.40	144,5	226	12.516
66	12.21	10.08	140,0	205	11.315
67	12.21	9.96	136,7	215	11.710

68	12.03	9.96	140,8	207	11.443
69	12.21	10.42	149,6	210	11.866
70	12.49	10.20	137,0	215	11.721
71	19.60	15.40	126,8	217	11.455
72	11.47	9.80	149,9	219	12.333
73	12.21	10.30	146,2	215	12.017
74	14.34	11.04	121,7	211	10.959
75	13.51	10.82	131,7	218	11.688
76	13.22	10.66	133,5	219	11.802
77	12.95	10.76	141,8	215	11.880
78	14.25	11.24	127,8	205	10.894
79	13.32	10.80	135,0	215	11.654
80	12.58	10.30	137,7	207	11.342
81	12.77	10.68	143,7	205	11.432
82	13.51	10.86	132,7	213	11.473
83	12.95	10.44	133,5	211	11.400
84	12.40	10.28	141,2	211	11.658
85	13.14	10.76	137,7	219	11.946
86	12.95	10.54	136,1	208	11.338
87	12.77	10.50	138,9	217	11.884
88	12.77	10.24	132,1	211	11.350
89	12.95	10.54	136,1	207	11.287
90	12.77	10.29	133,4	219	11.795

Fig. 104 Original cylinder head before and after preparing for testing

10.6 Aditional photos from the development of valve guide materials

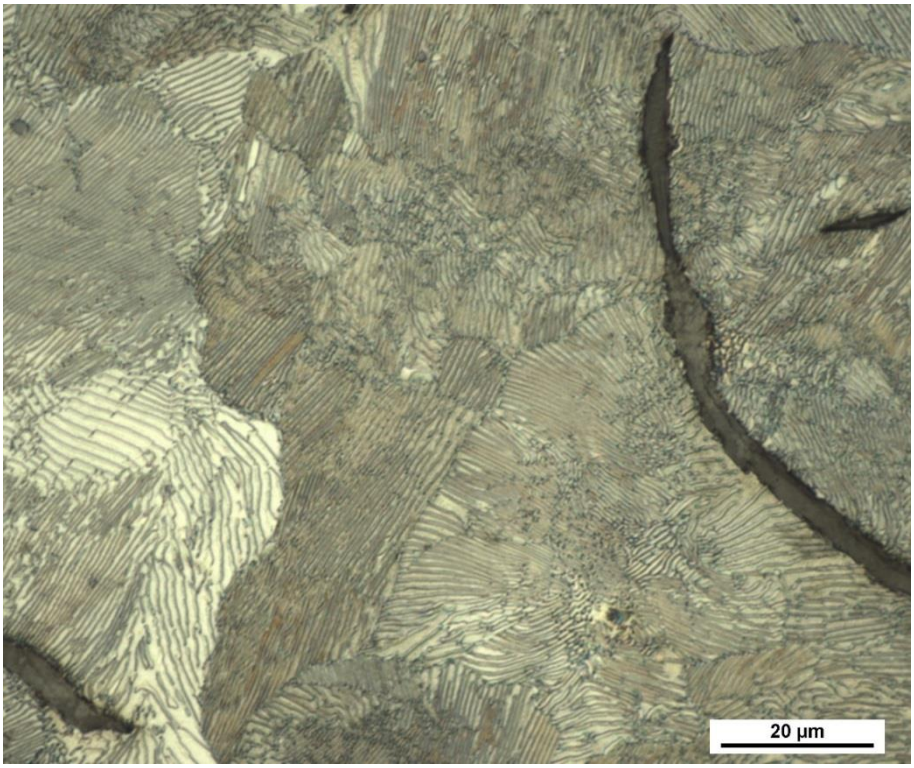

Fig. 105 EN-GJL 200 Microstructure

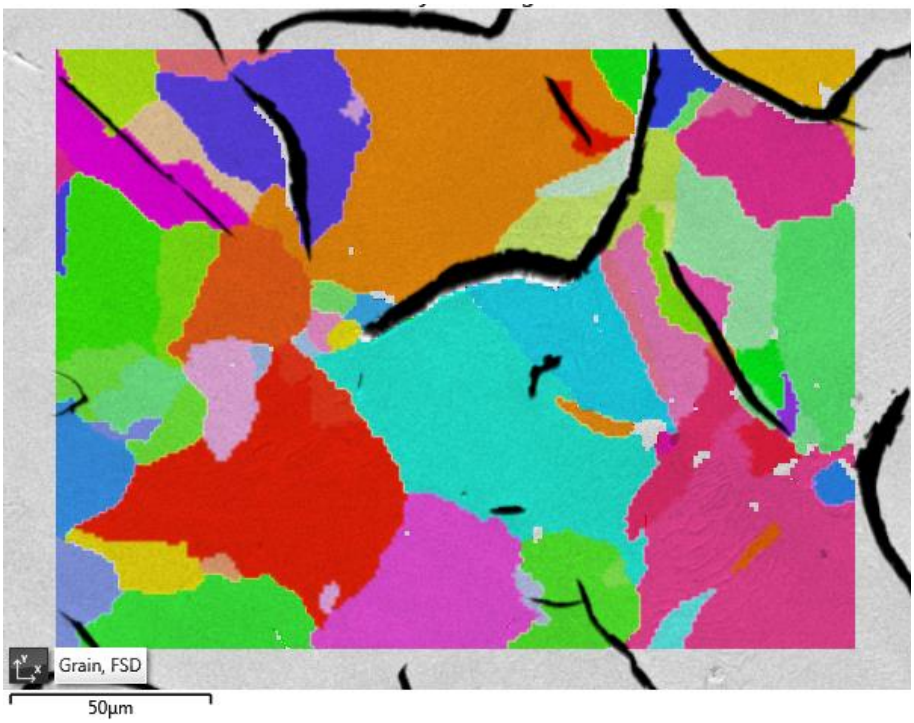

Fig. 106 EN- GJL 200 EBSD map. Magnification 500×. Colours represent detected grains. Average grain diameter is 25 µm.

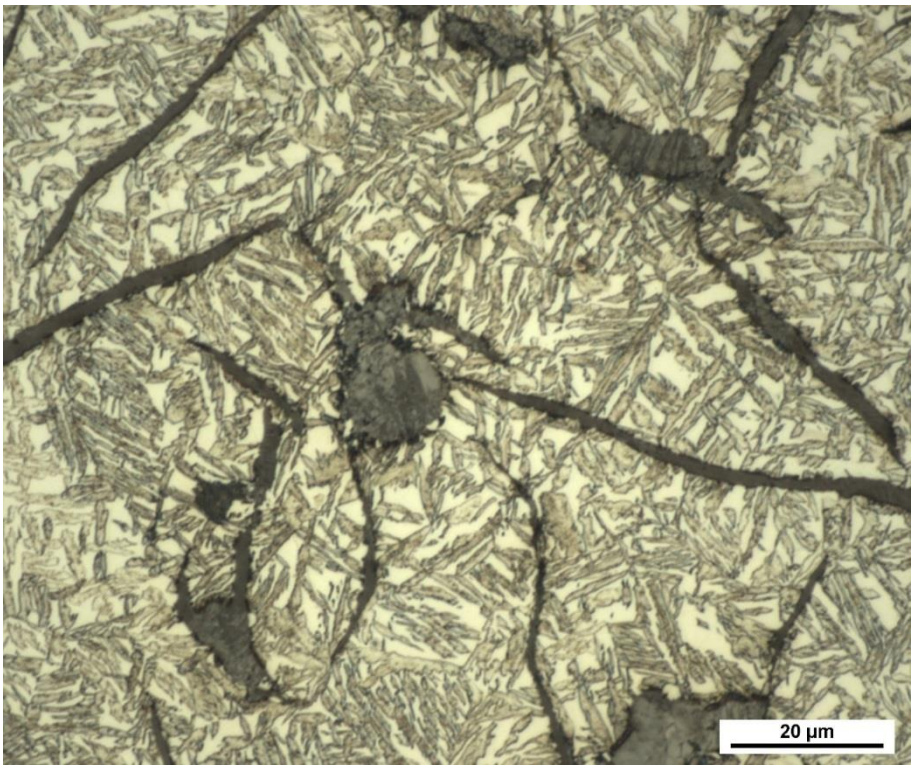

Fig. 107 AGI 410 Microstructure

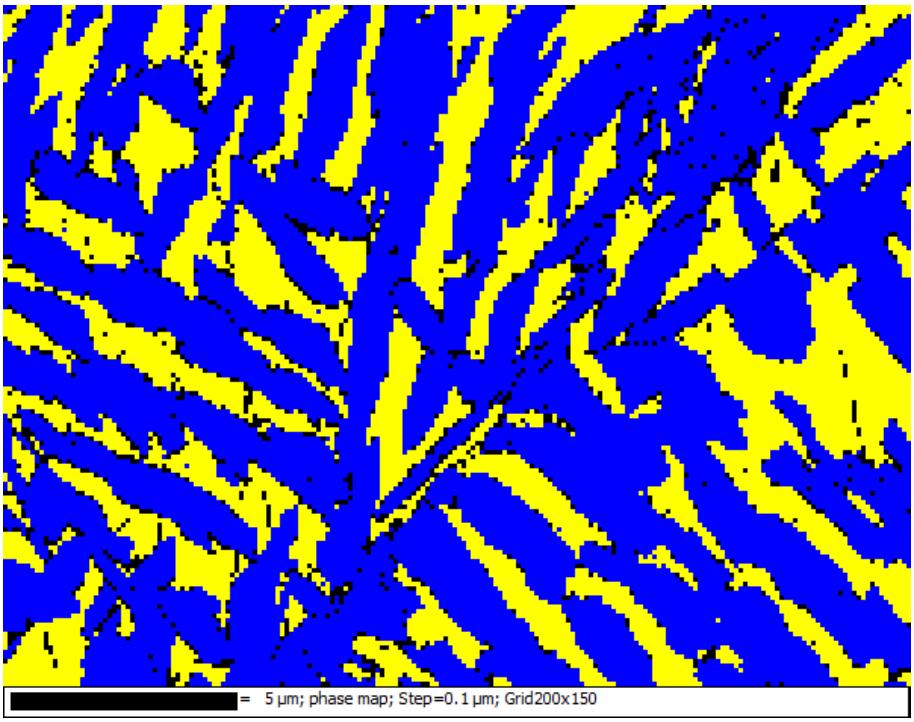

Fig. 108 AGI 410 EBSD map, MAG = 5000×. Blue colour represents ferrite with BCC lattice; yellow colour represents retained austenite with FCC lattice. Unindexed pixels are black.

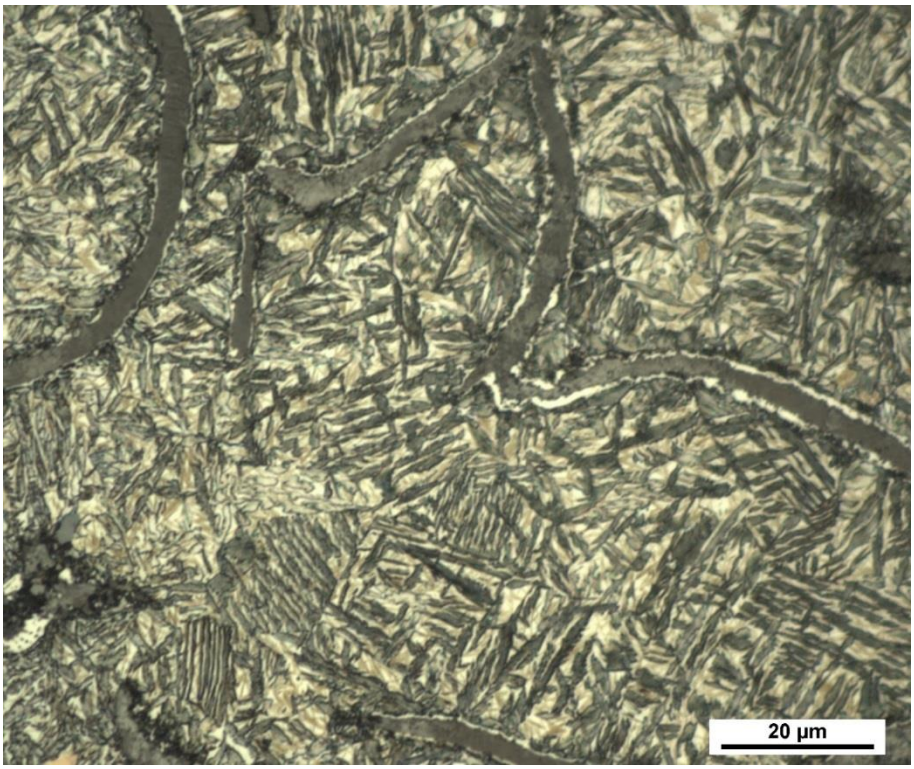

Fig. 109 AGI 410 N_{30} Microstructure

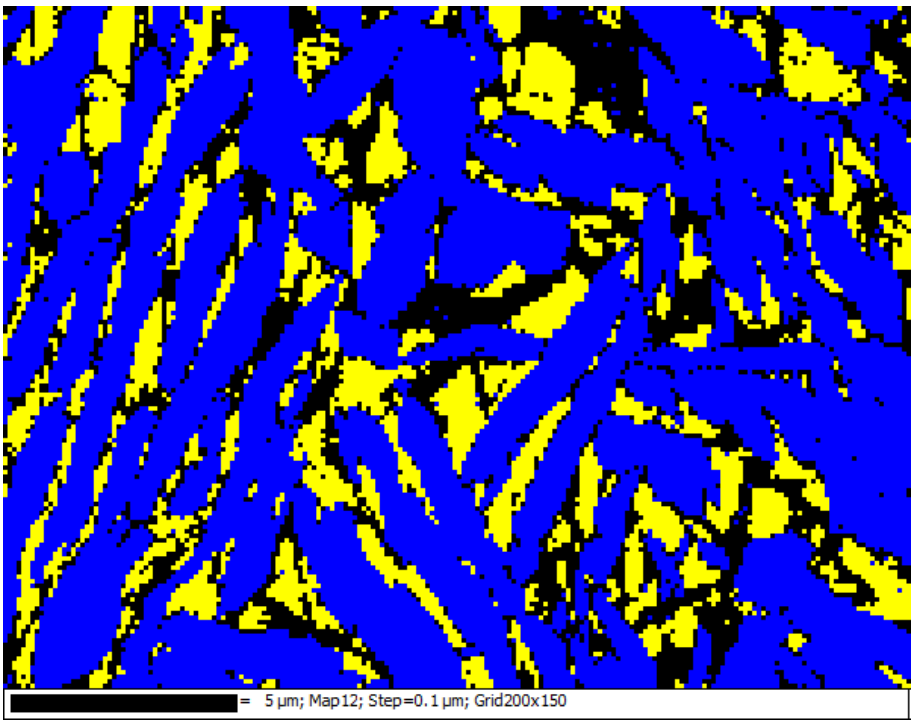

Fig. 110 AGI 410 N_{30} EBSD map MAG = 5000×. Blue colour represents ferrite with BCC lattice; yellow colour represents retained austenite with FCC lattice. Unindexed pixels are black.

10.7 Manufacturing drawings for ADI 280 and Q - Nitro valve seats

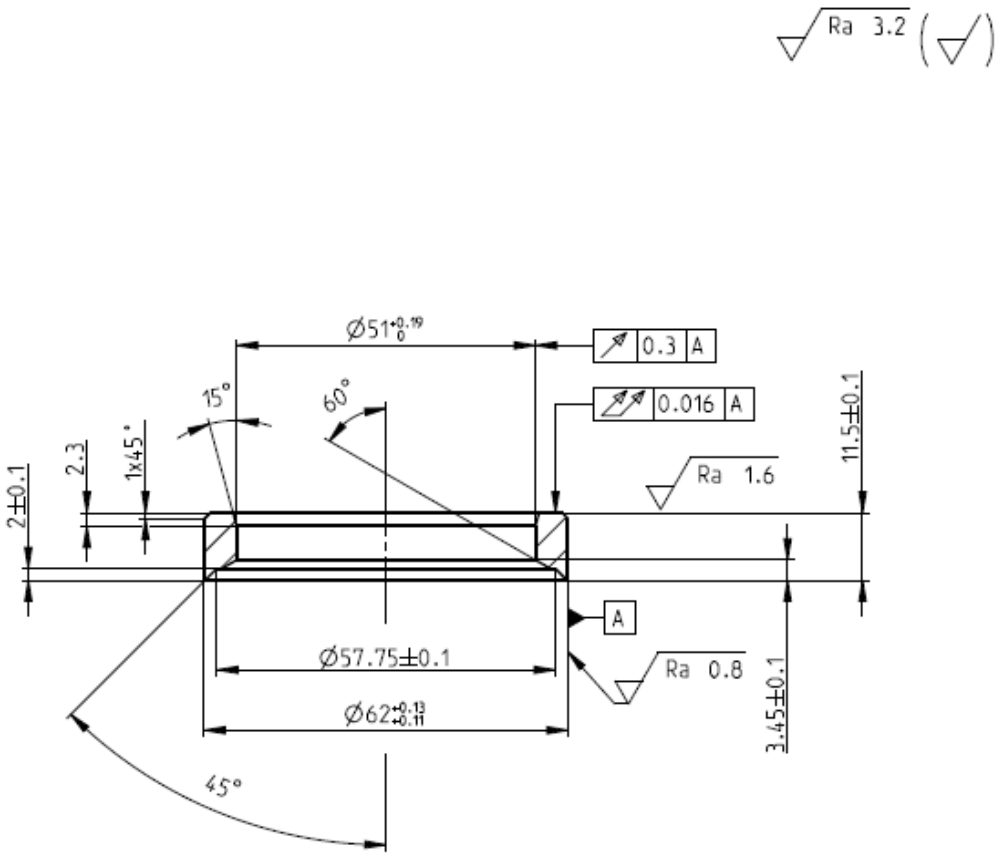

3. IZOTERMICKY KALIT NA AUSFERITICKOU STRUKTÚRU - TVRDOST 400-450HB
(2.) POUŽÍT ALTERNATIVNĚ EN-GJS-800
(1.) POLOTOVAR SHODNÝ S Č. V. 5036 031

NEPŘEDEPSANÉ ÚCHYLKY	DÉLKOVÉ ROZMĚRY					
	DO 6	PŘES 6 DO 30	PŘES 30 DO 120	PŘES 120 DO 400	PŘES 400 DO 1000	PŘES 1000
	±0.1	±0.2	±0.3	±0.5	±0.8	±1.2
	ZKOSENÍ A ZAOBLENÍ			ÚHLOVÉ ROZMĚRY (PRO DÉLKU KRATŠÍHO RAMENE)		
	DO 3	PŘES 3 DO 6	PŘES 6	DO 10	PŘES 10 DO 50	PŘES 50 DO 120
	±0.2	±0.5	±1.0	±1°	±0°30'	±0°20'
GEOMETRICKÉ TOLERANCE	PŘÍMOSTI A ROVINNOSTI					
	DO 10	PŘES 10 DO 30	PŘES 30 DO 100	PŘES 100 DO 300	PŘES 300 DO 1000	PŘES 1000
	0.05	0.1	0.2	0.4	0.6	0.8
	KOLMOSTI (PRO DÉLKU KRATŠÍ STRANY)			SOUMĚRNOSTI		KRUHOVÉ HÁZENÍ
	DO 100	PŘES 100 DO 300	PŘES 300	DO 300	PŘES 300	VŠECHNY ROZMĚRY
	0.4	0.6	0.8	0.6	0.8	0.2

				PŘESNOST: ISO 2768	MATERIÁL	
				TOLERANCE: ISO 8015	POLOTOVAR	(1.)(2.)
				PROMÍTÁNÍ:	NORMA	
				TŘ. ODPADU DLE ČSN 42 0030	HMOTNOST ODHADEM: 0,082kg	
				DUŠEVNÍ A PRŮMYSLOVÉ VLASTNICTVÍ		
ZMĚNA		DATUM	IND.	PODPIS	TEDOM a.s. DIVIZE MOTORY	
MĚŘÍTKO: 1:1	BEZPEČNOSTNÍ ZNAČKA:	KRESLIL		MRÁZ	ALL RIGHTS RESERVED POSTOUPITI TŘETÍM OSOBÁM NENÍ DOVOLENO	
		BEZPEČ. PŘEZK.			NÁZEV: SEDLO SACÍHO VENTILU-ADI	
		PŘEZKOUŠEL				
NEKÓT. RAD.		TECHNOLOG				
HRANY DÍLU		NORMALIZACE			Č. VÝKRESU: 18 075	INDEX:
Č. SESTAVY		SCHVÁLIL		MELICHERÍK		
ST. VÝKRES		DATUM		6.3.2018	POČET LISTŮ:	LIST Č.:

Fig. 111 Drawing of valve seat ADI 280

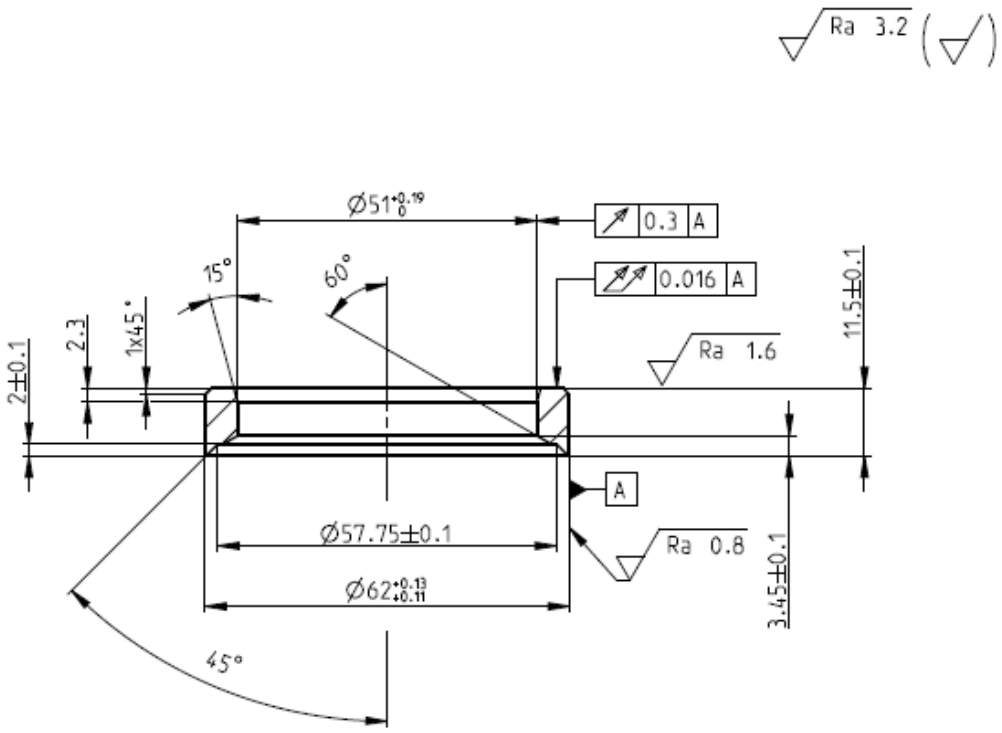

7. NÁSLEDNĚ SEDLÁ POPUSTIT PŘI TEPLOTĚ 180–200 °C – 2HOD.
6. PO 24HOD. NECHAT SEDLA OHŘÁT NA POKOJOVÚ TEPLOTU
5. PO 4HOD. POMALU OCHLADIT SEDLÁ V TEKUTÉM DUSÍKU (CCA 20 °C ZA MIN.) NA –195 °C A NÁSLEDNÍ VÝDRŽ NA TÉTO TEPLOTĚ PO DOBU 24HOD.
4. PO KALENÍ IZOTERMICKÁ VÝDRŽ NA POKOJOVÉ TEPLOTĚ – 4HOD.
3. KALIT NA TVRDOST 400–450HB
(2.) POUŽÍT ALTERNATIVNĚ EN-GJS-800
(1.) POLOTOVAR SHODNÝ S Č. V. 5036 031

NEPŘE-DEPSANÉ ÚCHYLKY	DÉLKOVÉ ROZMĚRY					
	DO 6	PŘES 6 DO 30	PŘES 30 DO 120	PŘES 120 DO 400	PŘES 400 DO 1000	PŘES 1000
	±0.1	±0.2	±0.3	±0.5	±0.8	±1.2
	ZKOSENÍ A ZAOBLENÍ			ÚHLOVÉ ROZMĚRY (PRO DÉLKU KRATŠÍHO RAMENE)		
	DO 3	PŘES 3 DO 6	PŘES 6	DO 10	PŘES 10 DO 50	PŘES 50 DO 120
	±0.2	±0.5	±1.0	±1°	±0°30'	±0°20'
GEOMETRICKÉ TOLERANCE	PŘÍMOSTI A ROVINNOSTI					
	DO 10	PŘES 10 DO 30	PŘES 30 DO 100	PŘES 100 DO 300	PŘES 300 DO 1000	PŘES 1000
	0,05	0,1	0,2	0,4	0,6	0,8
	KOLMOSTI (PRO DÉLKU KRATŠÍ STRANY)			SOUMĚRNOSTI		KRUHOVÉ HÁZENÍ
	DO 100	PŘES 100 DO 300	PŘES 300	DO 300	PŘES 300	VŠECHNY ROZMĚRY
	0.4	0.6	0.8	0.6	0.8	0.2

				PŘESNOST: ISO 2768	MATERIÁL	
				TOLERANCE: ISO 8015	POLOTOVAR	(1.)(2.)
				PROMÍTÁNÍ:	NORMA	
				TŘ. ODPADU DLE ČSN 42 0030	HMOTNOST ODHADEM: 0,082kg	
				DUŠEVNÍ A PRŮMYSLOVÉ VLASTNICTVÍ		
ZMĚNA		DATUM	IND.	PODPIS	TEDOM a.s. DIVIZE MOTORY	
MĚŘÍTKO: 1:1	BEZPEČNOSTNÍ ZNAČKA:	KRESLIL		MRÁZ	ALL RIGHTS RESERVED POSTOUPITI TŘETÍM OSOBÁM NENÍ DOVOLENO	
		BEZPEČ. PŘEZK.			NÁZEV: SEDLO SACÍHO VENTILU NITRO	
		PŘEZKOUŠEL				
NEKÓT. RAD.		TECHNOLOG				
HRANY DÍLU		NORMALIZACE				
Č. SESTAVY		SCHVÁLIL		MELICHERÍK	Č. VÝKRESU: 18 076	INDEX:
ST. VÝKRES		DATUM		7.3.2018	POČET LISTŮ:	LIST Č.:

Fig. 112 Drawing of valve seat – Q-Nitro

10.8 Additional images from the engine dyno test showcase the valve seat damages specifically observed in the ADI 280 material.

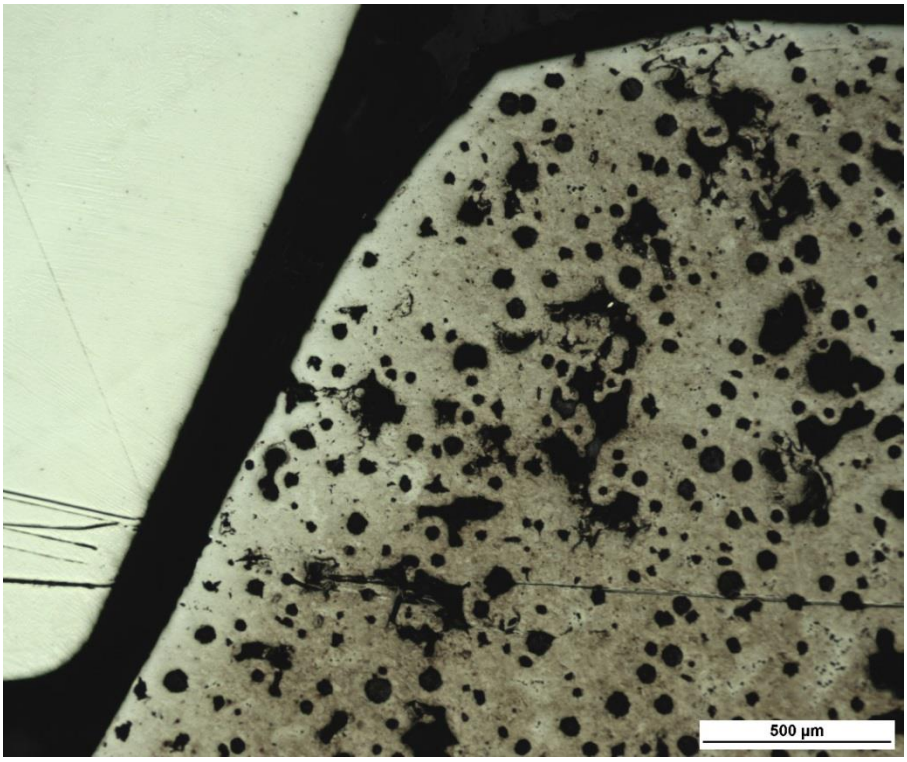

Fig. 113 Discontinuous cross-section of a grooved intake valve seat ADI 280.

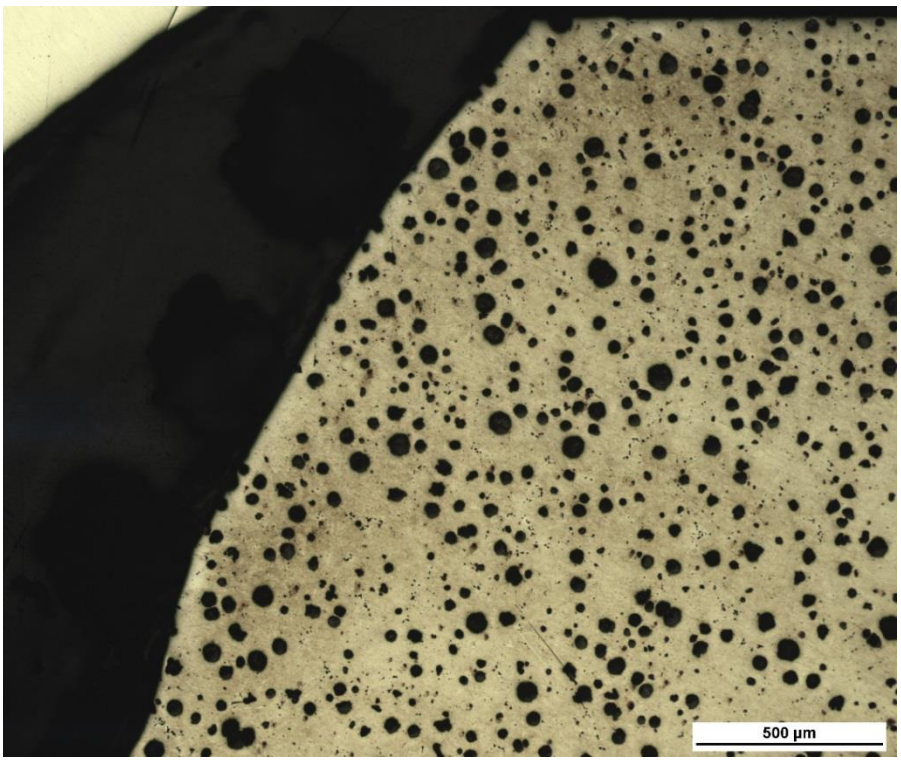

Fig. 114 For comparison with the surface of a flawless valve seat ADI 280.